Utrecht University
Faculty of Geosciences
Department of Earth Sciences

Jinfeng Liu – Mechanical effects of sorption processes in coal and implications for coalbed methane recovery

USES 111

ISSN 2211-4335

111

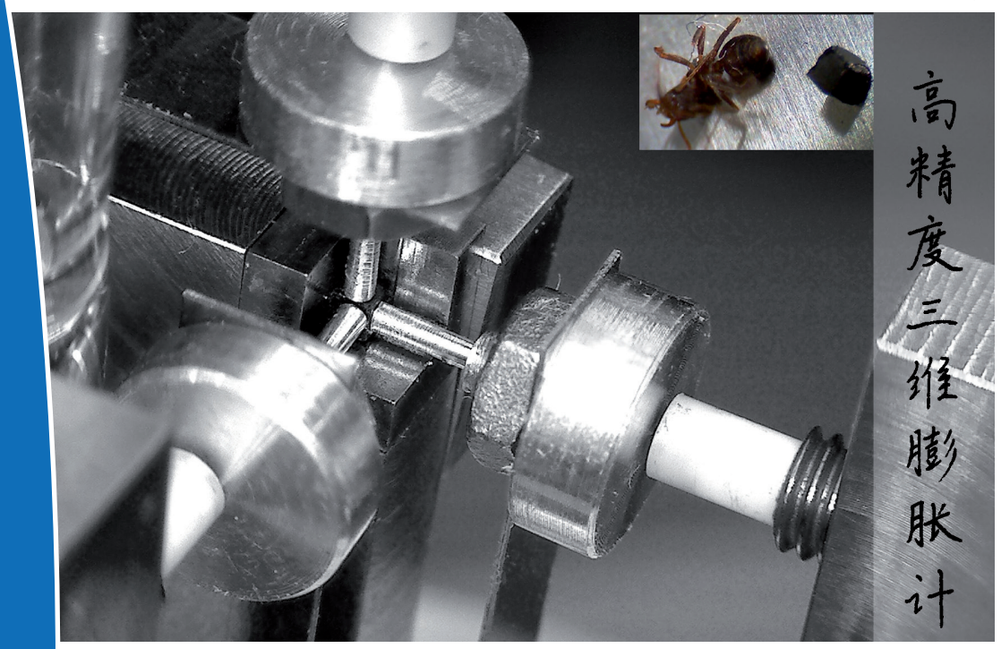

Mechanical effects of sorption processes in coal and implications for coalbed methane recovery

Jinfeng Liu

UTRECHT STUDIES IN EARTH SCIENCES

USES111-cover-Liu.indd 1 01-08-16 08:51

Mechanical effects of sorption processes in coal and implications for coalbed methane recovery

Jinfeng Liu

Utrecht University

No. 111

Members of the dissertation committee:

Prof. dr. ir. C.J. van Duijn
Eindhoven University of Technology, The Netherlands
and
Utrecht University, The Netherlands

Prof. dr. S. Durucan
Imperial College London, United Kingdom

Prof. dr. D. Elsworth
Pennsylvania State University, United States of America

Prof. dr. H. Zhou
China University of Mining and Technology, Beijing, China

Dr. B.M. Krooss
RWTH Aachen University, Germany

The research was carried out at:
High Pressure and Temperature Laboratory, Department of Earth Sciences, Faculty of Geosciences, Utrecht University
(Budapestlaan 4, 3584 CD Utrecht, The Netherlands)

Cover illustration: The cover is designed by M. Stoete, and the figure by Jinfeng Liu and Lizhong Wang. The apparatus shown is a high resolution 3D dilatometer, designed by E. de Graaff, with its name in Chinese written by Jingwei Zhang.

Printed by: Gildeprint

Copyright © Jinfeng Liu
All right reserved. No parts of this publication may be reproduced in any form, by print or photo print, microfilm or other means, without written permission by the publisher.

ISBN/EAN: 978-90-6266-435-1

Mechanical effects of sorption processes in coal and implications for coalbed methane recovery

Mechanische effecten van sorptie processen in kolen
en implicaties voor coalbed methaan winning

(met een samenvatting in het Nederlands)

Proefschrift

ter verkrijging van de graad van doctor aan de Universiteit Utrecht op gezag van de rector magnificus, prof.dr. G.J. van der Zwaan, ingevolge het besluit van het college voor promoties in het openbaar te verdedigen op vrijdag 23 september 2016
des middags te 4.15 uur

door

Jinfeng Liu

geboren op 30 augustus 1985
te Dongying, Shandong, China

Promotor: **Prof. dr. C.J. Spiers**

Copromotoren: **Dr. C. J. Peach**
Dr. P. A. Fokker

Dit proefschrift werd (mede) mogelijk gemaakt met financiële steun van Total S. A., France en The China Scholarship Council.

To youth

Table of Contents

Summary **11**

Chapter 1 General Introduction **19**

1.1. Motivation for this study: Enhanced Coalbed Methane production *20*

1.2. Coal and coalbed methane recovery *22*

1.3. Sorption processes in coal *24*

1.4. Mechanical effects on sorption processes in coal-CH_4 and coal-H_2O systems: an unsolved issue *28*

1.5. Scope and aims of this thesis *30*

References *33*

Chapter 2 Thermodynamic models for swelling of unconfined coal due to adsorption of mixed gases **41**

Abstract *42*

2.1. Introduction *43*

2.2. Modeling *49*

2.2.1. Hol and Spiers model for swelling due to adsorption of a single, pure gas or fluid 49

2.2.2. Present model development: Starting assumptions and cases considered 51

2.3. Comparison of model predictions with experimental data *64*

2.3.1. The data of Day et al. 64

2.3.2. End-member model parameters and calculation method 66

2.3.3. End-member models vs. the experimental data 69

2.3.4. Model 4 vs. Day et al.'s data 70

2.4. Discussion *73*

2.4.1. Physical meaning of model parameters and implications for Bowen Basin coal 74

2.4.2. Application of the generalized model (Model 4) to other coals and gas mixtures 75

2.4.3. Limitation of the present study 76

2.5. Conclusions *77*

Acknowledgements *79*

References *79*

Chapter 3 Effect of lithostatic stress on methane sorption by coal: Theory vs. experiment and implications for predicting in-situ coalbed methane content **83**

Abstract *84*
3.1. Introduction *85*
3.2. Theoretical model *87*
3.2.1. Attachment energy for adsorption of a single molecule by stressed coal 90
3.2.2. Adsorption energy for n molecules 95
3.2.3. Chemical potential per molecule for n molecules adsorbed by stressed coal 98
3.2.4. Equilibrium concentration of adsorbed species α in stressed coal 99
3.2.5. Adsorption under stress-free conditions 103
3.2.6. Adsorption under hydrostatic applied stress 105
3.2.7. Adsorption under stressed versus unstressed conditions: A comparison 105
3.3. Experimental test of the effect of hydrostatic stress on adsorption of CH_4 by coal *107*
3.3.1. Methods 107
3.3.2. Results 116
3.4. Discussion *121*
3.4.1. Experimental data versus theory 121
3.4.2. In-situ CBM content predicted by our model 126
3.5. Implications for (E)CBM *129*
3.5.1. Effect of lithostatic stress on CBM saturation and its impact on production 129
3.5.2. Effect of lithostatic stress on coal seam permeability 131
3.5.3. Suggestions on strategies of (E)CBM production and CO_2 sequestration in coal seams 132
3.6. Conclusions *133*
Appendix I *135*
Acknowledgements *138*
References *138*

Chapter 4 Coupling of swelling, internal stress evolution and diffusion in coal matrix material during exposure to methane **143**
Abstract *144*
4.1. Introduction *145*
4.2. Theoretical models *149*
4.2.1. Starting assumptions 149
4.2.2. Assumed diffusion mechanisms and governing equations 152
4.2.3. Time-dependent swelling of a spherically symmetric coal particle 157
4.3. Swelling experiments on coal exposed to CH_4 *161*

4.3.1. Sample material and preparation 161
4.3.2. Experimental methods 163
4.3.3. Experimental results 164
4.4. Model fits *166*
4.4.1. Choice of fixed parameter values 166
4.4.2. Model results 169
4.5. Discussion *171*
4.5.1. Mechanisms for diffusion occurring inside the coal matrix material 172
4.5.2. Swelling data for CH_4 pressure cycles 1 vs. 2 178
4.5.3. Comparison with previous work 179
4.5.4. Likely implications for ECBM 181
4.6. Conclusions *182*
Acknowledgements *183*
References *184*

Chapter 5 Anisotropic swelling behaviour of coal matrix cubes exposed to water vapour: Effects of relative humidity and sample size **189**
Abstract *190*
5.1. Introduction *191*
5.2. Experimental methods *194*
5.2.1. Approach 194
5.2.2. Starting material and sample preparation 194
5.2.3. Apparatus 196
5.2.4. Dilatometer calibration and corrections 199
5.2.5. Testing procedure 201
5.2.6. Data acquisition and processing 202
5.3. Results *204*
5.3.1. Swelling strain development with time 204
5.3.2. Equilibrium swelling strain versus relative humidity 207
5.3.3. Equilibrium volumetric swelling strain versus relative humidity 208
5.3.4. Optical observations on samples before and after testing 212
5.4. Discussion *213*
5.4.1. Anisotropic swelling and hysteresis 213
5.4.2. Effects of sample size on equilibration rate and equilibrium swelling strain 219
5.4.3. Relationship between equilibrium swelling strain and RH: comparison with theory 221

5.4.4. Implications for ECBM 227
5.5. Conclusions *229*
Appendix *230*
Acknowledgements *234*
References *234*

Chapter 6 Effect of applied stress on swelling of coal due to adsorption of water **239**
Abstract *240*
6.1. Introduction *241*
6.2. Thermodynamic models for swelling of coal matrix material due to adsorption of water under a general stress state σ_{ij} *244*
6.2.1. Starting assumptions and cases considered 244
6.2.2. Model 1: Monolayer sorption/swelling model (modified Hol and Spiers model) 247
6.2.3. Model 2: Dent-based swelling model 250
6.2.4. Model 3: DW-based swelling model 251
6.2.5. Swelling under stressed versus unstressed conditions: A comparison of model predictions 253
6.3. Experiments *253*
6.3.1. Staring materials and sample preparation 254
6.3.2. Apparatus 257
6.3.3. Testing procedures 258
6.3.4. Calibrations 261
6.3.5. Data acquisition and processing 262
6.4. Results *264*
6.4.1. Compression test data: P_disc_5 vs. pre-compacted Powder_1 264
6.4.2. Swelling data: P_disc_5 vs. pre-compacted powdered samples 269
6.4.3. Swelling kinetics data 273
6.5. Discussion *274*
6.5.1. Mechanisms responsible for the stress-driven reduction in swelling 275
6.5.2. Comparison of the samples used in the present study: disc versus powders 287
6.5.3. Effect of water on mechanical response of the samples 289
6.5.4. Likely implications for (E)CBM 289
6.6. Conclusions *291*
Acknowledgements *292*

References *293*

Chapter 7 Conclusions and suggestions for future research **297**

7.1. Main conclusions *299*

7.1.1. Swelling of unconfined coal matrix upon adsorption of mixed gases: Thermodynamics models 299

7.1.2. Effect of lithostatic stress on methane sorption by coal: Theory vs. experiment 300

7.1.3. Coupling of swelling, internal stress evolution and diffusion in coal matrix material during exposure to methane 301

7.1.4. Anisotropic swelling behaviour of coal matrix cubes exposed to water vapour: Effects of relative humidity and sample size 302

7.1.5. Effect of applied stress on swelling of coal upon adsorption of water 303

7.2. Implications for ECBM production *304*

7.3. Suggestions for future research *307*

References *311*

Samenvatting **313**

Acknowledgements **321**

Curriculum Vitae **326**

Summary

Subsurface coal seams generally consist of low permeability coal matrix material cross cut by a multiscale network of joints or cleats. These systems often contain large amounts of methane (CH_4) and water, in part trapped in fluid form in the cleat system but mostly trapped in adsorbed form in the nanoporous coal matrix. Other gases, such as CO_2, N_2, can also be adsorbed by coal matrix material. The adsorption of these gas species causes coal swelling of several percent, while desorption produces similar shrinkage. The swelling/shrinkage response of the coal matrix to adsorption/desorption strongly influences coal seam (fracture) permeability under in-situ conditions (i.e. under laterally confined conditions), and is therefore of key importance in determining the feasibility of methane extraction from coal via (enhanced) coalbed methane (ECBM) production. ECBM typically involves injection of preferentially sorbing CO_2 into a coal seam to enhance methane extraction, and it is a potential means of long-time geological storage of CO_2. However, a coupling between stress, strain and sorption in coal-CO_2 system resulted in a major reduction in CO_2 injectivity and poor CH_4 recovery in almost all field experiments performed to date. Against this background, removing adsorbed water and CH_4 from coal seams, for example by N_2 flushing or other novel methods, might initiate self-enhancing shrinkage and (micro)cracking of the coal, hence enhanced methane production. However, the coupling between stress, strain, sorption and diffusion in coal-CH_4 and coal-H_2O systems is still poorly understood. In this thesis, I present the results of a theoretical and experimental study of the response of dry coal matrix material to pure CH_4, pure H_2O and CH_4-CO_2 mixtures under in-situ (E)CBM conditions, with the aim of providing fundamental data that can contribute to assessing future strategies for ECBM.

In **Chapter 1**, the scope and scientific context of this thesis are introduced, as well as a discussion of previous work. The key knowledge gaps are identified on this basis. The aims of the current thesis are then defined.

The first core issue addressed in the thesis (**Chapter 2**) is the swelling of unconfined

coal matrix due to adsorption of mixed gases. To tackle this, I develop new thermodynamic models, addressing the equilibrium state and specifically focusing on a binary gas mixture. Four models were derived, covering three possible end-members interactions, plus a generalized case. The end-member models correspond to adsorption of gases α and β at fully separate sites (Model 1), at fully shared sites (Model 2) and at partially shared sites (Model 3). Another model, Model 4, describes a general case, covering Models 1-3. Model predictions were compared with literature data on the swelling behaviour of Bowen Basin coal exposed to CH_4/CO_2 mixtures at total pressures up to 15MPa and at 55˚C. The experimentally observed swelling for Bowen Basin coal was best explained by Model 3. This implies that adsorption and swelling for this type of coal is determined by both the partial pressures of the gas species and by selective adsorption (preferred affinity for sorption) of the gas species at the adsorption sites. It follows that Model 3 should be the most suitable for evaluating whether CO_2-N_2 mixtures will be effective in limiting coal swelling and permeability reduction in ECBM operations in sub-bituminous coals, such as those of the Bowen Basin. Another advantage of Model 3 is that it is easy to parameterize and its applicability to specific coals and gas mixtures is easily evaluated. Though more difficult to parameterize, the generalized swelling model (Model 4) can be applied to any coal rank, and to any binary gas mixture. Its broader applicability therefore makes it an important tool for modeling swelling and coal seam (fracture) permeability evolution during ECBM operations.

In **Chapter 3**, the effect of a lithostatic stress on CH_4 sorption by coal is investigated. I revise and generalize an existing thermodynamic model, derived by Hol and Spiers (2012a), for the effects of stress on CO_2 sorption by coal and apply this to CH_4. The revised model predicts that in-situ CBM content is indeed determined not only by the geological factors generally considered, such as coal rank, coal composition, moisture content and temperature, but also by lithostatic or confining stress, which is usually ignored. This prediction was tested by means of experiments performed on a composite

cylindrical (solid) sample of Brzeszcze 364 high volatile bituminous coal subjected to 10 MPa methane pressure at a temperature of 40˚C, varying the hydrostatic stress in the range 11 to 43MPa. In these experiments, I quantified the amount of CH_4 desorbed from the coal matrix as a result of an increase in hydrostatic stress exerted onto the coal sample, by subtracting the poroelastic expulsion of CH_4 from the total CH_4 expelled, assuming the former to equal the gas volume expelled in control experiments with Helium. The experimental results show that the equilibrium sorption capacity for CH_4 at 10 MPa gas pressure and 11 MPa confining pressure (1 MPa Terzaghi effective stress) was 0.808 mol/kg_{coal}. This was reduced by at least ~6% when increasing the confining pressure to 43 MPa (33 MPa effective stress). These measurements are in line with the revised model predictions, confirming its validity. I apply the model to predict in-situ CBM concentration as a function of coal seam depth for dry, high volatile bituminous coal, assuming a geothermal gradient of 32˚C/km. The results indicate a maximum CH_4 concentration of ~0.76 mol/kg_{coal} at a burial depth of ~900 m, which is ~3% lower than conventional predictions. Though this difference is relatively minor, it helps explain why gas saturation in subsurface coal seams is generally lower than expected from conventional sorption measurements on unconfined coal powders. More importantly, the results confirm that there is an intimate coupling between in-situ stress, strain and sorption in coal that needs to be considered when developing gas-enhanced CBM strategies, regardless of gas species involved.

The coupling between swelling, internal stress evolution, sorption and diffusion in coal matrix material exposed to methane is further investigated in **Chapter 4**. I construct theoretical models for time-dependent swelling of coal matrix material upon adsorption of a single gas, taking into account the coupled effects of stress, strain, chemical potential and diffusion. Two models were developed. These correspond to diffusion and hence swelling rates being controlled by the jump frequency of adsorbed molecules between closely spaced adsorption sites (Model A), versus transport controlled by

diffusion of unadsorbed molecules through diffusion paths linking distant adsorption sites (Model B). To test the validity of these models, I performed axial swelling experiments on a single 4mm sized cylindrical sample of, medium volatile bituminous coal, exposed to CH_4 at gas pressures up to 40 MPa, and at a constant temperature of 40˚C, using 1D high pressure dilatometry. The experimental data are compared with the model predictions, and show that time-dependent swelling of the coal sample upon adsorption of CH_4 is well explained by Model B, using a single diffusion coefficient, independent of gas pressure and adsorbed concentration. The implication is that time-dependent swelling was controlled by the diffusion of unadsorbed molecules and not by the jump frequency of adsorbed molecules or by pore size distribution effects cited in the literature. The models demonstrate that swelling-driven internal stress evolution can significantly influence adsorption and diffusion in coal matrix material, if the partial molar volume (V_0) of the adsorbed molecules is sufficiently large. However, in the present experiments the effect seems to have been negligible compared to that of the diffusion mechanism, as V_0 for CH_4 sorption by coal is small. Nonetheless, the models presented describe a full coupling between stress, strain, sorption and diffusion in coal matrix material in terms of parameters that have clear physical meaning and are easily obtained from sorption and swelling experiments on coal of any rank and exposed to any gas. They therefore offer an important basis for modelling permeability evolution with time during (enhanced) coalbed methane operations.

Another important issue for ECBM production is the need to accurately determine the swelling/shrinkage of coal matrix material due to adsorption/desorption of water vapour. In **Chapter 5**, I report dilatometry experiments conducted on 1 and 4 mm sized cubic samples of Brzeszcze high volatile bituminous coal. These were performed using a sensitive, purpose-built, 3-dimensional (3D) dilatometer. The aim was to accurately and continuously measure the volumetric response of coal matrix material during exposure to water vapour at relative humidities varied in the range of 0.1 to 95%, at a temperature

of 40˚C. The results show that the swelling strains attained at apparent equilibrium tend to be a factor of up to 1.45 higher perpendicular to bedding than in the bedding plane. In addition, the sample size strongly influences the swelling kinetics, but not the equilibrium swelling strains. The volumetric swelling strains attained at equilibrium show a near-linear dependence on relative humidity, reaching 1.37-1.43% at around 95% relative humidity. In an attempt to explain the observed behaviour, three models for swelling of unconfined coal matrix material due to water sorption were developed. These correspond to mono-layer adsorption, multiple-layer sorption, and combined mono- plus multiple-layer sorption. The experimental data are equally well fitted by all three models, so that the mechanism responsible for swelling could not be uniquely identified. However, the findings do demonstrate that decreasing in-situ water activity causes significant anisotropic shrinkage of coal matrix material, pointing to injection and recirculation of dry nitrogen as a promising strategy for stimulating coal seams for CBM production and as a pre-treatment for later CO_2 injection and storage.

Chapter 6 attempts to determine whether or not applied stress significantly reduces the swelling response of coal caused by exposure to and adsorption of water, and, if so, to determine the mechanisms responsible. Such an effect would reduce the effectiveness of coal drying, by procedures such as N_2 flushing and shrinkage, as a stimulation option. To achieve my aims here, I first extend the thermodynamic model developed in Chapter 3 for the stress-strain-sorption behaviour of coal matrix material to address not only monolayer but also multiple layer adsorption of water. I then report the results of experiments designed to determine the effects of applied stress on swelling strain development in coal samples exposed to distilled water at atmospheric pressure (0.1 MPa). The experiments were performed on both coal disc and pre-compacted powder samples of Brzeszcze high volatile bituminous coal at a constant temperature of 40˚C, using a unaxial compaction apparatus. The mechanical response of the samples under both vacuum (i.e. 0% relative humidity) and wet (i.e. 100% relative humidity)

conditions were first examined. The evacuated samples showed reversible, elastic behaviour. Wet samples exhibited elastic deformation, time-dependent reversible deformation, plus permanent time-dependent deformation (creep). Axial swelling strains are measured for samples due to adsorption of distilled water (i.e. 100% relative humidity) at a constant fluid pressure of 0.1 MPa, under constant applied uniaxial stresses (25-100 MPa). The experimental results demonstrate the swelling strains due to water adsorption attained at (apparent) equilibrium were reduced by applied stresses. Comparison with predictions made using the three models investigated shows that stress-driven reduction in sorption-induced swelling is caused by the combined effects of a) permanent time-dependent (compressive) deformation (creep), b) the thermodynamic effect of a stress-driven reduction in water sorption capacity and c) stress-driven closure of transport paths within the coal matrix. For the solid disc investigated, mechanism (c) contributed mostly, while for powdered samples, mechanism (a) dominated. Nonetheless, the results show that the effects of stress on the swelling response of (Brzeszcze) high volatile bituminous to water are small, and in fact negligible at typical in-situ stresses of 10-30 MPa. This means that large shrinkage effects due to drying seen in unconfined experiments should not be changed by in-situ stresses. Therefore, flushing water from coal seams under in-situ (E)CBM may indeed offer potential for initiating self-enhancing shrinkage and (micro)cracking of the coal, thus enhancing methane production.

Chapter 7 summarises the main findings and considers the implications of this work for ECBM. Unanswered questions are identified and suggestions for future research are made. The major overall conclusions that can be drawn for (E)CBM are as follows: First, in-situ lithostatic stresses will directly reduce the sorption capacity of coal matrix. This effect will lead to lower CBM content predictions than made previously using conventional methods. Second, swelling rates upon CO_2 injection appear to be much higher than shrinkage rates upon CBM recovery. This implies that using CO_2 stimulation

as a technique for secondary enhanced CBM recovery may not be the best strategy. Third, using (liquid) N_2 as a hydraulic-fracturing fluid to stimulate the coal seams for CBM production, then circulating dry N_2 to promote shrinkage due to removal of adsobed water and methane might be a suitable strategy for (E)CBM recovery. After methane recovery, CO_2 can be injected into the coal seam for geological storage, resulting in self-sealing of fractures in the coal bed system due to the relatively large swelling strain caused by CO_2 sorption.

Chapter 1

General Introduction

1.1. Motivation for this study: Enhanced Coalbed Methane production

Coal seams contain vast quantities of adsorbed natural gas (methane), the cleanest and least CO_2 intensive fossil fuel (Moore, 2012; White et al., 2005). Global warming and increasing energy demand are accordingly driving coal-rich countries to consider extracting methane (CH_4) from, and storing its carbon dioxide (CO_2) combustion product in, both unminable and recently even mineable coal seams (e.g. Damen et al., 2005; Reeves, 2001; White et al., 2005). Indeed, CO_2-enhanced coalbed methane (ECBM) production coupled with the storage of CO_2 in subsurface coal seams forms a topic of intense ongoing interest in the energy sector. Several demonstration projects (e.g. in Canada, U.S.A., Poland, Japan and China) have shown the potential of enhanced coalbed methane (ECBM) production (Fujioka et al., 2010; Mavor et al., 2004; van Bergen et al., 2009a; van Bergen et al., 2006; White et al., 2005; Wong et al., 2007). However, commercial application still has to be realized and most sites to date have experienced rapid permeability reduction in the coal seam, leading to operational difficulties such as reduced injectivity with time (e.g. Fujioka et al., 2010; van Bergen et al., 2009a; Wong et al., 2007) and the need for stimulation measures (e.g. Fokker and van der Meer, 2004).

This reduction in permeability is generally recognised to be caused by the net swelling of the coal matrix as a result of CO_2 injection and preferential sorption over CH_4, with fine scale kinetic control by diffusion processes (Busch and Gensterblum, 2011; Busch et al., 2003; Busch et al., 2004; Cui et al., 2007; Day et al., 2010; Durucan and Shi, 2009; Hol et al., 2012a; Karacan, 2003; Liu et al., 2011a; Peng et al., 2014; Shi and Durucan, 2003; van Bergen et al., 2009b; Viete and Ranjith, 2006; White et al., 2005). Field experiments and laboratory studies have shown that the key requirement for successful CO_2-ECBM is the presence of well-connected "transport paths" in the target coal seam, such as open fracture or pore networks, which enable gas flow (e.g. Levine, 1996; Liu et al., 2011a; Mazumder et al., 2006; Zhang et al., 2008). Understanding,

managing and stimulating the development of such transport paths in coal is therefore crucial for enabling, and predicting the performance of, future methane production and carbon dioxide storage operations in coal seams. Indeed, the main challenge in extracting CH_4 from coal, and storing CO_2 in its place, is to create sufficient transport paths and to maintain existing ones open, despite net swelling and resulting self-stressing of the coal upon the injection of CO_2. The dynamics of these processes and how they control reservoir behaviour presently still remain unclear.

The swelling and shrinking behaviour of coal upon exposure to fluids and gases is complex. Recent experimental research suggests that removing water can result in coal shrinkage, perhaps counteracting the swelling upon injection of CO_2 (Fry et al., 2009). In addition, it has been shown that injection of CO_2-N_2 mixtures instead of pure CO_2 potentially reduces swelling due to a smaller swelling effect of N_2 adsorption compared with CO_2 (Day et al., 2012; Durucan and Shi, 2009; Syed et al., 2013). Injectivity reduction experienced during ECBM operations imply a strong coupling between sorption behaviour, changes in the mechanical state of coal related to adsorption-induced swelling, and changes in coal seam transport properties (Espinoza et al., 2014; Hol et al., 2012a; Liu et al., 2011a; Nikoosokhan et al., 2014; Wang et al., 2012). Moreover, both theoretical and experimental studies have demonstrated this coupling in coal-CO_2 systems under in-situ stress conditions, and pointed out that increased in-situ stresses reduce the sorption capacity of the coal matrix through direct thermodynamic effects and gas accessibility effects (Hol et al., 2012a; Pan and Connell, 2007; Pone et al., 2009; Vandamme et al., 2010). However, understanding and quantifying this coupling between stress, strain, sorption and transport in coal-CH_4 and coal-H_2O systems, and the associated kinetic processes still presents a major challenge.

The motivation for the present thesis to help address this challenge, and to provide a basis for developing more advanced, predictive ECBM reservoir models. Such models are crucial for forecasting reservoir behaviour and hence for assessing the feasibility of

ECBM operations and for selecting optimum performance conditions. In this general introduction, I briefly review the state-of-the-art understanding on coal, coalbed methane, and sorption processes in coal, as well as the interactions between sorption, mechanical and transport processes in coal seam systems. I simultaneously identify the outstanding issues that need to be addressed and then define which of these issues have been tackled in the present PhD study.

1.2. Coal and coalbed methane recovery

Subsurface coal seams typically consist of coal matrix (solid) material cut by a multi-scale network of joints or cleats (Hol et al., 2012a; Laubach et al., 1998; Levine, 1996). At the sub-maceral scale, coal matrix material consists of a macromolecular network, built up of aliphatic- and aromatic-bonded carbon (50-96% C) plus mainly organically bonded oxygen and hydrogen. During coalification (i.e. formation of the coal), as the coal rank increases, so does the carbon content and the proportion of aromatic structures, ultimately yielding a graphite-like arrangement of carbon crystallites, at carbon contents higher than 95%. In such crystallites, the spacing between individual polyaromatic sheets is of the order of ~0.3 or 0.4 nm (Hirsch, 1954). The corresponding intersheet regions or sheet pores form the smallest void spaces in coal. The amount of nanoscale and polyaromatic porosity in this size range increases linearly with crystalline carbon content, as shown in sorption experiments (e.g. Busch and Gensterblum, 2011). The porosity in virgin coal matrix material (i.e. in the macerals) originates from pores of a range of sizes. Though somewhat inconsistent with current nanoscience terminology, the pores are usually classified as micropores (< 2 nm) mesopores (2-50 nm) and macropores (> 50 nm), following the IUPAC convention for colloid and surface chemistry (Harris et al., 2002). In this study, we will refer to the micro- and mesopores as "nanopores" thereby including nanoscale intermolecular voids, *i.e.* sheet pores between polyaromatic sheets. Cleats, the joint-like features present in

coal layers (Laubach et al., 1998) which cut the matrix into blocks, are formed as the result of matrix dehydration and shrinkage during coalification; their orientation is related to the tectonic stress field present during formation (Solano-Acosta et al., 2007).

Coal matrix-cleat systems often contain large amounts of methane (CH_4) and water, generated during coalification (Levine, 1993; Moore, 2012). Most of the trapped methane, typically ~95%-98%, is stored in the coal matrix via sorption (Gray, 1987; White et al., 2005). Upon desorption, the methane can be recovered in the form of natural gas – this is referred to as coalbed methane production or CBM production (Levine, 1996; Moore, 2012). Primary CBM recovery is achieved by reducing the gas and water pressures in the cleat system, thus enabling desorption and production of methane. Compared to conventional natural gas reservoirs, such as sandstone formations, however, coal beds have low permeability. This limits the potential of primary CBM production to 20-60% of the estimated reserves (White et al., 2005). Consequently, there are still large amounts of water and methane trapped in the coal matrix via sorption (Busch and Gensterblum, 2011). Other gases, such as N_2, CO_2 and flue gas, have therefore been injected in attempts to enhance the coalbed methane production – this is called ECBM (White et al., 2005). Of particular interest among these is CO_2-ECBM, because coal preferentially adsorbs CO_2 over CH_4 (Busch et al., 2003; Fitzgerald et al., 2005; Gensterblum et al., 2014; Merkel et al., 2015; Ottiger et al., 2008; Pini et al., 2010). Coal seams can therefore be viewed as a potential lithology for ECBM combined with geological storage of CO_2. The exchange, or preferential adsorption effect, is considered to be due to either the reduction of CH_4 partial pressure as CO_2 penetrates the system or to the truly selective adsorption of CO_2 over CH_4 (Busch and Gensterblum, 2011). A problem with CO_2-ECBM, however, is that the partial replacement of CH_4 by CO_2 leads to a net swelling, reflecting a new equilibration with respect to the composition of the gas/fluid mixture present in the coal seam (Busch and Gensterblum, 2011; Day et al., 2012). The swelling/shrinkage effects related to sorption and desorption

of both CO_2 and CH_4 strongly reduce the permeability in coal seams during CO_2-Enhanced Coalbed Methane (ECBM) production (Liu et al., 2011a). However, the effects of sorption of mixed gases (such as CO_2-CH_4 and CO_2-N_2 mixtures) on swelling of coal matrix material are still poorly understood.

Besides coal seam permeability development, the CBM gas content is a key factor in assessing the economic feasibility of (E)CBM production. Estimates of CBM content are generally based on the sorption capacity of unstressed coal powders determined in the laboratory by means of manometric, volumetric or gravimetric measurements (Busch and Gensterblum, 2011; Moore, 2012). It is well established that CH_4 sorption capacity is influenced by coal rank, coal composition, moisture content and temperature (Busch and Gensterblum, 2011; Bustin and Clarkson, 1998; Gensterblum et al., 2014; Gensterblum et al., 2013; Moore, 2012). However, the gas content measurements are usually performed under unconfined conditions, i.e. at zero conventional stress, or at zero Terzaghi effective stress where the fluid pressure equals the confining pressure and where sorption-induced swelling of the coal is opposed by the fluid pressure only (Busch and Gensterblum, 2011). Given that subsurface coal seams are confined, and the impact of stress on coal sorption, this also poses a knowledge gap for the assessment of ECBM economics.

1.3. Sorption processes in coal

Fluids (such as CO_2, CH_4, H_2O) that reside in the macropores, cleats and cracks of coal behave as a free phase, and they are transported according to Darcy's law. Molecular interactions between the coal and gas play no role at this scale and the equation of state (EoS) of the bulk gas will be obeyed. Accordingly, poroelastic theory (Biot, 1941; Wang, 2000) is expected to describe the stress-strain changes resulting from production or injection-induced fluid pressure changes in the macropore and cleat network (Yi et al., 2009). By contrast, in the nanopores and the molecular interstices,

with dimensions <30 nm, gas molecules are affected by surface forces that attract and physically adsorb them in a reversible manner (Busch and Gensterblum, 2011; Crosdale et al., 1998; Goodman et al., 2005; Krooss et al., 2002; Melnichenko et al., 2009; Moore, 2012; Radliński et al., 2009; Zhou and Zhou, 2009). Due to these molecular interactions with the solid, the equation of state used to describe the bulk phase is not applicable (Goodman et al., 2005; Melnichenko et al., 2009). It is these interaction forces between the solid surfaces (molecules) and adsorbed molecules that are responsible for adsorption and for the associated swelling of the coal (Goodman et al., 2005), which is accordingly quite different in origin from the poro-elastic deformation effects.

The physical adsorption of gas by coal, such as CO_2, CH_4, and N_2, occurs due to long-range van der Waals forces, attracting gas molecules into the nanoscale porosity of the coal matrix, and onto the surfaces of larger pores and cleats (Goodman et al., 2005; Radliński et al., 2009; Zhou and Zhou, 2009). The adsorption of gases such as CH_4, CO_2, is generally described by Langmuir-type behaviour, i.e. filling of available adsorption sites, and it is known to be affected by a number of physical factors, including the partial pressure of gas, the temperature, coal rank, and water content (Busch and Gensterblum, 2011; White et al., 2005). An increase in temperature and water content decreases gas adsorption; increasing the gas partial pressure increases adsorption. Coal rank has a variable effect: coals generally classified with low rank show a slight decrease in adsorption capacity with increasing coal rank, whereas coals classified with high rank show a slight increase in adsorption capacity with increasing coal rank. This is attributed to the micropore density (Prinz and Littke, 2005), and contents of oxygen-bearing functional groups (Gensterblum et al., 2014).

Unlike monolayer (Langmuir type) adsorption, adsorption of water by coal matrix is more complicated. Numerous studies have demonstrated that water molecules are primarily trapped by oxygen-bearing functional groups present in the coal matrix via hydrogen bonds (c.f. Allardice and Evans, 1971; Busch and Gensterblum, 2011; Kaji et

al., 1986; Mu and Malhotra, 1991; Suárez et al., 1993; Yu et al., 2013). This trapping mechanism usually forms a first layer of adsorbed water molecules with relative high binding energy (c.f. Dubinin, 1980; Dubinin and Serpinsky, 1981). The thus-adsorbed water molecules form the secondary sites for attachment of additional water molecules with lower binding energy, thereby forming water clusters (c.f. Charrière and Behra, 2010; Lynch and Webster, 1982; McCutcheon et al., 2003; Nishino, 2001; Švábová et al., 2011). The total water adsorption capacity of coal is directly related to water activity or relative humidity, and is well described by the Dent model and D'Arcy and Watt model (Charrière and Behra, 2010; McCutcheon et al., 2003; Švábová et al., 2011).

Swelling is the first striking mechanical effect of adsorption of gas exhibited by coal matrix material. Numerous laboratory studies have been performed to determine the magnitude of coal swelling upon adsorption of CO_2 and of CH_4. In these studies, unconfined coal samples were typically exposed to gas at pressure and temperature conditions relevant to ECBM operations (e.g. Cui et al., 2007; Day et al., 2008a, 2012; Day et al., 2010; Durucan et al., 2009; Espinoza et al., 2013; Hol and Spiers, 2012; Levine, 1996; Majewska et al., 2010; Mazumder et al., 2006; Pan and Connell, 2009; van Bergen et al., 2009b; Vandamme et al., 2010). These studies have shown that the observed swelling of coal is directly related to the gas pressure and to the amount of gas adsorbed (Astashov et al., 2008; Day et al., 2008a; Day et al., 2010; Hol et al., 2012a; Hol and Spiers, 2012; Kelemen and Kwiatek, 2009; Pini et al., 2009). By contrast, only a few studies focused on swelling/shrinkage of coal during exposure to water vapour. Suuberg et al. (1993) reported up to 30% volumetric shrinkage of coal upon drying, for various coal ranks ranging from bituminous to lignite. The measured volumetric shrinkage was shown to be linearly related to the mass loss upon drying. A similar linear relation between sample volume change and water content of coal, ranging from sub-bituminous to bituminous, was also reported by Fry et al. (2009). These authors measured swelling behaviour of coal blocks ($3\times1\times1 cm^3$) during exposure to water

vapour at up to 97% RH (relative humidity) at room temperature, using both screw micrometer and optical methods.

Time-dependent sorption and the associated swelling of coal is generally considered to be controlled by diffusion, as experimental studies show that sorption and swelling rates strongly depend on coal sample or particle size (Busch and Gensterblum, 2011; Busch et al., 2004; Gruszkiewicz et al., 2009). Since transport through open fractures or cleats in coal is relatively rapid, the process controlling the diffusion kinetics is the diffusion through the coal matrix. Many experimental studies have been performed on the sorption kinetics of coal with respect to CH_4, CO_2 and N_2 (c.f. Busch and Gensterblum, 2011). They typically focus on the time-evolution of sorbed concentration, i.e. the approach to equilibrium, that follows a step change in gas pressure applied to a granular coal sample. The (apparent) diffusion coefficients controlling sorption rate are then calculated by fitting a diffusion model to the transient sorption data. The most widely applied diffusion models are the so-called unipore and bidisperse models (c.f. Busch and Gensterblum, 2011). Both modelling approaches are based on Fick's laws of diffusion within the pore networks considered (c.f. Busch and Gensterblum, 2011), meaning that driving force for diffusion is the concentration gradient of the diffusing (gas) species within the coal, and that swelling of coal matrix and associated internal stress development are negligible for the diffusion characteristics (e.g. Busch and Gensterblum, 2011; Busch et al., 2004; Clarkson and Bustin, 1999; Cui et al., 2004; Shi and Durucan, 2003). However, the unipore model assumes diffusion through a network of unimodally distributed nm-scale pores. The bidsperse model assumes a bimodal distribution of pore sizes supporting different diffusion mechanisms and rates, specifically a fast diffusion along the macropores controlled by molecule-molecule collision or viscous flow and a slow diffusion along the micropores controlled by molecule-pore walls collision or surface diffusion (c.f. Clarkson and Bustin, 1999; Cui et al., 2004; Shi and Durucan, 2003). The (apparent) diffusion coefficients obtained by

fitting these models, analytically or numerically, are generally found to depend not only on coal rank, gas species, and temperature, but also on external gas pressure/density and adsorbed concentration (e.g. Busch and Gensterblum, 2011; Busch et al., 2004; Clarkson and Bustin, 1999; Cui et al., 2004; Shi and Durucan, 2003; Staib et al., 2013). The dependence on gas pressure is generally argued to be caused by changes in diffusion mechanism in the coal due to changes in mean free path of gas molecules upon changes in external gas pressure (Clarkson and Bustin, 1999; Cui et al., 2004), and by opening or closure of transport paths -- shrinkage versus swelling of the coal due to desorption and adsorption (Busch et al., 2004; Shi and Durucan, 2003). It should be noted though that none of the models described above consider the potential effects of swelling and internal stress evolution within the coal on sorption capacity or on the driving force for the diffusion process. However, these effects cannot be ignored in the context of ECBM operations.

1.4. Mechanical effects on sorption processes in coal-CH_4 and coal-H_2O systems: an unsolved issue

During (E)CBM production, ad/desorption of fluid species such as CO_2 and CH_4 causes swelling/shrinkage of coal, hence leading to changes in stress state and inevitably in cleat permeability under in situ conditions where displacements are constrained (Espinoza et al., 2014; Liu et al., 2011a; Liu et al., 2011b; Nikoosokhan et al., 2014; Pan and Connell, 2012). The change in stress state also results in changes in the ad/desorption process. Hol et al. (2011; 2012a) investigated the coupling of stress-strain-sorption behaviour in a coal-CO_2 system, and developed a thermodynamic model to describe how the equilibrium concentration of fluid species adsorbed by coal is affected by compressive stresses applied in excess of the fluid pressure. The model was experimentally proved to apply to CO_2 by the authors in the context of investigating CO_2-ECBM. However, a number of errors were made in deriving this model, and

although the form of the final equations obtained is correct, the physical meaning of the equilibrium constant for sorption that appears is not. The equilibrium constant in their model depends strongly on both temperature and gas pressure, whereas for a given reaction it should depend on temperature only (Chang, 2000; Hill, 2012). A corrected thermodynamic model is therefore needed to properly capture the process of gas adsorption by stressed coal and to predict the true equilibrium CBM content of coal and the associated swelling strain response, under in-situ conditions where the coal experiences large compressive effective stresses.

Pone et al. (2009) measured the CH_4 sorption capacity of bituminous coal (a cylinder of 25mm in diameter) under both stressed (confined) and unstressed (unconfined) conditions using volumetric methods. They presented evidence that confining stresses of 6.9 and 13.8MPa caused a reduction in CH_4 sorption capacity of 85% and 91% respectively, at a CH_4 pressure of 3.8MPa at room temperature. It is unclear, though, how much of this reduction was due to a direct effect of stress on equilibrium sorption capacity versus or to a reduction in the volume of coal sample that was accessible to CH_4 due to a decreasing sample permeability with increasing confining stress. To obtain a reliable estimate of in-situ CBM content, a physically based and experimentally verified stress-strain-sorption model is required that describes the effect of in-situ stress on the CH_4 sorption capacity of coal at thermodynamic equilibrium.

Adsorption of water by coal, unlike adsorption of CH_4 and CO_2, is widely accepted to form multiple layers. However, no attention has to date been given to the effect of in-situ stress on water sorption and the associated swelling and it is still unknown whether the in-situ stress reduces the sorption capacity of water by coal, and thereby reducing the associated swelling. Moreover, it is still unclear whether the applied stresses would close the micro-pores or pre-existing cracks inside the coal matrix, and hence reducing the access of water vapour into the matrix (Cui et al., 2004; Day et al., 2008b; Hol et al., 2011; Hol et al., 2012b; Pone et al., 2009), and whether permanent

compaction creep would occur when the coal is subjected to a stress state during long-time exposure to water. Understanding these effects on deformation of coal matrix also plays an important role in optimizing ECBM operation strategies.

Furthermore, it is important to understand how the coupled effects of swelling, internal stress evolution, adsorption and diffusion influence the swelling kinetics of coal matrix material when exposed to an adsorbing gas. Mazumder et al. (2011) applied models developed for non-Fickian diffusion in polymers to describe CO_2 diffusion in coal. They made the observation that similar effects of swelling on diffusion of solvent molecules occurred in polymers (Govindjee and Simo, 1993; Hui et al., 1987a, b; Thomas and Windle, 1982). In polymers, a transition from a glassy phase to a rubbery phase can take place when solvent molecules penetrate the polymer structure, causing polymer swelling (Haward, 2012). As a result, diffusion does not obey Fick's equations: the driving force originates from the gradient in both swelling stress and the solvent concentration (Govindjee and Simo, 1993; Hui et al., 1987a, b; Thomas and Windle, 1982). Mazumder et al., 2011 employed these models upon the assumption that coal matrix material behaves as a glassy polymer that undergoes this transition when CO_2 penetrates (Goodman et al., 2006; Karacan, 2007; Larsen, 2004; Mazumder et al., 2011). However, it still remains unclear whether or not this phase transition actually does occur (Hol et al., 2012b). It should be noted here that far fewer studies have been conducted on the kinetics of coal matrix swelling due to adsorption than on sorption kinetics without consideration of swelling effects. More importantly, little attention has been given to relating inhomogeneous swelling to diffusion, adsorption and internal stress evolution, despite the fact that swelling behaviour plays such an important role in coal seam permeability evolution during (E)CBM production.

1.5. Scope and aims of this thesis

This thesis focuses on the mechanisms, dynamics and thermodynamics that

determine the coupling between mechanics, sorption and diffusion of dry coal matrix material under isothermal conditions, including the effects of a pure fluid or gas (such as CH_4, H_2O) and a gas mixture (such as a CH_4-CO_2 mixture or mixtures involving water or nitrogen). Effects addressed include sorption of a pure gas and of binary gas mixtures by coal and the associated swelling, diffusion and swelling kinetics, the effects of in-situ stresses on adsorbed concentrations, and the coupled effects of swelling and stress on sorption and diffusion. The implications for the behaviour of coal under in-situ ECBM conditions are also considered.

The specific aims of the thesis are:

1. To develop thermodynamic models for the swelling of unconfined coal matrix upon adsorption of mixed gases. As a first step, the models considered address the equilibrium state and focus on binary gas mixtures, treating three possible end-member interactions between coal matrix and mixed gases plus a generalized case (see Chapter 2).
2. To evaluate more rigorously the magnitude of the effect of in-situ lithostatic stresses on the sorption capacity of coal matrix material in relation to predicting in-situ coalbed methane (CBM) content. This is done by revising the previously-developed thermodynamic model by Hol et al. (2012a), describing the effects of stress on CO_2 sorption by coal, and applying it to CH_4 with experimental verification (see Chapter 3).
3. To determine the coupled effects of swelling, internal stress evolution, chemical potential and diffusion on the swelling kinetics of coal matrix material during exposure to methane (see Chapter 4).
4. To accurately quantify and explain the volumetric response of coal matrix to exposure to water vapour at relative humidities in the range 0.1-95% under unconfined conditions, and to determine the effect of sample size on both swelling kinetics and equilibrium swelling strains (see Chapter 5).

5. To determine whether applied stresses reduce the swelling of coal upon adsorption of water, and if so to further investigate the likely mechanisms responsible for the stress-driven reduction in swelling observed in the experiments (see Chapter 6).
6. In the experimental studies presented in Chapters 3-6, small, matrix-scale samples (i.e. crushed or powdered samples, or mm-sized cylinders or cubes) are used to eliminate any effect related to the presence of cleats and to obtain a purely matrix-related understanding of the response of coal to CH_4, H_2O. This enables the models developed for coal matrix behaviour to be tested independently of larger scale effects of the cleat system. The basic observations and conclusions drawn in this thesis are analysed in an attempt to assess the implications for CBM and ECBM reservoir behaviour and production. However, the work is also highly relevant for understanding the mechanical effects of sorption processes, and the role of diffusion processes, in relation to other unconventional gas plays such as shale gas reservoirs, and in relation to research on the integrity of shale caprocks in the context of geological storage of CO_2 .

References

Allardice, D., Evans, D., 1971. The-brown coal/water system: Part 2. Water sorption isotherms on bed-moist Yallourn brown coal. Fuel 50, 236-253.

Astashov, A., Belyi, A., Bunin, A., 2008. Quasi-equilibrium swelling and structural parameters of coals. Fuel 87, 3455-3461.

Biot, M.A., 1941. General theory of three-dimensional consolidation. J Appl Phys 12, 155-164.

Busch, A., Gensterblum, Y., 2011. CBM and CO_2-ECBM related sorption processes in coal: A review. International Journal of Coal Geology 87, 49-71.

Busch, A., Gensterblum, Y., Krooss, B.M., 2003. Methane and CO_2 sorption and desorption measurements on dry Argonne premium coals: pure components and mixtures. International Journal of Coal Geology 55, 205-224.

Busch, A., Gensterblum, Y., Krooss, B.M., Littke, R., 2004. Methane and carbon dioxide adsorption–diffusion experiments on coal: upscaling and modeling. International Journal of Coal Geology 60, 151-168.

Bustin, R., Clarkson, C., 1998. Geological controls on coalbed methane reservoir capacity and gas content. International Journal of Coal Geology 38, 3-26.

Chang, R., 2000. Physical chemistry for the chemical and biological sciences. University Science Books.

Charrière, D., Behra, P., 2010. Water sorption on coals. J Colloid Interf Sci 344, 460-467.

Clarkson, C., Bustin, R., 1999. The effect of pore structure and gas pressure upon the transport properties of coal: a laboratory and modeling study. 2. Adsorption rate modeling. Fuel 78, 1345-1362.

Crosdale, P.J., Beamish, B.B., Valix, M., 1998. Coalbed methane sorption related to coal composition. International Journal of Coal Geology 35, 147-158.

Cui, X., Bustin, R.M., Chikatamarla, L., 2007. Adsorption-induced coal swelling and stress: Implications for methane production and acid gas sequestration into coal seams. Journal of Geophysical Research: Solid Earth 112.

Cui, X., Bustin, R.M., Dipple, G., 2004. Selective transport of CO_2, CH_4, and N_2 in coals: insights from modeling of experimental gas adsorption data. Fuel 83, 293-303.

Damen, K., Faaij, A., van Bergen, F., Gale, J., Lysen, E., 2005. Identification of early opportunities for CO_2 sequestration—worldwide screening for CO_2-EOR and CO_2-ECBM projects. Energy 30, 1931-1952.

Day, S., Fry, R., Sakurovs, R., 2008a. Swelling of Australian coals in supercritical CO_2. International Journal of Coal Geology 74, 41-52.

Day, S., Fry, R., Sakurovs, R., 2012. Swelling of coal in carbon dioxide, methane and their mixtures. International Journal of Coal Geology 93, 40-48.

Day, S., Fry, R., Sakurovs, R., Weir, S., 2010. Swelling of coals by supercritical gases and its relationship to sorption. Energ Fuel 24, 2777-2783.

Day, S., Sakurovs, R., Weir, S., 2008b. Supercritical gas sorption on moist coals. International Journal of Coal Geology 74, 203-214.

Dubinin, M., 1980. Water vapor adsorption and the microporous structures of carbonaceous adsorbents. Carbon 18, 355-364.

Dubinin, M., Serpinsky, V., 1981. Isotherm equation for water vapor adsorption by microporous carbonaceous adsorbents. Carbon 19, 402-403.

Durucan, S., Ahsanb, M., Shia, J.-Q., 2009. Matrix shrinkage and swelling characteristics of European coals. Energy Procedia 1, 3055-3062.

Durucan, S., Shi, J.-Q., 2009. Improving the CO_2 well injectivity and enhanced coalbed methane production performance in coal seams. International Journal of Coal Geology 77, 214-221.

Espinoza, D., Vandamme, M., Dangla, P., Pereira, J.M., Vidal-Gilbert, S., 2013. A transverse isotropic model for microporous solids: Application to coal matrix adsorption and swelling. Journal of Geophysical Research: Solid Earth 118, 6113-6123.

Espinoza, D., Vandamme, M., Pereira, J.-M., Dangla, P., Vidal-Gilbert, S., 2014. Measurement and modeling of adsorptive–poromechanical properties of bituminous coal cores exposed to CO_2: Adsorption, swelling strains, swelling stresses and impact on fracture permeability. International Journal of Coal Geology 134, 80-95.

Fitzgerald, J., Pan, Z., Sudibandriyo, M., Robinson Jr, R., Gasem, K., Reeves, S., 2005. Adsorption of methane, nitrogen, carbon dioxide and their mixtures on wet Tiffany coal. Fuel 84, 2351-2363.

Fokker, P., van der Meer, L., 2004. The injectivity of coalbed CO_2 injection wells. Energy 29, 1423-1429.

Fry, R., Day, S., Sakurovs, R., 2009. Moisture-induced swelling of coal. International Journal of Coal Preparation and Utilization 29, 298-316.

Fujioka, M., Yamaguchi, S., Nako, M., 2010. CO_2-ECBM field tests in the Ishikari Coal Basin of Japan. International Journal of Coal Geology 82, 287-298.

Gensterblum, Y., Busch, A., Krooss, B.M., 2014. Molecular concept and experimental

evidence of competitive adsorption of H_2O, CO_2 and CH_4 on organic material. Fuel 115, 581-588.

Gensterblum, Y., Merkel, A., Busch, A., Krooss, B.M., 2013. High-pressure CH_4 and CO_2 sorption isotherms as a function of coal maturity and the influence of moisture. International Journal of Coal Geology 118, 45-57.

Goodman, A., Campus, L., Schroeder, K., 2005. Direct evidence of carbon dioxide sorption on Argonne premium coals using attenuated total reflectance-fourier transform infrared spectroscopy. Energ Fuel 19, 471-476.

Goodman, A., Favors, R., Larsen, J.W., 2006. Argonne coal structure rearrangement caused by sorption of CO_2. Energ Fuel 20, 2537-2543.

Govindjee, S., Simo, J.C., 1993. Coupled stress-diffusion: Case II. J Mech Phys Solids 41, 863-887.

Gray, I., 1987. Reservoir engineering in coal seams: Part 1-The physical process of gas storage and movement in coal seams. SPE Reservoir Engineering 2, 28-34.

Gruszkiewicz, M., Naney, M., Blencoe, J., Cole, D.R., Pashin, J.C., Carroll, R.E., 2009. Adsorption kinetics of CO_2, CH_4, and their equimolar mixture on coal from the Black Warrior Basin, West-Central Alabama. International Journal of Coal Geology 77, 23-33.

Harris, R.K., Becker, E.D., Cabral de Menezes, S.M., Goodfellow, R., Granger, P., 2002. NMR nomenclature: nuclear spin properties and conventions for chemical shifts. IUPAC Recommendations 2001. International Union of Pure and Applied Chemistry. Physical Chemistry Division. Commission on Molecular Structure and Spectroscopy. Magnetic Resonance in Chemistry 40, 489-505.

Haward, R.N., 2012. The physics of glassy polymers. Springer Science & Business Media.

Hill, T.L., 2012. An introduction to statistical thermodynamics. Courier Corporation.

Hirsch, P., 1954. X-ray scattering from coals, Proceedings of the Royal Society of London A: Mathematical, Physical and Engineering Sciences. The Royal Society, pp. 143-169.

Hol, S., Peach, C.J., Spiers, C.J., 2011. Applied stress reduces the CO_2 sorption capacity of coal. International Journal of Coal Geology 85, 128-142.

Hol, S., Peach, C.J., Spiers, C.J., 2012a. Effect of 3-D stress state on adsorption of CO_2 by coal. International Journal of Coal Geology 93, 1-15.

Hol, S., Spiers, C.J., 2012. Competition between adsorption-induced swelling and elastic compression of coal at CO_2 pressures up to 100MPa. J Mech Phys Solids 60, 1862-1882.

Hol, S., Spiers, C.J., Peach, C.J., 2012b. Microfracturing of coal due to interaction with CO_2 under unconfined conditions. Fuel 97, 569-584.

Hui, C.Y., Wu, K.C., Lasky, R.C., Kramer, E.J., 1987a. Case II diffusion in polymers. I. Transient swelling. J Appl Phys 61, 5129-5136.

Hui, C.Y., Wu, K.C., Lasky, R.C., Kramer, E.J., 1987b. Case II diffusion in polymers. II. Steady-state front motion. J Appl Phys 61, 5137-5149.

Kaji, R., Muranaka, Y., Otsuka, K., Hishinuma, Y., 1986. Water absorption by coals: effects of pore structure and surface oxygen. Fuel 65, 288-291.

Karacan, C.Ö., 2003. Heterogeneous sorption and swelling in a confined and stressed coal during CO_2 injection. Energ Fuel 17, 1595-1608.

Karacan, C.Ö., 2007. Swelling-induced volumetric strains internal to a stressed coal associated with CO_2 sorption. International Journal of Coal Geology 72, 209-220.

Kelemen, S., Kwiatek, L., 2009. Physical properties of selected block Argonne Premium bituminous coal related to CO_2, CH_4, and N_2 adsorption. International Journal of Coal Geology 77, 2-9.

Krooss, B., Van Bergen, F., Gensterblum, Y., Siemons, N., Pagnier, H., David, P., 2002. High-pressure methane and carbon dioxide adsorption on dry and moisture-equilibrated Pennsylvanian coals. International Journal of Coal Geology 51, 69-92.

Larsen, J.W., 2004. The effects of dissolved CO_2 on coal structure and properties. International Journal of Coal Geology 57, 63-70.

Laubach, S., Marrett, R., Olson, J., Scott, A., 1998. Characteristics and origins of coal cleat: A review. International Journal of Coal Geology 35, 175-207.

Levine, J.R., 1993. Coalification: The evolution of coal as source rock and reservoir rock for oil and gas: Chapter 3.

Levine, J.R., 1996. Model study of the influence of matrix shrinkage on absolute permeability of coal bed reservoirs. Geological Society, London, Special Publications 109, 197-212.

Liu, J., Chen, Z., Elsworth, D., Qu, H., Chen, D., 2011a. Interactions of multiple processes during CBM extraction: A critical review. International Journal of Coal Geology 87, 175-189.

Liu, J.S., Chen, Z.W., Elsworth, D., Miao, X.X., Mao, X.B., 2011b. Evolution of coal permeability from stress-controlled to displacement-controlled swelling conditions. Fuel 90, 2987-2997.

Lynch, L.J., Webster, D.S., 1982. Effect of thermal treatment on the interaction of brown coal and water: a nuclear magnetic resonance study. Fuel 61, 271-275.

Majewska, Z., Majewski, S., Ziętek, J., 2010. Swelling of coal induced by cyclic

sorption/desorption of gas: experimental observations indicating changes in coal structure due to sorption of CO_2 and CH_4. International Journal of Coal Geology 83, 475-483.

Mavor, M.J., Gunter, W.D., Robinson, J.R., 2004. Alberta multiwell micro-pilot testing for CBM properties, enhanced methane recovery and CO_2 storage potential, SPE Annual Technical Conference and Exhibition. Society of Petroleum Engineers.

Mazumder, S., Karnik, A.A., Wolf, K.-H.A., 2006. Swelling of coal in response to CO_2 sequestration for ECBM and its effect on fracture permeability. Spe J 11, 390-398.

Mazumder, S., Vermolen, F., Bruining, J., 2011. Analysis of a Model for Anomalous-Diffusion Behavior of CO_2 in the Macromolecular-Network Structure of Coal. Spe J 16, 856-863.

McCutcheon, A.L., Barton, W.A., Wilson, M.A., 2003. Characterization of water adsorbed on bituminous coals. Energ Fuel 17, 107-112.

Melnichenko, Y., Radlinski, A., Mastalerz, M., Cheng, G., Rupp, J., 2009. Characterization of the CO_2 fluid adsorption in coal as a function of pressure using neutron scattering techniques (SANS and USANS). International Journal of Coal Geology 77, 69-79.

Merkel, A., Gensterblum, Y., Krooss, B.M., Amann, A., 2015. Competitive sorption of CH_4, CO_2 and H_2O on natural coals of different rank. International Journal of Coal Geology 150, 181-192.

Moore, T.A., 2012. Coalbed methane: A review. International Journal of Coal Geology 101, 36-81.

Mu, R., Malhotra, V., 1991. A new approach to elucidate coal-water interactions by an in situ transmission FT-ir technique. Fuel 70, 1233-1235.

Nikoosokhan, S., Vandamme, M., Dangla, P., 2014. A poromechanical model for coal seams saturated with binary mixtures of CH_4 and CO_2. J Mech Phys Solids 71, 97-111.

Nishino, J., 2001. Adsorption of water vapor and carbon dioxide at carboxylic functional groups on the surface of coal. Fuel 80, 757-764.

Ottiger, S., Pini, R., Storti, G., Mazzotti, M., 2008. Competitive adsorption equilibria of CO_2 and CH_4 on a dry coal. Adsorption 14, 539-556.

Pan, Z., Connell, L.D., 2007. A theoretical model for gas adsorption-induced coal swelling. International Journal of Coal Geology 69, 243-252.

Pan, Z., Connell, L.D., 2009. Comparison of adsorption models in reservoir simulation of enhanced coalbed methane recovery and CO_2 sequestration in coal. Int J Greenh Gas Con 3, 77-89.

Pan, Z., Connell, L.D., 2012. Modelling permeability for coal reservoirs: A review of

analytical models and testing data. International Journal of Coal Geology 92, 1-44.

Peng, Y., Liu, J., Wei, M., Pan, Z., Connell, L.D., 2014. Why coal permeability changes under free swellings: New insights. International Journal of Coal Geology 133, 35-46.

Pini, R., Ottiger, S., Burlini, L., Storti, G., Mazzotti, M., 2009. Role of adsorption and swelling on the dynamics of gas injection in coal. Journal of Geophysical Research: Solid Earth 114.

Pini, R., Ottiger, S., Burlini, L., Storti, G., Mazzotti, M., 2010. Sorption of carbon dioxide, methane and nitrogen in dry coals at high pressure and moderate temperature. Int J Greenh Gas Con 4, 90-101.

Pone, J.D.N., Halleck, P.M., Mathews, J.P., 2009. Sorption capacity and sorption kinetic measurements of CO_2 and CH_4 in confined and unconfined bituminous coal. Energ Fuel 23, 4688-4695.

Prinz, D., Littke, R., 2005. Development of the micro-and ultramicroporous structure of coals with rank as deduced from the accessibility to water. Fuel 84, 1645-1652.

Radliński, A.P., Busbridge, T.L., Gray, E.M., Blach, T.P., Cheng, G., Melnichenko, Y.B., Cookson, D.J., Mastalerz, M., Esterle, J., 2009. Dynamic micromapping of CO_2 sorption in coal. Langmuir 25, 2385-2389.

Radliński, A.P., Busbridge, T.L., Gray, E.M.A., Blach, T.P., Cookson, D.J., 2009. Small angle X-ray scattering mapping and kinetics study of sub-critical CO_2 sorption by two Australian coals. International Journal of Coal Geology 77, 80-89.

Reeves, S.R., 2001. Geological Sequestration of CO_2 in Deep, Unmineable Coalbeds: An Integrated Research and Commerical-Scale Field Demonstration Project, SPE annual technical conference and exhibition. Society of Petroleum Engineers.

Shi, J., Durucan, S., 2003. A bidisperse pore diffusion model for methane displacement desorption in coal by CO_2 injection. Fuel 82, 1219-1229.

Solano-Acosta, W., Mastalerz, M., Schimmelmann, A., 2007. Cleats and their relation to geologic lineaments and coalbed methane potential in Pennsylvanian coals in Indiana. International Journal of Coal Geology 72, 187-208.

Staib, G., Sakurovs, R., Gray, E.M.A., 2013. A pressure and concentration dependence of CO_2 diffusion in two Australian bituminous coals. International Journal of Coal Geology 116, 106-116.

Suárez, N., Laredo, E., Nava, R., 1993. Characterization of four hydrophilic sites in bituminous coal by ionic thermal current measurements. Fuel 72, 13-18.

Suuberg, E.M., Otake, Y., Yun, Y., Deevi, S.C., 1993. Role of moisture in coal structure and

the effects of drying upon the accessibility of coal structure. Energ Fuel 7, 384-392.

Švábová, M., Weishauptová, Z., Přibyl, O., 2011. Water vapour adsorption on coal. Fuel 90, 1892-1899.

Syed, A., Durucan, S., Shi, J.-Q., Korre, A., 2013. Flue gas injection for CO_2 storage and enhanced coalbed methane recovery: mixed gas sorption and swelling characteristics of coals. Energy Procedia 37, 6738-6745.

Thomas, N.L., Windle, A., 1982. A theory of case II diffusion. Polymer 23, 529-542.

van Bergen, F., Krzystolik, P., van Wageningen, N., Pagnier, H., Jura, B., Skiba, J., Winthaegen, P., Kobiela, Z., 2009a. Production of gas from coal seams in the Upper Silesian Coal Basin in Poland in the post-injection period of an ECBM pilot site. International Journal of Coal Geology 77, 175-187.

van Bergen, F., Pagnier, H., Krzystolik, P., 2006. Field experiment of enhanced coalbed methane-CO_2 in the upper Silesian basin of Poland. Environmental Geosciences 13, 201-224.

van Bergen, F., Spiers, C., Floor, G., Bots, P., 2009b. Strain development in unconfined coals exposed to CO_2, CH_4 and Ar: Effect of moisture. International Journal of Coal Geology 77, 43-53.

Vandamme, M., Brochard, L., Lecampion, B., Coussy, O., 2010. Adsorption and strain: the CO_2-induced swelling of coal. J Mech Phys Solids 58, 1489-1505.

Viete, D., Ranjith, P., 2006. The effect of CO_2 on the geomechanical and permeability behaviour of brown coal: implications for coal seam CO_2 sequestration. International Journal of Coal Geology 66, 204-216.

Wang, H., 2000. Theory of linear poroelasticity with applications to geomechanics and hydrogeology. Princeton University Press.

Wang, S., Elsworth, D., Liu, J., 2012. A mechanistic model for permeability evolution in fractured sorbing media. Journal of Geophysical Research: Solid Earth 117.

White, C.M., Smith, D.H., Jones, K.L., Goodman, A.L., Jikich, S.A., LaCount, R.B., DuBose, S.B., Ozdemir, E., Morsi, B.I., Schroeder, K.T., 2005. Sequestration of carbon dioxide in coal with enhanced coalbed methane recovery a review. Energ Fuel 19, 659-724.

Wong, S., Law, D., Deng, X., Robinson, J., Kadatz, B., Gunter, W.D., Jianping, Y., Sanli, F., Zhiqiang, F., 2007. Enhanced coalbed methane and CO_2 storage in anthracitic coals—Micro-pilot test at South Qinshui, Shanxi, China. Int J Greenh Gas Con 1, 215-222.

Yi, J., Akkutlu, I.Y., Karacan, C.O., Clarkson, C., 2009. Gas sorption and transport in coals:

A poroelastic medium approach. International Journal of Coal Geology 77, 137-144.

Yu, J., Tahmasebi, A., Han, Y., Yin, F., Li, X., 2013. A review on water in low rank coals: the existence, interaction with coal structure and effects on coal utilization. Fuel Process Technol 106, 9-20.

Zhang, H., Liu, J., Elsworth, D., 2008. How sorption-induced matrix deformation affects gas flow in coal seams: a new FE model. Int J Rock Mech Min 45, 1226-1236.

Zhou, Y., Zhou, L., 2009. Fundamentals of high pressure adsorption. Langmuir 25, 13461-13466.

Chapter 2

Thermodynamic models for swelling of unconfined coal due to adsorption of mixed gases

Jinfeng Liu, Colin J. Peach, Hongwei Zhou, Christopher J. Spiers

Also published in Fuel, 157 (2015) 151–161

Abstract

Permeability evolution in coal seams during CO_2-Enhanced Coalbed Methane (ECBM) production is strongly influenced by swelling/shrinkage effects related to sorption and desorption of both CO_2 and CH_4. Other gases, such as N_2 , have also been proposed for injection in ECBM operations. In addition, water vapour will almost always be naturally present. Much work has been done on the sorption/swelling response of coal exposed to pure gases. However, to address in-situ coal-seam conditions realistically, an understanding of the swelling behaviour of coal matrix material due to multiple-species adsorption is needed. Here, we construct new thermodynamic models for swelling of unconfined coal due to adsorption of multiple gas/fluid species, addressing the equilibrium state and focusing on a binary gas mixture. Four models are derived, covering three possible end-member interactions, plus a generalized case. The end-member models considered correspond to adsorption of gases α and β at fully separate sites, at fully shared sites and at partially shared sites (Model 1-3, respectively). We compare our model predictions with literature data on the swelling behaviour of Bowen Basin coal exposed to CH_4/CO_2 mixtures at total pressures up to 15MPa and at 55˚C. The results show that swelling of the Bowen Basin coal exposed to CO_2/CH_4 mixtures is best explained by Model 3, which in turn implies that adsorption and swelling is in this case determined by both partial pressure and selective adsorption (affinity) effects. Model 3 is easy to parameterize and its applicability to specific coals and gas mixtures is easily evaluated. Though more difficult to parameterize, our generalized swelling model (Model 4) can be applied to any coal rank, and to any binary gas mixture. It therefore offers an important tool for modeling swelling and permeability evolution during ECBM operations.

2.1. Introduction

The laboratory finding that coal matrix material has higher sorption capacity for pure CO_2 than for pure CH_4 at given pressure and temperature (*PT*) conditions has led to the now well-known concept of enhanced coalbed methane (ECBM) production coupled with storage of CO_2 in underground coal seams (White et al., 2005). In this concept, CO_2 injection into a coal seam displaces the coalbed methane, which is then recovered and used for energy production, while the CO_2 generated is, in effect, re-injected (Busch and Gensterblum, 2011). Several field tests (e.g. in Canada, U.S.A., Poland, Japan and China) have confirmed the potential of CO_2- ECBM production (Fujioka et al., 2010; Reeves, 2004; van Bergen et al., 2009a). However, most sites investigated to date have shown reduced CO_2 injectivity with time due to permeability reduction in the coal seam (Fujioka et al., 2010; van Bergen et al., 2009a; van Bergen et al., 2006). These effects are generally recognized to be caused by sorption-induced swelling of the coal as a result of CO_2 injection and sorption, while CH_4 is desorbed (Busch et al., 2003; Day et al., 2008a; Day et al., 2008c; Hol et al., 2012a; Pan and Connell, 2007; van Bergen et al., 2009b; Vandamme et al., 2010). This exchange, or preferential adsorption effect, is considered to be due to either the reduction of CH_4 partial pressure as CO_2 penetrates the system or to truly selective adsorption of CO_2 over CH_4 (Busch and Gensterblum, 2011). The resulting partial replacement of CH_4 by CO_2 leads to net swelling, reflecting equilibration with respect to the new composition of the gas/fluid mixture present in the coal seam (Busch and Gensterblum, 2011; Day et al., 2012).

However, most experimental measurements and theoretical models for adsorption and swelling of coal focus on a single, pure gas, and not on mixed gases. Much less is known about competitive adsorption between CH_4 and CO_2, and there is insufficient evidence to resolve whether the controlling factor is a partial pressure or a selective sorption effect. To avoid confusion about the meaning of these terms that has crept into the literature in recent years, in this paper we use the term "preferential adsorption" of

species α to mean that the number of adsorption sites occupied by α, in a given coal mass at equilibrium with a gas/fluid mixture containing species α plus β, is greater than the number of sites occupied by β, regardless of the reason. We use the term "selective adsorption" of species α to mean that the number of adsorption sites occupied by α is greater than occupied by β, due to different site accessibilities (i.e. different affinities), even when α and β are present in the gas/fluid phase at equal activities (see Table 1. for definition of terms).

We return now to the lack of evidence on whether preferential adsorption of CH_4 and CO_2 in coal is controlled by partial pressure or selective sorption effects. To date, strongly conflicting experimental results have been reported. For example, in experiments on high volatile bituminous coal performed by using mixtures containing 25-75% CO_2 at 25°C and 0.1-4 MPa total pressure, Majewska et al. (2009) observed that CH_4 preferentially adsorbed with respect to CO_2. Czerw (2011) repeated the experiments of Majewska et al., using the same apparatus, similar coals and a 75:25 CO_2-CH_4 mixture at 25°C and 4 MPa total pressure, but reported that CO_2 preferentially adsorbed with respect to CH_4. Similarly, Busch et al. (2003; 2006) reported that whereas preferential adsorption of CO_2 and preferential desorption of CH_4 were observed in high rank coals at all total pressures investigated (1-23 MPa), low rank samples showed preferential adsorption of CH_4 at low pressures and preferential desorption of CO_2 at all pressures. These authors (Busch et al., 2006) further reported that preferential sorption is independent of CO_2-CH_4 mixture composition, (i.e. of partial pressure), and proposed that preferential sorption is determined purely by selective sorption. On the other hand, in experiments on the effect of moisture on the (otherwise) pure CO_2 and pure CH_4 sorption capacity of bituminous coals at 55°C and total pressures up to 20MPa, Day et al. (Day et al., 2008a) found that the heat of adsorption (i.e. hence K) for pure CO_2 and CH_4 are similar when drying, falling only slightly when water is present. Their calculations were done based on Dubinin–Radushkevich model applied for pure CO_2 and pure CH_4,

ignoring potential effects of water in this model. They therefore proposed that CO_2 and CH_4 have about the same access to all adsorption sites, i.e. that selective adsorption effects are negligible. The important question thus remains as to whether sorption by coal of a given rank exposed to mixed gases is solely determined by partial pressure or also by selective adsorption. Understanding the relative importance of these effects, via a physically correct sorption model, clearly plays a crucial role in assessing whether CO_2-ECBM operations are feasible in practice.

Focusing on the swelling response to mixed gas sorption, Day et al. (Day et al., 2012) recently reported measurements performed on four Australian coals, exposed to CO_2, methane and mixtures of the two. Measurements were made on laterally unconstrained (i.e. mechanically unconfined), monolithic samples (30×9×9 mm) at 55˚C, applying total gas pressures up to ~15 MPa. Volumetric swelling strain ranged from about 1.0% to 5.5%, depending on coal rank and the proportion of CO_2 in the CH_4-CO_2 mixture. These authors found that the swelling observed using mixed gases lay between the values obtained for the pure end members. They also performed experiments in which CO_2 was injected in an attempt to displace CH_4 from the same coals. In these runs, coal samples were first equilibrated with CH_4 at a pressure of 15MPa at 55˚C. CO_2 was then injected, keeping the total pressure constant. It was found that CH_4 was completely displaced from the coal, causing it to swell to the same level as if exposed to pure CO_2 at the same *PT* conditions. Upon subsequent injection of helium, which does not adsorb, the CO_2 was completely displaced by helium, causing the coal to shrink to its original dimensions. On this basis, Day et al. (2012) proposed that CH_4 and CO_2 have similar access to all adsorption sites, and that the swelling behaviour of the coal studied is determined solely by the partial pressures of the sorbing gases, with no selective sorption effects. In these experiments, the swelling strains developed upon exposure to CH_4-CO_2 mixtures were linearly dependent on CO_2 mole percentage. Assuming that this partial pressure relationship holds for nitrogen and that swelling due to nitrogen

adsorption is about half that due to methane, Day et al. (2012) proposed that a mixture of 30% CO_2 and 70% N_2 would induce the same swelling effect as pure methane at 15MPa total pressure. They accordingly suggested that a 30:70 CO_2-N_2 mixture might be suitable for injecting in ECBM operations, as there would then be no net swelling of the coal when methane is displaced. Similarly, Fujioka et al. (2010) showed that N_2 flooding temporarily improved the daily CO_2 injection rate in CO_2-ECBM field tests in the Ishikari coal basin of Japan, and proposed that N_2 flooding may help reverse the permeability reduction caused by CO_2 injection, due to the smaller swelling caused by N_2 sorption. To evaluate such shrinkages, however, a reliable, physically based model describing the sorption and swelling behaviour of coal exposed to mixed gases is pre-requisite.

Aside from recent developments in molecular dynamics modeling (Brochard et al., 2012), current models for mixed gas adsorption and swelling in coal are based on the extended Langmuir model (ELM) (Langmuir, 1918; Pan and Connell, 2007; Pan and Connell, 2009). The best known of these is the model developed by Pan and Connell (2007). However, the ELM is only applicable to mixed gases when adsorption sites are the same for each component, and when the gas phase behaves as an ideal gas (Do, 1998; Pan and Connell, 2009). These represent highly restrictive assumptions. An alternative, more general approach lies in extending the thermodynamic model developed by Hol et al. (2012a) for the equilibrium concentration of a pure gas/fluid (CO_2) adsorbed by unconfined coal matrix material (or indeed any material exhibiting monolayer adsorption, i.e. any Langmuir type sorbent). This model describes the change in adsorbed concentration as a combined effect of the changing chemical activity of the fluid and the changing availability (i.e. occupancy) of adsorption sites, and for an ideal gas reduces to the Langmuir model for a single gas/fluid species. Hol et al. (2012a; 2012) applied this model to the swelling of coal matrix material due to CO_2 adsorption, assuming that swelling is linearly proportional to adsorbed concentration. The result

obtained successfully described the swelling behaviour of high volatile bituminous coal matrix exposed to CO_2 at pressures up to 100 MPa at 40 °C.

In present paper, based on the work of Hol et al. (2012a), we construct a new thermodynamic framework for modeling adsorption-induced swelling of unconfined coal matrix material exposed to a binary gas/fluid mixture. Three models are derived to address three possible end-member interactions. These are also cast in a single generalized model. We evaluate the four models by comparing their predictions with the experimental measurements on mixed gas sorption and swelling of coal reported by Day et al. (2012). In contrast to Day et al.'s conclusion that only partial pressure is important in causing coal swelling due to mixed gas sorption, we find that selective adsorption also plays a significant role.

Table 1. Definition of terms used in this paper for the case of adsorption of gas/fluid species α and β, i.e. for adsorption from a binary gas mixture. Note that $n_s^{\alpha\beta}$ *is the number out of all adsorption sites fully accessible to α and β,* C_s^i *is the concentration of available adsorption sites accessible to component i in mole per kg coal,* K^i *is the equilibrium constant for the adsorption process of species i,* a_g^i *is the activity of the free gas/fluid species i.*

Term	Definition	Controlling factors	Model developed in this study
Preferential adsorption	The number of adsorption sites occupied by one component is greater than that occupied by the other component, regardless of the reason.	C_s^i, K^i, ϕ, a_g^i	
Selective adsorption	The number of adsorption sites occupied by one component is greater than that occupied by the other component even when each gas component has equal activity, due to different site accessibilities.	C_s^i, K^i, ϕ	
Site-sharing factor ϕ	The fraction of the total adsorption sites n_s^{total} present in the coal matrix material that is accessible to gas α and to gas β. $\phi = n_s^{\alpha\beta} \big/ n_s^{total}, 0 \le \phi \le n_s^{\alpha} \big/ n_s^{\beta} \le 1$	K^i	
Independent adsorption sites	The adsorption sites accessible to each gas component (α, β) are fully separate and independent, such that $\phi = 0$.	K^i	Model 1
Fully shared adsorption sites	All adsorption sites are fully accessible to (i.e. can take up) both gas components (α, β), so that $\phi = 1$.	K^i	Model 2
Partially shared adsorption sites: Type I	All adsorption sites accessible to gas α are also accessible to gas β, while all remaining adsorption sites are accessible only to gas β.	K^i	Model 3

	$(\phi = n_s^{\alpha} / n_s^{\beta} < 1)$.		
Partially shared adsorption sites: Type II	$n_s^{\alpha\beta} = \phi n_s^{total}$ sites are accessible to both gases (*c.f. Model 2*). The remaining adsorption sites can only take up one component (*c.f.* Model 1), such that $(n_s^{\alpha} - \phi n_s^{total})$ adsorption sites are accessible only to gas α, while $(n_s^{\beta} - \phi n_s^{total})$ adsorption sites are accessible only to gas β.	K^i	Model 4

2.2. Modeling

2.2.1. Hol and Spiers model for swelling due to adsorption of a single, pure gas or fluid

This forms the basis for the mixed gas sorption/swelling model developed in this paper. The key result derived by Hol et al. (2012a) is the following expression for the occupied fraction θ of adsorption sites present in a stress-free coal particle immersed in an adsorbing gas or fluid at fixed *PT* conditions:

$$\theta = \frac{\exp(\frac{\mu_{g0} - \mu_s}{kT})a_g}{1 + \exp(\frac{\mu_{g0} - \mu_s}{kT})a_g} \tag{1a}$$

or $\theta = \frac{Ka_g}{1 + Ka_g}$ (1b)

Here $K = \exp(\frac{\mu_{g0} - \mu_s}{kT})$ is the equilibrium constant for the adsorption process, μ_s is the chemical potential of a single adsorbed molecule located in the potential well associated with the adsorption sites present (Tuin and Stein, 1995), a_g is the chemical activity of the free gas or fluid at pressure *P*, and μ_{g0} is the potential of the free gas or fluid in the reference state defined by the fluid activity $a_g = 1$.

In equation (1), the site occupancy θ is seen to depend on a) the activity, hence pressure or chemical potential of the free fluid phase, and b) the equilibrium constant *K*, which is expressed statistically through the gas activity independent potential $\mu_s = \mu_s(T)$. For an ideal gas, the activity becomes equal to the gas pressure and the model reduces to the Langmuir model (Langmuir, 1918). The equivalent relation for the equilibrium concentration of gas or fluid molecules adsorbed by stress-free coal matrix material at fixed pressure and temperature is

$$C = C_s\theta = \frac{C_s K a_g}{1 + K a_g} \tag{2}$$

where C_s (*mol/kg*) is the concentration of available localized adsorption sites present in the coal (i.e. sites capable of adsorbing a given gas/fluid species). Assuming that each adsorbed molecule contributes a fixed amount of swelling to the host sorbent, the swelling exhibited by unconfined coal matrix due to adsorption of a single pure fluid is accordingly given by Hol et al. (2012a) as

$$e_{ads}^{eq} = \frac{C_s K a_g}{1 + K a_g} V_0 \rho \tag{3}$$

where ρ is the density of the coal, and where V_0 is the absolute change in coal

volume when one mole of the gas/fluid species is adsorbed (assumed to be insensitive to adsorbed concentration). At low gas pressures where site occupancies are low, i.e. when $\theta^i << 1$, equation 3 can be simplified to

$$e_{ads}^{eq} = C_s K a_g V_0 \rho \tag{4}$$

which is easily seen from equations 1b and 2 that the denominator term in equation 3 approaches 1. For practical application, note that all parameters in this model can be obtained from basic, Langmuir-type, isothermal laboratory experiments on adsorption and swelling (Hol et al., 2012a).

2.2.2. Present model development: Starting assumptions and cases considered

We now proceed to address swelling of unconfined coal induced by adsorption from a binary gas/fluid mixture. For simplicity, we henceforth use the term "gas", to cover both gas and supercritical fluid components. We assume there is no chemical or physical interaction between the two gases. Following Hol et al. (2011; 2012a), we begin by considering a small cube of nano-porous coal matrix material of mass *m* and side *l* ($l \leq 1mm$), which hosts $n_s^i (i = \alpha, \beta ...)$ localized adsorption sites for the two gas components α and β. The cube is assumed to contain nano-pores only, so that there is no Darcian flow and negligible storage of free (unadsorbed) mixed gases. In other words, the coal particle is so small that it is cleat free and can take up gases only by diffusion and adsorption. The material is assumed homogeneous in structure and composition at the length scale *l*, but may be anisotropic in properties. The coal is now exposed to gases α and β at constant total pressure *P* and at constant temperature *T* (Fig. 1).

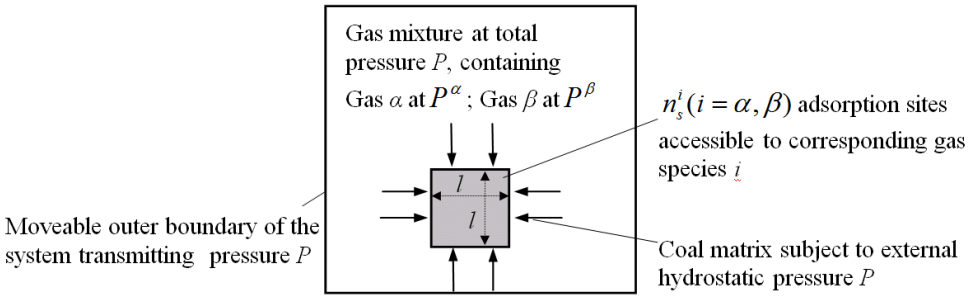

Fig.1. Representative volume of coal matrix material used in the present analysis of adsorption under mechanically unconfined or stress-free conditions. The representative volume consists of a small cube of coal matrix material of mass m and side l ($l \leq 1mm$), containing $n_s^i(i=\alpha,\beta)$ localized adsorption sites accessible to the corresponding gas species i. The cube is free of cleats and consists entirely of nanoporous coal matrix material. Once the coal particle is exposed to gas α and gas β at constant total pressure P and at constant temperature T, it is assumed to take up α and β only by diffusion and adsorption.

In considering mixed gases, it is important to recognize that the properties of the available adsorption sites in the coal matrix are likely to be different for each gas (Gensterblum et al., 2014; Ottiger et al., 2008b). For example some adsorption sites can perhaps adsorb several gas species, while other adsorption sites can take up only a specific gas species. In other words, different sorption sites may be characterized by either similar or very different K^i values, for the various gases present. On this basis, we now focus on three physically possible end-member cases (1-3), and then consider a generalized case (4).

Case 1. Independent adsorption of each gas. In this case, the adsorption sites present full with two categories characterized by widely different K^i values for α and β (Fig. 2). In other words, n_s^{α} adsorption sites can in effect only take up gas α, while n_s^{β}

adsorption sites can only take up gas β. The total number of adsorption sites n_s^{total} present in the coal matrix is therefore equal to the sum of adsorption sites for each component, i.e. $n_s^{total} = n_s^{\alpha} + n_s^{\beta}$.

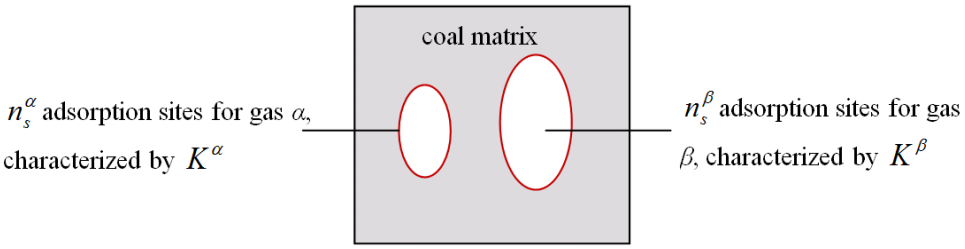

Fig. 2. *Schematic illustration of the independent adsorption sites distribution. The model is characterized by* n_s^{α} *adsorption sites for gas α and* n_s^{β} *adsorption sites for gas β. These two categories of site represent completely separate adsorption sites for α and β in the coal sorbent phase. The number of total adsorption sites* n_s^{total} *present in the coal is therefore equal to the sum of* n_s^{α} *and* n_s^{β}. *Note that the different sites are drawn schematically in different special domains but are actually distributed throughout the coal particle considered.*

Case 2. Fully shared adsorption sites. In this case, all adsorption sites are characterized by different, but not widely different, equilibrium constants K^{α} and K^{β}. In other words, all the available adsorption sites are accessible to gas α and to gas β (Fig. 3). This means the number of available adsorption sites for each component is identical ($n_s^{\alpha} = n_s^{\beta} = n_s^{\alpha\beta}$) (Day et al., 2012; Day et al., 2008c), and that the total number of adsorption sites present in the coal matrix material is given as $n_s^{total} = n_s^{\alpha\beta}$.

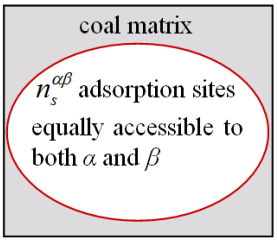

Fig. 3. Schematic illustration of the fully shared adsorption sites distribution. The model is characterized by $n_s^{\alpha\beta}$ adsorption sits for α and for β. These sites are characterized by similar (though different) equilibrium constants for α and β.

Case 3. Partially shared adsorption sites: Type I. In this case, only a sub-set of the population of adsorption sites is shared by α and β (*c.f.* case 2). In other words, n_s^{α} sites present in the coal matrix material are accessible to both gases α and β, while $(n_s^{\beta} - n_s^{\alpha})$ adsorption sites, which are a different type of site compared to the n_s^{α} adsorption sites, can only be occupied by gas β (Fig. 4). This means that $n_s^{\alpha\beta} = n_s^{\alpha}$ and $n_s^{\alpha} < n_s^{total} = n_s^{\beta}$. The adsorption sites that are accessible to α and β are characterized by broadly similar site potential for these species, while these accessible only to gas β are characterized by a highly unfavorable site potential for gas α.

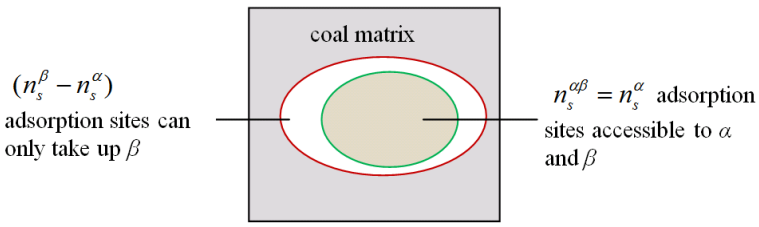

Fig. 4. Schematic illustration of the site population distribution corresponding to the Type I partially shared adsorption sites case. Here n_s^{α} *adsorption sites are shared by both gases* α *and* β*, and* $(n_s^{\beta} - n_s^{\alpha})$ *adsorption sites are accessible only to gas* β*, i.e.* $n_s^{\alpha\beta} = n_s^{\alpha}$ and $n_s^{\alpha} < n_s^{total} = n_s^{\beta}$.

Case 4. Partially shared adsorption sites: Type II. In this fully general case (Fig. 5), a fraction ϕ $(0 \le \phi \le n_s^{\alpha} / n_s^{\beta} \le 1)$ of the total number of adsorption sites n_s^{total} is accessible to gas α and to gas β, i.e. $n_s^{\alpha\beta} = \phi n_s^{total}$ sites are accessible to both gases (*c.f.* case 2). The other adsorption sites can only take up one component so that a population of $(n_s^{\alpha} - \phi n_s^{total})$ adsorption sites is accessible only to gas α, while $(n_s^{\beta} - \phi n_s^{total})$ adsorption sites can only take up gas β. Here, $n_s^{total} = \dfrac{n_s^{\alpha} + n_s^{\beta}}{1 + \phi}$. When $\phi = 0$, this case reduces to end member case 1. When $\phi = 1$, it reduces to case 2. When $\phi = n_s^{\alpha} / n_s^{\beta}$, it reduces to case 3.

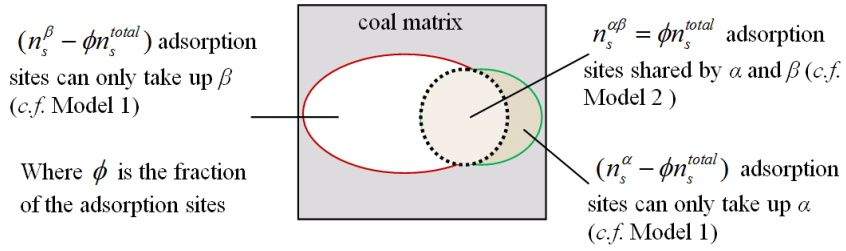

Fig. 5. Schematic illustration of the site population distribution corresponding to Type II partial sharing of adsorption sites. $n_s^{\alpha\beta} = \phi n_s^{total}$ *adsorption sites are accessible to both gases* α *and* β*, while* $(n_s^{\beta} - \phi n_s^{total})$ *adsorption sites are accessible only to gas* β *and* $(n_s^{\alpha} - \phi n_s^{total})$ *adsorption*

sites are accessible only to α .

With respect to the above four cases, four models for swelling of unconfined coal exposed to gases α and β are now derived.

2.2.2.1. Model 1: Independent adsorption sites

This model corresponds to case 1. Here fully independent sorption of α and β, determined by a_g, C_s and K for each gas (see equation 2), leads to independent swelling responses, further determined by V_0 for α and for β (see equation 3) (Hol et al., 2012a). These swelling responses sum to give total volumetric strain. Model 1 can accordingly be derived from the Hol and Spiers model for single-gas adsorption-induced swelling (Hol et al., 2012a), i.e. from equations (2) and (3), by applying these equations to the adsorption sites accessed by α and β independently. This yields

$$e_{ads}^{eq} = \frac{C_s^{\alpha} a_g^{\alpha} K^{\alpha}}{1 + a_g^{\alpha} K^{\alpha}} V_0^{\alpha} \rho + \frac{C_s^{\beta} a_g^{\beta} K^{\beta}}{1 + a_g^{\beta} K^{\beta}} V_0^{\beta} \rho \tag{5}$$

where C_s^i is the concentration of the adsorption sites accessible to component i in *mol/kg*, K^i is the equilibrium constant for gas species i, a_g^i is the activity of the free gas species i, and V_0^i is the absolute change in coal volume due to adsorption of one mole of the component i. Note here that V_0^i is assumed to be insensitive to the concentration of the species i, following Hol et al (2012a). It is also important to note here that while the equilibrium constant K^i for each species is independent of the partial pressure of the species i, it is sensitive to coal rank, fluid species and temperature.

2.2.2.2. Model 2: Fully shared adsorption sites

To obtain an expression for Model 2, which corresponds to case 2 (see Fig. 3), we consider the thermodynamic potential changes associated with reversible adsorption first

of a single molecule and then of a population of $n^i (i = \alpha, \beta)$ molecules of gas species *i*. We then derive an expression for swelling, assuming that the volume change associated with a single adsorbed molecule is insensitive to adsorbed concentration of either component, and that the total volume change is the sum of the contribution due to each component (α, β) weighted according to sorbent concentration (Hol et al., 2012a).

2.2.2.2.1. Attachment energy for adsorption of a single molecule of species i

When a single molecule of species *i* (α or β) is adsorbed by the small, representative matrix cube specified above, the internal energy change of the solid phase (subscript *s*) is given by the Gibbs equation (Hol et al., 2012a),

$$\Delta U_s^i = -P\Omega_0^i + T\Delta S_s^i + \mu_s^i \tag{6}$$

In this relation, Ω_0^i is volume change exhibited by the matrix particle, ΔS_s^i is the corresponding entropy change, and μ_s^i is the chemical potential of the adsorbed molecule within the potential well associated with the sorption site.

For each component *i* in the gas phase (subscript *g*), the internal energy change that occurs when a single molecule is removed from the gas mixture by adsorption is given, via an analogous Gibbs equation (Hol et al., 2012a), as

$$\Delta U_g^i = P\Omega_g^i + T\Delta S_g^i - \mu_g^i \tag{7}$$

In this case, Ω_g^i is the partial molecular volume of the gaseous species *i* in the mixture at total pressure *P*, μ_g^i is the chemical potential of gaseous species *i* at partial pressure P^i, and ΔS_g^i is the entropy change associated with removing one molecule of species *i* from the gas mixture.

For the combined solid-gas system (subscript *a*), we hence get, adding (5) and (6),

$$\Delta\mu_a^i = \mu_s^i - \mu_g^i = \Delta U_a^i + P(\Omega_0^i - \Omega_g^i) - T\Delta S_a^i \quad (8a)$$

or $$\Delta\mu_a^i = \mu_s^i - \mu_g^i = \Delta F_a^i + P\Delta V_a^i \quad (8b)$$

for each species *i*. Here, $\Delta\mu_a^i$ is simultaneously the change in potential associated with the adsorbed molecule *i* and the change in the energy of the system due to the attachment of the adsorbed molecule *i*. The term $\Delta V_a^i = \Omega_0^i - \Omega_g^i$ is the associated volume change of the system, while ΔF_a^i is the corresponding change in Helmholtz free energy. The term ΔS_a^i is the entropy change of the system. By definition, under the present hydrostatic conditions, where both *P* and *T* are constant, the corresponding change in Gibbs potential of component *i* is

$$\Delta G_a^i = \Delta F_a^i + P\Delta V_a^i \quad (9)$$

where now we can identify $\Delta G_a^i = \Delta\mu_a^i$ as the partial Gibbs energy change associated with attachment of a single adsorbed molecule of component *i*. Physically, this ΔG_a^i represents the Gibbs energy of component *i* that must be supplied to remove an adsorbed molecule of species *i* from an adsorption site into the free gas phase.

2.2.2.2.2. Adsorption energy associated with uptake of n_i molecules of species i=α, β

For a total population of shared adsorption sites $n^{\alpha\beta}$, and assuming that each adsorption site remains empty or else takes up one gas molecule, then n^i molecules of gas species i, (i.e. n^α molecules of α and n^β molecules of β), can only be distributed over ($n^{\alpha\beta}$- n^j) adsorption sites, where n^j represents n^β and n^α ($j \neq i$) respectively. From combination theory, the number of different ways that n^i molecules can be distributed

over these available sites can be written as $W^i = \frac{(n_s^{\alpha\beta} - n^j)!}{n^i!(n_s^{\alpha\beta} - \sum_{l=\alpha,\beta} n^l)!}$. This contributes a configurational entropy term $\Delta S^i = -k \ln W^i$ to the overall change in Gibbs potential that occurs when n^i molecules of species *i* are adsorbed. The adsorption energy for n^i molecules of species *i* is accordingly given as

$$\Delta G^i = n^i \Delta G_a^i - kT \ln \frac{(n_s^{\alpha\beta} - n^j)!}{n^i!(n_s^{\alpha\beta} - \sum_{l=\alpha,\beta} n^l)!} \tag{10}$$

Because we assume that there is no interaction between gases α and β, the total change in Gibbs energy for the whole system, when n^α and n^β molecules of α and β are adsorbed, can thus be written as

$$\Delta G = \sum \Delta G^i \tag{11a}$$

or

$$\Delta G = n^\alpha \Delta G_a^\alpha + n^\beta \Delta G_a^\beta - kT \ln \frac{(n_s^{\alpha\beta} - n^\alpha)!}{n^\alpha!(n_s^{\alpha\beta} - \sum_{l=\alpha,\beta} n^l)!} - kT \ln \frac{(n_s^{\alpha\beta} - n^\beta)!}{n^\beta!(n_s^{\alpha\beta} - \sum_{l=\alpha,\beta} n^l)!} \tag{11b}$$

where $\sum_{l=\alpha,\beta} n^l = n^\alpha + n^\beta$

2.2.2.2.3. Equilibrium concentration of components adsorbed from a mixture of gases α and β

For mixed gases, we assume that the adsorption of each gas proceeds until equilibrium is reached, subject to the condition that there is zero interaction between components. At that point, the total Gibbs energy must be minimum and its partial derivatives equal to zero, *i.e.* $(\frac{\partial \Delta G}{\partial n^i})_{P^i,T} = 0$. Applying Stirling's approximation

$\ln x! \approx \mathrm{x}(\mathrm{lnx}-1)$ for large x to the above expression for ΔG (equation 11) and differentiating now gives

$$(\frac{\partial \Delta G}{\partial n^i})_{P^i,T} = \Delta G_a^i + kT \ln(\frac{\theta^i}{1-\sum_{l=\alpha,\beta} \theta^l}) = 0 \tag{12}$$

where $\theta^i = n^i / n_s^{\alpha\beta}$ is the concentration of adsorbed species i amongst the total number of adsorption sites $n_s^{\alpha\beta}$. This in turn means that at equilibrium

$$\theta^i = \frac{\exp(\frac{-\Delta G_a^i}{kT})}{1+\exp(\frac{-\Delta G_a^i}{kT}) + \frac{\theta^j}{\theta^i}\exp(\frac{-\Delta G_a^i}{kT})}, \qquad (\mathrm{j} \neq \mathrm{i}) \tag{13a}$$

or $$\frac{\theta^i}{1-\theta^j} = \frac{\exp(\frac{-\Delta G_a^i}{kT})}{1+\exp(\frac{-\Delta G_a^i}{kT})}, \qquad (\mathrm{j} \neq \mathrm{i}) \tag{13b}$$

which on further manipulation, putting $i = \alpha, \beta$ and simultaneously putting $j = \beta, \alpha$, yields

$$\theta^i = \frac{\exp(\frac{-\Delta G_a^i}{kT})}{1+\sum_{l=\alpha,\beta} \exp(\frac{-\Delta G_a^l}{kT})} \tag{14}$$

Now from the thermodynamics of fluid systems, the potential of the free species i is given by

$$\mu_g^i = \mu_{g0}^i + kT \ln a_g^i \tag{15}$$

where $a_g^i = a_g^i(P^i, T)$ is the chemical activity of the free gaseous species i at partial pressure P^i and temperature T in the gas mixture, and where μ_{g0}^i is the potential of

each gas in the reference state $a_g^i = 1$. Recalling that $\Delta G_a^i = \Delta \mu_a^i = (\mu_s^i - \mu_g^i)$ from equations 8 and 9, and combining equations 14 and 15, we hence obtain the following expressions for the concentration of adsorbed molecules per available site $n_s^{\alpha\beta}$, for each component α and β in the gas mixture, namely

$$\theta^i = \frac{a_g^i \exp(\frac{\mu_{g0}^i - \mu_s^i}{kT})}{1 + \sum_{l=\alpha,\beta} a_g^l \exp(\frac{\mu_{g0}^l - \mu_s^l}{kT})} \tag{16a}$$

or $$\theta^i = \frac{a_g^i K^i}{1 + \sum_{l=\alpha,\beta} a_g^l K^l} \tag{16b}$$

where $K^i = \exp(\frac{\mu_{g0}^i - \mu_s^i}{kT})$ is the equilibrium constant for adsorption of species *i*, which depends only on temperature *T* for a given coal and gas species *i*. In these relations, if the free gas components outside the coal particle behave as ideal gases, then, for reference states defined by the partial pressures $P_0^i = 1$ and $a_g^i = P^i$, the adsorption model reduces to the well-known Langmuir isotherm for mixed gases (Langmuir, 1918).

2.2.2.2.4. Swelling strain development

Finally, using the relation for swelling strain $e_{ads}^{eq} = C_s \theta V_0 \rho$ given by Hol and Spiers (Hol and Spiers, 2012), we can obtain an expression for the swelling strain predicted by Model 2, i.e. for case 2. This is given

$$e_{ads}^{eq} = C_s^{\alpha\beta}(\theta^\alpha V_0^\alpha + \theta^\beta V_0^\beta)\rho \tag{17a}$$

or $e_{ads}^{eq} = C_s^{\alpha\beta}(\frac{a_g^\alpha K^\alpha}{1+a_g^\alpha K^\alpha + a_g^\beta K^\beta}V_0^\alpha + \frac{a_g^\beta K^\beta}{1+a_g^\alpha K^\alpha + a_g^\beta K^\beta}V_0^\beta)\rho$ (17b)

where $C_s^{\alpha\beta} = n_s^{\alpha\beta} / (N_A \bullet m)$ is the (constant) number of potential adsorption sites in moles per kg of coal and $V_0^i (i = \alpha, \beta) = N_A \Omega_0^i = 1/\rho\,(\partial e_{ads}^i / \partial C^i)$ is the absolute change in coal volume when one mole of gas species *i* is adsorbed, which is assumed to be insensitive to the concentration of the species *i*, and where N_A is Avogadro constant.

2.2.2.3. Model 3: Partially shared adsorption sites, Type I

This model corresponds to case 3 (see Fig. 4), which assumes that a selective sorption effect between α and β plays a role in swelling behaviour. Here adsorption of α and β into the n_s^α shared sites leads to a swelling response described by Model 2 (17a,b). At the same time, adsorption of β into the $(n_s^\beta - n_s^\alpha)$ β-only sites leads to a swelling response described by Hol and Spiers Model for β (see equation 3), but replacing C_s in equation 3 by $(C_s^\beta - C_s^\alpha)$. The total swelling strain due to adsorption of mixed gases predicted by Model 3 can therefore be written as

$$e_{ads}^{eq} = C_s^\alpha(\frac{a_g^\alpha K^\alpha}{1+a_g^\alpha K^\alpha + a_g^\beta K^\beta}V_0^\alpha + \frac{a_g^\beta K^\beta}{1+a_g^\alpha K^\alpha + a_g^\beta K^\beta}V_0^\beta)\rho + (C_s^\beta - C_s^\alpha)\frac{a_g^\beta K^\beta}{1+a_g^\beta K^\beta}V_0^\beta \rho \quad (18)$$

where $C_s^\alpha = C_s^{\alpha\beta}$ and $C_s^\alpha < C_s^{total} = C_s^\beta$.

2.2.2.4. Model 4: Partially shared adsorption sites, Type II

Following the same approach applied above to obtain Model 3, using the Hol and Spiers Model and our Model 2, a generalized model corresponding to case 4 (see Fig. 5)

can be derived. This involves applying Model 2 to the fraction ϕ of the total number of sorption sites n_s^{total} that is accessible to α and to β. Model 1 is applied to the $(n_s^{\alpha} - \phi n_s^{total})$ sites that are accessible only to α, and the $(n_s^{\beta} - \phi n_s^{total})$ sites that are accessible only to β. The result is given by

$$\begin{aligned} e_{ads}^{eq} = \phi C_s^{total} \left(\frac{a_g^{\alpha} K^{\alpha}}{1 + a_g^{\alpha} K^{\alpha} + a_g^{\beta} K^{\beta}} V_0^{\alpha} + \frac{a_g^{\beta} K^{\beta}}{1 + a_g^{\alpha} K^{\alpha} + a_g^{\beta} K^{\beta}} V_0^{\beta}\right) \rho \\ + (C_s^{\beta} - \phi C_s^{total}) \frac{a_g^{\beta} K^{\beta}}{1 + a_g^{\beta} K^{\beta}} V_0^{\beta} \rho + (C_s^{\alpha} - \phi C_s^{total}) \frac{a_g^{\alpha} K^{\alpha}}{1 + a_g^{\alpha} K^{\alpha}} V_0^{\alpha} \rho \end{aligned} \tag{19}$$

where $C_s^{total} = \dfrac{C_s^{\alpha} + C_s^{\beta}}{1 + \phi}$ is the concentration of total adsorption sites present in the coal matrix material, and where ϕ ($0 \le \phi \le n_s^{\alpha} / n_s^{\beta} \le 1$) is the site-sharing factor. Recall here that $C_s^i = n_s^i / (N_A \bullet m)$. This then gives $n_s^{\alpha} / n_s^{\beta} = C_s^{\alpha} / C_s^{\beta}$. When $0 < \phi < C_s^{\alpha} / C_s^{\beta} < 1$, this model represents the generalized model corresponding to Fig.5 described above. When $\phi = 0$, the model reduces to Model 1. When $\phi = 1$, it reduces to Model 2. When $\phi = C_s^{\alpha} / C_s^{\beta}$, it reduces to Model 3.

Finally, at low gas pressures where site occupancies are low, i.e. when $\theta^i << 1$, it is easily seen from equations 13 and 14 that the denominator terms in equation 19 all approach 1 (Hol et al., 2011; Hol et al., 2012a). The generalized model can then be simplified to

$$e_{ads}^{eq} = (C_s^{\alpha} a_g^{\alpha} K^{\alpha} V_0^{\alpha} + C_s^{\beta} a_g^{\beta} K^{\beta} V_0^{\beta}) \rho \tag{20}$$

in which ϕ no longer appears, as all terms in equation 19 containing ϕ now drop out. This simplified model can therefore be directly applied to the three end-member cases when gas pressures are low.

2.3. Comparison of model predictions with experimental data

We now compare the predictions of our models with available experimental data. This requires experimental data on both the sorption capacity and swelling behaviour of a given coal exposed to pure α and β (to obtain $V_0^\alpha, V_0^\beta, C_s^\alpha, C_s^\beta, K^\alpha, K^\beta$), as well as swelling data obtained on the same coal exposed to mixed gases. The only data that we are aware of that are suitable for this purpose are those of Day et al. for two almost identical sub-bituminous coals from the Bowen Basin, Queensland, Australia (denoted as Coal N and Coal C by Day et al (2012; 2010). As Day et al (2012; 2010) do not quote the errors or give error bars for the data, had no choice but to assume that their experimental data are accurate enough for our purpose. Since our three end-member models each have a clear physical meaning, we first compare the predictions of the three end-member models with Day et al.'s experimental data (Day et al., 2012) to assess which model fits best. We then compare our Model 4 with Day et al.'s data (Day et al., 2012) by varying the site-sharing factor ϕ to evaluate whether Model 4 offers any improvement upon Models 1, 2 and 3.

2.3.1. The data of Day et al.

We start by reviewing the data presented by Day et al. on the swelling response of Coal N versus gas composition (Day et al., 2012). These data consist of volumetric strain values measured as a function of CO_2 and CH_4 partial pressures, the latter being specified in terms of mixture composition. Note that sorption was not measured in these

experiments, nor was bulk modulus or density. The experiments on Coal N were carried out at total pressures in the range 1-15MPa at a temperature of 55˚C. The gas mixture composition (% CO_2), measured using Gas Chromatography, was systematically varied in the range 0-100%, thus including measurements for pure CH_4 and pure CO_2. The total volumetric strain e_v^{eq} measured by Day et al. (2012) includes both a) the elastic compression response e_{el}^{eq} of the coal sample due to imposed total gas pressure *P*, and b) the adsorption-induced swelling strain e_{ads}^{eq} (Hol and Spiers, 2012; Pan and Connell, 2007; Vandamme et al., 2010), so that

$$e_v^{eq} = e_{ads}^{eq} + e_{el}^{eq} \tag{21}$$

Here we emphasize that the term e_{el}^{eq} represents an elastic response of the coal matrix, rather than a poro-elastic response. This is because our model assumes that the nanoporous matrix only allows penetration of the gas or fluid species by diffusion and adsorption, i.e. there is zero fluid pressure in the matrix (Hol and Spiers, 2012; Pan and Connell, 2007; Vandamme et al., 2010), so that

$$e_{el}^{eq} = P / K_s \tag{22}$$

where K_s is the bulk modulus of the coal matrix.

The swelling due to adsorption alone can thus be expressed as

$$e_{ads}^{eq} = e_v^{eq} - P / K_s \tag{23}$$

We applied this equation to obtain the true adsorption-induced swelling strain e_{ads}^{eq} of Coal N from total strain, using the bulk modulus K_s presented by Day et al. for Coal C (Day et al., 2012; Day et al., 2010). We plot the quantity e_{ads}^{eq} versus CO_2 concentration

(mole percentage) in the CO_2-CH_4 mixture in Figure 6.

We now review the data presented by Day et al on swelling response versus sorption, but for Coal C (Day et al., 2010). These authors measured the volumetric strain of Coal C exposed to pure CO_2 and CH_4, using the same experimental methods for Coal N under the same *PT* conditions. In addition, they measured the concentrations of CO_2 and CH_4 adsorbed when crushed Coal C was independently exposed to pure CO_2 and pure CH_4, under the same *PT* conditions, using a gravimetric method. On the basis of these measurements, Day et al. plotted the quantity e_v^{eq} versus adsorbed concentration *C* for pure CO_2 and CH_4. We obtained the true adsorption-induced swelling strain e_{ads}^{eq} of Coal C versus adsorbed CO_2 and CH_4 concentration, using equation 23 to correct for elastic compression. This yielded a near-linear relationship with a best fit slope of 0.0232 kg/mol (R^2=0.951) for CO_2 and 0.0203 kg/mol (R^2=0.959) for CH_4.

2.3.2. End-member model parameters and calculation method

We now calculate the parameters V_0, C_s and *K* for Coal N for pure CO_2 and pure CH_4, following the approach adopted by Hol and Spiers (Hol and Spiers, 2012) for a pure single gas. Recall that these parameters are assumed to be insensitive to the adsorbed gas concentration. The values of $V_0^{CO_2}$ and $V_0^{CH_4}$ for Coal N were first calculated from the above-mentioned relationship between e_{ads}^{eq} versus *C* obtained. This was done for Coal C exposed to pure CO_2 and CH_4, using the relation $V_0 = 1/\rho\,(\partial e_{ads}^{eq} / \partial C)$ (see equations 2 and 3). The results obtained were $V_0^{CO_2} = 1.42 \times 10^{-5}$ and $V_0^{CH_4} = 1.24 \times 10^{-5}$. The parameters C_s and *K* for pure CO_2 and pure CH_4 were then derived from the data on volumetric strain of Coal N versus pure gas pressure (the 0% and 100% end member) measured by Day et al. (2012). We first calculated the value of

$C_s \times K$, using the relationship between adsorption-induced swelling and gas activity at low gas pressure expressed in equation 4. Inserting the value $C_s \times K$ thus obtained into equation 3, we then calculated the value of K using equation 3 for adsorption-induced swelling versus gas activity at high pressures. However, due to the paucity of swelling data at low pressures (<0.1 MPa), the uncertainty in calculating the value of $C_s \times K$ is large. To reduce this uncertainty, we optimized the value of K by varying the values of $C_s \times K$ to achieve the best fit of equation 3 to the full set of experimental data for pure CO_2 and pure CH_4 for Coal N. We conducted this process by the SOLVER function of Microsoft Excel (following Day et al. (2008c)). Finally, this procedure yielded $C_s^{CO_2} = 3.335 mol/kg$, $K^{CO_2} = 0.0288$ (R^2=0.987) and $C_s^{CH_4} = 2.054 mol/kg$, $K^{CH_4} = 0.0126$ (R^2=0.986). Note that throughout these calculations, the CO_2 activity was computed using the EoS for CO_2 developed by Span & Wagner (1996), while the CH_4 activity was calculated according to the EoS for CH_4 developed by Setzmann and Wagner (1991). The density of Coal N needed to calculate swelling, via equation 3, was estimated from work on Coal C by Day et al. (2010). In the following, we now proceed to insert appropriate values for the key parameters V_0, C_s and K for both CO_2 and CH_4 in Models 1-3. The values used for each model are summarized in Table 2.

2.3.2.1. The parameter values in Model 1

Model 1 assumes the adsorption sites and process for CO_2 are fully separate and independent compared with those for CH_4. We therefore took the above-mentioned values of C_s and K, which give the best fit for pure CO_2 and CH_4, as the parameter values appropriate for Model 1 (see Table 2).

2.3.2.2. The parameter values in Model 2

Model 2 assumes $C_s^{\alpha\beta} = C_s^{CO_2} = C_s^{CH_4}$. This means that the above best fit parameter values C_s (3.335, 2.054) and K (0.0288, 0.0126), obtained for pure CO_2 and

CH_4, are not appropriate for Model 2. In exploring the applicability of Model 2 to describe swelling upon exposure to the mixed gases, we followed the same steps described above, but forced the requirement that $C_s^{\alpha\beta} = C_s^{CO_2} = C_s^{CH_4}$ as a constraint. Best fitting of equation 3 to the experimental data for pure CO_2 and pure CH_4 for Coal N then give $C_s^{CO_2} = 3.255 mol/kg$ $K^{CO_2} = 0.0318$ (R^2=0.982) and $C_s^{CH_4} = 3.255 mol/kg$, $K^{CH_4} = 0.0044$ (R^2=0.824) (see Table 2). Note here, however, that a significant difference exists between the values obtained for K^{CO_2} and K^{CH_4}, which is inconsistent with our assumption in Model 2 that all adsorption sites must be characterized by similar equilibrium constants K^{α} and K^{β}.

2.3.2.3. The parameter values in Model 3

Model 3 assumes $C_s^{CO_2} > C_s^{CH_4}$, which is consistent with the best fit values we obtained for C_s for pure CO_2 and CH_4 (section 2.3.2). We therefore took the best fit values of parameters C_s and K, for pure CO_2 and CH_4, as the appropriate parameter values for Model 3 (see Table 2.).

Table 2. Summary of model parameters used in Models 1-3 for calculating swelling of the Bowen Basin sub-bituminous coal N, under the conditions of the mixed gas swelling experiments reported by Day et

al.(2012).

Models	Parameters and conditions for which they were determined							
	$V_0^{CH_4}$ (m^3/mol) 55˚C pure CH_4	$V_0^{CO_2}$ (m^3/mol) 55˚C pure CO_2	$C_s^{CH_4}$ (mol/kg) 55˚C pure CH_4	$C_s^{CO_2}$(mol/kg) 55˚C pure CO_2	K^{CH_4} 55˚C pure CH_4	K^{CO_2} 55˚C pure CO_2	ρ (kg/m^3) 55˚C pure He	K_s (GPa) 55˚C pure He
1	1.24×10^{-5}	1.42×10^{-5}	2.054	3.335	0.0126	0.0288	1.637	9.41
2	1.24×10^{-5}	1.42×10^{-5}	3.255	3.255	0.0044	0.0323	1.637	9.41
3	1.24×10^{-5}	1.42×10^{-5}	2.054	3.335	0.0126	0.0288	1.637	9.41

2.3.3. End-member models vs. the experimental data

Using the parameter values mentioned above, we applied Models 1, 2 and 3 to systematically calculate e_{ads}^{eq} as a function of CO_2 concentration (mole percentage) in the gas mixture, for total pressures in the range 1-15MPa and a temperature 55˚C, as used in the experiments performed by Day et al. (2012). To do this, data on the activity of CO_2 and CH_4 in the mixed gas state are also needed. These were calculated using the EoS for CO_2 and CH_4 mixtures developed by Kunz et al. (2006).

We now compare the predictions of the three end-member models with the data on e_{ads}^{eq} versus CO_2 concentration in the CO_2-CH_4 mixture obtained from the data of Day et al. (2012) for Coal N from the Bowen Basin at 55˚C (Fig. 6). The results show that Models 2 and 3 (for full and Type I partial sharing of sites) are in good agreement with the experimental data, whereas Model 1 (independent adsorption sites) fits poorly. Additionally, the predictions made by Model 1 were inconsistent with the trend observed by the authors that the swelling of coal increased with increasing CO_2 concentration and yielded the peak value when exposed to pure CO_2 (100%). This all suggests at least some degree of site sharing by CO_2 and CH_4. Day et al. (2012) proposed that their results can be explained entirely in terms of CO_2 vs. CH_4 concentration (or partial

pressure) in the gas mixture, with negligible effect of selective adsorption, i.e. by our Model 2 for full site sharing. To assess if Model 2 or Model 3 best explains their results, the fit quality of Models 2 and 3 to the lab data has been investigated by calculating the coefficient of determination (R^2) in the fit of Models 2 and 3. The R^2 value obtained by fitting Model 2 to all experimental data shown in Fig. 6 is 0.949, while that obtained for Model 3 is 0.955. Model 3 accordingly fits Day et al. data best, though the values of R^2 for Models 2 and 3 are similar and the difference in R^2 is not necessarily statistically significant. At the same time, however, the ratio of *K* values ($K^{CO_2} : K^{CH_4}$) equals 7.34 for the Model 2 fit, indicating apparent selectivity to CO_2 with respect to CH_4. This is inconsistent with the assumptions underlying Model 2 whereby CO_2 and CH_4 are taken to have the same access to all adsorption sites. This means Model 2 is not physically acceptable for describing the swelling of sub-bituminous coal in the Bowen Basin due to adsorption of CO_2-CH_4 mixtures, and we reject it on this basis opting for Model 3 as the better description. This result implies that the swelling of sub-bituminous coal from the Bowen Basin due to sorption of mixed gases (CO_2 and CH_4) is not only determined by the partial pressures of the sorbing gases, as proposed by Day et al. (2012), but is also sensitive to selective adsorption of CO_2 (i.e. to the ratio of the adsorption site concentrations $C_s^{CO_2} : C_s^{CH_4}$ and the ratio of the equilibrium constants $K^{CO_2} : K^{CH_4}$).

2.3.4. Model 4 vs. Day et al.'s data

Model 4 (see equation 19) represents the general condition corresponding to Fig.5, when $0 < \phi < C_s^{CH_4} / C_s^{CO_2}$, but reduces to Model 1 (see equation 5) when $\phi = 0$ and to Model 3 (see equation 18) when $\phi = C_s^{CH_4} / C_s^{CO_2}$. To examine whether Model 4 (for the general case where $0 < \phi < C_s^{CH_4} / C_s^{CO_2}$) can work better for CO_2-CH_4 mixtures than Model 3, we inserted the values for the key parameters V_0, C_s and *K* for CO_2 and

CH_4 which were used in Model 3 (see Table 2). For Model 4, the site sharing factor ϕ was accordingly varied in the range $0 < \phi < C_s^{CH_4} \big/ C_s^{CO_2} = 2.054 / 3.335 = 0.616$. The predictions made by applying Model 4, for the site-sharing factor value ϕ between 0 and 0.616, are compared with the data on e_{ads}^{eq} versus CO_2-CH_4 mixture composition for Coal N in Fig. 7. The e_{ads}^{eq} vs. CO_2 concentration results, obtained by varying ϕ in the specified range, lie between those obtained using Models 1 ($\phi = 0$) and 3 ($\phi = 0.616$). The results further indicate that the greater the site-sharing value ϕ, the better Model 4 fits the data of Day et al. This was confirmed by evaluating the quality of the fit to the individual data points of Day et al. (2012), yielding the R^2 values shown in Fig.7 for each value of ϕ. The implication is that for Model 4, at least in this case, the greater the extent of site sharing assumed in the model, then the better the description of Day et al.'s data. This all suggests that Model 3 is a better option at least for swelling of Bowen Basin sub-bituminous coal due to adsorption of CO_2-CH_4 mixtures.

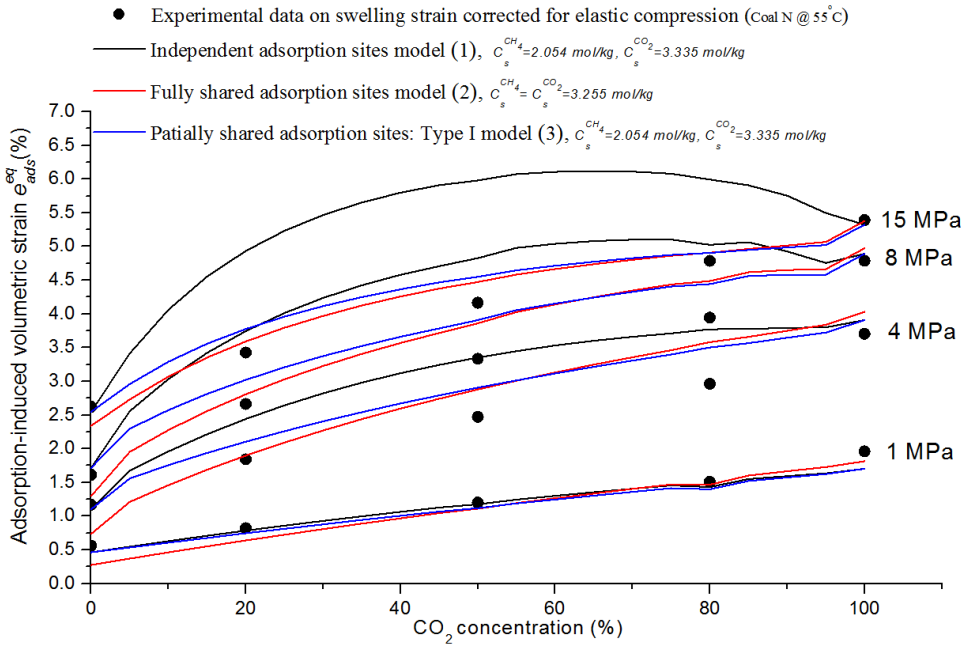

Fig. 6. Adsorption-induced swelling strains calculated from the experimental data of Day et al. (2012) for Coal N (sub-bituminous coal from the Bowen Basin, Queensland) exposed to CH_4-CO_2 mixtures. The swelling data are plotted as a function of CO_2 concentration (mole percentage) in the CH_4-CO_2 mixture at the total pressures shown and at 55˚C. The predictions made using the present three end-member models (Models 1-3) are overlain for comparison.

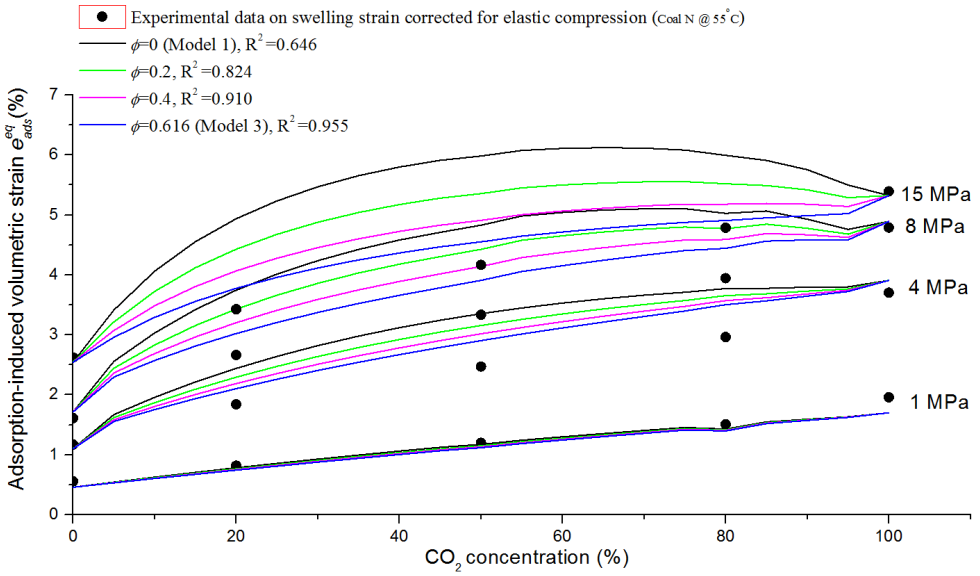

Fig. 7. Comparison of our generalized model (Model 4) , applied by varying the site-sharing factor ϕ from 0 to 0.616, with the experimental data obtained from the paper by Day et al. (2012) for Coal N from the Bowen Basin, Queensland, at 55˚C (c.f. Fig.6). The deviation of the model predictions from the experimental data are shown in terms of R^2 values.

2.4. Discussion

Overall, our results have demonstrated that the Type 1 partially shared adsorption sites model (Model 3) best describes the experimental data on Bowen Basin sub-bituminous coal presented by Day et al. (2012). This finding implies that coal swelling due to adsorption of CO_2 and CH_4 from the gas mixture is, at least in this case, determined by both partial pressure and selective adsorption effects, and not simply by partial pressure (as claimed by Day and co-workers) or by selective adsorption alone (Busch et al., 2006). This finding is also supported by the study of Gensterblum et al. (2014). We explain this inference below by considering the physical meaning of the quantities appearing in the models.

2.4.1. Physical meaning of model parameters and implications for Bowen Basin coal

In our models for adsorption-induced swelling of coal due to exposure to a binary gas mixture (see equations 5, 17, 18 and 19), swelling of the coal matrix is determined by the parameters C_s, K, V_0, ϕ and by a_g for each gas component. All of these quantities have physical meaning and their values can be obtained from a basic study of the coal and/or gas components. Let us consider their roles systematically. First, selective adsorption of the two gases is controlled by the parameters $C_s^{\alpha}, C_s^{\beta}, K^{\alpha}, K^{\beta}$ and ϕ. These all depend on coal rank and gas species. Here $C_s^{\alpha}, C_s^{\beta}$ and ϕ, through the associated values of the site potentials μ_s^i, determine the total number of potential sites for adsorption and the degree of site sharing, and therefore play a key role in controlling coal selectivity to each component. In turn, $K^i = \exp(\frac{\mu_{g0}^i - \mu_s^i}{kT})$ for species *i*, is determined by the site potential μ_s^i, by the gas potential at a given reference state μ_{g0}^i, and by temperature. This together with a_g^i dictates the occupancy of sites by species *i*. In general, like K^i, V_0^i also depends on coal rank, gas species and temperature, linking adsorbed concentration to swelling behaviour (equations 5,17,18, and 19). Finally, the activities of the gas species a_g^i, of course, depend on partial pressure (or concentration in the gas mixture) and temperature.

This all demonstrates that the swelling response of a given coal matrix material exposed to a binary gas mixture reflects the combined effects of four factors: 1) the composition of the binary mixture, i.e. the partial pressure, hence the activity and the chemical potential of the two components present in the free gas phase, 2) the

equilibrium constant K for species i, expressed statistically through the gas activity independent chemical potential $\mu_s^i(T)$, 3) the adsorption site population for each component, expressed through the maximum adsorption site concentration per *kg* of coal C_s^i and the site-sharing fraction ϕ, and 4) the partial molar volume of each gas component in the adsorbed state, expressed by V_0. Physically, the good fit between Model 3 and Day et al.'s data means, for the Bowen Basin coal, that injected CO_2 will displace CH_4 from coal due to both the reduction of CH_4 partial pressure and to truly selective sorption of CO_2 over CH_4 (refer Table 1). This is consistent with the conventional expectation, based on pure gas sorption experiments, that CO_2 can displace CH_4 not only due to partial pressure effects, as inferred by Day et al. (2012), but also to selective adsorption effects (Busch et al., 2006). The good fit of our Model 3 to the data of Day et al. also implies that swelling of coal due to sorption of a CO_2-N_2 mixture will perhaps be more complicated than suggested by Day et al., who assumed a purely partial pressure effect (Day et al., 2012). This in turn means that to evaluate if a CO_2-N_2 mixture is suitable for injecting in ECBM operations, our Model 3 should be preferred, being more physically proper, at least for the Bowen Basin sub-bituminous coal, which shows selectivity to CO_2 with respect to CH_4. Another important advantage of Model 3 is that it is easy to parameterize, since the parameters appearing in it are consistent with those obtained from swelling/sorption data for the corresponding pure components. This means Model 3 can be easily applied in practice to predict the swelling of coal due to adsorption of binary gas mixtures.

2.4.2. Application of the generalized model (Model 4) to other coals and gas mixtures

Application of our generalized model (Model 4) to the data of Day et al. (2012) for the Bowen Basin sub-bituminous coal has shown that the end member model, Model 3 (for which $\phi = C_s^{CH_4} / C_s^{CO_2} = 0.616$), explains the observed swelling behaviour upon

exposure to CO_2-CH_4 mixture best. However, other coals and gas mixtures, characterized by different values of C_s^i, K^i, V^i and ϕ may show behaviour that is better described by Models 1 or 2, or by our generalized model applied for $0 < \phi < C_s^\alpha / C_s^\beta$. This may offer an explanation of why conflicting results have been reported in the literature on what controls swelling in mixed gas environments. Since the generalized model covers all possible distributions of adsorption sites that can be described in terms of single values for K^i, it can be widely applied to any coal rank, and to binary gas mixtures at any *PT* conditions, provided proper parameter values are available. The generalized model therefore offers an important tool for future reservoir modeling, as sorption-induced swelling of coal exposed to mixed gases strongly influences coal seam permeability and stress state, hence reservoir integrity and borehole stability. In reservoir modeling exercise, of this type, Model 4 can be applied for the two dominant gas species. Extending Model 4 from binary to multiple component gas mixtures is clearly desirable in this context. However, quantifying the combined effects of partial pressure and selective adsorption, using an approach analogous to Model 4, will become complicated for multiple component mixtures (≥ 3 gas species), because multiple possibilities in the sharing of adsorption sites for different components then arise. We therefore reserve these developments for a future paper.

2.4.3. Limitation of the present study

Our comparison of Models 1-4 with the swelling data of Day et al. shows that Model 3 (R^2=0.955) fits best. The fit is not especially good, but it is acceptable. The limited quality of fit could be due to four possible reasons: 1) insufficient data points lead to significant errors in the values of the fitting parameters C_s and K obtained using the method employed; 2) the V_0 values, which we obtained from sorption isotherm and swelling data for similar but nonetheless different Bowen Basin coal, might lead to errors; 3) the experimental swelling data presented by Day et al. (2012) pertain to rather

large samples (30mm×9mm×9mm) that might not have fully equilibrated with respect to changing gas mixture composition, leading to low measured swelling values; 4) interactions between CO_2 and CH_4 in the sorption process might be not negligible, though we assume them to be so in our modelling approach (Brochard et al., 2012; Kowalczyk et al., 2008). Under point 3 above, we do not wish to imply any shortcomings in the approach adopted by Day et al. in their truly excellent work, but note that numerous previous experiments show incomplete equilibrium effects caused by either long equilibration time (Czerw, 2011; Day et al., 2012; Majewska et al., 2009) or the change of transport path due to swelling effect (Hol et al., 2012b; Kowalczyk et al., 2008; Peng et al., 2014). This means that more experimental data using samples of different sizes and longer equilibration times are required to evaluate our models thoroughly.

In addition, the present models focus on unconfined coal, without considering the effects of in-situ stress. However, both lithostatic stress and self-stressing due to laterally constrained swelling (Hol et al., 2012a), under in situ conditions, reduce the adsorption capacity of coal for pure CO_2 and pure CH_4 (Hol et al., 2011; Hol et al., 2012a; Peng et al., 2014), thus influencing stress-strain development, cleat aperture evolution (Nikoosokhan et al., 2014) and hence permeability change (Espinoza et al., 2014) during CO_2-ECBM production. This means that a further constitutive model that fully couples stress-strain-sorption behaviour of coal exposed to mixed gases should be considered in future work. Moreover, building upon the studies by Nikoosokhan et al. (2014) and Espinoza et al. (2014), both experimental data and coupled models are needed, linking permeability to the stress-strain-sorption behaviour of stressed coal exposed to mixed gases.

2.5. Conclusions

This paper has constructed thermodynamic models for adsorption induced swelling

of unconfined coal matrix material exposed to a binary gas/fluid mixture, based on the adsorption-induced swelling model for unconfined coal exposed to a single pure gas or fluid proposed by Hol et al. (2012a).

Three models were derived corresponding to three physical possible end-member interactions. These were also cast as a fourth, generalized model. Model 1 addresses the independent adsorption sites. Adsorption of gas/fluid species α and β accordingly leads to independent swelling responses that sum to give total volumetric strain. Model 2 describes the adsorption-induced swelling of coal exposed to a binary gas/fluid mixture when adsorption sites are fully shared by each component. This model is thermodynamically equivalent to the extended Langmuir model for ideal gases. When applied for ideal gases (low pressure), the adsorbed concentrations predicted reduce to the Langmuir isotherm for mixed gases. Model 3 addresses Type I partially shared adsorption sites for an end-member case. This model implies that the swelling of coal matrix material due to adsorption of a binary gas/fluid mixture is determined both by partial pressures of sorbing gases and by truly selective adsorption effects. Model 4 describes Type II partially shared adsorption sites for the general case. This model covers Models 1-3.

When compared with experimental data on the swelling behaviour of sub-bituminous coal from the Bowen Basin, exposed to CH_4-CO_2 mixtures, Model 3 is preferred. This finding illustrates that CH_4 is displaced by CO_2 due to both the reduction of CH_4 partial pressure (dilution of CH_4) in the mixed gas phase and selective adsorption of CO_2. Our results therefore differ from previous suggestions that CH_4 and CO_2 have access to all adsorption sites and that swelling solely depends on partial pressure (Day et al., 2012; Day et al., 2008c), or that swelling solely depends on site accessibility (Busch et al., 2006). Since Model 3 is easy to parameterize, it can be easily applied in practice to predict the swelling behaviour of coal exposed to CH_4-CO_2 mixture during ECBM production, at least to sub-bituminous coals similar to those of the Bowen Basin. Our

results further imply that Model 3 should be the most suitable for evaluating if CO_2-N_2 mixtures will be effective in limiting coal swelling and permeability reduction in ECBM operations in sub-bituminous coals, such as those of the Bowen Basin. On the other hand, our generalized model, Model 4, can be widely applied to any coal rank, to any binary gas mixture and to any *PT* conditions, provided that proper parameter values are available. Model 4 therefore offers an important tool for modeling swelling and permeability evolution during ECBM operations, and through it, generality may prove to explain why sorption and swelling of some coals seem to be dominated by partial pressure effects and others by selective sorption effects.

Acknowledgements

We are grateful to TOTAL S.A. for financial support for this research, and especially acknowledge Sandrine Vidal-Gilbert for her support and suggestions on this research. The China Scholarship Council (CSC) is also gratefully acknowledged for its financial support of first author Liu.

References

Brochard, L., Vandamme, M., Pellenq, R.J.-M., Fen-Chong, T., 2012. Adsorption-induced deformation of microporous materials: coal swelling induced by CO_2–CH_4 competitive adsorption. Langmuir 28, 2659-2670.

Busch, A., Gensterblum, Y., 2011. CBM and CO_2-ECBM related sorption processes in coal: A review. International Journal of Coal Geology 87, 49-71.

Busch, A., Gensterblum, Y., Krooss, B.M., 2003. Methane and CO_2 sorption and desorption measurements on dry Argonne premium coals: pure components and mixtures. International Journal of Coal Geology 55, 205-224.

Busch, A., Gensterblum, Y., Krooss, B.M., Siemons, N., 2006. Investigation of high-pressure selective adsorption/desorption behaviour of CO_2 and CH_4 on coals: an experimental study. International Journal of Coal Geology 66, 53-68.

Czerw, K., 2011. Methane and carbon dioxide sorption/desorption on bituminous

coal—Experiments on cubicoid sample cut from the primal coal lump. International Journal of Coal Geology 85, 72-77.

Day, S., Fry, R., Sakurovs, R., 2008a. Swelling of Australian coals in supercritical CO_2. International Journal of Coal Geology 74, 41-52.

Day, S., Fry, R., Sakurovs, R., 2012. Swelling of coal in carbon dioxide, methane and their mixtures. International Journal of Coal Geology 93, 40-48.

Day, S., Fry, R., Sakurovs, R., Weir, S., 2010. Swelling of coals by supercritical gases and its relationship to sorption. Energ Fuel 24, 2777-2783.

Day, S., Sakurovs, R., Weir, S., 2008b. Supercritical gas sorption on moist coals. International Journal of Coal Geology 74, 203-214.

Do, D.D., 1998. Adsorption analysis: equilibria and kinetics. World Scientific.

Espinoza, D., Vandamme, M., Pereira, J.-M., Dangla, P., Vidal-Gilbert, S., 2014. Measurement and modeling of adsorptive–poromechanical properties of bituminous coal cores exposed to CO_2: Adsorption, swelling strains, swelling stresses and impact on fracture permeability. International Journal of Coal Geology 134, 80-95.

Fujioka, M., Yamaguchi, S., Nako, M., 2010. CO_2-ECBM field tests in the Ishikari Coal Basin of Japan. International Journal of Coal Geology 82, 287-298.

Gensterblum, Y., Busch, A., Krooss, B.M., 2014. Molecular concept and experimental evidence of competitive adsorption of H_2O, CO_2 and CH_4 on organic material. Fuel 115, 581-588.

Hol, S., Peach, C.J., Spiers, C.J., 2011. Applied stress reduces the CO_2 sorption capacity of coal. International Journal of Coal Geology 85, 128-142.

Hol, S., Peach, C.J., Spiers, C.J., 2012a. Effect of 3-D stress state on adsorption of CO_2 by coal. International Journal of Coal Geology 93, 1-15.

Hol, S., Spiers, C.J., 2012. Competition between adsorption-induced swelling and elastic compression of coal at CO_2 pressures up to 100MPa. J Mech Phys Solids 60, 1862-1882.

Hol, S., Spiers, C.J., Peach, C.J., 2012b. Microfracturing of coal due to interaction with CO_2 under unconfined conditions. Fuel 97, 569-584.

Kowalczyk, P., Ciach, A., Neimark, A.V., 2008. Adsorption-induced deformation of microporous carbons: Pore size distribution effect. Langmuir 24, 6603-6608.

Kunz, O., Klimeck, R., Wagner, W., Jaeschke, M., 2006. The GERG-2004 Wide-Range Reference Equation of State for Natural Gases and Other Mixtures. Fortschr. Ber. VDI, VDI-Verlag, Düsseldorf 1.

Langmuir, I., 1918. The adsorption of gases on plane surfaces of glass, mica and platinum. J

Am Chem Soc 40, 1361-1403.

Majewska, Z., Ceglarska-Stefańska, G., Majewski, S., Ziętek, J., 2009. Binary gas sorption/desorption experiments on a bituminous coal: Simultaneous measurements on sorption kinetics, volumetric strain and acoustic emission. International Journal of Coal Geology 77, 90-102.

Nikoosokhan, S., Vandamme, M., Dangla, P., 2014. A poromechanical model for coal seams saturated with binary mixtures of CH_4 and CO_2. J Mech Phys Solids 71, 97-111.

Ottiger, S., Pini, R., Storti, G., Mazzotti, M., 2008. Measuring and modeling the competitive adsorption of CO_2, CH_4, and N_2 on a dry coal. Langmuir 24, 9531-9540.

Pan, Z., Connell, L.D., 2007. A theoretical model for gas adsorption-induced coal swelling. International Journal of Coal Geology 69, 243-252.

Pan, Z., Connell, L.D., 2009. Comparison of adsorption models in reservoir simulation of enhanced coalbed methane recovery and CO_2 sequestration in coal. Int J Greenh Gas Con 3, 77-89.

Peng, Y., Liu, J., Wei, M., Pan, Z., Connell, L.D., 2014. Why coal permeability changes under free swellings: New insights. International Journal of Coal Geology 133, 35-46.

Reeves, S.R., 2004. The Coal-Seq project: Key results from field, laboratory and modeling studies, Proceedings of the 7th International Conference on Greenhouse Gas Control Technologies (GHGT-7). Citeseer, pp. 1399-1406.

Setzmann, U., Wagner, W., 1991. A new equation of state and tables of thermodynamic properties for methane covering the range from the melting line to 625 K at pressures up to 100 MPa. Journal of Physical and Chemical Reference Data 20, 1061-1155.

Span, R., Wagner, W., 1996. A new equation of state for carbon dioxide covering the fluid region from the triple‐point temperature to 1100 K at pressures up to 800 MPa. Journal of Physical and Chemical Reference Data 25, 1509-1596.

Tuin, G., Stein, H., 1995. The excess Gibbs free energy of adsorption of sodium dodecylbenzenesulfonate on polystyrene particles. Langmuir 11, 1284-1290.

van Bergen, F., Krzystolik, P., van Wageningen, N., Pagnier, H., Jura, B., Skiba, J., Winthaegen, P., Kobiela, Z., 2009a. Production of gas from coal seams in the Upper Silesian Coal Basin in Poland in the post-injection period of an ECBM pilot site. International Journal of Coal Geology 77, 175-187.

van Bergen, F., Pagnier, H., Krzystolik, P., 2006. Field experiment of enhanced coalbed methane-CO_2 in the upper Silesian basin of Poland. Environmental Geosciences 13, 201-224.

van Bergen, F., Spiers, C., Floor, G., Bots, P., 2009b. Strain development in unconfined coals exposed to CO_2, CH_4 and Ar: Effect of moisture. International Journal of Coal Geology 77, 43-53.

Vandamme, M., Brochard, L., Lecampion, B., Coussy, O., 2010. Adsorption and strain: the CO_2-induced swelling of coal. J Mech Phys Solids 58, 1489-1505.

White, C.M., Smith, D.H., Jones, K.L., Goodman, A.L., Jikich, S.A., LaCount, R.B., DuBose, S.B., Ozdemir, E., Morsi, B.I., Schroeder, K.T., 2005. Sequestration of carbon dioxide in coal with enhanced coalbed methane recovery a review. Energ Fuel 19, 659-724.

Chapter 3

Effect of lithostatic stress on methane sorption by coal: Theory vs. experiment and implications for predicting in-situ coalbed methane content

Jinfeng Liu, Christopher J. Spiers, Colin J. Peach, Sandrine Vidal-Gilbert

Also in press in International Journal of Coal Geology

Abstract

Recent research has demonstrated that confining stresses applied to the solid framework of coal can reduce its gas sorption capacity by several percent to perhaps several tens of percent. To evaluate the magnitude of this effect more rigorously in relation to predicting in-situ coalbed methane (CBM) content, a better understanding of the effects of stress on methane sorption by coal is needed. In this paper, a previous thermodynamic model for the effects of stress on CO_2 sorption by coal is revised and applied to CH_4. The revised model predicts that in-situ CBM content is indeed determined not only by the geological factors generally considered, such as coal rank, coal composition, moisture content and temperature, but also by lithostatic or confining stress, which is usually ignored. This prediction is tested by means of experiments performed on a composite cylindrical sample of Brzeszcze 364 high volatile bituminous coal subjected to 10 MPa methane pressure at a temperature of 40˚C, varying the hydrostatic stress or confining pressure in the range 11-43 MPa. In these experiments, we determined if CH_4 was desorbed as confining pressure was increased by subtracting the poroelastic expulsion of CH_4 from the total CH_4 expelled, assuming the former to equal the gas volume expelled in control experiments performed using Helium. The experimental results show that the equilibrium sorption capacity for CH_4 at 10 MPa gas pressure and 11 MPa confining pressure (1MPa Terzaghi effective stress) was 0.808 mol/kg_{coal}. This was reduced by at least ~ 6% by increasing the confining pressure to 43 MPa (33 MPa effective stress), confirming the validity of our model. We apply our model to predict in-situ CBM concentration as a function of coal seam depth for dry, high volatile bituminous coal, assuming a geothermal gradient of 32˚C/km. The results indicate a maximum CH_4 concentration of ~ 0.76 mol/kg_{coal} at a burial depth of ~ 900 m, which is ~ 3% lower than conventional predictions. This reduction is minor but helps to explain why gas saturation is generally lower than expected from conventional sorption measurements on unconfined coal powders. More importantly, our results confirm that there is an intimate coupling between in-situ stress, strain and sorption in coal that needs to be considered in developing gas-enhanced CBM strategies.

3.1. Introduction

Subsurface coal seams typically consist of coal matrix (solid) material cut by a multiscale network of joints or cleats (Hol et al., 2012a; Laubach et al., 1998; Levine, 1996). These systems often contain large amounts of methane (CH_4) generated during the formation of the coal, i.e. during the so-called coalification process (Levine, 1993; Moore, 2012). Most of the methane ultimately trapped (~ 95%-98%) is stored in the coal matrix via sorption (Gray, 1987; White et al., 2005). This can potentially be recovered economically in the form of natural gas, referred to as coalbed methane (CBM). The recovery or production of this methane is likewise termed CBM production (Levine, 1996; Moore, 2012). Compared to conventional natural gas reservoirs, such as sandstone formations, coal beds have low permeability, which usually limits primary CBM production by pressure depletion methods to 20-60% of the estimated reserves (White et al., 2005). Other gases, such as N_2, CO_2 and flue gas, have therefore been injected in attempts to enhance coalbed methane (ECBM) production (White et al., 2005). Of these, particular interest focuses on CO_2-ECBM, because coal preferentially adsorbs CO_2 over CH_4 (Fitzgerald et al., 2005; Gensterblum et al., 2014; Liu et al., 2015; Merkel et al., 2015; Ottiger et al., 2008a; Pini et al., 2010), and can therefore be viewed as a potential lithology for combined ECBM plus geological storage of CO_2.

Besides coal reservoir permeability, CBM content is a key factor in assessing the economic feasibility of (E)CBM production. Estimation of CBM content is generally based on the sorption capacity of unstressed coal powders determined in the laboratory by means of manometric, volumetric or gravimetric measurements. These are performed under unconfined conditions, i.e. at zero conventional or Terzaghi effective stress where the fluid pressure equals the confining pressure and where sorption-induced swelling of the coal is opposed only by the fluid pressure (Busch and Gensterblum, 2011).

It is well-established that CH_4 sorption capacity is influenced by coal rank, coal composition, moisture content and temperature (Busch and Gensterblum, 2011; Bustin

and Clarkson, 1998; Gensterblum et al., 2014; Gensterblum et al., 2013; Moore, 2012). However, Pone et al. (2009) measured the CH_4 sorption capacity of bituminous coal (a cylinder of 25 mm in diameter) under both stressed (confined) and unstressed (unconfined) conditions using volumetric methods. They present evidence that confining stresses of 6.9 and 13.8 MPa caused a reduction in CH_4 sorption capacity of 85 and 91% respectively, at a CH_4 pressure of 3.8 MPa at room temperature. It is unclear, though, how much of this reduction was due to a) a direct effect of stress on equilibrium sorption capacity versus b) a reduction in the volume of coal sample that was accessible to CH_4 as sample permeability decreased with increasing confining stress. To obtain a reliable estimate of in-situ CBM content, a physically based and experimentally verified stress-strain-sorption model is required to describe the effect of in-situ stress on the CH_4 sorption capacity of coal at thermodynamic equilibrium.

Such a thermodynamic model was developed by Hol et al. (2012a) to describe how the equilibrium concentration of gas/fluid species adsorbed by coal is affected by compressive stresses applied in excess of the fluid pressure. This was experimentally proved to apply to CO_2 by the authors in the context of investigating CO_2-ECBM. However, a number of errors were made in deriving this model, which mean that though the form of the final equations obtained is correct, the physical meaning of the equilibrium constant for sorption that appears is not. Indeed, in the model by Hol et al., the equilibrium constant depends strongly on both temperature and gas pressure, whereas for a given reaction it should depend only on temperature (Chang, 2000; Hill, 2012). A corrected thermodynamic model is therefore needed to properly capture the physical process of gas adsorption by stressed coal, and to predict the true equilibrium CBM content of coal and the associated swelling strain response, under in-situ conditions where coal supports positive effective stress.

In the present paper, we revise the thermodynamic model developed by Hol et al. (2012a) for the effect of an applied stress state (σ_{ij}) on the concentration of gas/fluid

species that can be adsorbed by coal, or by any other sorbent, and we show that the same result is obtained using both statistical mechanics and kinetic approaches. A corrected expression for thermodynamic equilibrium constant is thus obtained, which is confirmed to depend only on temperature for a given coal and gas species. To evaluate whether our model is applicable to adsorption of CH_4 by coal, and to the estimation of in-situ CBM content, we also report experiments. These were performed on a composite cylindrical sample of Brzeszcze high volatile bituminous coal to determine the dependence of adsorbed CH_4 concentration on applied effective stress. The experiments were conducted at a fixed temperature of 40˚C and a fixed CH_4 pressure of 10 MPa, varying the applied hydrostatic pressure in the range 11-43 MPa (conventional effective stress of 1-33 MPa). The results show at least ~ 6% reduction in adsorbed CH_4 concentration at a confining pressure of 43 MPa (effective stress 33 MPa). We compare our model with our experimental results and show that our model successfully describes the adsorption process under stressed conditions. Finally, we discuss the implications for predicting in-situ CBM content.

3.2. Theoretical model

To gain clear insight into the effect of stress on sorption behavior, we begin by re-deriving the model presented by Hol et al. (2012a) for the sorption capacity of a single gas or fluid species under stressed conditions, using a corrected method. For simplicity, we henceforth use the term "gas", to cover both gas and (supercritical) fluid. We use the term "stressed coal" to refer to coal that supports a positive (conventional) effective stress in excess of the applied gas pressure. Compressive stresses and gas pressure are measured positive, as is swelling strain.

In our derivation, we consider the closed system specified in Fig. 1, consisting of a small coal matrix cube of mass m and side l ($\leq$1mm), surrounded by a pure gas phase (α)

present at constant pressure P, absolute temperature T and chemical potential μ_g. We assume the gas phase to be pressurized via a movable outer boundary subjected to a constant pressure boundary condition. The coal matrix cube, also at uniform temperature T, is independently subjected to a general stress state σ_{ij} via a permeable loading frame that allows free access of gas to the coal (*Fig. 1*). Following Hol et al. (2011; 2012a), the cube is considered homogeneous in structure and composition at the particle length scale l, but may be anisotropic in properties. It is further assumed to contain nano-pores only, so that there is no Darcian flow and negligible storage of free (unadsorbed) gas. In other words, the coal particle is so small that it is cleat free and can take up gas only by molecular diffusion and adsorption. The coal particle is accordingly elastic but not poro-elastic. Lastly, we assume that the coal cube hosts n_s localized adsorption sites, each of which consists of a potential well capable of trapping a single molecule of the gas α, as illustrated in Fig. 2.

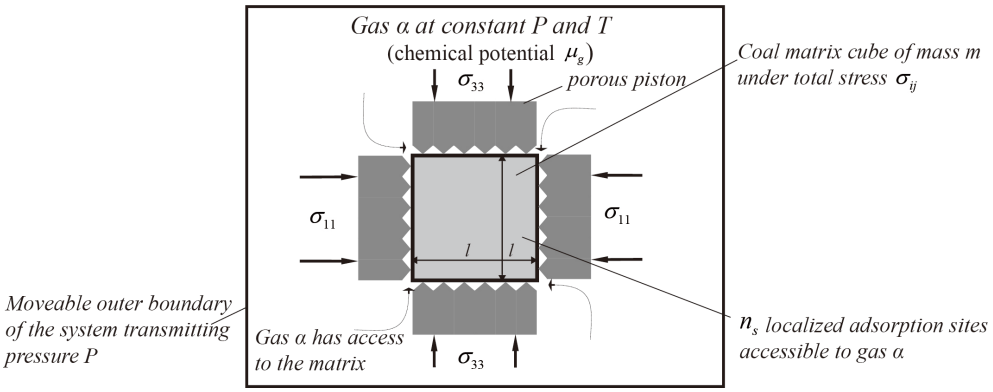

Fig.1. Representative volume of coal matrix material used in the present analysis of adsorption under conditions of constant stress σ_{ij}. The representative volume consists of a small cube of coal matrix material, of mass m and side l ($l \leq 1$ mm), containing n_s localized adsorption sites accessible to gas α. The cube is so small that it is free of cleats and consists entirely of nanoporous coal matrix

material. Once the coal particle is exposed to gas α at constant pressure P and at constant temperature T, it is accordingly assumed to take up gas α only by diffusion and adsorption.

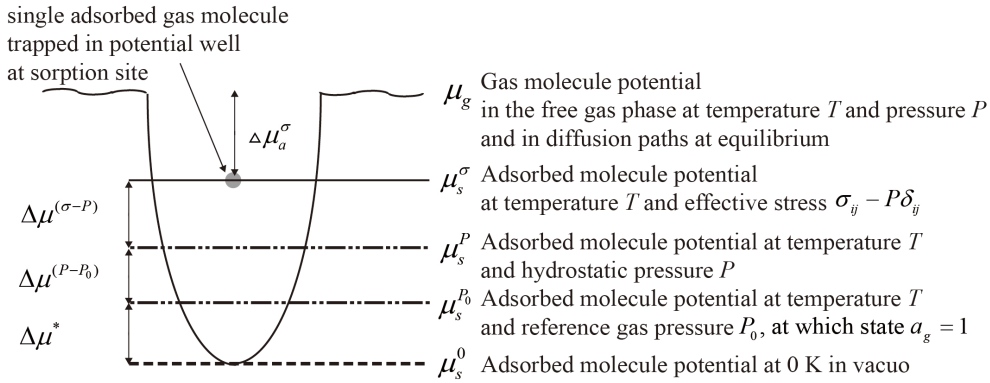

Fig. 2. Potential well associated with an adsorption site present in coal matrix material under stress σ_{ij} *(see Fig. 1). Here* μ_g *represents the chemical potential of a single molecule present in free gas phase at pressure P and temperature T, and present in the diffusion paths inside the matrix at equilibrium. The quantity* $\mu_s^\sigma(\sigma,T)$ *represents the potential of a single adsorbed gas molecule located in the potential well under stress state* $\sigma_{ij} > P\delta_{ij}$*. This consists of the potential* μ_s^P *of the adsorbed gas molecule under unconfined hydrostatic (effective stress-free) conditions, where* $\sigma_{ij} = P\delta_{ij}$*, plus the extra potential* $\Delta\mu^{(\sigma-P)}$ *related to the applied effective stress* $\sigma_{ij} - P\delta_{ij}$*. The quantity* $\mu_s^P(P,T)$ *itself consists of the potential* $\mu_s^{P_0}(T)$*, measured at temperature T and reference gas pressure* P_0 *at which* a_g*=1, plus the potential* $\Delta\mu^{(P-P_0)}$ *related to the excess gas pressure P-*P_0*. The quantity* $\mu_s^{P_0}(T)$ *is only temperature dependent for a given gas at reference pressure* P_0*, consisting of the potential* μ_s^0 *at absolute 0 in vacuo, plus the potential* $\Delta\mu^*(T,P_0)$*. Finally,* $\Delta\mu_a^\sigma$ *represents the total change in potential associated with adsorbing a single molecule from the gas phase into the solid, yielding* $\Delta\mu_a^\sigma = \mu_s^{P_0}(T) + \Delta\mu^{(P-P_0)} + \Delta\mu^{(\sigma-P)} - \mu_g$*. Here* δ_{ij} *is Kronecker delta.*

3.2.1. Attachment energy for adsorption of a single molecule by stressed coal

3.2.1.1. Energy / Entropy balance for the solid phase

When a single molecule of gas species α is reversibly adsorbed by the coal matrix cube (Fig. 1), the first and second laws of thermodynamics for the solid phase (subscript *s*) yield the Gibbs equation

$$\Delta U_s^{\sigma} = -\sigma_{ij}\Delta\varepsilon_{ij}^{ads} l^3 + T\Delta S_s^{\sigma} + \mu_s^{\sigma} \tag{1}$$

In this relation, ΔU_s^{σ} (J•molecule^{-1}) is the change in internal energy of the solid phase. The term $-\sigma_{ij}\Delta\varepsilon_{ij}^{ads} l^3$ represents the stress-strain work done on the surroundings as the coal swells against the total applied stress σ_{ij} by an adsorption-induced swelling strain $\Delta\varepsilon_{ij}^{ads}$, ΔS_s^{σ} (J•K^{-1}•molecule^{-1}) is the entropy change of the solid, and μ_s^{σ} (J•molecule^{-1}) is the chemical potential of the adsorbed molecule within the potential well associated with the sorption site that traps it (see Fig. 2). Note that we treat the adsorbed gas molecule as being a "dissolved" component of the solid phase here, as opposed to assuming an independently identifiable adsorbed phase (following the treatment of Myers (2002) for stress-free sorption).

If the volume change of the coal particle associated with the swelling strain $\Delta\varepsilon_{ij}^{ads}$ per adsorbed molecule is Ω_0 (the partial molecular volume of the adsorbed gas in m^3•molecule^{-1}), then the particle undergoes a volumetric strain $\Delta\varepsilon_v^{ads} = \Omega_0 / l^3 = \Delta\varepsilon_{11}^{ads} + \Delta\varepsilon_{22}^{ads} + \Delta\varepsilon_{33}^{ads}$ per molecule adsorbed. This can be viewed as associated with an isotropic swelling strain, or mean extensional strain, of $\Delta\overline{\varepsilon}^{ads} = \Delta\varepsilon_v^{ads} / 3 = \Omega_0 / 3l^3$. We can hence split $\Delta\varepsilon_{ij}^{ads}$ into an isotropic swelling

strain component $\Delta\overline{\varepsilon}^{ads}\delta_{ij} = (\Omega_0 / 3l^3)\delta_{ij}$ and a deviatoric component $\Delta\varepsilon_{ij}^{'ads} = \Delta\varepsilon_{ij}^{ads} - (\Omega_0 / 3l^3)\delta_{ij}$, where δ_{ij} is the Kronecker delta (Fig. 3). The deviatoric strain components can further be specified as $\Delta\varepsilon_{ij}^{'ads} = \Delta\overline{\varepsilon}^{ads}A_{ij} = (\Omega_0 / 3l^3)A_{ij}$, where $A_{ij} = \Delta\varepsilon_{ij}^{'ads} / \Delta\overline{\varepsilon}^{ads}$ is a second rank tensor expressing the anisotropy of sorption-induced swelling strain. Hence, we can write $\Delta\varepsilon_{ij}^{ads} = \Delta\overline{\varepsilon}^{ads}\delta_{ij} + \Delta\varepsilon_{ij}^{'ads} = (\delta_{ij} + A_{ij})(\Omega_0 / 3l^3)$. Similarly expressing σ_{ij} in terms of the means stress ($\overline{\sigma} = \sigma_{kk} / 3$) and deviatoric stress ($\sigma_{ij}^{'} = \sigma_{ij} - \overline{\sigma}\delta_{ij}$) components, now means that the stress-strain work term in equation 1 can be written as $(\overline{\sigma} + 1/3\,\sigma_{ij}^{'}A_{ij})\Omega_0$ (Hol et al., 2012a).

The internal energy change for the solid phase in equation1 accordingly becomes,

$$\Delta U_s^{\sigma} = -(\overline{\sigma} + 1/3\,\sigma_{ij}^{'}A_{ij})\Omega_0 + T\Delta S_s^{\sigma} + \mu_s^{\sigma} \tag{2a}$$

so that $\mu_s^{\sigma} = \Delta U_s^{\sigma} - T\Delta S_s^{\sigma} + (\overline{\sigma} + 1/3\,\sigma_{ij}^{'}A_{ij})\Omega_0 = \Delta F_s^{\sigma} + (\overline{\sigma} + 1/3\,\sigma_{ij}^{'}A_{ij})\Omega_0$ (2b)

where ΔF_s^{σ} (J•molecule^{-1}) represents the change in Helmholtz free energy of the coal matrix particle for adsorption of a single molecule. Note that both Ω_0 and ΔF_s^{σ} are assumed here to be insensitive to the stress state supported by the coal particle, and to the gas pressure.

When the coal matrix cube is subjected only to the reference pressure P_0, defined as the gas pressure for which the activity $a_g = 1$, then $\sigma_{ij} = P_0\delta_{ij}$, $\overline{\sigma} = P_0$, $\sigma_{ij}^{'} = 0$ and equation 2b modifies to

$$\mu_s^{P_0} = \Delta F_s^{P_0} + P_0\Omega_0 \tag{3}$$

where $\mu_s^{P_0}$ (see Fig. 2) is the potential of the molecule in the adsorbed state at temperature T and reference gas pressure P_0. In addition, $\mu_s^{P_0}$ can be expressed as $\mu_s^{P_0} = \mu_s^0 + \Delta\mu^*(T, P_0)$, where μ_s^0 is the potential in vacuo at absolute zero, i.e. the minimum energy at ground state (c.f. Hill, 2012), and $\Delta\mu^*(T, P_0)$ is the energy of the adsorbed molecule at temperature T and reference pressure P_0 measured with respect to the ground state. Since P_0 is a constant for a given gas, this means the potential $\mu_s^{P_0}$ depends only on temperature T.

When the coal matrix cube is subjected to a general gas pressure P under otherwise stress-free conditions, we now get $\sigma_{ij} = P\delta_{ij}$ and equation 2b yields

$$\mu_s^P = \Delta F_s^P + P\Omega_0 \tag{4}$$

where μ_s^P (see Fig. 2) is the potential of the adsorbed molecule at temperature T and gas pressure P, and clearly depends on both.

Assuming $\Delta F_s^{P_0} \approx \Delta F_s^P \approx \Delta F_s^\sigma$ as already mentioned, and using equations 2b, 3 and 4, we hence obtain the relations

$$\mu_s^P = \mu_s^{P_0} + (P - P_0)\Omega_0 \tag{5a}$$

$$\mu_s^\sigma = \mu_s^{P_0} + (\overline{\sigma} - P_0 + \tfrac{1}{3}\sigma_{ij}' A_{ij})\Omega_0 \tag{5b}$$

$$\mu_s^\sigma = \mu_s^P + (\overline{\sigma} - P + \tfrac{1}{3}\sigma_{ij}' A_{ij})\Omega_0 \tag{5c}$$

between the potentials $\mu_s^{P_0}$, μ_s^P and μ_s^σ represented in Fig.2,

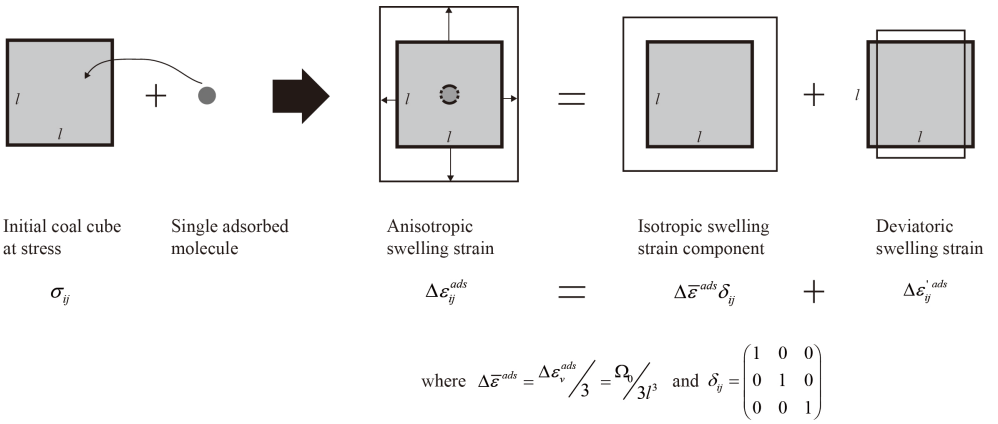

Fig.3. Illustration of anisotropic swelling strain due to adsorption of a single gas molecule by coal cube of edge dimension l and volume l^3. $\Delta\varepsilon_v^{ads} = \Delta\varepsilon_{kk}^{ads}$ is the volumetric strain produced by adsorbing a single molecule having partial molecular volume Ω_0.

3.2.1.2. Energy / Entropy balance for the gas phase

For the gas phase (subscript *g*) in Fig.1, the internal energy change that occurs when a single molecule is removed by adsorption is given, via the Gibbs equation analogous to equation 1, as

$$\Delta U_g^P = P\Omega_g^P + T\Delta S_g^P - \mu_g \tag{6a}$$

so that $\mu_g = -(\Delta U_g^P - T\Delta S_g^P) + P\Omega_g^P = -\Delta F_g^P + P\Omega_g^P$ (6b)

In this case, Ω_g^P (m^3•molecule^{-1}) is the molecular volume of the gas phase at pressure P and temperature T, ΔS_g (J•K^{-1}• molecule^{-1}) is the entropy change associated with removing one molecule from the gas, and ΔF_g^P (J• molecule^{-1}) is the corresponding change in Helmholtz energy of the gas phase. The quantity μ_g represents the chemical potential of a single gas molecule (Fig.2), which can be expressed from the thermodynamics of fluid systems as

$$\mu_g = \mu_{g0} + kT \ln a_g \tag{7}$$

where $a_g = a_g(P,T)$ is the chemical activity of the free gas at pressure P and temperature T, and where μ_{g0} is the potential of gas species α at the reference pressure P_0, for which $a_g = 1$. Of course, when the gas pressure $P = P_0$, equation 6b becomes

$$\mu_{g0} = -\Delta F_g^{P_0} + P_0\Omega_g^{P_0} \tag{8}$$

where $\Omega_g^{P_0}$ is the molecular volume of gas phase at pressure P_0 and temperature T.

3.2.1.3. Combined solid-gas system

For the combined solid-gas system (subscript a), with the solid at stress σ_{ij}, the gas at pressure P and the system at uniform temperature T, we now get, adding (2a) and (6a),

$$\Delta\mu_a^\sigma = \mu_s^\sigma - \mu_g = \Delta U_a^\sigma + P(\Omega_0 - \Omega_g^P) - T\Delta S_a^\sigma + (\overline{\sigma} - P)\Omega_0 + \tfrac{1}{3}\sigma_{ij}' A_{ij}\Omega_0 \tag{9a}$$

or $$\Delta\mu_a^\sigma = \mu_s^\sigma - \mu_g = \Delta F_a^\sigma + P(\Omega_0 - \Omega_g^P) + (\overline{\sigma} - P)\Omega_0 + \tfrac{1}{3}\sigma_{ij}' A_{ij}\Omega_0 \tag{9b}$$

Here, ΔU_a^σ (J•molecule^{-1}) is the internal energy change of the system, ΔS_a^σ (J•K^{-1}• molecule^{-1}) is its entropy change, ΔF_a^σ (J• molecule^{-1}) is the corresponding change in Helmholtz free energy, and $\Delta\mu_a^\sigma$ (J• molecule^{-1}) is the change in potential associated with the adsorbed molecule, i.e. the change in the free energy of the system due to the attachment of the adsorbed molecule. Physically, the attachment energy $\Delta\mu_a^\sigma$ represents (negative) energy change (i.e. the energy released from the system) when a single gas molecule is adsorbed by the stressed coal at gas pressure *P* and system temperature *T*, or conversely, the energy that must be supplied to remove a single adsorbed molecule localized in the potential well into the free phase at these conditions.

Similarly, from (3) minus (8), the change in potential of the combined solid-gas system due to adsorption of a single molecule by unstressed coal at the reference gas pressure P_0 and temperature *T*, is

$$\Delta\mu_a^{P_0} = \mu_s^{P_0} - \mu_{g0} = \Delta F_a^{P_0} + P_0(\Omega_0 - \Omega_g^{P_0}) \tag{10}$$

This attachment energy $\Delta\mu_a^{P_0}$ depends only on temperature for a given coal type and gas species. Likewise, when the coal matrix cube is subjected to gas pressure *P* only, i.e. to hydrostatic conditions defined $\sigma_{ij} = P\delta_{ij}$, the attachment energy, from equation 4 minus 6b, is given

$$\Delta\mu_a^P = \mu_s^P - \mu_g = \Delta F_a^P + P(\Omega_0 - \Omega_g^P) \tag{11}$$

where the quantity $\Delta\mu_a^P$ is now a function of temperature and pressure.

3.2.2. Adsorption energy for n molecules

For a total population of adsorption sites n_s, we assume that each adsorption site

remains empty or else takes up one gas molecule. We further assume that there is no interaction between adsorbed molecules. Then from combination theory, the number of different ways that *n* adsorbed molecules can be distributed over the n_s available sites can be written as $W^i = \frac{n_s!}{n!(n_s-n)!}$. Following numerous previous authors (e.g. Hill, 2012; Hol et al., 2012a; Tuin and Stein, 1995), this contributes a configurational entropy term $\Delta S^i = -k \ln W^i$, and hence an energy term $-kT \ln W^i$ to the potential of the adsorbed molecules and hence to the overall change in energy that occurs when *n* molecules of species *α* are adsorbed. The change in energy of the solid due to adsorption of *n* molecules is accordingly given not as $n\mu_s^\sigma$ but as

$$\Delta\Phi_s = n\mu_s^\sigma - kT \ln \frac{n_s!}{n!(n_s-n)!} \tag{12}$$

while the total energy change of the coal-gas system due to adsorption of *n* molecules is given as

$$\Delta\Phi_a = n\Delta\mu_a^\sigma - kT \ln \frac{n_s!}{n!(n_s-n)!} \tag{13}$$

where *k* is Boltzmann's constant.

By comparison with the Gibbs free energy for a reaction under hydrostatic conditions, written in generic form as $(\Delta G)_{P,T} = \Delta U - T\Delta S + P\Delta V$, it is evident from equations 2b, 9a, 12 and 13 that the quantities $\mu_s^\sigma(\sigma_{ij}, T)$, $\Delta\mu_a(\sigma_{ij}, P, T)$, $\Delta\Phi_s(\sigma_{ij}, T, n)$ and $\Delta\Phi_a(\sigma_{ij}, P, T, n)$ are all Gibbs-like free energies generalized to stressed conditions, i.e. to include stress-strain work independently of $P\Delta V$ work. Now, the present Langmuir-type adsorption process can be formulated as the reaction

$$\alpha_{(\text{gas})} + \mathrm{C}^*_{(\text{solid})} \rightleftharpoons \alpha : \mathrm{C}^*_{(\text{solid})}$$

where α represents molecules in the free gas phase, C^* represents sorption sites in the stressed coal matrix, and $\alpha : \mathrm{C}^*$ represents the complex formed when a gas molecule is bound to an adsorption site (Butt et al., 2006; Hol et al., 2012a). The total free energy change for adsorption of *n* molecules via this reaction is of course

$$\Delta\Phi_R = \Delta\Phi_{\alpha:\mathrm{C}^*} - \Delta\Phi_{\mathrm{C}^*} - n\mu_g \tag{14}$$

where $\Delta\Phi_{\alpha:\mathrm{C}^*}$ is the free energy contributed to the solid phase by *n* filled sorption sites and $\Delta\Phi_{\mathrm{C}^*}$ is the free energy contributed to the solid by *n* sites before sorption. The term $(\Delta\Phi_{\alpha:\mathrm{C}^*} - \Delta\Phi_{\mathrm{C}^*})$ represents the change in free energy of the coal matrix due to adsorption of *n* molecules, so it must be equal to $\Delta\Phi_s$. Inserting this into equation 14 gives

$$\Delta\Phi_R = \Delta\Phi_s - n\mu_g \tag{15}$$

At the same time, subtracting equation 12 from 13 gives $\Delta\Phi_a - \Delta\Phi_s = n(\Delta\mu_a^\sigma - \mu_s^\sigma)$, which on inserting $\Delta\mu_a^\sigma = \mu_s^\sigma - \mu_g$ from equation 9 yields

$$\Delta\Phi_a = \Delta\Phi_s - n\mu_g \tag{16}$$

Equations 15 and 16 accordingly demonstrate that the total energy change $\Delta\Phi_a$ of a stressed coal plus gas system due to adsorption of *n* molecules is identical to the free energy change $\Delta\Phi_R$ for the Langmuir-type reaction.

3.2.3. Chemical potential per molecule for n molecules adsorbed by stressed coal

Focusing now on the solid system only, if *n* molecules are adsorbed, the sorption of a further *dn* molecules leads to an internal energy change given by the infinitesimal equivalent of the Gibbs equation presented in equation 1, written here as $dU_s = -\sigma_{ij} d\varepsilon_{ij}^{ads} + TdS_s + \mu_s dn$ or $\mu_s dn = dU_s - TdS_s + \sigma_{ij} d\varepsilon_{ij}^{ads}$, where μ_s is the molecule-specific potential of the *n* adsorbed molecules. Again by analogy with the generic Gibbs energy change $(\Delta G)_{P,T} = \Delta U - T\Delta S + P\Delta V$ in hydrostatic systems, the term $\mu_s dn$ can be identified as the free energy change $(d\Phi_s)_{\sigma_{ij},T} = dU_s - TdS_s + \sigma_{ij} d\varepsilon_{ij}^{ads} = \mu_s dn$ associated with adsorption by a non-hydrostatically stressed solid. It follows that $\mu_s = (\frac{\partial \Phi_s}{\partial n})_{\sigma_{ij},T}$, where $\Phi_s = \Phi_{s0} + \Delta\Phi_s$ is the total free energy of the stressed solid plus *n* adsorbed gas molecules, Φ_{s0} is the free energy of the stressed solid when *n=0*, and $\Delta\Phi_s$ is the change in energy due to adsorption of *n* molecules as given by equation 12. Since Φ_{s0} is a constant at constant σ_{ij} and *T*, it further follows that

$$\mu_s = (\frac{\partial \Delta\Phi_s}{\partial n})_{\sigma_{ij},T} \tag{17}$$

Applying Stirling's approximation $\ln x! \approx \mathrm{x}(\ln \mathrm{x} - 1)$ for large *x* to equation 12, and differentiating the expression for $\Delta\Phi_s$ obtained, now leads to the result

$$\mu_s = \mu_s^{\sigma} + kT\ln(\frac{\theta}{1-\theta}) \tag{18}$$

where $\theta = n/n_s$ is the concentration of adsorbed gas measured in terms of adsorption site occupancy.

3.2.4. Equilibrium concentration of adsorbed species α in stressed coal

3.2.4.1. Site occupancy at equilibrium and equilibrium constant

We now assume that the adsorption proceeds until equilibrium is reached. At that point, the chemical potential of the adsorbed molecules (μ_s) must be equal to that of the gas molecules (μ_g), so that

$$\mu_s \equiv \mu_s^{\sigma} + kT\ln(\frac{\theta}{1-\theta}) = \mu_g \tag{19}$$

Using equations 5 and 7 for μ_s^{σ} and μ_g, we hence obtain the following expressions for the equilibrium concentration of adsorbed molecules per available site n_s, namely

$$\theta = \frac{a_g \exp(\frac{\mu_{g0} - \mu_s^{P_0}}{kT})\exp(\frac{-(\overline{\sigma} - P_0)\Omega_0}{kT})\exp(\frac{-\sigma_{ij}^{'}A_{ij}\Omega_0}{3kT})}{1 + a_g \exp(\frac{\mu_{g0} - \mu_s^{P_0}}{kT})\exp(\frac{-(\overline{\sigma} - P_0)\Omega_0}{kT})\exp(\frac{-\sigma_{ij}^{'}A_{ij}\Omega_0}{3kT})} \tag{20a}$$

or $$\theta = \frac{a_g \exp(\frac{\mu_{g0} - \mu_s^{P}}{kT})\exp(\frac{-(\overline{\sigma} - P)\Omega_0}{kT})\exp(\frac{-\sigma_{ij}^{'}A_{ij}\Omega_0}{3kT})}{1 + a_g \exp(\frac{\mu_{g0} - \mu_s^{P}}{kT})\exp(\frac{-(\overline{\sigma} - P)\Omega_0}{kT})\exp(\frac{-\sigma_{ij}^{'}A_{ij}\Omega_0}{3kT})} \tag{20b}$$

Taking the conventional definition of a thermodynamic equilibrium constant as being temperature dependent only (see Chang, 2000; Hill, 2012), the true thermodynamic

equilibrium constant for sorption in our model (equation 20) is the quantity given

$$K^0 = \exp(\frac{\mu_{g0} - \mu_s^{P_0}}{kT}) \tag{21}$$

Here, the term $(\mu_s^{P_0} - \mu_{g0}) = \Delta\mu_a^{P_0}$ (equation 10) represents the potential change of the coal-gas system due to adsorption of a single gas molecule in the hydrostatic reference state at which $P=P_0$, $a_g=1$ and $\sigma_{ij} = P_0\delta_{ij}$. In line with conventional definitions, this is 'the standard free energy change' for the sorption reaction (Hill, 2012). By contrast, the term

$$K = \exp(\frac{\mu_{g0} - \mu_s^{P}}{kT}) \tag{22}$$

is not a true equilibrium constant, as it is clearly seen, from equations 4 and 5a, that μ_s^P and hence K depend on gas pressure P via the partial molecular volume Ω_0, such that

$$K = K^0 \exp(\frac{-(P - P_0)\Omega_0}{kT}) \tag{23}$$

An alternative way to obtain equations 20 to 23, describing equilibrium between the stressed solid and the surrounding gas, is to minimise the free energy Φ_a of the combined solid-gas system. If the free energy of the system before adsorption is Φ_{a0}, then $\Phi_a = \Phi_{a0} + \Delta\Phi_a$, when $\Delta\Phi_a$ is the total free energy change due to sorption of n molecules, given by equation 13. Since Φ_{a0} is a constant at fixed σ_{ij}, P and T, $(\frac{\partial\Phi_a}{\partial n})_{\sigma_{ij},P,T} = (\frac{\partial\Delta\Phi_a}{\partial n})_{\sigma_{ij},P,T}$. At equilibrium, Φ_a is minimum and its derivative

must equal zero. Differentiating equation 13 for $\Delta\Phi_a$ with respect to *n*, after applying Stirling's approximation, and setting $(\frac{\partial\Delta\Phi_a}{\partial n})_{\sigma_{ij},P,T}=0$, yields

$$\mu_a^\sigma + kT\ln(\frac{\theta}{1-\theta}) = 0 \tag{24}$$

Since $\Delta\mu_a^\sigma = \mu_s^\sigma - \mu_g$ (equation 9), and since the molecule specific potential $\mu_s \equiv \mu_s^\sigma + kT\ln(\frac{\theta}{1-\theta})$ (equation 18), we hence obtain $\mu_s \equiv \mu_s^\sigma + kT\ln(\frac{\theta}{1-\theta}) = \mu_g$, which is identical to the equilibrium condition expressed in equation 19, and thus yields the same expression for θ as given in equation 20.

The essential difference between our result for equilibrium adsorbed concentration θ given in equation 20 (specifically in 20b) and that obtained by Hol et al. (2011; 2012a) lies in the quantity *K* given in equation 22. Using our notation, Hol et al. obtained $K=\exp(\frac{\mu_{g0}+\mu_g-\mu_s^P}{kT})$. The main error made by Hol et al. (2011; 2012a) in their derivation is that, by incorrectly writing $\Phi_a=\Phi_{a0}+\Delta\Phi_a$ (see above) as $\Phi_a=\Phi_{a0}+\Delta\Phi_a-n\mu_g$, they set $\mu_s=(\frac{\partial\Delta\Phi_a}{\partial n})_{\sigma_{ij},P,T}$ instead of $\mu_s=(\frac{\partial\Delta\Phi_s}{\partial n})_{\sigma_{ij},T}$ as in our equations 17 and 18. Their equilibrium condition is accordingly incorrect and the result they obtain, though similar to equation 20 in form,

contains $(\mu_{g0} + \mu_g)$ instead of μ_{g0}.

3.2.4.2. Equilibrium concentration of adsorbed species α in mol/kg

The total number of localized adsorption sites (in *mol*) present in one kilogram of coal matrix, C_s (*mol/kg*) for a specific gas species, is now assumed to be a characteristic of the (macro)molecular structure of the solid. It therefore depends only on coal type, specifically through the reference potential $\mu_s^{P_0} = \mu_s^0 + \Delta\mu^*$ (see Fig. 2), and hence through equilibrium constant K^0. C_s is further assumed to be independent of the adsorbed concentration, gas pressure, state of stress and temperature. Using equations 20-22, and switching to molar quantities, we thus obtain the following final expressions for adsorbed concentration of species α in *mol/kg*, namely

$$C = C_s\theta = \frac{C_s a_g K^0 \exp(\frac{-(\overline{\sigma} - P_0)V_0}{RT}) \exp(\frac{-\sigma_{ij}^{'} A_{ij} V_0}{3RT})}{1 + a_g K^0 \exp(\frac{-(\overline{\sigma} - P_0)V_0}{RT}) \exp(\frac{-\sigma_{ij}^{'} A_{ij} V_0}{3RT})} \tag{25a}$$

$$\text{or} \quad C = C_s\theta = \frac{C_s a_g K \exp(\frac{-(\overline{\sigma} - P)V_0}{RT}) \exp(\frac{-\sigma_{ij}^{'} A_{ij} V_0}{3RT})}{1 + a_g K \exp(\frac{-(\overline{\sigma} - P)V_0}{RT}) \exp(\frac{-\sigma_{ij}^{'} A_{ij} V_0}{3RT})} \tag{25b}$$

where $V_0 = N_A\Omega_0$ is partial molar volume of the adsorbed gas species, N_A is the Avogadro constant, and R is the gas constant. At low gas pressures (low a_g) and/or when the solid supports high stresses (high $\overline{\sigma}$ or $\sigma_{ij}^{'}$), site occupancies are low with $\theta << 1$, and the right hand term in the denominator of equations 20 and 25 becomes $<< 1$. Equation 20 hence 25 can therefore be simplified to yield

$$C \approx C_s a_g K^0 \exp(\frac{-(\overline{\sigma} - P_0)V_0}{RT}) \exp(\frac{-\sigma_{ij}^{'} A_{ij} V_0}{3RT}) \quad (26a)$$

or $$C \approx C_s a_g K \exp(\frac{-(\overline{\sigma} - P)V_0}{RT}) \exp(\frac{-\sigma_{ij}^{'} A_{ij} V_0}{3RT}) \quad (26b)$$

The present, revised models (20, 25) and their simplified forms for low gas pressure (e.g. 26) demonstrate that the sorption process is controlled by the combined effects of five factors: 1) the activity $a_g(P,T)$ and/or the chemical potential of the free gas phase, 2) the reference potential $\mu_s^{P_0}(T)$ or $(\mu_{g0} - \mu_s^{P_0})$ and hence the equilibrium constant K^0, which depend on temperature only, 3) the adsorption site concentration per kilogram of coal C_s, 4) the partial molar volume V_0 of the adsorbed gas species, which depends on coal rank and gas species, and 5) the total stress state σ_{ij} supported by the coal matrix. We note that the present analysis applies to "monolayer adsorption", i.e. one-site/one-molecule adsorption, of any sorbate by any stress-supporting solid phase. It accordingly should apply to "monolayer adsorption" of CO_2, CH_4, and N_2 by coal. Importantly, our results (25, 26) are identical to those obtained by other possible approaches, specifically statistical mechanics and kinetic approaches. To demonstrate this equivalence, these approaches are presented in Appendix I.

3.2.5. Adsorption under stress-free conditions

If the solid (coal) phase is exposed to gas at pressure P under otherwise stress-free conditions, i.e. with $\sigma_{ij} = P\delta_{ij}$, our adsorption model (equation 25) reduces to

$$C = C_s\theta = \frac{C_s a_g K^0 \exp(\frac{-(P - P_0)V_0}{RT})}{1 + a_g K^0 \exp(\frac{-(P - P_0)V_0}{RT})} \quad (27a)$$

or $C = C_s\theta = \dfrac{C_s a_g K}{1 + a_g K}$ (27b)

If the free gas outside the solid behaves as an ideal gas, then a_g can be replaced by P. Moreover, if the gas pressure P is close to the reference pressure P_0=0.1MPa=1bar, then $K = K^0 \exp(\dfrac{-(P - P_0)\Omega_0}{kT})$ (equation 23) approaches K^0 and becomes insensitive to gas pressure. Under these conditions, equation 27b reduces to the well-known Langmuir isotherm $C = \dfrac{C_L K_L P}{1 + K_L P}$, where C_L and K_L are the Langmuir constants (Langmuir, 1918) and are identified as C_s and K in equation 27b respectively. K_L is accordingly seen to depend on gas pressure P via Ω_0. Note, however, that in the classical Langmuir model, swelling of the adsorbent is neglected so that $\Omega_0 = 0$, forcing the Langmuir constant K_L to appear pressure independent with $K_L = K = K^0$ (Myers and Monson, 2002).

On the basis of the adsorption model for unstressed conditions expressed in equation 27b, Liu et al. (2015) developed thermodynamic models for swelling of unconfined coal matrix due to adsorption of mixed gases. The "equilibrium constant" defined in those models is not the true equilibrium constant K^0 expressed in equation 21, but the quantity K expressed in equation 22, which is a function of temperature and gas pressure. However, the validity of the model equations presented by Liu et al. (2015) is unaffected by this as is the physical basis put forward by Liu et al. for the selective sorption of mixed gases by coal. The parameters obtained by Liu et al., in fitting their mixed gas model to experimental data for mixed gases at different partial pressures, might be slightly affected, however, as are all fits for K or K_L obtained by fitting the classical

Langmuir equation to gas sorption data.

3.2.6. Adsorption under hydrostatic applied stress

The present relations for θ and C (i.e. equations 20, 25 and 26) apply for a general three-dimensional stress σ_{ij} applied to coal matrix material. For the special case of a hydrostatic (i.e. isotropic) stress state $\sigma > P$, the mean stress $\bar{\sigma} = \sigma$ and the deviatoric components of the stress tensor disappear, so that $\sigma'_{ij} = 0$. In this case, our expression for adsorbed concentration (equation 25) reduces to

$$C = C_s\theta = \frac{C_s a_g K^0 \exp(\frac{-(\sigma - P_0)V_0}{RT})}{1 + a_g K^0 \exp(\frac{-(\sigma - P_0)V_0}{RT})} \tag{28a}$$

or $$C = C_s\theta = \frac{C_s a_g K \exp(\frac{-(\sigma - P)V_0}{RT})}{1 + a_g K \exp(\frac{-(\sigma - P)V_0}{RT})} \tag{28b}$$

Note that this result for an applied isotropic stress σ applies regardless of whether swelling properties of coal are isotropic or anisotropic (i.e. independently of A_{ij}). Interestingly, the same results also apply for isotropic coal subjected to an anisotropic stress, because then $\mathbf{A_{ij}=0}$ in equation 25**.** An expression of the same form as 28b was obtained by Hol et al. (2011; 2012a) for sorption by coal subjected to a hydrostatic stress $\sigma > P$. Once again, however, the quantity K was erroneously given as $K = \exp(\frac{\mu_{g0} + \mu_g - \mu_s^P}{kT})$ and not as $K = \exp(\frac{\mu_{g0} - \mu_s^P}{kT})$.

3.2.7. Adsorption under stressed versus unstressed conditions: A comparison

The adsorbed concentration C at equilibrium under an applied stress state $\sigma_{ij} > P\delta_{ij}$ or $\sigma > P$, expressed through equations 25b and 28b, is clearly lower than

that under stress-free conditions, where $\sigma_{ij} = P\delta_{ij}$, predicted by 27b or by the classical Langmuir relation. This is due to the stress-strain work done that must be done in association with sorption-induced swelling against the positive Terzaghi effective stress $(\overline{\sigma} - P)$ and against the deviatoric stress $\sigma_{ij}^{'}$ under stressed conditions. Under in-situ conditions in a coal seam, the lithostatic stress state means that in general both $\sigma_{ij} > P\delta_{ij}$ and $\overline{\sigma} > P$.

On this basis, our model for adsorption under a hydrostatic effective stress ($\sigma - P$), i.e. equation 28b, predicts a reduction in sorption capacity relative to the hydrostatic state where $\sigma = P$ (equation 27b) given by $\frac{C^{\sigma}}{C^{P}} = \frac{\exp(\frac{-(\sigma - P)V_0}{RT})(1 + a_g K)}{1 + a_g K \exp(\frac{-(\sigma - P)V_0}{RT})}$. Similar reductions are predicted for more general stress states. To calculate the magnitude of the resulting reduction in adsorption capacity, the partial molecular volume Ω_0 or partial molar volume V_0 of the adsorbed gas species must be known. Assuming V_0 is insensitive to stress state, this can be derived from sorption induced swelling experiments on either stressed or unstressed coal, via the expression $e_v^{ads} = C\rho V_0$ (Hol et al., 2012a; Hol and Spiers, 2012). Here e_v^{ads} represents the engineering volumetric swelling strain caused by sorption, C represents the adsorbed concentration (mol/kg$_{coal}$) and ρ represents the density of coal (kg/m^3). For CO_2, V_0 typically lies in the range $1\text{-}2\times10^{-5}$ m^3/mol (Hol et al., 2011; Hol et al., 2012a; Hol and Spiers, 2012), and its value for CH_4 is similar to that for CO_2 (Day et al., 2010).

3.3. Experimental test of the effect of hydrostatic stress on adsorption of CH_4 by coal

As shown above, our models (i.e. equations 25b and 28b) predict that in situ stress reduces the CH_4 sorption capacity of coal compared with the predictions made by the widely used Langmuir model which neglects sorption-induced swelling and hence the effect of stress. The present experiments were conducted to test our model for applied hydrostatic stresses $\sigma > P$, i.e. to test equation 28b explicitly. The previous experimental study performed by Pone et al. (2009) suggests that the application of a positive Terzaghi effective stress to solid cylindrical coal samples (25 mm in diameter) indeed leads to a reduction in CH_4 sorption capacity. However, it is unclear in the study of Pone et al. how much of this reduction was due to a) a direct effect of stress on equilibrium sorption capacity, versus b) a reduction in the volume of the coal sample that was accessible to CH_4 through a decrease in sample permeability with increasing confining stress. To more rigorously test our thermodynamic model, the present experiments were performed on a single composite coal sample containing artificially introduced transport paths, which minimized the influence of the positive Terzaghi effective stress on sample permeability and accessibility of the sample volume to CH_4.

3.3.1. Methods

To achieve our aim, we applied the volumetric method (Busch & Gensterblum, 2011; Hol et al., 2012) to measure the CH_4 expulsion from a solid coal sample exposed to a constant CH_4 pressure of 10 MPa at a temperature of 40˚C, increasing the applied hydrostatic confining pressure in steps from 11 MPa to 43 MPa, and allowing the sample to reach equilibrium. Note that the expulsion of CH_4 measured here is due to a) free methane expulsion from the pore volume/cleats of the sample caused by poro-elastic effects, and b) any desorption from the matrix. To obtain the true amount of desorption of CH_4 from the coal matrix, we applied the same experimental procedures used for CH_4

expulsion measurement to perform expulsion experiments using He (non-sorbing gas). In this way, we could correct our measured data for gas expulsion from the sample due to poro-elastic effects.

3.3.1.1. Sample preparation and treatment

The sample material used in present experiments consisted of high volatile bituminous coal collected from Brzeszcze 364, Poland. The composition and properties of the coal are described by Hol et al. (2011). Specifically, the Brezeszcze coal used in this study contains 2.93% moisture content, and 5.16% ash content.

In order to a) speed up CH_4 equilibration with the sample, while minimizing the free CH_4 volume in the sample, and b) ensure the amount of CH_4 desorbed from the solid sample could be measured accurately enough, we prepared a composite cylindrical sample of the Brzeszcze coal consisting of a stack of 20 coal discs, as shown in Fig. 4a. Each disc consisted of a flat-ground coal matrix disc, of 25 mm in diameter and 2.2 to 3.3 mm in thickness, cored normal to bedding. In contrast to the composite sample prepared by Hol et al. (2012a), who employed a single 1mm hole drilled through the center of each disc in similar experiments using CO_2, we drilled 5 cylindrical holes of 1mm in diameter through each disc, as shown in Fig. 4b. This was done to further shorten the effective diffusion path into the discs and to reduce equilibration time, which for CH_4 is longer than for CO_2 at given *PT* conditions (Busch and Gensterblum, 2011; Pone et al., 2009). To further shorten CH_4 diffusion paths in the coal matrix, we pre-treated the sample with CH_4 at 10 MPa pressure, to generate micro-fractures in the matrix (Hol et al., 2012b).

The mass and bulk volume of the composite sample, measured before the CH_4 expulsion experiment, were 34.69 g and 28.59 ml, respectively. To seal the sample from the confining medium used to apply a hydrostatic stress, the sample was enclosed in a 1 mm thick, annealed lead (Pb) jacket, by welding brass end-cups into the lead jacket, as shown in Fig.4c. Using lead allowed us to accurately measure the volumetric

deformation of the sample due to CH_4 injection, and to avoid jacket failure when the confining pressure reached the higher values used. Before assembling the sample inside the apparatus and drying it there in-situ, we pre-dried the sample in a high vacuum oven at an in-situ temperature of 40 ˚C for more than a week (in fact ~12 days) to remove the residual water, air and gas.

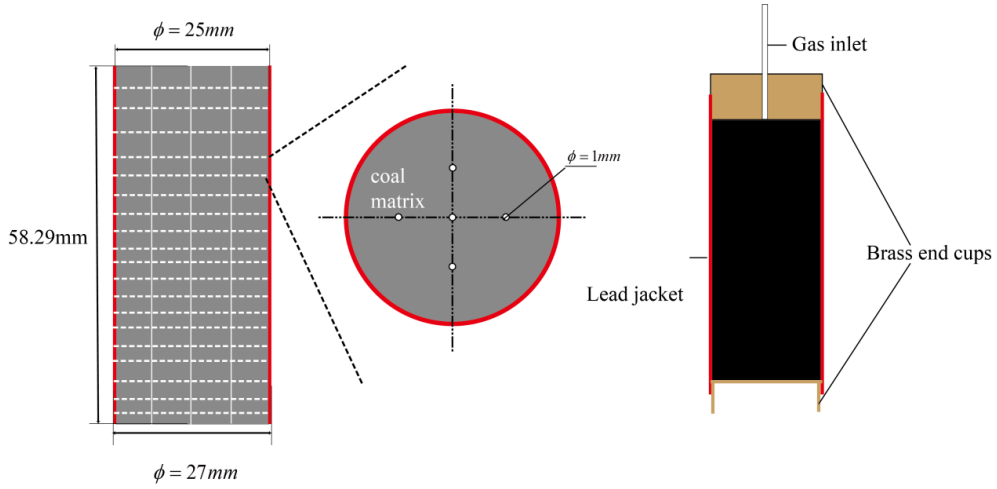

Fig.4. Schematic illustration of composite coal sample. (a) Cylindrical stack of 20, flat-ground coal matrix discs of 25 mm in diameter and 2.2-3.3 mm in thickness. (b) The positioning of the 5 cylindrical holes of 1 mm in diameter drilled in each disc. c) The composite sample sealed in 1mm thick Pb jacket.

3.3.1.2. Apparatus

The apparatus used in the present experiments (Fig.5) consisted of a stainless steel pressure vessel (30 mm inner diameter), housing the jacketed sample, placed in a temperature controlled water bath. The jacked sample was hydrostatically pressurized externally, within the vessel, using water as a confining fluid, driven by an ISCO 65D servo-controlled volumetric pump. He or CH_4 were introduced into the sample via a high pressure CH_4/He line passing through the closure nut of the pressure vessel. The internal CH_4/He pressure was controlled by an independent ISCO 65D volumetric

(syringe) pump (c.f. Hol and Spiers, 2012). Both ISCO pumps were operated in constant pressure mode in the present experiments, allowing the internal and external pressures to be controlled to within ±0.049 MPa. The volume change measured by these pumps was taken as a measure of the bulk volumetric strain of the sample (H_2O pump), and the volume of CH_4/He injected into or expelled from the sample (CH_4/He pump). To control sample temperature, the vessel was placed into the Lauda water bath at 40±0.1˚C. A foam-polystyrene box was also constructed around the syringe pumps and water bath to control the air temperature around the setup at 38.6±0.2˚C, using an internal lamp, fan and CAL 9900 PID-controller (c.f. Hol and Spiers, 2012). Temperature was measured at the locations shown in Fig.5 (T_{pt}) using PT-100 sensors with a resolution of 0.01˚C.

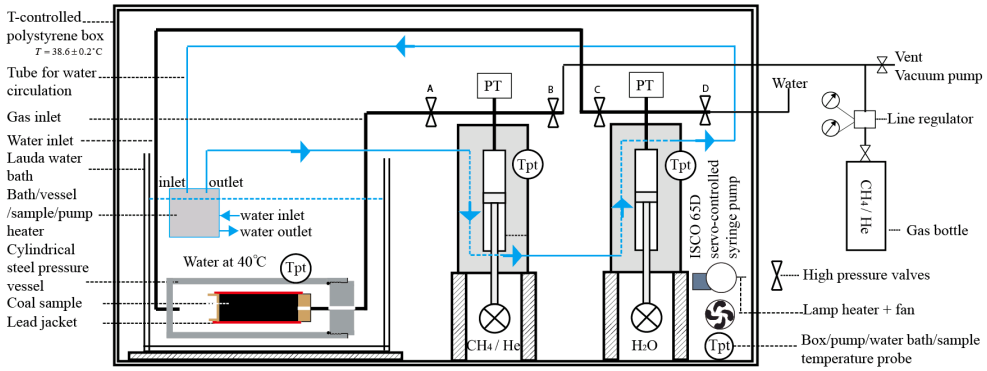

Fig.5. Schematic illustration of the complete experimental setup. The sample, sealed in a 1mm thick annealed lead jacket, is located inside the steel pressure vessel. The vessel is placed in the Lauda water bath at 40±0.1˚C. In this system, one ISCO 65D syringe pump is used for CH_4 or He pressure control within the sample, and the other for the confining pressure control. An internally heated foam-polystyrene box is constructed around the syringe pumps and water bath to control the air temperature around the setup at 38.6±0.2˚C.

3.3.1.3. Data acquisition

The temperature of the system was recorded using a National Instruments, 16-channel DAOPad-6015 A/D convertor and VI-logger data acquisition system, at a sampling rate of 0.2 Hz. The pump pressure and volume signals were directly obtained in 16 bit digital

form from the ISCO 65D Pumps, at a sampling rate of 0.2 Hz using ISCO 65D Panel software.

3.3.1.4. Leakage rate calibration

Both the gas and water systems were tested for leaks before the experiments, at experimental conditions and with no sample present. The tests took ~1 day (versus ~30 days for the CH_4 runs). The pumps were operated in constant pressure mode and changes in both gas and water volume were recorded versus time. The CH_4/He volume decreased linearly (R^2>0.98) with time when maintaining a constant gas pressure of 10 MPa. The corresponding data yielded a leakage rate for CH_4 of ~12.3 μl/h and for He of ~52.6 μl/h. No measureable leakage could be detected using the H_2O pump at a pressure of 11MPa.

3.3.1.5. Experimental procedure

We performed two experiments, Exp1 and Exp2, on the single composite sample of stacked coal discs (Fig.4) at a constant temperature of 40˚C. The following stages were employed in both experiments, as illustrated in Fig.6.

I) Evacuation. To ensure that residual gas and water were completely removed from the sample, we evacuated the complete setup using a high vacuum pump (see Fig.5), while the sample was subjected to a confining pressure of 3 MPa at the experimental temperature of 40˚C. During this process, the sample shrank at a decreasing rate. We assumed that the sample reached equilibrium, i.e. that virtually all water was removed, when no further volume reduction could be detected by the confining pressure syringe pump. This took another 5 days. It can be expected that this high vacuum treatment at 40˚C for even 5 days will be as effective in drying coal as heating it to the boiling point of water at atmosphere pressure, though we did not check this.

II) Preparatory confining pressure cycling under vacuum. To minimize any irreversible (permanent) deformation or failure of the sample during the main phase of the experiments, we then cyclically stressed the sample up to 45 MPa confining pressure,

which is higher than the maximum confining pressure of 43 MPa used in the main phase of the experiments. This was achieved using the H_2O pump, while still applying a vacuum to the sample.

III) Helium expulsion test. To estimate the amount of CH_4 expelled from the free volume of the sample (i.e. non-adsorbed CH_4) by poro-elastic compaction during hydrostatic loading, helium (He), a non-sorbing gas, was used as a control gas . The He expulsion tests were conducted by first applying a confining pressure of 11 MPa and then injecting He into the sample at 10 MPa. The confining pressure was then stepped to 43 MPa following the same procedure described below for the subsequent CH_4 expulsion run, ultimately returning smoothly to 11 MPa (see Fig.6. and point V). The duration of each confining pressure step employed using He was around 25 hours.

IV) Initial equilibration of the sample with CH_4. After venting and then evacuation of residual helium from the sample under a confining pressure of 11 MPa, we injected CH_4 at a pressure of 10 MPa. Equilibrium was assumed to be reached when the CH_4 flow rate reached a constant value, which was equal to or close to the measured pre-test leakage rate of ~12.3 μl/h (*cf.* ~52.6 μl/h for He), and when sorption-induced swelling of the sample had stabilized. It took ~14 days to ensure that the sample equilibrated sufficiently with CH_4 at this stage. The constant flow rate of CH_4 attained at this stage was assumed to be the current leak rate. The difference between the current and pre-test leak rates is minor, and is assumed to be caused by fluctuations in system sealing capacity caused by small temperature changes and changing ISCO pump piston/seal postion during our long term tests. To minimize the effects of these fluctuations on leak rate correction, the average of the current and pre-test leak rates was taken as the leak rate during each stage of the adsorption process.

V) CH_4 expulsion test. Once the sample approached equilibrium with CH_4 at the initial confining pressure, the confining pressure was increased in steps, allowing equilibrium to be reached or at least closely approached after each increment. The

confining pressures used in the experiments were 16 MPa, 23 MPa, 32 MPa, and 43 MPa, generating conventional (Terzaghi) effective stress of 6, 13, 22 and 33 MPa (see Figure 6). The pressure increase in each step was applied in less than 10s. Around 40 hours was allowed after each step to ensure re-equilibration, i.e. to attain a constant CH_4 flow rate equal to, or at least close to, the constant flow rate attained in the previous step and in the pre-test leak calibration. Finally, the confining pressure was smoothly decreased to the initial confining pressure of 11 MPa (effective pressure of 1 MPa). Total test duration was around 10 days. Within this period, the constant CH_4 flow rates attained at each confining pressure used were slightly different, and also slightly different to the leak rate measured in the pre-test calibration. To correct for leakage at each confining pressure employed in the stepping sequence, we again took the average value of the constant CH_4 flow rates attained "before and after" each step.

VI) In addition to the above, two more CH_4 expulsion runs were performed in Exp2 only. These runs were executed directly after the CH_4 expulsion run (i.e. Fig.6, stage V), to examine the reversibility of the CH_4 sorption/desorption process.

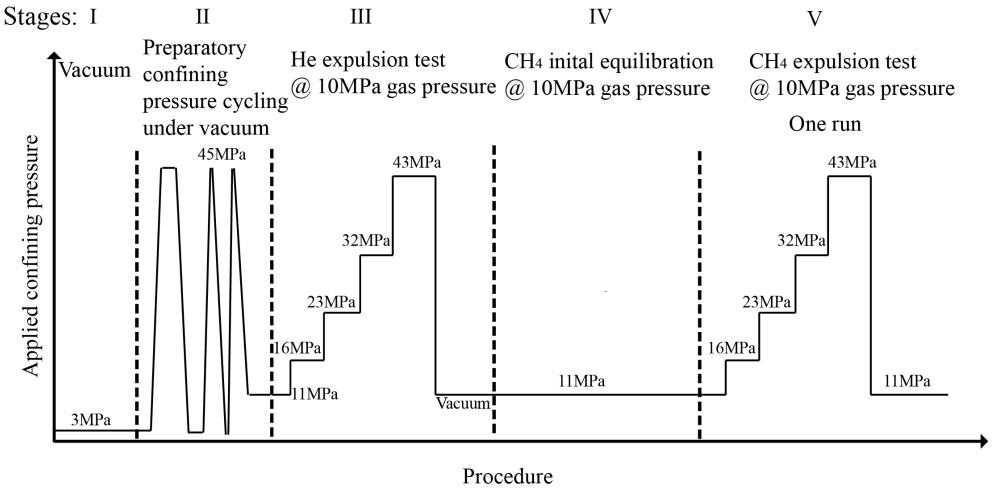

Fig.6. Illustration of the various stages employed in the experimental procedure adopted in executing Exp1 and Exp2.

3.3.1.6. Data processing

3.3.1.6.1. Initial CH4 uptake vs. associated swelling strain

The introduction of CH_4 into the sample at 10 MPa at the initial confining pressure of 11 MPa, led to an expansion of the sample measured by the ISCO H_2O pump. Now, the total amount of CH_4 entering the sample at this point consists of two components: an amount entering the free pore volume of the sample, and the amount taken up by diffusion plus adsorption in the coal matrix. The associated expansion is therefore expected to consist of a rapid poro-elastic expansion plus a time-dependent sorption-induced swelling component. Such behaviour indeed occurred (see Fig.7). We assume that the rapid increase in the H_2O pump volume seen within ~120 seconds after the introduction of CH_4 (Fig.7) was fully caused by the poro-elastic effect, and that sorption dominated thereafter, so that the volumes for both CH_4 and H_2O pumps at 350 s in Fig. 7 could be taken as the starting volumes for adsorption, i.e. the volume at sorption time t=0. On this basis, the amount of CH_4 uptake by the sample versus time was then calculated via the expression $\Delta V(t) = V^{start} - V(t) - Qt$. Here $V(t)$ (ml) represents the pump volume for CH_4 at time t, V^{start} (ml) represents the corresponding starting pump volume for CH_4, Q represents the leak rate (ml/hour) of the pump, and t (hours) represents elapsed adsorption time. We took the average value of ΔV over the final 5 hours of the initial equilibration interval as the total amount of gas uptake by the sample at equilibrium within that interval. To obtain the concentration of CH_4 (mol/kg_{coal}) taken up by the sample versus time, after initial introduction of CH_4 at 10 MPa pressure, we used the relation $C(t) = \frac{\Delta V(t)\rho_{CH_4}}{m}$, where ρ_{CH_4} is the density of CH_4 at 10 MPa pressure and 40˚C expressed in mmol/ml, and m (g) is mass of the coal sample.

The associated (positive) volumetric swelling strain of the sample measured due to

CH_4 adsorption was calculated using the relation $e_v^{ads}(t) = (\Delta V_{H_2O}(t) / V_{sample}) \times 100\%$, where $\Delta V_{H_2O}(t)$ is the volume change of the H_2O pump referred to the start of adsorption (i.e. the volume of the H_2O pump shown in Fig. 7 at 350 s), and V_{sample} is the initial volume of the sample under unconfined conditions, which was measured before the experiments. Again, we took the value of $e_v^{ads}(t)$ over the final 5 hours of the initial equilibration interval as the total swelling strain (e_{ads}^{eq}) of the sample caused by CH_4 adsorption at equilibrium within that interval.

3.3.1.6.2. CH_4/He expulsion

The amount of CH_4/He leaving the sample in response to each confining pressure step *i* versus time was calculated via the expression $\Delta \overline{V}_i(\Delta t_i) = V_i^{Pump}(\Delta t_i) - V_i^{start} + Q\Delta t_i$. Here, $\Delta \overline{V}_i$ (ml) is measured such that CH_4/He expulsion is taken as positive, $V_i^{Pump}(\Delta t_i)$ (ml) represents the internal gas pump volume during the confining pressure interval *i*, V_i^{start} (ml) represents the starting pump volume at the initiation of confining pressure step *i*, Q represents the leak rate (ml/hour) of the pump during each confining pressure interval *i*, and Δt_i represents elapsed time (hours) during the *i*th applied pressure interval referred to the starting time of each step. Again, we took the value of $\Delta \overline{V}_i$ over the final 5 hours of the current confining pressure step as the amount of gas expelled from the sample at equilibrium in response to the current increment of confining pressure. The total CH_4/He expulsion over *j* consecutive steps was hence calculated using $\Delta \overline{V}_j = \sum_1^j \Delta \overline{V}_i$.

3.3.1.6.3. Error analysis

Uncertainty in the amount of CH_4/He expulsion calculated using the methods described above was caused by 1) the noise on the pump volume signal due to the control accuracy in pressure control mode, and 2) slight differences in leak rate of the CH_4/He pump in each step. We analyze the uncertainty caused by each of these independently, using the standard deviation (SD) expressed as $\eta = \sqrt{\frac{1}{n}\sum(\overline{x}_i - x_i)^2}$ for data set X consisting of *n* data points. We took the largest error as the uncertainty in CH_4/He expulsion data. The biggest error for CH_4 expulsion data resulted from fluctuations in leak rate during long duration experiments (40-50 hours for each confining pressure step), while for He expulsion data resulted from the noise due to high compressibility of He.

3.3.2. Results

3.3.2.1. CH_4 uptake and swelling response during initial pressurization with CH_4

CH_4 uptake and the associated volume changes exhibited by the single composite sample during initial equilibration at a CH_4 pressure of 10 MPa and at a confining pressure of 11 MPa, in Exp1 and Exp2, are plotted as a function of time in Fig. 8. In both cases, equilibration took ~190 hours. The CH_4 uptake by the sample is seen to lie in the range of 6.33-6.47 ml, while the corresponding volumetric swelling is 0.368-0.399 ml, which means an equilibrium swelling strain of 1.29-1.39%. The density of the CH_4 at 10 MPa and 40˚C is 4.3651 mmol/ml (Setzmann and Wagner, 1991), which in turn means that the CH_4 uptake of the sample at equilibrium is 0.799-0.816 mol/kg_{coal}. The uptake of CH_4 ($C(t)$) expressed in mol/kg_{coal} is plotted against the measured volumetric swelling strain ($e_v^{ads}(t)$) in Fig. 9. The volumetric swelling strain developed close to linearly with CH_4 uptake during initial equilibration at constant confining pressure of 11 MPa and 10 MPa CH_4 pressure.

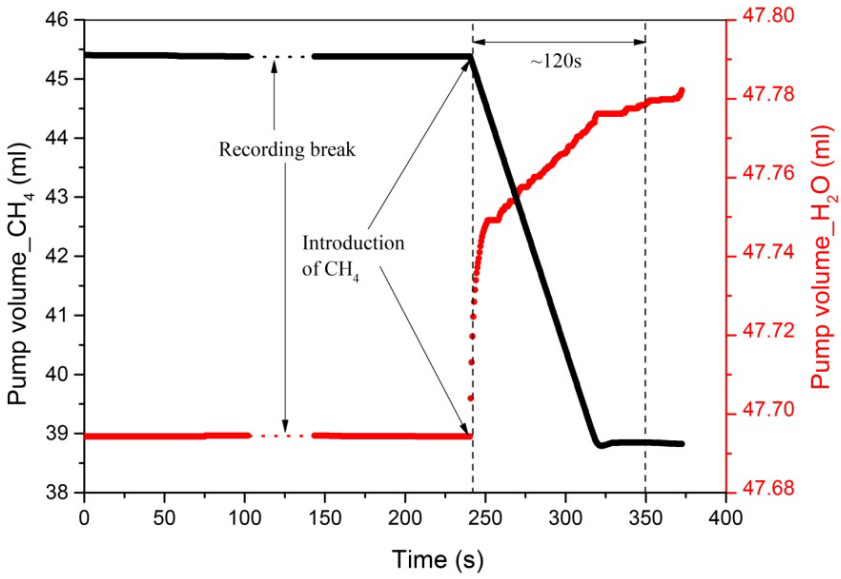

Fig. 7. The initial, short-term response of the system due to CH_4 injection into the sample at 10 MPa pressure under a confining pressure of 11 MPa, in Exp2, Stage IV. Both pumps were controlled in constant pressure mode, and their maximum flow rates were set at 5ml/min when maintaining the constant pressure. To maintain CH_4 pressure at 10 MPa after introduction, the CH_4 pump hit the maximum flow rate of 5 ml/min.

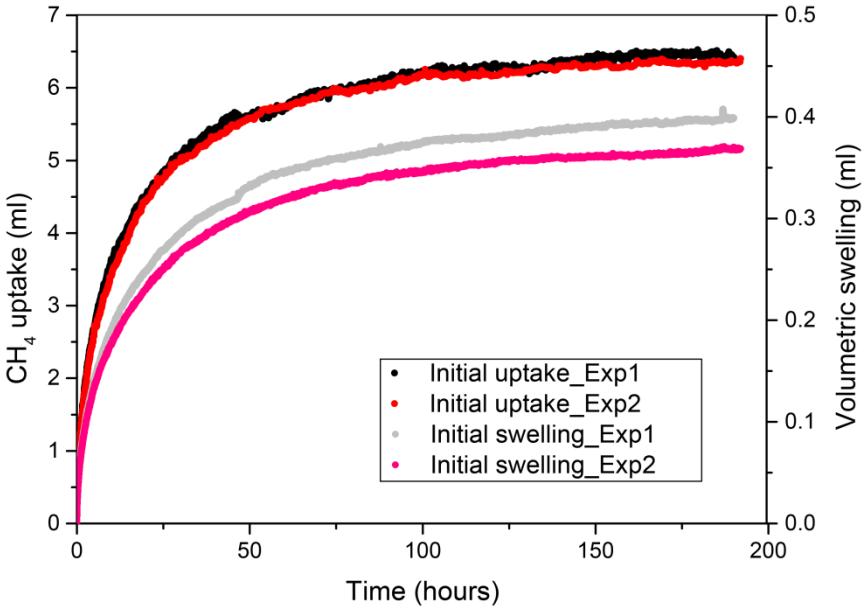

Fig. 8. CH_4 uptake/swelling versus time during initial isothermal equilibration of the Brzeszcze coal sample (disc stack) subjected to a confining pressure of 11 MPa with CH_4 pressure of 10 MPa (Stage IV of Exp1 and Exp 2). The swelling (ml) was obtained from the volume change of the H_2O pump, while the CH_4 uptake (ml) was derived from both volume change and leakage rate of the CH_4 pump.

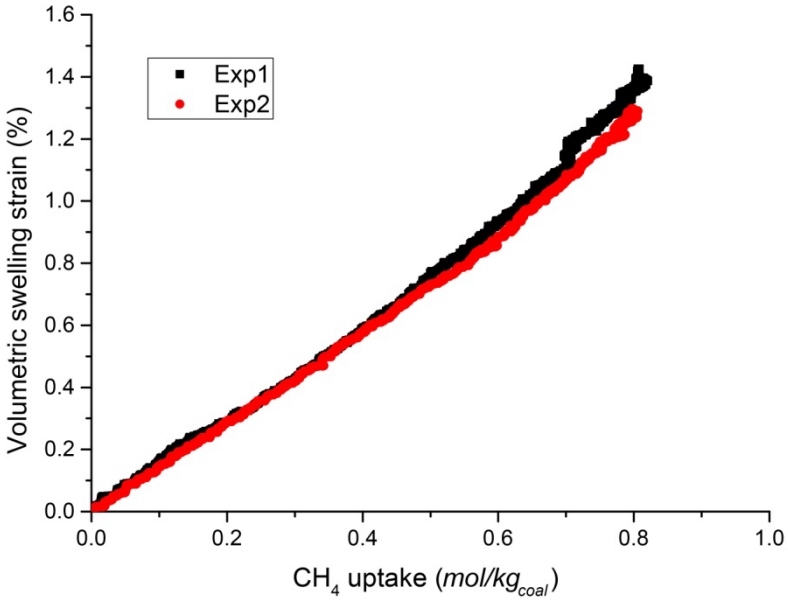

Fig. 9. Total volumetric swelling strain versus total CH_4 uptake of the Brzeszcze sample (disc stack) during initial equilibration in Stage IV of Exp1 and Exp2 at a CH_4 pressure of 10 MPa and at a confining pressure of 11 MPa at 40˚C (see Fig.8).

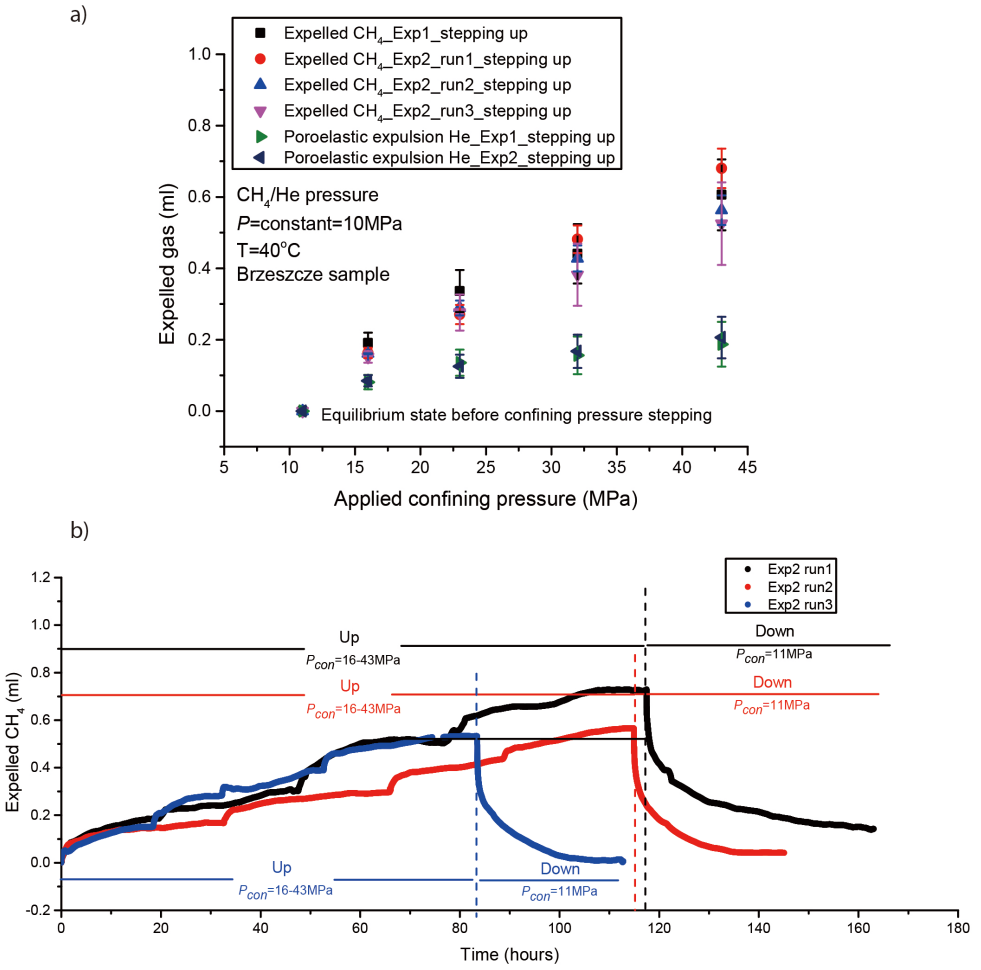

Fig. 10. CH_4/He expulsion data. a) The absolute amount of CH_4/He expelled from the Brzeszcze coal sample (disc stack) at equilibrium, as a function of confining pressure applied after initial equilibration of the sample at a confining pressure of 11 MPa with CH_4/He pressure of 10 MPa. b) Expelled CH_4 from Brzeszcze sample (disc stack) versus time during the three runs conducted in Exp2.

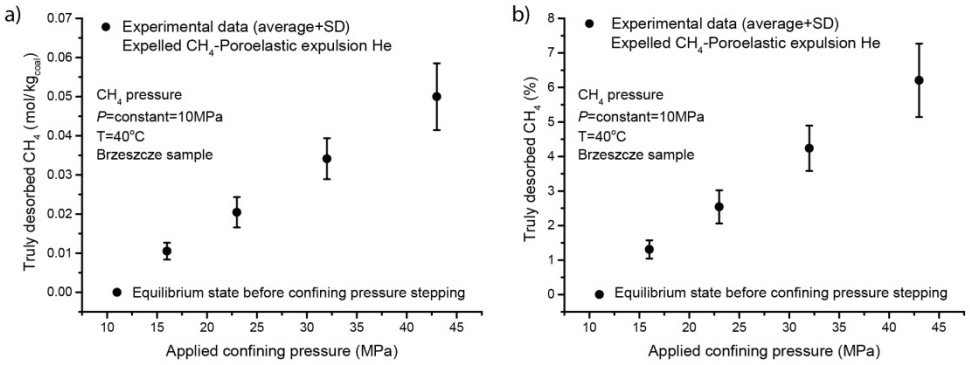

Fig. 11. Truly desorbed CH_4 at equilibrium, averaged for all experiments/runs, versus the applied confining pressure after initial equilibration of the sample at a confining pressure of 11 MPa with CH_4 pressure of 10 MPa. The mean data point values plus standard deviation (SD) shown were derived from the experimental data shown in Fig. 10a, by means of standard statistical analysis. (a) shows absolute amount of CH_4 truly desorbed per applied confining pressure step, expressed in mol/kg_{coal}. (b) shows the truly desorbed amount of CH_4 as a percentage (%) of the uptake value of 0.808 mol/kg_{coal} (average) at initial equilibrium before increasing the confining pressure.

3.3.2.2. He and CH_4 expulsion data (confining pressure stepping)

The total amount (ml) of He and CH_4 expelled from the sample at equilibrium versus the applied confining pressure for both experiments (i.e. for Exp1 and Exp2) are presented in Fig.10a. An increase in expulsion of both CH_4 and He is clearly seen in Fig.10a as a result of upward confining pressure stepping. At 43MPa confining pressure, i.e. 33 MPa effective stress, ~0.59 ml (average) CH_4 and ~0.2 ml (average) He are expelled from the sample. The data trends for both CH_4 and He are near-linear in the interval 16-43 MPa, but show a non-linear region in the interval 11-16 MPa. Moreover, Fig. 10b illustrates the amount of expelled CH_4 (ml) versus time during the three CH_4 expulsion runs performed in Exp2 (i.e. the run shown in stage V in Fig.6 plus the two additional runs of stage VI). This indicates that transfer of CH_4 from / into the sample caused by the change in confining pressure was reversible in Runs 2 and 3, though irreversible in Run1.

3.4. Discussion

Our experiments show that the equilibrium CH_4 uptake by the Brzeszcze high volatile bituminous coal, at 40˚C, at a pressure of 10MPa, and under a confining pressure of 11 MPa, is 0.799-0.816 mol/kg_{coal}. This is similar to the value of 0.616 mol/kg_{coal} obtained by Busch (2005) for the sorption capacity of similar coal from the Brzeszcze mine, measured unconfined at 10 MPa CH_4 pressure at 45˚C. The sorption-induced volumetric swelling strain measured in the present experiments was 1.29-1.39%, which is also in good agreement with the volumetric swelling strains of 1.07-1.96% measured for Bituminous Coals A and I by Day et al. (2010). More importantly, our experiments demonstrate that increasing the hydrostatic confining pressure resulted in CH_4 being expelled from the solid sample in excess of helium expulsion (see Fig.10a). This means the CH_4 indeed desorbed from the coal matrix due to application of the hydrostatic stress, which is consistent with our model prediction.

In the following, we compare our experimental data with our theory for sorption under stress. We start by determining the partial molar volume (V_0) of the adsorbed CH_4 using our experimental data on CH_4 uptake vs. associated swelling strain. We go on to calculate the amount of CH_4 truly desorbed from the sample using the CH_4 and He expulsion data. We subsequently compare the CH_4 capacity of the sample under stressed conditions, derived from the experimental data, with our model. Finally, we apply our modified model to predict in-situ CBM content.

3.4.1. Experimental data versus theory

3.4.1.1. V_0 determination

The linear relation between CH_4 uptake ($C(t)$) and associated volumetric swelling strain ($e_v^{ads}(t)$) shown in Fig.9 indicates that the measured volumetric swelling strain is caused by adsorption of CH_4, and that this relation can be expressed as

$e_v^{ads}(t) = \rho V_0 C(t)$ in line with our model (Hol et al., 2012a; Hol and Spiers, 2012), with V_0 being independent of the adsorbed concentration ($C(t)$). We obtained the value of V_0 from a best fit of the above expression to the experimental data shown in Fig.9, which yields 1.40-1.46 $\times 10^{-5}$ m^3/mol for the volume change of the sample due to adsorption of one mole of CH_4. This result is consistent with values (i.e. e_v^{ads} / C) of 1 to 2×10^{-5} m^3/mol reported for CH_4 in the literature (Day et al., 2010; Hol et al., 2011; Hol et al., 2012a; Hol and Spiers, 2012; Levine, 1996; Pan and Connell, 2007).

3.4.1.2. Truly desorbed CH_4

The expelled CH_4 data shown in Fig.10a represent the combined effects of expulsion due to poro-elastic compression plus any stress-induced desorption, i.e. desorption from the solid sample caused by the effect of hydrostatic confining pressure. Under the assumption that all He-accessible pores were filled with free CH_4, the amount of CH_4 truly desorbed from the sample ($C_{des}^{CH_4}$) was calculated using the expression $(C_{des}^{CH_4})_i = [s(\Delta \overline{V}_i^{CH_4}) - s(\Delta \overline{V}_i^{He})] \bullet \rho_{CH_4}$. Here $s(\Delta \overline{V}_i^{CH_4})$ and $s(\Delta \overline{V}_i^{He})$ represent the average volumes of CH_4 (four data points) and of He (two data points) expelled at the *ith* confining pressure shown in Fig.10a, while ρ_{CH_4} is the density of CH_4 (4.3651 mmol/ml) at a pressure of 10 MPa and at 40˚C (Setzmann and Wagner, 1991). For each average in the above expression, the standard derivation (SD) was taken as the uncertainty in each quantity.

The truly desorbed amounts of CH_4 obtained, expressed as $C_{des}^{CH_4}$ in mol/kg_{coal} and as a percentage (%) of the initial uptake of 0.808 mol/kg_{coal} (average) at the confining pressure of 11MPa, are plotted versus applied confining pressure in Figs. 11a and 11b. An essentially linear increase in desorption is clearly seen in Fig. 11, in direct proportion

to upward confining pressure stepping. This implies that the non-linear region observed in the interval 11-16 MPa in Fig. 10a, for both CH_4 and He, resulted from the closure of cracks and the gaps between the discs of the sample upon loading. At 43 MPa confining pressure, i.e. 33 MPa effective stress, about 0.05 mol/kg_{coal} of CH_4 is desorbed from the sample (Fig. 11a), which corresponds to a reduction of ~ 6.2% in the initial uptake (Fig. 11b).

This reduction, caused by the positive effective stress applied in our experiments, is much smaller than that (> 85%) reported by Pone et al (2009) for solid (not composite) samples of cylindrical bituminous coal (25mm in diameter). This suggests that the large reduction in CH_4 sorption capacity reported by Pone et al. (2009) is probably not due solely to a direct effect of stress on equilibrium sorption capacity, but also to a reduction in the volume of coal sample that was accessible to CH_4 as sample permeability decreased with increasing confining stress.

3.4.1.3. Comparison with present model for stressed coal

Strictly speaking, the truly desorbed CH_4 (i.e. in excess of He poroelastic expulsion) shown in Fig. 11a should be referred to as the change in excess sorption capacity, while the change in absolute sorption capacity cannot be directly measured from the experiments. However, since our model considers coal matrix material which contains nanopores only, it treats the adsorbed gas molecules as being a "dissolved" component of the solid phase (following Myers, 2002), as opposed to assuming an independently identifiable adsorbed phase. This means that the excess sorption capacity in our model should equal the absolute sorption capacity.

To compare our results with our thermodynamic model as written in equation 28, we first convert the truly desorbed CH_4 ($C_{des}^{CH_4}$) into the sorption capacity (uptake, C) at the *ith* applied hydrostatic stress via the expression $C_i = C_0 - (C_{des}^{CH_4})_i$. Here C_0 is the average of the initial uptake that we measured during Exp1 and Exp2 at a confining

pressure of 11 MPa and at 10 MPa CH_4 pressure. The data points with the calculated error bars are shown in Fig. 12. Taking a thermodynamic reference state defined at P=0.1 MPa, we then determined the CH_4 activity (a_g) to be 87.58 at a pressure of 10 MPa and 40˚C (Setzmann and Wagner, 1991). Our model (equation 28) was subsequently fitted to our data (Fig. 12) under the assumption that the partial molar volume of the adsorbed gas molecule V_0 is insensitive to the stress state. Taking the average value of V_0 obtained from the $e_v^{ads}(t)$ vs. $C(t)$ data shown in Fig.9 to be $1.43\times10^{-5} m^3/mol$, the best fit of the model (equation 28) to our data (R^2=0.994) shown in Fig. 12 gave the parameters C_s=1.219 mol/kg and K^0=0.0235 obtained fitting equation 28a, versus C_s=1.219 mol/kg and K=0.0223 obtained fitting equation 28b. This difference in K^0 versus K points to the effect of gas pressure on μ_s^P (see equation 5) and hence on K. Alternatively, the thermodynamic equilibrium constant K^0=0.0235 can be obtained using equation 23, by inserting the value of K (0.0233) retrieved from fitting equation 28b to our data, along with the constant CH_4 pressure of 10 MPa that was employed in all experiments.

Note that the parameter values (C_s, K^0) obtained by fitting equation 28a are independent of gas pressure and stress state, and so can be applied for all gas pressures and stress states. The parameter values (C_s, K) obtained fitting equation 28b are also independent of stress state but depend on gas pressure. These parameters, C_s and K in equation 28b, can be identified with the Langmuir constants (C_L, K_L see Section 3.2.5). and their values (C_s, K) obtained by fitting equation 28b fall within the range of Langmuir constants ($0.9 \le C_L \le 2.5$ mol/kg_{coal} and $0.02 \le K_L \le 0.05$) reported in the literature for unstressed, high volatile bituminous coal, i.e. our values for C_s and K fall within the range obtained from best fitting of the classical Langmuir equation to isothermal CH_4 sorption data (e.g. Cui et al., 2007; Dutta et al., 2011; Gensterblum et al., 2013; Laxminarayana and Crosdale, 1999; Levine, 1996; Merkel et al., 2015; Pan and

Connell, 2007; Pini et al., 2010). The quality of fit obtained in Fig. 12, and the similarity between our C_s and K values versus C_L and K_L in the literature, indicate that our model successfully describes adsorption under stressed conditions.

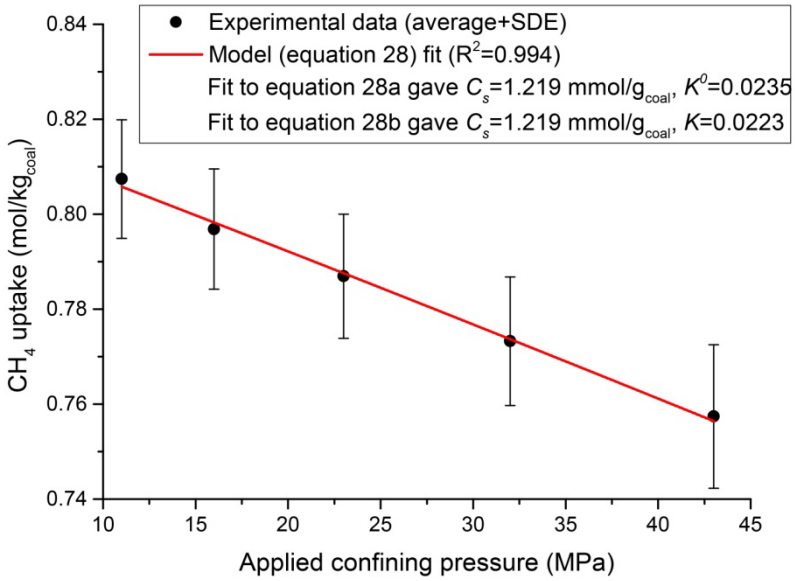

Fig. 12. CH_4 uptake versus applied confining pressure. The black dots represent CH_4 sorption capacity derived from our experimental data expressed in mol/kg_{coal}, and the red line represents the best fit of our thermodynamic model (equation 28).

3.4.1.4. Magnitude of the stress effect for CH_4 and comparison with CO_2

The experiments reported here have shown at least a ~ 6% reduction in CH_4 sorption capacity of Brzeszcze coal due to the application of 33 MPa effective hydrostatic stress for a CH_4 pressure of 10 MPa at 40˚C. Moreover, our results support the applicability of our model. Considering this, the deviatoric stress term in equation 25 means that a ~ 6% reduction may even be an underestimate of the reduction when coal is subjected to a general stress state σ_{ij}. Crucially, the effect of stress on adsorption strongly depends on the partial molar volume V_0 of the adsorbed gas species (*c.f.* equation 25). In this context, the higher value of V_0 (*i.e.* $V_0 = N_A\Omega_0$) for CH_4, for a given coal type, the

lower the sorption capacity at the same stress state. Conversely, if V_0 is negligible, i.e. V_0=0, the effect of stress on sorption capacity would disappear.

In similar experiments using CO_2, Hol et al. (2012a) measured CO_2 expulsion from the high volatile bituminous coal from Brzeszcze at a constant CO_2 pressure of 15 MPa, at a temperature of 40˚C, varying the confining pressure from 16 MPa to 40 MPa. They found that 0.11 mol/kg_{coal} of CO_2 was expelled from the sample at an effective confining pressure of 25MPa, of which 0.001-0.021 mol/kg_{coal} was estimated to be due to poro-elastic expulsion. This corresponds to a 6.5-8% reduction in CO_2 sorption capacity at the effective confining pressure of 25 MPa, implying that the sorption capacity of Brzeszcze high volatile bituminous coal for CO_2 is more sensitive to the effect of stress than that for CH_4. Despite this, however, it is important to note that selective sorption of CH_4 or CO_2 from a CH_4-CO_2 mixture (*c.f.* Liu et al., 2015) by Brzeszcze coal, as modelled by Liu et al. (2015), is not affected by the stress state. This is because the parameters C_s, K, K^0 in the present model, and the equivalent parameters C_s and K in the models presented by Liu et al., are independent of stress state.

3.4.2. In-situ CBM content predicted by our model

Our experimental results and our model both confirm that the in situ CBM content is determined not only by geological factors generally accounted for, such as coal rank, coal composition, moisture and temperature, but also by another important geological factor, in-situ lithostatic stress state, which is usually ignored. To evaluate the magnitude of the lithostatic stress effect by comparison with the results predicted by our model for unstressed coal expressed in well-know Langmuir form, i.e. equation 27b, we now proceed to apply our model expressed in 25b to give a general prediction for CBM content distribution with burial depth.

To do that, we first need to calculate the values of parameters (C_s, K, V_0) for a given coal at different burial depths, i.e. at different temperatures. We focus on high volatile bituminous coal, for which the parameters at 40˚C are known from our experiments.

Beside this, we consider only dry conditions, though sorption capacity decreases with moisture content (Busch and Gensterblum, 2011; Gensterblum et al., 2014; Gensterblum et al., 2013; Merkel et al., 2015; Weniger et al., 2012). We consider only dry conditions because our present model is only valid for pure gas adsorption, i.e. not valid for CH_4 and water vapor mixtures. The potential effects of water are similarly ignored in essentially all previous adsorption modeling and model fitting studies on coal (Day et al., 2011; Day et al., 2008; Gensterblum et al., 2014; Gensterblum et al., 2013; Merkel et al., 2015; Weniger et al., 2012), but should be evaluated in future.

Returning to the issue of temperature dependence, we start with the quantity K (equation 22). From equations 4, 7 and 22, μ_s^P, μ_{g0}, K are all the function of temperature, though μ_s^P also weakly depends on gas pressure. We assume that the quantity K can be mathematically expressed as $K = B\exp(DT)$, where B and D are constants, hence capturing the form of the expected T-dependence of K. We fitted this to describe the temperature dependence of K values obtained by fitting equation 27b to the isothermal sorption (absolute) data obtained for high volatile bituminous coal (dry) at different temperatures by Gensterblum et al. (2013). This yielded D=-0.03 (R^2=0.92). Inserting the value of K at an absolute temperature of 313K (40˚C) as obtained from our present experimental data (i.e. inserting K_{313}=0.0233), we obtain B=267.4. The quantities C_s and V_0 are assumed to be insensitive to temperature, and are consequently set at the values obtained in the present experiments, i.e. at C_s=1.219 mol/kg and V_0=1.43×10^{-5} m^3/mol.

Based on bottom hole temperature of exploration wells, plus mud weight information from exploration drilling for coal in the Carboniferous of the Ruhr Basin in Germany, Freudenberg et al. (1996) estimated a geothermal gradient of 0.032˚C/m, and a methane pressure gradient of 0.0097 MPa/m. We follow Freudenberg et al. (1996) in assuming these gradients. A lithostatic stress gradient of 0.025 MPa/m was taken, under the

assumption that the overlying rock mass determines to the vertical stress, and that the average density of rock is 2500 kg/m^3. For simplicity, we assume that coal seams experience a hydrostatic stress, i.e. $\sigma = \sigma_{vertical}$. The CBM concentration at equilibrium was then calculated both via equation 27b without considering the stress effect, i.e. using a conventional Langmuir-type model written in terms of gas activity, and via equation 28b considering the additional effect of the in-situ stress (assumed hydrostatic).

The resulting model predictions for CBM concentration and its reduction compared with conventional predictions are plotted as a function of depth in Fig. 13. The results illustrate that 1) the highest in-situ CBM concentration predicted by equation 28b occurs at a burial depth of ~900 m, which is 75 m shallower than that predicted by equation 27b; 2) the highest in-situ CBM concentration predicted by equation 28b yields a value of 0.76 mol/kg$_{coal}$, which is 2.9% lower than that predicted by equation 27b; 4) the deeper the coal seam, the more significant the effect of stress; 5) a ~ 6% reduction in CBM content occurs at a depth of ~1800 m compared with that predicted by equation 27b.

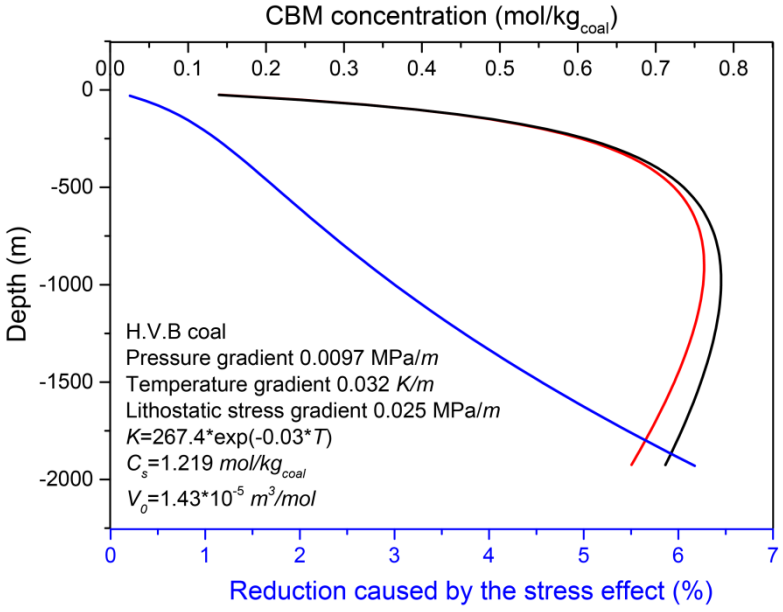

Fig. 13. Model predictions of equilibrium CBM content for dry high volatile bituminous coal as a function of depth. The gaspressure, temperature and lithostatic stress gradients used in the model were derived from Freudenberg et al. (1996), while K, C_s and V_0 were based on the present experimental results and those of Gensterblum et al. (2013) (see text). The black line represents the methane content concentration predicted by equation 27b without considering the effect of in-situ stress, while the red line predicted by equation 28b considering the in-situ stress effect. The blue line represents the reduction (%) in CBM content concentration caused by the effect of in-situ stress.

3.5. Implications for (E)CBM

Our results have confirmed that the in-situ lithostatic stress can reduce the CH_4 sorption capacity of coal, and imply a reduction in the prediction of the CBM content compared with those made using the Langmuir type isotherm applied for unconfined conditions. This finding has the following implications for (E)CBM.

3.5.1. Effect of lithostatic stress on CBM saturation and its impact on production

Coal is generally believed to be under-saturated with methane in-situ, i.e. CBM content is lower than the sorption capacity of unstressed coal measured at in-situ *P-T* conditions (Moore, 2012). The reasons for this given by Moore (2012) are a) gas is expelled or leaks from coal during uplift, and b) gas is stripped from coal by moving water. The level of gas saturation plays a significant role in assessment of CBM production (Moore, 2012). This is generally calculated by comparing the gas desorbed from coal samples recovered in a sealed the canister, i.e. in-situ gas content ($C_{in\text{-}place}$), with the sorption capacity measured by determining the adsorption isotherm for the unstressed sample at the correct *P-T* conditions ($C_{unstressed}$) (Mares et al., 2009; Moore, 2012).

However, our results clearly indicate that the in-situ stress reduces CH_4 sorption capacity compared with that for unstressed coal measured at given *PT* conditions in laboratory. This means that if gas saturation is calculated via the conventional methods given by Moore (2012) described above, i.e. as $C_{in\text{-}place}$ / $C_{unstressed}$, the reduction in

sorption capacity caused by the lithostatic stress also contributes to in-situ CBM content being apparently under-saturated. This further suggests that the true gas saturation, calculated from in-situ gas content over the sorption capacity for stressed coal ($C_{stressed}$), i.e. from $C_{in\text{-}place}$ / $C_{stressed}$ (not from $C_{in\text{-}place}$ / $C_{unstressed}$), should provide an indicator of the real loss of gas in coal seams. At the same time, variation in spatially distributed measurements of the gas content in place in a coal seam might be in part due to spatial variation in the stress state.

The effect of lithostatic stress on gas saturation for CBM productions is illustrated in Fig. 14. Taking Brzeszcze high volatile bituminous coal as an example, and assuming that in situ temperature is 40˚C at a burial depth of around 1200 m, we plotted sorption capacity under a given in-situ stress state as a function of methane pressure (i.e. using equation 27b and 28b). We assume that in-situ gas content concentration for Brzeszcze high volatile bituminous coal at a depth of 1200 m is only 70% of the maximum sorption capacity for unstressed coal at corresponding *PT* conditions (Fig. 14a), i.e. we assume 70% conventional gas saturation. In practice, gas cannot be recovered until the reservoir is depressurized (i.e. de-watered) to a pressure of P_c, which is commonly referred to as critical desorption pressure (Moore, 2012). The conventional model for unstressed conditions (equation 27b) predicts that P_c, in Fig. 14a, is 5 MPa, while the model for stressed conditions (equation 28b) predicts that is 6 MPa. This means a reduced time for triggering of gas production under in-situ conditions (stressed), than that typically expected based on adsorption isotherms for unstressed coal. Conversely, as illustrated in Fig. 14b, a lower amount of gas would be produced at the in-situ stress state for a fixed critical desorption pressure P_c than expected on the basis of conventional sorption data for unstressed coal.

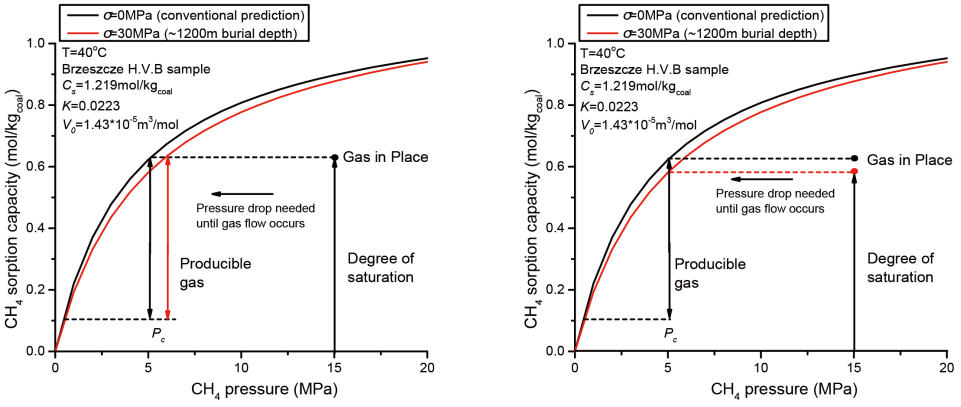

Fig.14. Effect of in-situ stress on gas production assuming Brzeszcze high volatile bituminous coal with a given gas saturation. a) for the same gas saturation and b) for the same critical desorption pressure P_c.

3.5.2. Effect of lithostatic stress on coal seam permeability

During (E)CBM production, ad/desorption of gas species such as CO_2 and CH_4 causes swelling/shrinkage of coal, hence leading to changes in stress state and inevitably in cleat permeability under in situ conditions where displacements are constrained (Espinoza et al., 2014; Liu et al., 2011; Pan and Connell, 2012). The change in stress state also results in changes in the ad/desorption process. This fully coupled stress-strain-sorption behavior of coal can be captured by inserting the revised model developed in this paper into the constitutive model proposed by Hol et al. (2012a). The modified constitutive model is formulated as

$$\varepsilon_{ij}^{eq} = \varepsilon_{ij}^{poro} - \frac{V_0 \rho (A_{ij} + \delta_{ij})}{3} C \tag{29}$$

where ε_{ij}^{eq} represents the total strain, ε_{ij}^{poro} represents the anisotropic elastic properties on the scale of the REV expressed by the poro-elastic equation (Biot, 1941;

Wang, 2000), and $\frac{V_0\rho(A_{ij}+\delta_{ij})}{3}C$ represents the swelling/shrinkage of the coal matrix caused by adsorption of gas species expressed through equation 25. Note here that compressive stress and strain are positive. This full coupling of stress, strain and sorption offers an important tool for modeling permeability evolution during (E)CBM. Its implications for (E)CBM, especially for permeability evolution during (E)CBM production are beyond the present scope and are reserved for a future reservoir modeling study.

3.5.3. Suggestions on strategies of (E)CBM production and CO_2 sequestration in coal seams

Our sorption model for a general stress state (equation 25) clearly shows that the equilibrium concentration of gas adsorbed by coal is a function of gas pressure, stress state, and the temperature. This, combined with poro-elastic deformation as described by equation 29, offers a theoretical basis for developing new techniques making use of the effect of in-situ stress, temperature and gas pressure on gas sorption, which can potentially be applied in (E)CBM production. For example, if there is a CH_4-rich coal seam that been partially mined, the gradient in stress state between the mined and unmined regions will provide an additional driving force, in excess of the gradient in gas pressure and concentration, for CH_4 flow from the unmined coal to the mined region. In such cases, a coal seam that has been partially mined, or where the stress state has been otherwise perturbed, might perhaps become more gas productive. Moreover, our model offers an improved tool for estimating the amount of CO_2 that can be adsorbed by coal seams or can be sequestrated in coal seams at given injection pressure, stress state and temperature.

3.6. Conclusions

The main findings and conclusions of this study are summarized as follows.

1. A corrected model for adsorption of any pure gas species by coal under stressed conditions has been derived. In the present model, the true equilibrium constant K^0 for sorption is expressed through the standard free energy change $(\mu_s^{P_0}(T) - \mu_{g0}(T))$, which depends only on temperature for a given coal and gas/fluid species. Our model demonstrates that an applied effective stress reduces the gas sorption capacity of coal and that the magnitude of the reduction depends on the partial molecular volume (Ω_0) of the adsorbed molecule.

2. To test our thermodynamic model, and specifically to test the effect of stress on the CH_4 sorption capacity of coal, we performed experiments on a single composite coal sample (Brzeszcze 364 high volatile bituminous coal) containing artificially introduced transport paths, which minimized the influence of the positive Terzaghi effective stress on sample permeability and hence accessibility of the sample to CH_4. The amount of CH_4 expelled from the sample was measured by increasing the hydrostatic stress or confining pressure in the range 11-43 MPa, after initial equilibration of the sample with CH_4 at a fixed methane pressure of 10 MPa and at a fixed temperature of 40˚C. The true amount of CH_4 desorbed from the sample was obtained by subtracting the poro-elastic gas expulsion determined by means of helium (a non-sorbing gas) control experiments. The results show that about 0.05 mol/kg_{coal} of CH_4 desorbed from the solid sample when the applied confining pressure increased from 11 MPa to 43 MPa, which corresponds to ~ 6.2% of the initial uptake of 0.808 mol/kg_{coal}.

3. The present model describes our experimental data well. The results indicate that our model successfully captures the physical process of gas adsorption by coal that supports a stress state applied in excess of the pressure of the sorbing gas species.

4. We apply our model to predict the in-situ CBM concentration distribution with depth for dry, high volatile bituminous coal, for an assumed geothermal gradient of 32˚C/km. The results indicate a maximum CH_4 concentration of ~ 0.76 mol/kg_{coal} at a burial depth of ~ 900m, which is ~ 3% lower than conventional predictions made without considering sorption-induced swelling and hence the effect of stress. This reduction is minor but helps to explain why gas saturation is generally lower than expected from conventional sorption measurements on unconfined coal powders. More importantly, our results confirmed that there is an intimate coupling between in-situ stress, strain and sorption in coal that needs to be considered in gas-enhanced CBM strategies.

Appendix I

I.1 Statistic mechanics approach to obtaining sorbed concentration under stress

I.1.1. Canonical partition function for adsorption of n molecules

For a total population of adsorption sites n_s (fixed), we assume that each adsorption site remains empty or else takes up one gas molecule, and that there is no interaction between adsorbed molecules. When n molecules are adsorbed (where $n < n_s$), the canonical partition function for the solid system is written (Hill, 2012)

$$Q(n_s, n, T) = q(\sigma_{ij}, T)^n \frac{n_s!}{n!(n_s - n)!} \tag{30}$$

The term $\frac{n_s!}{n!(n_s - n)!}$ is the degeneracy factor or the number of the ways W' in which the n molecules can be arranged in the n_s adsorption sites. The term q is the partition function for one single adsorbed molecule in the stressed solid, written

$$q = \exp[\frac{-\mu_s^{\sigma}}{kT}] \tag{31}$$

where quantity μ_s^{σ} represents chemical potential of one adsorbed molecule under stressed conditions (see Fig.2), as given by equation 5b

I.1.2. Chemical potential per molecule for n molecules adsorbed by stressed coal

In line with standard statistical mechanics theory, the chemical potential per molecule for n adsorbed molecules is given as

$$\mu_s = kT(\frac{\partial \ln Q}{\partial n}) \tag{32}$$

Applying Stirling's approximation $\ln x! \approx \mathrm{x}(\mathrm{lnx}-1)$ for large x to the above expression (32), we obtain

$$\mu_s = kT(\ln\frac{n}{n_s - n} - \ln q) = kT\ln\frac{\theta}{1-\theta} + \mu_s^{\sigma} \tag{33}$$

where $\theta = \frac{n}{n_s}$. Equation 33 is identical to equation 18.

I.1.3. Equilibrium condition

At equilibrium, the chemical potential of adsorbed α must be equal to that of species α in free gas phase, so that $\mu_s = kT\ln\frac{\theta}{1-\theta} + \mu_s^{\sigma} \equiv \mu_g$, which is identical to the equilibrium condition expressed in equation 19, and thus yields the same expression for θ as given in equation 20.

I.2. Kinetic methods

I.2.1. Rate of adsorption

Once again, for a total population of adsorption sites n_s (fixed), we assume that each adsorption site remains empty or else takes up one gas molecule, and that there is no interaction between adsorbed molecules. When n ($n<n_s$) molecules are adsorbed, the rate of adsorption by the remaining adsorption sites is

$$R_+ = f_+(n_s - n) \tag{34}$$

Here f_+ represents the frequency (probability) of one single diffusing gas molecule jumping over an energy barrier μ_e into the potential well associated with the

adsorption site, yielding,

$$f_+ = \nu_+ \exp[\frac{-(\mu_e - \mu_g)}{kT}] \tag{35}$$

where ν_+ is the self-vibration rate of the diffusing gas molecule. The quantity μ_g represents the chemical potential of a single diffusing gas molecule (Fig.2), which is equal to the potential in the free gas phase expressed as equation 7.

I.2.2. Rate of desorption

The rate of desorption of *n* molecules that are trapped in the adsorption sites is

$$R_- = f_- n \tag{36}$$

where f_- represents the frequency (probability) of one single gas molecule that jumps out of the adsorption site, written

$$f_- = \nu_- \exp[\frac{-(\mu_e - \mu_s^\sigma)}{kT}] \tag{37}$$

Here ν_- is the self-vibration rate of the adsorbed molecule. μ_s^σ is the chemical potential of a single adsorbed molecule expressed by the equation 5b (see Fig.2).

I.2.3. Equilibrium condition

At equilibrium, the rate of adsorption must equal that of desorption, so that $R_+ = R_-$. Using equations 7 and 34-37 gives

$$\frac{n}{n_s - n} = \frac{\nu_+}{\nu_-} \exp(\frac{\mu_{g0} - \mu_s^\sigma}{kT}) a_g \tag{38}$$

Assuming $\frac{\nu_+}{\nu_-} \approx 1$, inserting $\theta = \frac{n}{n_s}$, and rearranging, gives the expression for adsorbed concentration

$$\theta = \frac{a_g \exp(\frac{\mu_{g0} - \mu_s^\sigma}{kT})}{1 + a_g \exp(\frac{\mu_{g0} - \mu_s^\sigma}{kT})} \tag{39}$$

Using equation 5 for μ_s^σ, equation 39 becomes equation 20.

Acknowledgements

The China Scholarship Council (CSC) and Total S.A. are gratefully acknowledged for their financial support of first author Jinfeng Liu and of the research project. Sander Hol is also thanked for discussions and help in understanding his model and the experimental apparatus at Utrecht in the early stages of this project.

References

Biot, M.A., 1941. General theory of three-dimensional consolidation. J Appl Phys 12, 155-164.

Busch, A., 2005. Thermodynamic and Kinetic Processes associated with CO_2-Sequestration and CO_2-Enhanced Coalbed Methane Production from unminable Coal Seams. Bibliothek der RWTH Aachen.

Busch, A., Gensterblum, Y., 2011. CBM and CO_2-ECBM related sorption processes in coal: A review. International Journal of Coal Geology 87, 49-71.

Bustin, R., Clarkson, C., 1998. Geological controls on coalbed methane reservoir capacity and gas content. International Journal of Coal Geology 38, 3-26.

Butt, H.-J., Graf, K., Kappl, M., 2006. Physics and chemistry of interfaces. John Wiley

& Sons.

Chang, R., 2000. Physical chemistry for the chemical and biological sciences. University Science Books.

Cui, X., Bustin, R.M., Chikatamarla, L., 2007. Adsorption-induced coal swelling and stress: Implications for methane production and acid gas sequestration into coal seams. Journal of Geophysical Research: Solid Earth 112.

Day, S., Fry, R., Sakurovs, R., 2011. Swelling of moist coal in carbon dioxide and methane. International Journal of Coal Geology 86, 197-203.

Day, S., Fry, R., Sakurovs, R., Weir, S., 2010. Swelling of coals by supercritical gases and its relationship to sorption. Energ Fuel 24, 2777-2783.

Day, S., Sakurovs, R., Weir, S., 2008. Supercritical gas sorption on moist coals. International Journal of Coal Geology 74, 203-214.

Dutta, P., Bhowmik, S., Das, S., 2011. Methane and carbon dioxide sorption on a set of coals from India. International Journal of Coal Geology 85, 289-299.

Espinoza, D., Vandamme, M., Pereira, J.-M., Dangla, P., Vidal-Gilbert, S., 2014. Measurement and modeling of adsorptive–poromechanical properties of bituminous coal cores exposed to CO_2: Adsorption, swelling strains, swelling stresses and impact on fracture permeability. International Journal of Coal Geology 134, 80-95.

Fitzgerald, J., Pan, Z., Sudibandriyo, M., Robinson Jr, R., Gasem, K., Reeves, S., 2005. Adsorption of methane, nitrogen, carbon dioxide and their mixtures on wet Tiffany coal. Fuel 84, 2351-2363.

Freudenberg, U., Lou, S., Schlüter, R., Schütz, K., Thomas, K., 1996. Main factors controlling coalbed methane distribution in the Ruhr District, Germany. Geological Society, London, Special Publications 109, 67-88.

Gensterblum, Y., Busch, A., Krooss, B.M., 2014. Molecular concept and experimental evidence of competitive adsorption of H_2O, CO_2 and CH_4 on organic material. Fuel 115, 581-588.

Gensterblum, Y., Merkel, A., Busch, A., Krooss, B.M., 2013. High-pressure CH_4 and CO_2 sorption isotherms as a function of coal maturity and the influence of moisture. International Journal of Coal Geology 118, 45-57.

Gray, I., 1987. Reservoir engineering in coal seams: Part 1-The physical process of gas storage and movement in coal seams. SPE Reservoir Engineering 2, 28-34.

Hill, T.L., 2012. An introduction to statistical thermodynamics. Courier Corporation.

Hol, S., Peach, C.J., Spiers, C.J., 2011. Applied stress reduces the CO_2 sorption capacity

of coal. International Journal of Coal Geology 85, 128-142.

Hol, S., Peach, C.J., Spiers, C.J., 2012a. Effect of 3-D stress state on adsorption of CO_2 by coal. International Journal of Coal Geology 93, 1-15.

Hol, S., Spiers, C.J., 2012. Competition between adsorption-induced swelling and elastic compression of coal at CO_2 pressures up to 100MPa. J Mech Phys Solids 60, 1862-1882.

Hol, S., Spiers, C.J., Peach, C.J., 2012b. Microfracturing of coal due to interaction with CO_2 under unconfined conditions. Fuel 97, 569-584.

Langmuir, I., 1918. The adsorption of gases on plane surfaces of glass, mica and platinum. J Am Chem Soc 40, 1361-1403.

Laubach, S., Marrett, R., Olson, J., Scott, A., 1998. Characteristics and origins of coal cleat: A review. International Journal of Coal Geology 35, 175-207.

Laxminarayana, C., Crosdale, P.J., 1999. Role of coal type and rank on methane sorption characteristics of Bowen Basin, Australia coals. International Journal of Coal Geology 40, 309-325.

Levine, J.R., 1993. Coalification: The evolution of coal as source rock and reservoir rock for oil and gas: Chapter 3.

Levine, J.R., 1996. Model study of the influence of matrix shrinkage on absolute permeability of coal bed reservoirs. Geological Society, London, Special Publications 109, 197-212.

Liu, J., Chen, Z., Elsworth, D., Qu, H., Chen, D., 2011. Interactions of multiple processes during CBM extraction: A critical review. International Journal of Coal Geology 87, 175-189.

Liu, J., Peach, C.J., Zhou, H., Spiers, C.J., 2015. Thermodynamic models for swelling of unconfined coal due to adsorption of mixed gases. Fuel 157, 151-161.

Mares, T.E., Moore, T.A., Moore, C.R., 2009. Uncertainty of gas saturation estimates in a subbituminous coal seam. International Journal of Coal Geology 77, 320-327.

Merkel, A., Gensterblum, Y., Krooss, B.M., Amann, A., 2015. Competitive sorption of CH_4, CO_2 and H_2O on natural coals of different rank. International Journal of Coal Geology 150, 181-192.

Moore, T.A., 2012. Coalbed methane: A review. International Journal of Coal Geology 101, 36-81.

Myers, A., 2002. Thermodynamics of adsorption in porous materials. Aiche J 48, 145-160.

Myers, A., Monson, P., 2002. Adsorption in porous materials at high pressure: theory and experiment. Langmuir 18, 10261-10273.

Ottiger, S., Pini, R., Storti, G., Mazzotti, M., 2008. Competitive adsorption equilibria of CO_2 and CH_4 on a dry coal. Adsorption 14, 539-556.

Pan, Z., Connell, L.D., 2007. A theoretical model for gas adsorption-induced coal swelling. International Journal of Coal Geology 69, 243-252.

Pan, Z., Connell, L.D., 2012. Modelling permeability for coal reservoirs: A review of analytical models and testing data. International Journal of Coal Geology 92, 1-44.

Pini, R., Ottiger, S., Burlini, L., Storti, G., Mazzotti, M., 2010. Sorption of carbon dioxide, methane and nitrogen in dry coals at high pressure and moderate temperature. Int J Greenh Gas Con 4, 90-101.

Pone, J.D.N., Halleck, P.M., Mathews, J.P., 2009. Sorption capacity and sorption kinetic measurements of CO_2 and CH_4 in confined and unconfined bituminous coal. Energ Fuel 23, 4688-4695.

Setzmann, U., Wagner, W., 1991. A new equation of state and tables of thermodynamic properties for methane covering the range from the melting line to 625 K at pressures up to 100 MPa. Journal of Physical and Chemical Reference Data 20, 1061-1155.

Tuin, G., Stein, H., 1995. The excess Gibbs free energy of adsorption of sodium dodecylbenzenesulfonate on polystyrene particles. Langmuir 11, 1284-1290.

Wang, H., 2000. Theory of linear poroelasticity with applications to geomechanics and hydrogeology. Princeton University Press.

Weniger, P., Franců, J., Hemza, P., Krooss, B.M., 2012. Investigations on the methane and carbon dioxide sorption capacity of coals from the SW Upper Silesian Coal Basin, Czech Republic. International Journal of Coal Geology 93, 23-39.

White, C.M., Smith, D.H., Jones, K.L., Goodman, A.L., Jikich, S.A., LaCount, R.B., DuBose, S.B., Ozdemir, E., Morsi, B.I., Schroeder, K.T., 2005. Sequestration of carbon dioxide in coal with enhanced coalbed methane recovery a review. Energ Fuel 19, 659-724.

Chapter 4

Coupling of swelling, internal stress evolution and diffusion in coal matrix material during exposure to methane

Jinfeng Liu, Peter A. Fokker, Christopher J. Spiers

Also submitted to Journal of Geophysical Research: Solid Earth

Abstract

Recent research has demonstrated an intimate thermodynamic coupling between stress state, swelling strain, the chemical potential of adsorbed gas molecules and the adsorption capacity of coal matrix material. This means that local sorption-induced swelling within a coal matrix particle can potentially influence diffusion in coal, because internal swelling stresses can change the local chemical potential and equilibrium concentration of the adsorbed molecules, and hence the driving force for their diffusion. In the present study, we construct theoretical models for time-dependent swelling of coal matrix material upon adsorption of a single gas, taking into account this coupling between stress, strain, chemical potential and diffusion. Two models are developed. These correspond to diffusion and hence swelling rates being controlled by the jump frequency of adsorbed molecules between closely spaced adsorption sites (Model A), versus transport controlled by diffusion of unadsorbed molecules through diffusion paths linking distant adsorption sites (Model B). To test these models, we performed axial swelling experiments on a single 4mm sized cylindrical sample of medium volatile bituminous coal, exposed to CH_4 at pressures up to 40 MPa, at 40˚C, using 1D high pressure dilatometry. The experimental data were compared with our model predictions. The results show that the time-dependent swelling behaviour of the coal matrix sample due to adsorption of CH_4 can be accurately explained only by Model B, applied assuming a single-valued diffusion coefficient that is independent of gas pressure and adsorbed concentration. The implication is that time-dependent swelling was controlled by the diffusion of unadsorbed molecules and not by the jump frequency of adsorbed molecules or by pore size distribution effects cited in the literature. Our models demonstrate that swelling-driven internal stress evolution can significantly influence adsorption and diffusion in coal matrix material, if the partial molar volume (V_0) of the adsorbed molecules is sufficiently large. However, in our experiments the effect seems to have been negligible compared to that of diffusion mechanism, as V_0 for CH_4 sorption by coal is small. Nonetheless, the models presented describe a full coupling between stress, strain, sorption and diffusion in coal matrix material in terms of parameters that have clear physical meaning and are easily obtained from sorption and swelling experiments on coal of any rank exposed to any gas. They therefore offer an important tool for modelling permeability evolution with time during (enhanced) coalbed methane operations.

4.1. Introduction

It is well established that the adsorption of gases, such as CH_4, CO_2, N_2, and H_2O, by coal can cause swelling strains of up to 1-5%, and that this swelling develops in a time-dependent manner reflecting the time-dependence of the adsorption process (Day et al., 2010; Fry et al., 2009; Hol and Spiers, 2012; van Bergen et al., 2009b). The kinetics of coal matrix swelling and shrinkage due to gas adsorption and desorption can strongly influence the evolution of coal seam permeability during coalbed methane (CBM) production and CO_2 enhanced CBM production (e.g. Espinoza et al., 2014; Liu et al., 2011; Peng et al., 2014). Understanding the swelling kinetics of coal matrix material, in a quantitative way, is therefore of central importance for modelling reservoir behaviour during both CBM and ECBM operations.

Time-dependent sorption and the associated swelling by coal is generally considered to be controlled by diffusion, as experimental studies show that sorption and swelling rates strongly depend on coal sample or particle size (Busch and Gensterblum, 2011; Busch et al., 2004; Gruszkiewicz et al., 2009; Chapter 5). Since transport through open fractures or cleats in coal is relatively rapid, the key parameter describing the diffusion kinetics is the diffusion coefficient for the intervening coal matrix. Many experimental studies have been performed on the sorption kinetics of coal with respect to CH_4, CO_2 and N_2 (c.f. Busch and Gensterblum, 2011). These typically focus on the evolution of sorbed concentration, i.e. the approach to equilibrium, that follows a step change in gas pressure applied to an unconfined granular coal sample. The (apparent) diffusion coefficient controlling sorption rate by the coal grains is then calculated by fitting a diffusion model to the transient sorption data. The most widely applied diffusion models are the so-called unipore and bidisperse models (c.f. Busch and Gensterblum, 2011). The first assumes that diffusion in the coal matrix occurs through a network of unimodally distributed nm-scale pores, whereas the second assumes a bimodal distribution of macroscale (~ 30-50 nm) versus microscale (~ 1-30 nm) pore sizes supporting different

diffusion mechanisms and rates (specifically fast diffusion through the macropores controlled by molecule-molecule collision or viscous flow, accompanied by slow diffusion through the micropores controlled by molecule/pore-walls collisions or surface diffusion (c.f. Clarkson and Bustin, 1999; Cui et al., 2004; Shi and Durucan, 2003). Both the unipore and bidisperse modelling approaches are based on Fick's laws of diffusion within the pore networks considered (c.f. Busch and Gensterblum, 2011). Both assume a) that the driving force for diffusion is the concentration gradient of the diffusing (gas) species within the coal, and b) that any effects of sorption-induced swelling of the coal matrix and associated internal stress development are negligible (e.g. Busch and Gensterblum, 2011; Busch et al., 2004; Clarkson and Bustin, 1999; Cui et al., 2004; Shi and Durucan, 2003). Both analytical and numerical methods have been used to explore the behaviour predicted by these models and to calculate the relevant (apparent) diffusion coefficients by fitting to experimental data (Clarkson and Bustin, 1999). The (apparent) diffusion coefficients obtained are generally found to depend not only on coal rank, gas species, and temperature, but also on applied gas pressure/density and adsorbed concentration (e.g. Busch and Gensterblum, 2011; Busch et al., 2004; Clarkson and Bustin, 1999; Cui et al., 2004; Shi and Durucan, 2003; Staib et al., 2013). The observed dependence on gas pressure is generally argued to be caused by a) changes in diffusion mechanism in the coal due to changes in the mean free path of diffusing gas molecules upon changes in external gas pressure (Clarkson and Bustin, 1999; Cui et al., 2004), and/or b) dilation and constriction of transport paths caused by shrinkage and swelling of the coal due to gas desorption and adsorption (Busch et al., 2004; Shi and Durucan, 2003). However, none of the models described above consider the potential effects of swelling and internal stress evolution within the coal on sorption capacity or on the driving force for the diffusion process.

In addition to the above treatments of the kinetics of diffusion-controlled adsorption in coal as a multiscale porous material, coal has also been treated as a polymeric

material into which gas can diffuse (e.g. Goodman et al., 2006; Karacan, 2003; Larsen et al., 1985; Mazumder et al., 2011). In polymers, a transition from a glassy phase to a rubbery phase occurs when solvent molecules penetrate the polymer structure, causing polymer swelling (Haward, 2012). This swelling effect leads to diffusion of the dissolved species not obeying Fick's equations, as the driving force for diffusion in this case is provided by the gradient in both solute concentration and swelling stress (Govindjee and Simo, 1993; Hui et al., 1987a, b; Thomas and Windle, 1982). This glass-rubber phase transition behaviour of polymers has been applied to interpret coal swelling due to CO_2 adsorption, by assuming that coal matrix material behaves as a glassy polymer that undergoes this transition when CO_2 diffuses or dissolves into it (Goodman et al., 2006; Karacan, 2007; Larsen, 2004; Mazumder et al., 2011). Mazumder et al. (2011) applied the above non-Fickian diffusion model for polymers to describe CO_2 diffusion in coal, taking into account the effect of swelling stress on diffusion. However, it still remains unclear whether or not the phase transition assumed to occur in coal due to sorption of CO_2 or other gases (such as CH_4, N_2) actually does occur (Hol et al., 2012b). Furthermore, Mazumder et al. do not present experiments and have no calibration of their model.

In line with the above-mentioned effect of swelling stress on sorption and diffusion in polymers, recent research has independently demonstrated that the sorption capacity of coal matrix material, with respect to CH_4 and CO_2, is influenced by stresses supported by the solid framework (Hol et al., 2011; Hol et al., 2012a; Liu et al., Chapter 3; Pone et al., 2009). This effect of applied stress on adsorbed concentration at equilibrium has been explained in terms of thermodynamic theory by Hol et al. (2012a) and Liu et al. (Chapter 3). These authors showed that applied compressive stress increases the adsorption energy of adsorbed molecules, and hence reduces adsorbed concentration at thermodynamic equilibrium. The magnitude of this effect was shown to depend on the swelling strain contributed per molecule adsorbed. This means that local

sorption-induced swelling within a coal particle or sample can potentially influence diffusion in the coal, because internal swelling stresses generated by non-uniform swelling can change the local chemical potential and equilibrium concentration of the adsorbed molecules, and hence the driving force for their diffusion.

Compared to studies on sorption kinetics, far fewer studies have been conducted on the kinetics of coal matrix swelling due to adsorption. Recently, Staib et al. (2014) investigated the effects of gas pressure and coal rank on the swelling kinetics of coal by performing swelling tests on cm-scale samples ($3\times1\times1cm^3$) at gas pressures up to 15 MPa at 55˚C, using an optical cell. They qualitatively compared swelling rates at different gas pressures by plotting normalized swelling (i.e. instantaneous volumetric strain per gas pressure step, normalized with respect to the strain achieved at equilibrium) versus time. As observed in studies of adsorption kinetics, Staib et al. also found that swelling rates depended on gas pressure. However, no models currently exist relating the external swelling response to the inwardly progressing diffusion flux and associated inwardly progressing, adsorption, swelling and internal stress evolution. In other words, no models are available for predicting the time-dependent swelling behaviour of coal matrix material upon exposure to a single gas, or for quantitatively interpreting experimental data such as that reported by Staib et al. (2014), despite the fact that swelling behaviour plays such an important role in coal seam permeability evolution during (E)CBM production.

In the present study, we investigate the coupling between coal matrix swelling, internal stress evolution, adsorption and diffusion. We first construct theoretical models for the time-dependent swelling of a coal matrix particle exposed to a single adsorbing gas, allowing for these effects. Two models are developed, covering two basic mechanisms for diffusive transport of gas molecules inside the coal matrix. To determine which mechanism controls the diffusion process, swelling experiments were performed on a single, 4mm by 4 mm cylindrical sample of medium volatile bituminous coal, from

Pingdingshan, China. This was exposed to CH_4 gas at pressures cycled up and down in the range of 0 to 40 MPa, and at a constant temperature of 40˚C, using 1D, high pressure dilatometry to measure the swelling response. The results obtained are compared with our model predictions. This suggests that time-dependent swelling of coal matrix material due to adsorption of a single gas is controlled not by the jump frequency of adsorbed gas molecules between adsorption sites, but by the diffusion of unadsorbed gas molecules, with this being characterized by a pressure-independent diffusion coefficient.

4.2. Theoretical models

We start by developing theoretical models for time-dependent swelling of a coal matrix particle exposed to a pure gas/fluid phase. We take into account not only diffusion and adsorption but also the coupling between stress, strain and sorption capacity embodied in the thermodynamic theory by Hol et al. (2012a) and Liu et al. (Chapter 3). Two models are derived based on two possible mechanisms for diffusion occurring inside the coal matrix material. We formulate our models for an isotropic, spherically symmetric coal particle or sample geometry. For later comparison with other particle or sample shapes, we assume that the effect of a non-spherical form can be captured using a numerical shape factor. For simplicity, we henceforth use the term "gas", to cover both gas and (supercritical) fluid.

4.2.1. Starting assumptions

We consider the spherical coal particle geometry specified in Fig.1. The particle consists of a small coal matrix sphere (e.g. 0.5-5 mm) of volume V (m^3) and density ρ (kg/m^3), surrounded by a pure gas phase (β) at constant pressure P, absolute temperature T and chemical potential μ_g. The density of the coal particle is assumed constant during the sorption processes despite small volumetric changes caused by adsorption-induced swelling. The matrix material is considered homogeneous in structure and composition

at the particle length scale, and isotropic in diffusion and mechanical properties, the latter being linear elastic. It is further assumed to contain nano-pores only, so that there is no Darcian flow and negligible storage of free, unadsorbed gas. In other words, the coal particle is so small that it is cleat free and can take up gas only by diffusion and adsorption. Lastly, we assume that the coal hosts C_s localized adsorption sites (mol) per kg, each of which consists of a potential well capable of trapping a single molecule of the gas β via sorption. C_s is assumed to depend solely on coal rank and gas species. Note that we treat the adsorbed gas molecule as being a "dissolved" component of the solid phase here, following the rigorous thermal treatment by Myers (2002) of stress-free sorption, as opposed to assuming an independently identifiable adsorbed phase. Focusing now on an infinitesimally small representative volume of coal within the spherical particle, located at the generic point Q in Fig.1, for example, then the corresponding pointwise potential of adsorbed molecules is given by Liu et al. (Chapter 3), in J/mol, as

$$\mu_s = \mu_s^{P_0} + (\bar{\sigma} - P_0)V_0 + RT\ln\left(\frac{\theta}{1-\theta}\right) \quad (1)$$

Here, the quantity θ represents the pointwise adsorption site occupancy, R is the gas constant and the term $R\ln\left(\frac{\theta}{1-\theta}\right)$ is the molar configurational entropy of the adsorbed molecules. The quantity V_0 (m^3/mol) represents the partial molar volume of adsorbed gas molecules, while the term $(\bar{\sigma} - P_0)V_0$ represents the stress-strain work done on the surroundings as coal swells against the total local mean stress $\bar{\sigma}$, i.e. $\bar{\sigma} = \frac{\sigma_{rr}+2\sigma_{\varphi\varphi}}{3}$. The quantity $\mu_s^{P_0}$ represents the potential of adsorbed molecules at reference pressure P_0=0.1MPa, which depends solely on temperature for a given gas. From equation 1, it is clear that the pointwise chemical potential of the adsorbed species (μ_s) depends not only on site occupancy, as in classical sorption models that neglect solid stresses in excess of the applied gas pressure (Myers, 2002), but also on the total mean stress $\bar{\sigma}$. The magnitude of this stress effect further depends on the partial molar volume of the

adsorbed molecules V_0, i.e. the swelling caused by adsorption of 1 mole of gas.

Assuming that V_0 is insensitive to both stress state and adsorbed occupancy (Hol et al., 2012a; Hol and Spiers, 2012; Liu et al., Chapter 3) and that the volumetric swelling of a small (pointwise) volume dV of coal upon adsorption of n moles of the sorbing species is fully defined as nV_0, then the pointwise volumetric strain de_v^{ads} can be written as $C_s\rho V_0\theta$ (Hol et al., 2012a; Hol and Spiers, 2012). For a mm-scale spherical particle of coal matrix into which molecules of species β are diffusing radially, the total volumetric strain of the particle due to adsorption as a function of time is accordingly given as

$$e_v^{ads}(t) = \frac{1}{V} C_s \rho V_0 \iiint \theta(r,t)\, dV \tag{2}$$

This means that to obtain complete expressions for time-dependent swelling of a spherical coal particle during adsorption, we need to calculate the adsorbed occupancy $\theta(r,t)$.

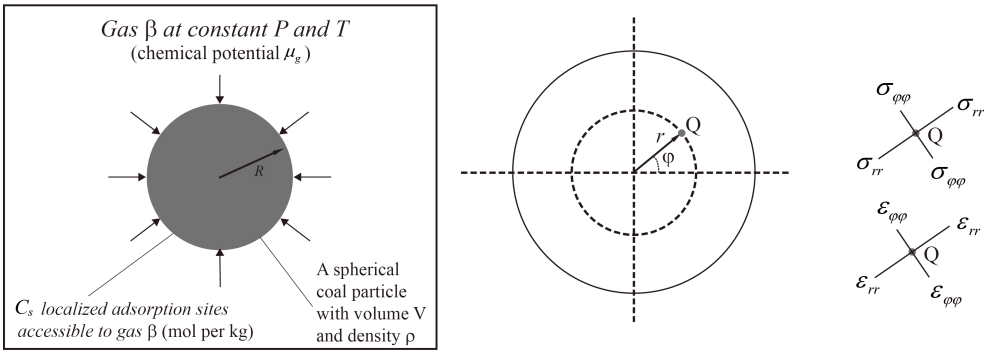

a) b)

Fig.1. Spherical coal matrix sample/particle geometry used in the present analysis of time-dependent swelling of a particle upon diffusion-controlled penetration and adsorption of a single gas species β. a) The assumed spherically symmetric particle or sample geometry. b) Spherical coordinate and stress/strain reference frame, illustrated in 2D section. Note that the spherical symmetry implies that the stress and strain components normal to the plane of the diagram are tangential components $\sigma_{\varphi\varphi} = \sigma_{\gamma\gamma}$ *and* $\varepsilon_{\varphi\varphi} = \varepsilon_{\gamma\gamma}$.

4.2.2. Assumed diffusion mechanisms and governing equations

We assume two possible elementary transport mechanisms for the diffusing gas species β, consistent with the concept of site adsorption and with previous site-to-site diffusion models (Shewmon, 1989).

4.2.2.1. Type A diffusion: Jump-controlled diffusion

In this case, we assume that the adsorption sites for species β inside the coal matrix are sufficiently closely spaced, that the rate of diffusion is controlled by the jump frequency of adsorbed molecules out of their adsorption sites into an adjacent sorption site (see Fig.2). Each adsorption site is either empty or is occupied by one adsorbed molecule. The successful jump rate of an adsorbed molecule into an empty adjacent site, and hence the mobility of the adsorbed molecules, is therefore proportional to the concentration $(1-\theta)$ of empty (unoccupied) adsorption sites. The energy or activation barrier to diffusion here is the depth of the potential well associated with the adsorption sites, and the driving force for diffusion is the difference in chemical potential between adsorbed molecules in adjacent sites, hence the gradient in chemical potential (Fig. 2b).

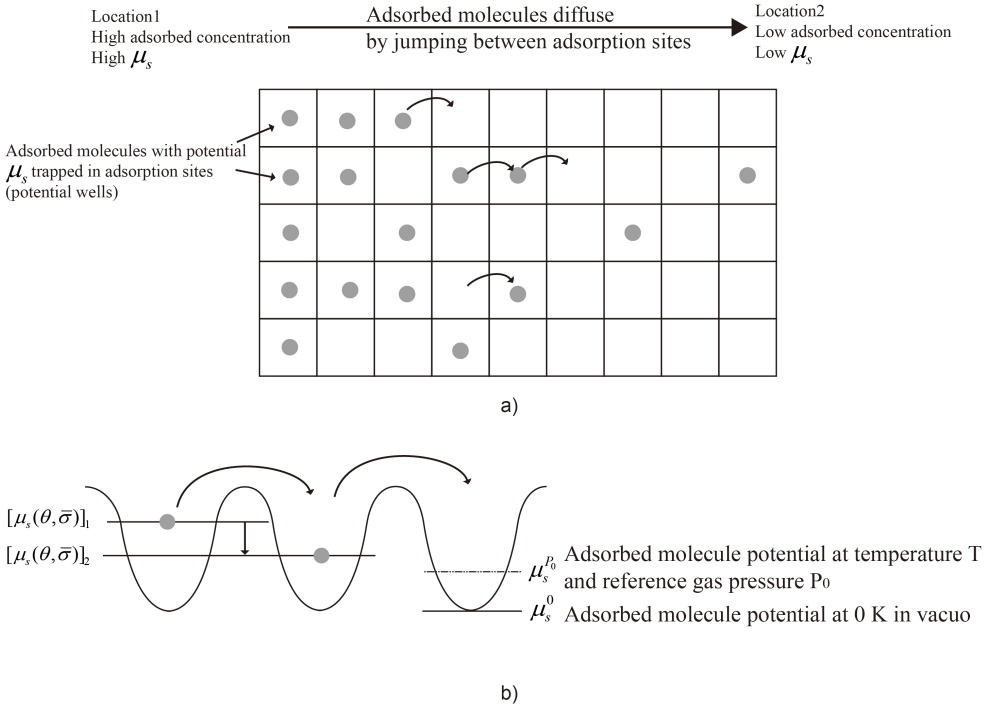

Fig.2. Schematic illustration of Type A diffusion. The adsorption sites are so closely spaced (see a) that adsorbed molecules diffuse at a rate controlled by the jump process between (out of) adsorption sites (see b). The successful jump rate of adsorbed molecules is proportional to the probability of an adjacent site being empty, and is hence to proportional to $(1-\theta)$*, where* θ *is site occupancy.*

In line with the above and with standard site-to-site diffusion theory (Shewmon, 1989), the inward (radial) diffusion flux of adsorbed molecules $\boldsymbol{J}$ ($\mathrm{mol \cdot m^2 \cdot s^{-1}}$), at any point in a coal matrix sample (here a spherical particle), can be expressed as

$$\mathbf{J} = -D(1-\theta)C_s\rho\frac{\theta}{RT}\nabla\mu_s \tag{3}$$

Here the quantity D represents the diffusion coefficient ($\mathrm{m^2 \cdot s^{-1}}$) for random walk, which solely depends on the molecular structure of the coal matrix material, while the term $(1-\theta)$ represents the jump probability weighting for adsorbed molecules due to the site occupancy effect described above. The term $\frac{D(1-\theta)C_s\rho\theta}{RT}$ represents the

phenomenological mobility coefficient relating **J** to $\nabla\mu_s$. Note here that when $\theta \ll 1$, i.e. for a "dilute solution", equation 3 reduces to Fick's first law expressed in terms of the chemical potential gradient of the diffusing species, i.e. to

$$\mathbf{J} = -DC_s\rho\frac{\theta}{RT}\nabla\mu_s \tag{4}$$

Inserting equation 1 into 3, we now obtain

$$\mathbf{J} = -DC_s\rho\left[\frac{\theta(1-\theta)\mathrm{V}_0}{RT}\nabla\bar{\sigma} + \nabla\theta\right] \tag{5}$$

which on applying the law of mass conservation for the diffusing species written

$$\frac{\partial\theta}{\partial t} = -\frac{1}{C_s\rho}\nabla\cdot\mathbf{J} \tag{6a}$$

yields $\frac{\partial\theta}{\partial t} = -\frac{1}{C_s\rho}\nabla\cdot\mathbf{J} = D\nabla\cdot\left[\frac{\theta(1-\theta)\mathrm{V}_0}{RT}\nabla\bar{\sigma} + \nabla\theta\right]$ (6b)

Note here that if sorption induced swelling does not occur, i.e. if the partial molar volume of adsorbed molecules is negligible, so that $\mathrm{V}_0 \approx 0$, then the non-linear term in equations 5 and 6 disappears. It is also seen from equation 6 that the pointwise sorption rate $\frac{\partial\theta}{\partial t}$ is influenced not only by diffusion coefficient *D*, but also by adsorption site occupancy θ via the term $\theta(1-\theta)$.

4.2.2.2. Type B diffusion: Path-controlled diffusion

In this case, we assume that the adsorption sites are distant from each other, and that transport between sorption sites is controlled by diffusion of the unadsorbed molecules through the relatively long intervening diffusion paths (see Fig.3). Here the barrier to diffusion of unadsorbed molecules is the activation barrier for diffusive jumps over the many small barriers (diffusive potential wells) offered by fluctuations in electron field density associated with individual atoms and bonds in the macromolecular coal structure along the diffusion path length. In this case, the driving force for diffusion is the potential gradient of the unadsorbed molecules present in the diffusion path. In any small (pointwise) elementary volume of coal, since jumping of adsorbed molecules out of their

sorption sites is assumed to be easy (rapid) compared to longer range diffusion of unadsorbed molecules, then the local potential of unadsorbed molecules must equal the potential of the adsorbed molecules (i.e. the adsorbed and unadsorbed species must be in equilibrium). In addition, since there will generally be a far higher concentration of diffusive potential wells in the coal matrix than diffusing molecules, diffusion of unadsorbed molecules is assumed to be treatable as diffusion in a "dilute" solution, with the elementary diffusive steps taken by unadsorbed molecules obeying random walk diffusion (in the absence of a potential gradient).

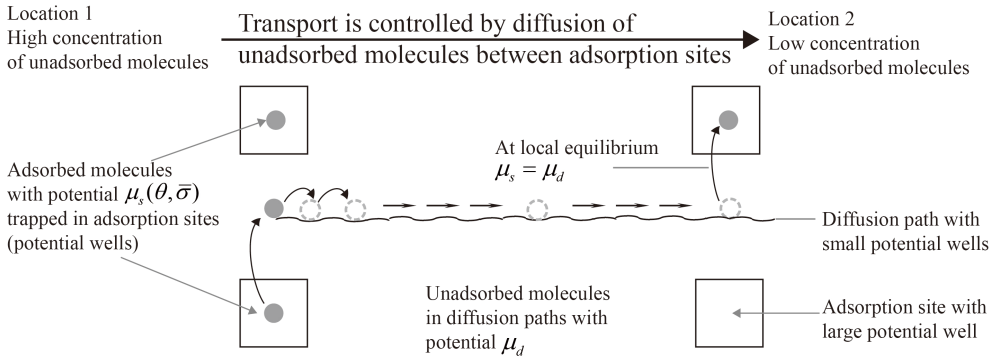

Fig.3. Schematic illustration of Type B diffusion. Adsorption sites are distant from each other, so that transport between adsorption sites is controlled by diffusion of unadsorbed molecules along the long, intervening diffusion path. In this case, the potential of unadsorbed molecules must be in local equilibrium with the adsorbed molecules, and the barrier to diffusion is the activation barrier associated with overcoming the many small barriers encountered in the diffusion path.

On the basis of the above, for Type B diffusion, the diffusion flux $\boldsymbol{J}$ ($\mathrm{mol \cdot m^2 \cdot s^{-1}}$) of unadsorbed molecules, can be formulated as

$$\mathbf{J} = -D\frac{C_d}{RT}\nabla\mu_d \tag{7}$$

where C_d ($\mathrm{mol \bullet m^{-3}}$) and μ_d ($\mathrm{J \bullet mol^{-1}}$) are the pointwise concentration and potential of unadsorbed molecules within the coal. This corresponds to the Fick's first law expressed in terms of chemical potential. For the present dilute solution of unadsorbed molecules

in the diffusion path network, we can further write

$$\mu_d = \mu_{g0} + RTln(^{C_d}/_{C_{d0}}) \tag{8a}$$

or $C_d = C_{d0}\exp\left(\frac{\mu_d - \mu_{g0}}{RT}\right)$ (8b)

where μ_{g0} and C_{d0} are the potential and concentration of unadsorbed molecules in the coal at a reference condition corresponding to equilibrium with an external gas phase at reference pressure P_0=0.1MPa. Inserting equation 8b into 7, we now obtain

$$\mathbf{J} = -D\frac{C_{d0}\exp\left(\frac{\mu_d - \mu_{g0}}{RT}\right)}{RT}\nabla\mu_d \tag{9}$$

Assuming local equilibrium between the unadsorbed and adsorbed molecules as discussed above, we also have

$$\mu_d = \mu_s \tag{10}$$

which combined with equations 1 and 9 yields

$$\mathbf{J} = -D\frac{C_{d0}exp\left(\frac{\mu_s - \mu_{g0}}{RT}\right)}{RT}\nabla\mu_s \tag{11a}$$

or $\mathbf{J} = -D\frac{C_{d0}\exp\left(\frac{\mu_s^{P_0} + (\bar{\sigma} - P_0)V_0 - \mu_{g0}}{RT}\right)}{RT}\frac{\theta}{1-\theta}\nabla\mu_s$ (11b)

Writing the equilibrium constant for sorption as $K^0 = \exp\left(\frac{\mu_{g0} - \mu_s^{P_0}}{RT}\right)$, following Liu et al. (Chapter 3), now gives

$$\mu_{g0} - \mu_s^{P_0} = RTlnK^0 \tag{12}$$

Which, inserted equation 11b and combining with equation 1, leads to the result

$$\mathbf{J} = \frac{-C_{d0}D}{K^0}\exp\left(\frac{(\bar{\sigma} - P_0)V_0}{RT}\right)\left[\frac{\theta \mathrm{V}_0}{(1-\theta)RT}\nabla\bar{\sigma} + \frac{1}{(1-\theta)^2}\nabla\theta\right] \tag{13}$$

Finally, assuming that the storage of unadsorbed molecules in the coal matrix is negligible, the conservation of mass requires that the rate of change of adsorbed molecule concentration, at any point, must equal the divergence of diffusion flux, yielding

$$\frac{\partial\theta}{\partial t} = -\frac{1}{C_s\rho}\nabla\cdot\mathbf{J} = \frac{DC_{d0}}{K^0C_s\rho}\nabla\left\{\exp\left(\frac{(\bar{\sigma} - P_0)V_0}{RT}\right)\left[\frac{\theta \mathrm{V}_0}{(1-\theta)RT}\nabla\bar{\sigma} + \frac{1}{(1-\theta)^2}\nabla\theta\right]\right\} \tag{14}$$

Note that this equation is highly non-linear, even if the partial molar volume of adsorbed molecules, and hence the magnitude of sorption-induced swelling, is negligible (i.e. $V_0 \approx 0$). Moreover, the sorption rate $\frac{\partial \theta}{\partial t}$ is influenced not only by the diffusion coefficient *D*, but also by the adsorbed occupancy θ via the terms $\frac{\theta}{(1-\theta)}$ and $\frac{1}{(1-\theta)^2}$. The Type B diffusion model thus predicts an increasing diffusion controlled adsorption rate with increasing sorbed concentration θ.

4.2.3. Time-dependent swelling of a spherically symmetric coal particle

We now consider how a spherical particle or sample of isotropic coal, as represented in Fig.1, will swell with time when exposed at its outer surface to a gas at constant pressure *P*. The application of this gas pressure to the outer boundary of the particle will of course drive diffusion of gas molecules radially into the coal particle. The associated sorption will cause a radially symmetric swelling and hence stress-strain field to develop, which will continuously evolve until a uniform equilibrium sorbed concentration and a uniform swelling strain are achieved throughout the particle. The evolution of the system with time will accordingly be determined by the diffusion equations 6 and 14, by the stress-strain behaviour of the coal (which we assume to be elastic) and by the initial and boundary conditions imposed on the system, with the externally measured sample volume strain being given by equation 2, for example.

For the case of spherical symmetry, the stress state at any radial coordinate is given by the principal stresses σ_{rr} and $\sigma_{\varphi\varphi} = \sigma_{\gamma\gamma}$. Displacements *u* are only possible in the radial direction and the principal strains are related to radial displacement via $\varepsilon_{rr} = \frac{\partial u}{\partial r}$ and $\varepsilon_{\varphi\varphi} = \varepsilon_{\gamma\gamma} = \frac{u}{r}$ (note that we take compression as positive and radial displacement to be positive inward). Applying Hooke's law for our assumed isotropic, elastically deformable particle now gives

$$\varepsilon_{rr} = \frac{1}{E}\left(\sigma_{rr} - 2\nu\sigma_{\varphi\varphi}\right) - \alpha\theta \tag{15a}$$

$$\varepsilon_{\varphi\varphi} = \frac{1}{E}[(1-\nu)\sigma_{\varphi\varphi} - \nu\sigma_{rr}] - \alpha\theta \tag{15b}$$

where $\alpha = \frac{1}{3}\mathrm{C_s V_0 \rho}$.

Rearranging the above equations and expressing the strains in terms of radial displacements, yields the following relations for the radial, tangential and mean stresses,

$$\sigma_{rr} = \frac{E}{1-2\nu}\left\{\frac{1-\nu}{1+\nu}\frac{\partial u}{\partial r} + \frac{2\nu}{1+\nu}\frac{u}{r} + \alpha\theta\right\} \tag{16a}$$

$$\sigma_{\varphi\varphi} = \frac{E}{1-2\nu}\left\{\frac{\nu}{1+\nu}\frac{\partial u}{\partial r} + \frac{1}{1+\nu}\frac{u}{r} + \alpha\theta\right\} \tag{16b}$$

$$\bar{\sigma} = \tfrac{1}{3}\left(\sigma_{rr} + 2\sigma_{\varphi\varphi}\right) = \frac{E}{1-2\nu}\left\{\frac{1}{3r^2}\frac{\partial}{\partial r}(r^2 u) + \alpha\theta\right\} \tag{16c}$$

These equations are exactly equivalent to the thermo-elastic equations for a radially symmetry isotropic body, i.e. a sphere, subjected to an instantaneously imposed fixed temperature at its external surface. In such a system, the thermal gradient leads to the inward conduction of heat and an inward progression of a radially symmetric temperature and stress-strain field, as described by Hetnarski et al. (2009), for example. In these authors' treatment, α is the thermal expansion coefficient and θ is the temperature increase.

In addition to equations 16, force balance applies everywhere in the interior at the present coal particle, which results in the stress equilibrium equation, $\frac{1}{r^2}\frac{\partial}{\partial r}(r^2\sigma_{rr}) - \frac{2\sigma_{\varphi\varphi}}{r} = 0$. Combined with the constitutive equations 16, this yields

$$\frac{\partial}{\partial r}\left[\frac{1}{r^2}\frac{\partial}{\partial r}(r^2 u) + \alpha\frac{1+\nu}{1-\nu}\theta\right] = 0 \tag{17}$$

In the dynamic problem at hand, both the displacement and occupancy (sorbed concentration) fields within the coal particle will in general be time dependent. Integration of equation 17 must therefore yield a solution of the form

$$\frac{1}{r^2}\frac{\partial}{\partial r}[r^2u(r,t)] + \alpha\frac{1+\nu}{1-\nu}\theta(r,t) = f(t) \tag{18}$$

where the function *f*(*t*) is an integration constant independent of position *r* but dependent on *t*. This equation can be further integrated to give

$$u(r) = \frac{1}{r^2}\int_0^r -\alpha r^2\frac{1+\nu}{1-\nu}\theta(r,t)dr + \frac{1}{3}rf(t) \tag{19}$$

The function *f(t)* is determined by the boundary conditions. At the external boundary of the spherical particle, i.e. at $r = b$, the normal stress equals the gas pressure *P*, so we have

$$P = [\sigma_{rr}]_{r=b} = \frac{E}{1-2\nu}\left[\frac{1-\nu}{1+\nu}\frac{\partial u}{\partial r} + \frac{2\nu}{1+\nu}\frac{u}{r} + \alpha\theta\right]_{r=b}$$

$$= E\left[\frac{2}{b^3}\int_0^b \alpha r^2\frac{1}{1-\nu}\theta(r',t)dr + \frac{1/3}{1-2\nu}f(t)\right] \tag{20}$$

which in turn yields

$$f(\mathrm{t}) = 3(1-2\nu)\frac{P}{E} - 2\frac{3\alpha}{b^3}\frac{1-2\nu}{1-\nu}\int_0^b r^2\theta(r,t)dr \tag{21}$$

Substituting this into 9 and 16, we obtain the following relations for the displacement and total stress fields inside the sample:

$$u(r,t) = -\frac{\alpha}{r^2}\frac{1+\nu}{1-\nu}\int_0^r r^2\theta(r,t)dr - 2\frac{\alpha r}{b^3}\frac{1-2\nu}{1-\nu}\int_0^b r^2\theta(r,t)dr + r(1-2\nu)\frac{P}{E} \tag{22a}$$

$$\sigma_{rr}(r,t) = \frac{-\alpha E}{1-\nu}\left\{\frac{2}{b^3}\int_0^b r^2\theta(r,t)dr - \frac{2}{r^3}\int_0^r r^2\theta(r,t)dr\right\} + P \tag{22b}$$

$$\sigma_{\varphi\varphi}(r,t) = \frac{-\alpha E}{1-\nu}\left\{\frac{1}{r^3}\int_0^r r^2\theta(r,t)dr + \frac{2}{b^3}\int_0^b r^2\theta(r,t)dr - \theta(r,t)\right\} + P \tag{22c}$$

$$\bar{\sigma} = \frac{-2E\alpha}{1-\nu}\left(\frac{1}{b^3}\int_0^b r^2\theta dr - \frac{1}{3}\theta\right) + P \tag{22d}$$

$$\tau_{max} = \frac{1}{2}\left|\sigma_{rr}(r,t) - \sigma_{\varphi\varphi}(r,t)\right| = \frac{\alpha E}{2(1-\nu)}\left[\frac{3}{r^3}\int_0^r r^2\theta(r,t)dr - \theta(r,t)\right] \tag{22e}$$

At the boundary, i.e. at *r*=*b*, we therefore have

$$u(b,t) = -\frac{3\alpha}{b^2}\int_0^b r^2\theta(r,t)dr + b(1-2\nu)\frac{P}{E} \tag{23a}$$

$$\varepsilon_r(b,t) = -\frac{3\alpha}{b^3}\int_0^b r^2\theta(r,t)dr + (1-2\nu)\frac{P}{E} \tag{23b}$$

$$\sigma_{rr}(b,t) = P \tag{23c}$$

$$\sigma_{\varphi\varphi}(b,t) = \frac{-\alpha E}{1-\nu}\left\{\frac{3}{b^3}\int_0^b r^2\theta(r,t)dr - \theta(r,t)\right\} + P \tag{23d}$$

If we now insert the local stress state (equation 22d) into diffusion equations 6 and 14, corresponding to Type A and B diffusion respectively, the following relations emerge:

For Type A diffusion (jump controlled diffusion): Model A

$$\frac{\partial\theta}{\partial t} = \frac{D}{r^2}\frac{\partial}{\partial r}\left\{r^2\left[\left(\frac{\frac{2}{9}EV_0^2C_s\rho}{1-\nu}\frac{\theta(1-\theta)}{RT}+1\right)\frac{\partial\theta}{\partial r}\right]\right\} \tag{24a}$$

If the partial molar volume of adsorbed molecules is negligible, i.e. $V_0 \approx 0$, this reduces to

$$\frac{\partial\theta}{\partial t} = \frac{D}{r^2}\frac{\partial}{\partial r}\left(r^2\frac{\partial\theta}{\partial r}\right) \tag{24b}$$

For Type B diffusion (path controlled diffusion): Model B

$$\frac{\partial\theta}{\partial t} = \frac{DC_{d_0}}{C_s\rho K^0}\frac{1}{r^2}\frac{\partial}{\partial r}\left\{r^2\left[\exp\left(\frac{\left[\frac{-2C_SV_0\rho E}{3(1-\nu)}\left(\frac{1}{b^3}\int_0^b r^2\theta dr-\frac{\theta}{3}\right)+P-P_0\right]V_0}{RT}\right)\left(\frac{\frac{2}{9}EV_0^2C_s\rho}{1-\nu}\frac{\theta}{(1-\theta)RT}+\frac{1}{(1-\theta)^2}\right)\frac{\partial\theta}{\partial r}\right]\right\} \tag{25a}$$

For simplicity, this can be reduced to

$$\frac{\partial\theta}{\partial t} = \frac{DC_{d_0}}{C_s\rho K^0}\frac{1}{r^2}\frac{\partial}{\partial r}\left\{r^2\left[exp\left(\frac{(P-P_0)V_0}{RT}\right)\left(\frac{\frac{2}{9}EV_0^2C_s\rho}{1-\nu}\frac{\theta}{(1-\theta)RT}+\frac{1}{(1-\theta)^2}\right)\frac{\partial\theta}{\partial r}\right]\right\} \tag{25b}$$

as the term $(\frac{1}{b^3}\int_0^b r^2\theta dr - \frac{\theta}{3})$ is a second-order correction term in case θ is not homogeneous in space, and vanishes quickly after a change in external pressure. In addition, if the partial molar volume of the adsorbed molecules is very small (i.e. $V_0 \approx 0$), equation 25b reduces to

$$\frac{\partial\theta}{\partial t} = \frac{DC_{d_0}}{C_s\rho K^0}\frac{1}{r^2}\frac{\partial}{\partial r}\left[r^2\left(\frac{1}{(1-\theta)^2}\frac{\partial\theta}{\partial r}\right)\right] \tag{25c}$$

Note that in both of the above models (equations 24a and 25b), the magnitude of the effect of swelling and internal stress evolution on diffusion depends on the term $\frac{\frac{2}{9}EV_0^2C_s\rho}{1-\nu}$.

Particle swelling as a function of time and imposed external gas pressure is of course given by equations 23a and b, with $\theta(r,t)$ being given by integrating equations 24a and 25b.

4.3. Swelling experiments on coal exposed to CH_4

To test the applicability of the above models, we performed axial swelling experiments on a single cylindrical sample of medium volatile bituminous coal, exposed to CH_4 at cycled gas pressures up to 40 MPa, and at a constant temperature of 40˚C, using 1D high pressure eddy-current dilatometry (Hol and Spiers, 2012). In these experiments, compressive stresses and gas pressure were measured positive, as were swelling strains.

4.3.1. Sample material and preparation

The coal used in this study was obtained from Pingmei Shenma Mine No.8 near Pingdingshan City in Henan Province, China. Petrographic and chemical analyses were performed on powdered samples of this material (grain size 170-250 μm), at the China University of Geosciences in Beijing (Table 1). These showed that Pingdingshan coal has a vitrinite reflectance of 1.31±0.06%, and contains 80.32% carbon, 1.52% nitrogen, 0.37% sulphur, and 3.94% oxygen.

To prepare the cylindrical sample, we drilled a core, with a diameter of 4 mm and length of ~ 6 mm, parallel to bedding and normal to the butt cleat plane, using a water-cooled pillar drill. The ends of the core were ground flat and parallel to produce final dimensions of ~ 4 mm diameter and ~4 mm length. The sample was then inspected using an optical microscope to exclude the presence of cleats and damage. The cylinder axis was defined as the *x*-direction of the sample. The *y*-direction was defined as lying parallel to the intersection of the bedding and butt cleat planes, while the *z*-direction was taken as normal to bedding (see Fig.4). Prior to experimentation, the sample was dried in

an oven at 50˚C for several days. The pre-test length and diameter of the sample were then measured, using a digital calliper (with a resolution of 0.01 mm), and its mass was measured using a METTLER TOLEDO MS205DU Semi-Micro Analytical Balance (resolution 0.01 mg). Averaged values of mass and dimensions obtained from multiple measurements are listed in Table 2. The sample length given in this table was taken as the starting dimension used for all subsequent calculations of strain in the axial (x) direction.

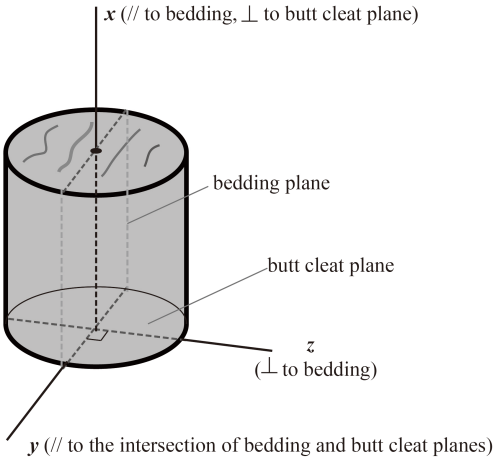

Fig.4. Schematic illustration of the present coal matrix sample geometry.

Table 1. Organic petrology, proximate analysis and ultimate analysis performed on a 170-250 μm grain size fraction of the Pingdingshan medium volatile bituminous coal used as sample material in the present study. The analyses were performed at the China University of Geosciences, Beijing.

Coal rank	**Medium volatile bituminous**	
Organic Petrology	Vitrinite Reflectance Rx %	1.31
	Vitrinite %	90.43
Proximate Analysis	Moisture %	0.7
	Volatile Matter %, dry	20.65
	Ash contant %, dry	12.61
	Fixed Carbon %	66.05
Ultimate Analysis	Carbon %	80.32

	Nitrogen %	1.52
	Sulfur %	0.37
	Oxygen %	3.94

Table 2. Starting mass and dimensions of the cylindrical Pingdingshan coal matrix sample used in this study. The length L_0 serves as the starting dimension for all axial swelling strain determinations.

	Initial sample mass(g)	**Initial sample length L_{0x}(mm)**	**Initial sample diameter L_{0y}=L_{0z}(mm)**	**Density ρ (kg/m^3)**
4-3	0.06792	3.76	4.01	1431.04

4.3.2. Experimental methods

We measured the dimensional change of the sample in the *x* direction using a high-pressure dilatometer system, described in detail by Hol and Spiers (2012). This consists of a mm-scale sample holder plus high-pressure eddy-current displacement sensor, housed in a 100MPa stainless steel pressure vessel. Axial expansion or contraction of the sample, caused by adsorption or desorption of gases introduced into the pressure vessel at high pressure, is transmitted to a Remanit stainless steel target, the motion of which is measured from changes in the eddy current field induced in the target by the eddy current sensor. This allows sample expansion and contraction to be measured with a resolution better than 50 nm. The eddy current sensor yields a linear sensitivity of 19.96 mV/μm over a displacement range of 120 μm, which is equivalent to an axial strain of ~2.5% for a 4mm long sample.

In the present experiments, CH_4 was injected into the pressure vessel at pressure up to 40MPa. Two methods were used to generate the pressure. For pressures up to ~ 9 MPa, CH_4 was introduced into the system directly from a CH_4 cylinder through a manually controlled regulator. This allowed stepwise increases in CH_4 pressure up to ~ 9 MPa (cylinder pressure) with an accuracy of ±0.01 MPa. To generate higher CH_4 pressures, an ISCO volumetric (syringe) pump was used in controlled pressure mode, allowing pressure control within ±0.02 MPa. To maintain a constant temperature in and around

the sample of 40˚C (±0.05˚C), the entire pressure vessel plus internal dilatometer system and sample were placed in a temperature-controlled water bath. The whole setup, including water bath, the ISCO volumetric pump and the high pressure tubing system, were housed in a heated foam-polystyrene box, maintained at an internal temperature of 38.6±0.2˚C using a construction lamp and CAL 9900 PID temperature controller.

After loading the sample studied into the dilatometer and pressure vessel, the system was evacuated by connecting it to a vacuum pump to remove residual gas and water from the sample and apparatus. This took about 5 hours (time to obtain a constant/stable eddy current sensor signal). CH_4 was then introduced into the system. The CH_4 pressure was then increased stepwise up to 40 MPa. After each pressure step, the sample expanded, in a time-dependent manner, to approach a new equilibrium state. After the equilibration at 40 MPa, the CH_4 pressure was decreased in a stepwise manner, and the vessel/sample finally re-evacuated. We assumed that equilibrium was reached or approached when no further change in eddy current sensor signal was recorded for around two hours, i.e. when a constant sample strain was reached. We performed two pressurisation and depressurisation cycles on the single sample investigated, continuously recording the axial dimensional changes of the sample during these pressure cycles. In each cycle, the axial swelling strain (%) of the sample versus time was calculated using the expression $e_x(t) = \frac{V_{t=0} - V(t)}{SL_{0x}}$, where $V_{t=0}$ represents the output voltage (mV) of the eddy current sensor at the start of the cycle, i.e. in the evacuated state at t=0. $V(t)$ represents the sensor output at time t. S represents the sensitivity of the eddy current sensor, and L_{0x} is the starting axial dimension (length) of the sample specified in Table 2.

4.3.3. Experimental results

The axial swelling strain versus time data obtained during the two CH_4 pressure cycles employed in the present experiments are shown in Fig.5. Upon applying each gas

pressure step, an instant compaction or expansion was observed, reflecting the elastic response of the sample to the change in hydrostatic pressure. The sample then slowly expanded or contracted. Equilibration after each pressure step took 3-70 hours. The swelling strain data attained at (apparent) equilibration are plotted in Fig. 6 as a function of CH_4 pressure. During the first pressurisation cycle, the (apparent) axial swelling strain continuously increased with increasing pressure, attaining a maximum swelling strain of 0.435% at 40 MPa CH_4 pressure. This swelling was partly irreversible, with the contraction data obtained upon depressurisation showing miner hysteresis, as well as 0.014% permanent swelling, which corresponds to 3.2% of the maximum swelling strain. By contrast, the swelling that occurred in the second pressure cycle was closely reversible. In this case the maximum swelling strain measured was 0.395% at 40 MPa CH_4 pressure, so ~10% less than the value obtained in the first pressure cycle.

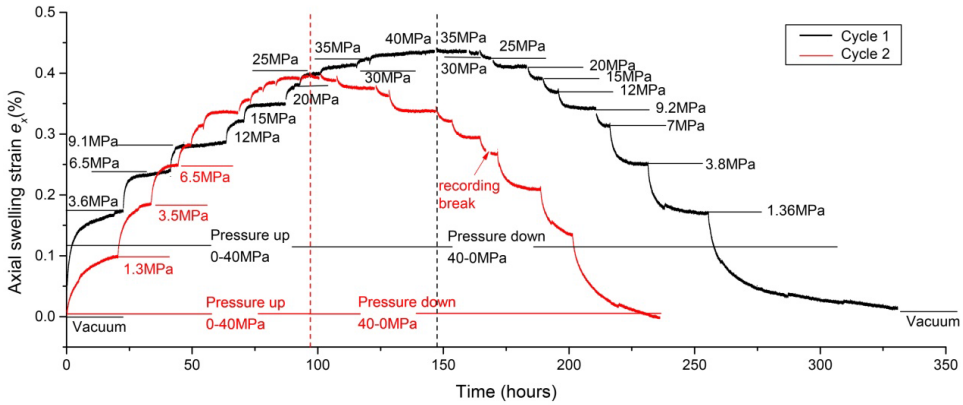

Fig.5. Axial swelling strain versus time for the two pressure cycles applied to the coal matrix sample investigated in this study.

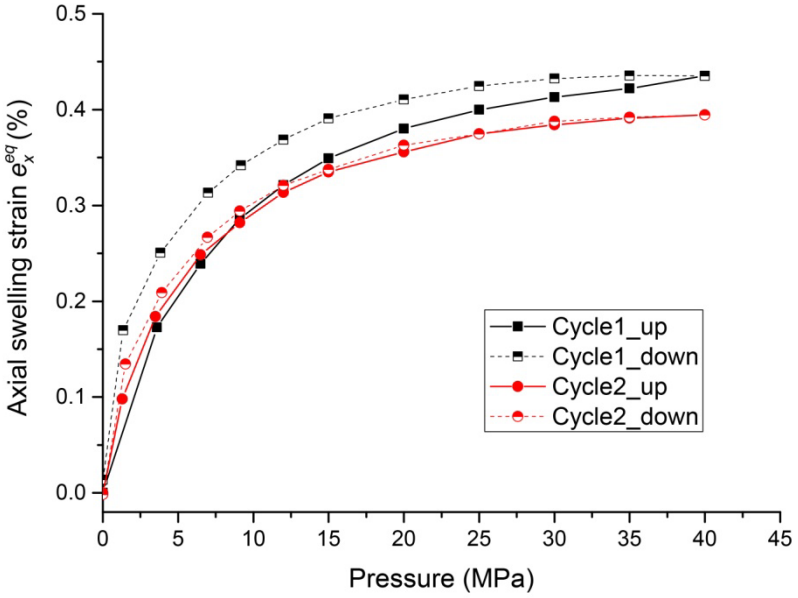

Fig.6. Equilibrium axial swelling strains versus CH_4 pressure for the two pressure cycles applied to the coal matrix cylinder investigated in this study.

4.4. Model fits

We now compare our models for swelling of a spherical coal sample with our experimental data for the 4mm coal matrix cylinder subjected to CH_4 pressure cycling. Our aim is to determine which model (Type A vs. Type B diffusion) can describe the experimental data best. To achieve this, the numerical solutions for the diffusion and particle swelling equations presented in Section 4.2.3 (i.e. equations 23, 24a and 25b) must be obtained, using reasonable parameter values and adjusting D to obtain the best fit between model and experiments.

4.4.1. Choice of fixed parameter values

To fit our models to the time-dependent experimental data obtained on swelling strain, we need input parameter values for the elastic constants E, ν, the partial molar volume of the adsorbed molecules V_0, the adsorbed occupancy at outer boundary $\theta^{eq}(P)$, the

adsorption sites density C_s and the equilibrium constant K^0. The following paragraphs describe how we obtained values for these parameters (see Table 3).

Espinoza et al. (2014) measured Poisson's ratio ν for a bituminous cylindrical coal sample (25 mm in diameter, 50 mm in length), obtaining 0.267 in radial direction and 0.198 in axial direction. For simplicity, we took the average value of 0.233 as the Poisson's ratio of our sample for the present calculations. Hol and Spiers (2012) measured the bulk modulus K_s of bituminous coal matrix cylinders (4 mm in diameter, ~4 mm in length) using Helium, obtaining 7.413-7.746 GPa. We took the average value of 7.65 GPa as the bulk modulus of our sample. Using these values of ν and K_s, the Young's modulus E was calculated using $E = 3K_s(1 - 2\nu)$, yielding E = 12.3 GPa.

To obtain values for the parameters C_s, K^0 and V_0, we consider the relations for equilibrium sorbed concentration or occupancy $\theta^{eq}(P)$, and for the associated swelling strain e_{ads}^{eq}, given by Liu et al (Chapter 3) under the present experimental conditions (i.e. $\sigma = P$). These can be written as

$$\theta^{eq} = \frac{a_g K^0 \exp\left(\frac{-(P-P_0)V_0}{RT}\right)}{1+a_g K^0 \exp\left(\frac{-(P-P_0)V_0}{RT}\right)} \quad (26a)$$

$$e_{ads}^{eq} = V_0 C_s \rho \frac{a_g K^0 \exp\left(\frac{-(P-P_0)V_0}{RT}\right)}{1+a_g K^0 \exp\left(\frac{-(P-P_0)V_0}{RT}\right)} \quad (26b)$$

where a_g is activity of CH_4 at pressure P and at 40˚C. Now, the sorption-induced volumetric swelling strain (e_{ads}^{eq}) of a cleat-free coal matrix sample can be calculated from the measured swelling strain (e_v) by correcting for the elastic deformation using the expression $e_{ads}^{eq} = e_v + {}^{P}/_{K_s}$ (c.f. Hol and Spiers, 2012). Using our experimental data for the swelling strain of our coal matrix sample measured in the x direction (see Fig.6 and Fig.7), and assuming $e_x = e_y$ and $e_z = 1.2e_x$ (Day et al., 2010), we obtain $e_v = 3.2e_x$, and $e_{ads}^{eq} = 3.2e_x + {}^{P}/_{K_s}$. Since the swelling of our sample was partly irreversible in the first CH_4 pressure cycle (see Figs. 5 and 6), but closely reversible in the second pressure cycle (see Figs. 5 and 6), we assumed the

swelling strains obtained in the second pressure cycle represent (reversible) sorption-induced swelling better, and we applied these data to calculate sorption-induced volumetric swelling strains using the above expression. The estimated adsorption-induced volumetric swelling strains are plotted in Fig.7 as a function of pressure. Taking the thermodynamic reference state defined at P=0.1 MPa, we can also obtain the CH_4 activity (a_g) at the experimentally imposed pressures and at 40˚C using the EOS for CH_4 (Setzmann and Wagner, 1991). A non-linear regression method was then used to fit equation 26b to the estimated data of $e_{ads}^{eq}(a_g, P)$ obtained for the second CH_4 pressure cycle. The best fit (R^2=0.998) gave $C_s = 1.5\ \mathrm{mol/kg_{coal}}$; $K^0 = 0.01$; $V_0 = 11.4 \times 10^{-6}\ \mathrm{mol/m^3}$ (see Fig. 7). These parameter values are consistent with the values reported in the literature: reported ranges are from 0.9 to 2.5 mol/kg_{coal} for C_s; from 0.02 to 0.05 for K^0; from 8 to 20 × 10^{-6} m^3/mol for V_0 (Cui et al., 2007; Dutta et al., 2011; Gensterblum et al., 2013; Laxminarayana and Crosdale, 1999; Levine, 1996; Merkel et al., 2015; Pan and Connell, 2007; Pini et al., 2010). Note that the literature values for C_s and K^0 are obtained from fitting the Langmuir relationship without considering stress effects on sorption, and can therefore not be directly compared with our values (see details in Chapter 3).

Table 3. Summary of parameter values applied in the present model.

Parameter	K^0	C_s (mol/kg_{coal})	E(GPa)	ν	V_0 (m^3/mol)
Values used in this study	0.01	1.5	12.3	0.233	11.4×10^{-6}

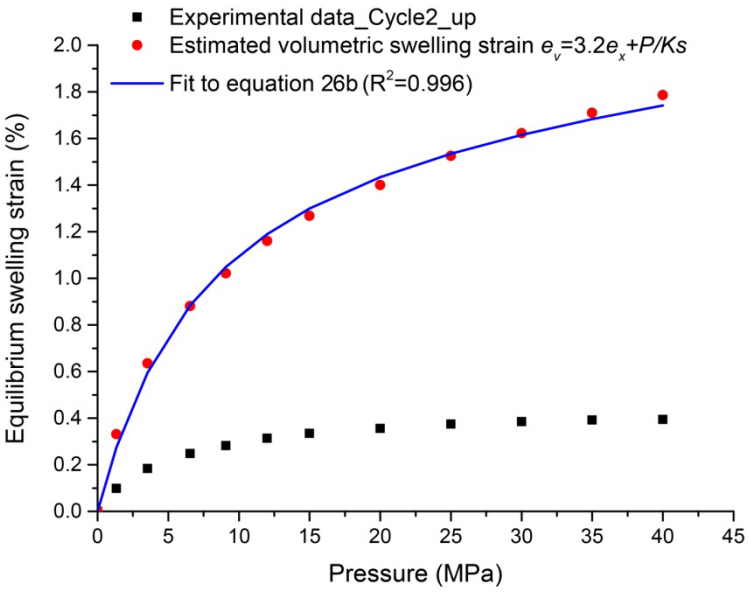

Fig.7. Swelling strain versus CH_4 pressure data for the present cylindrical coal sample, as determined for the second CH_4 pressure cycle. The solid square points represent swelling strains measured in the x direction in the second CH_4 pressure cycle. The solid red points represent the sorption-induced volumetric swelling strain estimated using $e_{ads}^{eq} = 3.2e_x + {}^{P}/_{K_s}$ *. The blue line represents the best fit of equation 26b to the estimated volumetric strain data. The resulting fitting parameter values are summarized in Table 3.*

4.4.2. Model results

To obtain solutions for the non-linear diffusion equations (see 24a and 25b), we use pdepe, a Matlab function that solves initial-boundary value problems for systems of parabolic and elliptic partial differential equations (PDEs) in one space variable *r* and time *t*. The ordinary differential equations (ODEs) resulting from discretization in space are integrated to obtain approximate solutions at specified times. The function returns values of the solution on a predefined mesh. We applied equation 23b by integrating the pdepe output field over the spatial dimension in order to obtain the sample strain response for comparison with the experimental data. Naming the concentration at time

t_i and location r_j as $c_{ij} = \alpha \cdot \theta(t_i, r_j)$, we obtain the simulated radial strain as a numerical implementation of Eq. 23b:

$$\varepsilon_{\mathrm{rr}}^{\mathrm{sim}}(t_i) = -\frac{1}{V}\sum_j c_{ij} \cdot 4\pi r_j^2 \delta r_j + (1-2\nu)\frac{P}{E} \quad (27)$$

In order to solve the diffusion equations, boundary conditions must be applied. We employed an equilibrium occupancy at the boundary, assuming that this level of occupancy is achieved immediately after applying a new external hydrostatic pressure, i.e. $\theta_{r=b} = \theta^{eq}(P)$. The value of the equilibrium occupancy follows from the thermodynamic relation of equation 26a.

The best fits of the models (A and B) to the experimental data that were obtained using the parameter values in Table 3, by adjusting the diffusion coefficients embodied in each model, are plotted in Fig. 8. The results illustrate that the experimental data are very well explained by Model B (Path controlled diffusion) using a single diffusion coefficient over all CH_4 pressures, particularly the data obtained in the second cycle from which the various fixed parameters were calculated. By contrast, Model A provides a much poorer fit to the experimental data, which is unsatisfactory. This suggests that swelling of Pingdingshan medium volatile bituminous coal upon adsorption of CH_4 is controlled by diffusion of unadsorbed molecules. The best fit of Model B to the experimental data gave a value for DC_{d0} of 1.54×10^{-10} m^2/s for the first CH_4 pressure cycle and of 2.04×10^{-10} m^2/s for the second, respectively. In this case, we cannot obtain the random walk diffusion coefficient D for unadsorbed molecules independently of C_{d0}, as this reference concentration C_{d0} is unknown, though it is a constant.

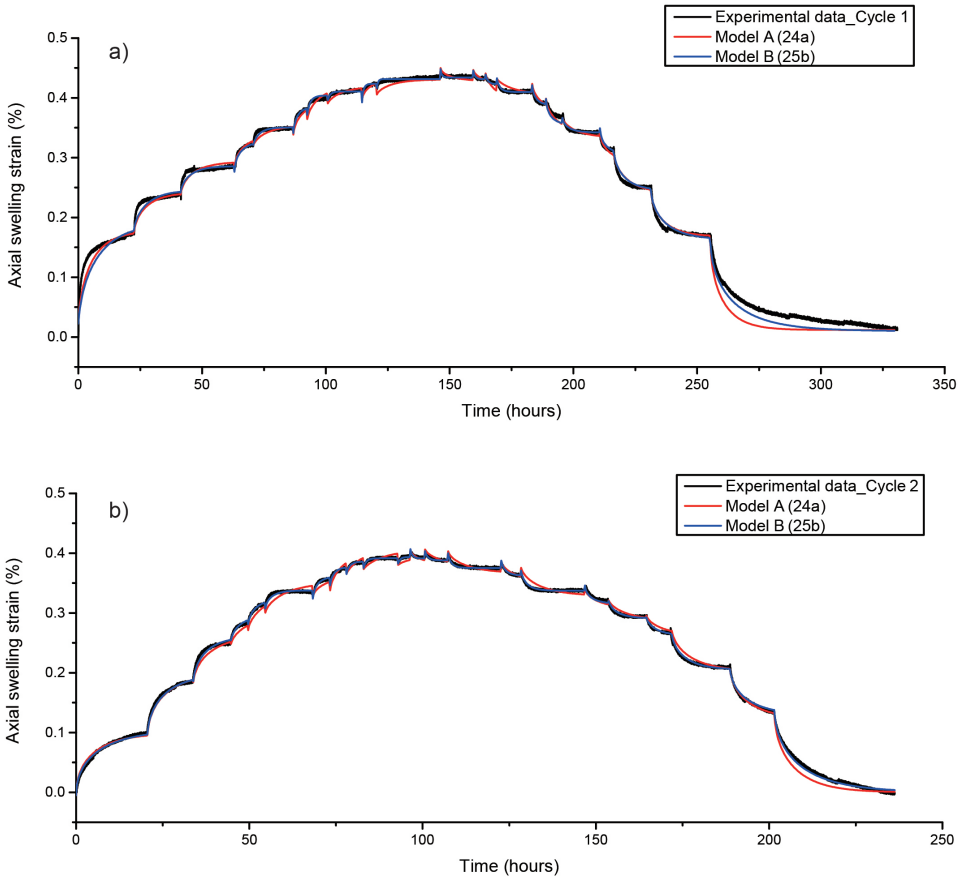

Fig.8. Axial swelling strain (%) versus time (hours) plotted a) for the first CH_4 pressure cycle, and b) for the second CH_4 pressure cycle. The black lines represent the experimental data; The red lines represent the best fit of Model A (24a, 27) to the experimental data using a constant D, while the blue lines represent the best fit of Model B (25b, 27) to the experimental data using a constant D. Note that the fit of Model B (path-controlled diffusion) is almost perfect for Cycle 2 from which the fixed (non-fitting) parameters were derived.

4.5. Discussion

We have developed two models for time-dependent swelling of a spherical sample/particle of coal matrix material upon adsorption of a single gas, considering the

coupled effects of swelling, internal stress evolution and diffusion. Model A assumed that the adsorbed molecules were transported inside the coal matrix at a rate controlled by jumps between potential wells associated with closely spaced adsorption sites (Type A diffusion). Model B assumed that the adsorbed molecules were transported at a rate controlled by diffusion of unadsorbed molecules between more distant adsorption sites (Type B diffusion). Experimental tests were performed on a single 4mm sized cylindrical coal matrix cylinder to measure the time-dependent swelling upon adsorption of CH_4. Comparison of the model results with the experimental data illustrates that Model B successfully described time-dependent swelling of Pingdingshan medium volatile bituminous coal upon adsorption of CH_4 at 40˚C.

In the following, we will further discuss the mechanisms of diffusion occurring inside the present coal matrix material and the influence of stress-strain-sorption effects on diffusion. We then attempt to explain the differences in swelling behaviour of the coal matrix sample that we measured between the two CH_4 pressure cycles used in our experiments. Finally, we compare our studies with the previous work and we consider the likely implications for ECBM.

4.5.1. Mechanisms for diffusion occurring inside the coal matrix material

Our experimental data are well described by our Model B using a single diffusion coefficient over all CH_4 pressure ranges, but not by our Model A. In addition, the fact that the calculated diffusion product $DC_{d0} = 2.04 \times 10^{-10}\ \mathrm{m^2 \cdot s^{-1}}$, obtained using Model B, is independent of CH_4 pressure and adsorbed concentration is internally consistent with its assumption that D is the diffusion coefficient for random walk of unadsorbed CH_4 molecules through the coal structure. This is important as such a diffusion coefficient should indeed depend solely on the molecular structure of coal. Furthermore, the better performance of Model B suggests that the adsorption sites for CH_4 in the present coal sample are distant from each other. This is also supported by the parameter value C_s=1.5 mol/kg_{coal} for CH_4, which corresponds to 1.5 moles of

adsorption sites homogenously distributed over one kilogram coal material (i.e. ~ 100 moles of carbon atoms). This implies that adsorbed molecules cannot be transported from adsorption site to adsorption site by direct jumps. In line with the assumptions and equations defining Model B, our findings accordingly suggest that a) the dynamic or transient swelling response of Pingdingshan medium volatile bituminous coal upon adsorption of CH_4 is dominated by diffusion of unadsorbed molecules, b) the driving force for diffusion is the gradient in the potential of adsorbed molecules, which is influenced by swelling of the coal matrix and the associated internal stress evolution, c) the effect of swelling and internal stress evolution on diffusion depends quadratically on the magnitude of the partial molar volume of the adsorbed molecules V_0 (refer equation 25b), and d) net sorption and sorption-induced swelling rates depend on both the diffusion coefficient D and on the adsorbed occupancy θ (equations 23b and 25b).

4.5.1.1. Role of distribution of adsorption sites

Our model results suggest that the distribution of adsorption sites plays an important role in the diffusion process of adsorbed molecules inside the coal matrix. If adsorption sites are sufficiently closely spaced, the molecules can be transported between adsorption sites by jumps, and swelling kinetics and diffusion will be described by Model A. If the adsorption sites are relatively distant, the adsorbed molecules are transported between adsorption sites by diffusion of unadsorbed molecules in the diffusion paths as the rate controlling step, and the swelling kinetics and diffusion can be described by Model B. This implies that the parameter C_s gives an indication regarding the likely mechanism of diffusion, assuming a homogeneous distribution of adsorption sites over the whole coal matrix material. Consequently, the swelling kinetics of coal upon adsorption of other gas species, such as CO_2, N_2, which generally have C_s in the range of 0.7-3 mol/kg_{coal}, i.e. 0.5-2 times C_s for CH_4 (e.g. Battistutta et al., 2010; Gensterblum et al., 2014; Gensterblum et al., 2013), might also be controlled by diffusion of unadsorbed molecules. Only for gas species with much larger adsorption

site densities, i.e. large values of C_s, might diffusion be controlled by the jump rate of adsorbed molecules as described by Model A. However, coal is a naturally heterogeneous material, and the distribution of adsorption sites for gas species cannot be expected to be homogeneous. Some adsorption sites for a gas species might therefore be localized, allowing diffusion to be controlled by jumps of adsorbed molecules, and others might be distant, forcing diffusion to be controlled by diffusion of unadsorbed molecules.

4.5.1.2. Role of swelling and internal stress evolution in determining the driving force for diffusion

Our models (see equations 22, 23, 24a, 25b) incorporate the effects of internal stress-strain evolution upon swelling and on the driving force for the diffusion processes. The magnitude of this latter effect on diffusion depends on ratio between the two terms in the right-hand-side of equations 24a and 25b: $\frac{\frac{2}{9}EV_0^2C_s\rho}{1-\nu}\frac{\theta(1-\theta)}{RT}$. Fig.9a plots this expression versus adsorbed occupancy θ at equilibrium for the parameter values used above (see Table 3). It is seen from Fig.9a that the effect of swelling on the driving force is small for our value of $V_0 = 11.4 \times 10^{-6}$ mol/m^3, with a maximum at $\theta = 0.5$. Fig. 9c shows best fits of equations 25b and 25c (Model B) to the experimental data for the second CH_4 pressure cycle – maintaining, however, the magnitude of the swelling effect. The results suggest that the effect of swelling on diffusion of CH_4 in the Pingdingshan medium volatile bituminous coal matrix is negligible. Because, however, the magnitude of the term $\frac{\frac{2}{9}EV_0^2C_s\rho}{1-\nu}\frac{\theta(1-\theta)}{RT}$ is proportional to V_0^2 (Fig. 9b), the higher V_0, the bigger the effect of swelling on diffusion: for gas species that have a larger partial molar volume of adsorbed molecules than CH_4 (e.g. >2 times the present V_0), the swelling effect may play a significant role in diffusion process.

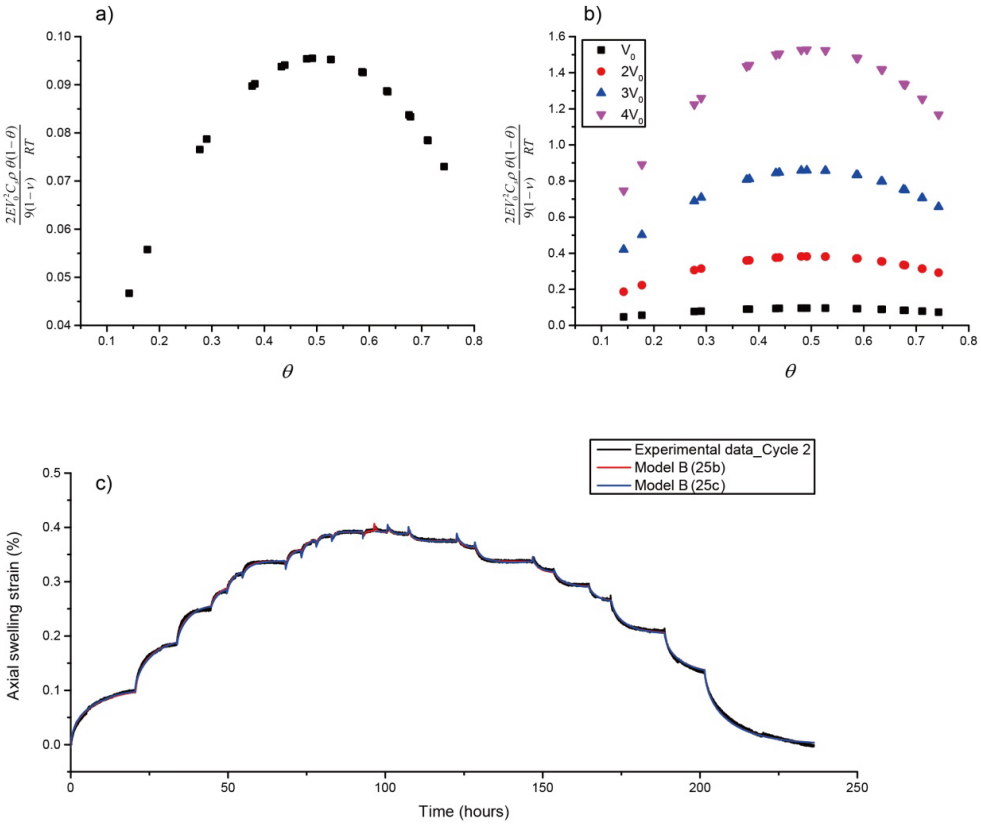

Fig.9. Effects of swelling and internal stress evolution on diffusion. a) Plot of the quantity $\frac{2}{9}\frac{EV_0^2C_s\rho}{1-\nu}\frac{\theta(1-\theta)}{RT}$ *versus* θ *at equilibrium, obtained using the parameter values employed in the present study. b) Plot of* $\frac{2}{9}\frac{EV_0^2C_s\rho}{1-\nu}\frac{\theta(1-\theta)}{RT}$ *versus* θ *for varying* V_0*. c) Axial swelling strain versus time comparing best fits of equations 25b and 25c to the experimental data for the second* CH_4 *pressure cycle conducted in the present experiments. This experimental cycle showed closely reversible sorption-induced swelling behaviour of the sample And was used to derive the non-fitting parameters used in Model B.*

4.5.1.3. Effect of internal stress evolution on changes in transport paths

We have formulated our models for a continuum, specifically for an isotropic, elastic coal specimen with spherical symmetry. The evolution of internal stresses upon diffusion

was formulated in equations 22. Plots showing the typical evolution of internal stress field, as calculated using Model B, are illustrated in Fig.10. Large tensile stresses (> 30 MPa) and shear stresses (> 25 MPa) were calculated. This suggests that tensile micro fractures might be formed during diffusion (Zhao et al., 2016). As a result, the real internal stresses might be lower than the calculated internal stresses. Moreover, the formation of micro-fractures during first exposure to CH_4 may have caused changes of transport paths for diffusion of unadsorbed molecules as well as permanent deformation of the sample. This would explain the permanent deformation we observed after the first CH_4 pressure cycle, and the mismatch of our Model B with the swelling data in the first pressure cycle. The second cycle shows reversible behaviour. Indeed, reversible deformation upon the real internal stress evolution (i.e. lower than calculated stress) after the formation of micro-fractures may also be possible (Hol et al., 2012b), explaining a) the closely reversible swelling of the sample observed during the second CH_4 pressure cycle, and b) the good fit of our Model B to the experimental data for Cycle 2.

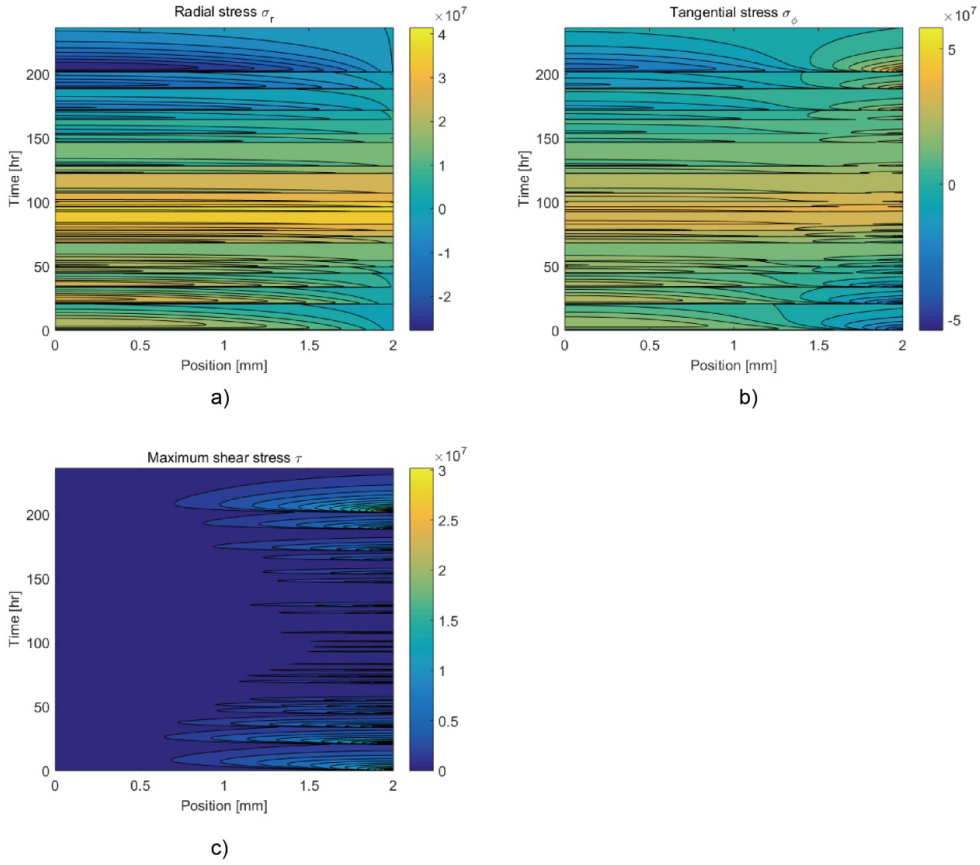

Fig.10. Typical evolution of internal stress field caused by swelling/shrinkage occurring during diffusion into the spherical coal matrix particle modelled in this study. a) Total radial stress calculated using equation 22b; b) Total tangential stress calculated using equation 22c; c) Maximum shear stress calculated using equation 22e.

4.5.1.4. Role of adsorbed concentration in determining swelling rates

In addition to the effect of swelling and the internal stress evolution on diffusion (which we have shown above is negligible for the sample used in the study), Model B (see equations 23 and 25c) demonstrates that particle/sample swelling rate depends not only on the random walk diffusion coefficient D for unadsorbed molecules, but also strongly on the adsorbed concentration θ via the term $1/(1-\theta)^2$. In this case, swelling rates increase with the increasing θ at a given D. By contrast, if the transport

of adsorbed molecules is dominated by direct jumps between adsorption sites (Type A diffusion), as described by Model A using equation 24b (assuming the effects of swelling and internal stress evolution on diffusion are negligible), then the swelling rates depend on the random walk diffusion coefficient *D* for adsorbed molecules only. In the context of our models, this means that the adsorbed concentration θ plays no role in swelling kinetics, except when the effect of swelling and the associated internal stress evolution on diffusion cannot be neglected.

4.5.2. Swelling data for CH_4 pressure cycles 1 vs. 2

Our experimental results showed an irreversible swelling and shrinkage effect during the first CH_4 pressure cycle, but not during the second cycle. This irreversible swelling might be caused by the formation of micro-fractures during the diffusion process (Hol et al., 2012b). This possibility is supported by the evolution of internal stresses calculated using our Model B as discussed in Section 4.5.1.3.

Our experimental results also show that the net linear swelling strains of the sample that we measured during the first cycle were larger than those measured during the second cycle. Recalling that the net linear swelling strains that we measured involved both elastic deformation upon changes in gas pressures and sorption-induced swelling, we propose the following possible causes:

1) Lower equilibrium swelling strains were attained in Cycle 2. This would be in accordance with the fact that the total time elapsed for Cycle 1 was longer than that elapsed for Cycle 2, but the diffusion coefficients calculated for both cycles were similar. This might reflect equilibration in Cycle 1 throughout the sample, and so on the full sample length scale, but with CH_4 molecules not penetrating the sample homogeneously. This would also fit with the notion of heterogeneous swelling producing microcrack damage and causing the observed hysteresis and permanent swelling seen in Cycle 1.

2) The elastic modulus of the sample was reduced upon the formation of micro-fractures during Cycle 1. Indeed, during Cycle 2, clearer and bigger instant elastic

responses than in Cylce 1 were observed (Fig.5).

3) Extensional creep occurred during Cycle 1 due to cumulative microcracking. For the first pressure steps of Cycle 1(6.5 MPa and 9.1 MPa), Fig.5 shows that the sample expanded to an apparent equilibrium swelling strain, and then continued to swell with time in a near linear manner. This behaviour might be related to the slow evolution of internal stress state and associated formation of micro-fractures. If extensional creep by this mechanism would result in permanent swelling, as observed in Cycle 1, it would not be expected to repeat itself during Cycle 2. However, the observed permanent deformation could also be caused by a residual amount of adsorbed CH_4 remaining in the sample after Cycle 1. This is potentially supported by the small shrinkage observed at the end of Cycle 2.

Based on our experiments, we cannot discriminate between these explanations; the only remark we wish to make is that it is probably related to microcracking associated with the large stresses.

4.5.3. Comparison with previous work

The similarities and differences between our findings and previous work can be summarized pointwise as follows:

1. Our Model B successfully describe the swelling kinetics of coal matrix material upon adsorption of CH_4 at CH_4 pressures varied in the range zero to 40 MPa, using a single, random walk diffusion coefficient describing diffusion of unadsorbed molecules as the rate limiting process. However, our Model B demonstrates that the swelling kinetics also strongly depend on adsorbed concentration. This finding is consistent with reports in the literature that diffusion coefficients calculated using the widely accepted unipore and bidisperse models strongly depend on adsorbed concentration (e.g. Busch et al., 2004; Clarkson and Bustin, 1999; Cui et al., 2004; Shi and Durucan, 2003).

2. Our models (A and B) consider diffusion occurring inside a single coal matrix particle, containing uniform nanopores only. The agreement obtained between Model B

and the experimental results suggests that a) samples of medium bituminous coal matrix material, as used in this study, can be treated as containing uniform nanopores only, at least on the ~ 4 mm length scale, and that b) the swelling kinetics of coal matrix material of medium bituminous rank are dominated by diffusion of unadsorbed molecules in nanopores. This differs from many studies in which diffusion is believed to occur through a bimodal or bidisperse pore network (e.g. Busch et al., 2004; Cui et al., 2004; Shi and Durucan, 2003). For bigger coal samples (> 4 mm) or for other coals, a bidisperse pore structure model might better represent the heterogeneous properties of coal (Busch and Gensterblum, 2011; Clarkson and Bustin, 1999; Cui et al., 2004; Shi and Durucan, 2003). In such cases, more complicated mechanisms for the diffusion processes in coal need to be considered.

3. While our results imply that the swelling kinetics of mm scale coal matrix samples, upon adsorption of CH_4, are controlled by diffusion of unadsorbed molecules through a uniform nanopore network inside the coal matrix, the observed swelling is caused by the absorbed molecules. This may point to the storage of unadsorbed molecules in nanopores being negligible. This would mean that only a few unadsorbed molecules exist in the nanopores, interacting with the molecular structure of the coal and not with each other, and that therefore they do not behave as a gas phase. Under these assumptions, we cannot quantify the diffusion coefficient D using our Model B, as the reference concentration of adsorbed molecules C_{d0} is unknown. In the literature, however, coal matrix is generally represented by a bidisperse pore structure model (Busch and Gensterblum, 2011; Clarkson and Bustin, 1999; Cui et al., 2004; Shi and Durucan, 2003). This model assumes gas diffuses into the coal matrix in the gas phase. Numerical solutions yield diffusion coefficients for methane in the range of 10^{-12}-10^{-15} m^2/s (c.f. Busch and Gensterblum, 2011). If in our models we assume that the unadsorbed molecules in the coal behave as gas phase, and using the molar density of CH_4 at P_0=0.1 MPa as the value of C_{d_0}, we arrive at a diffusion coefficient D=5.3×10^{-12}

m^2/s, which is consistent with the previous studies. However, we wish to stress that the real state of unadsorbed molecules diffusing in nanopores and how their state is influenced by pore dimensions remain unknown. To clarify these, an advanced spectroscopy technique or molecular dynamic methods is needed.

4.5.4. Likely implications for ECBM

The likely implications of our findings for ECBM are as follows:

1. Our findings suggest that for most coal ranks, the swelling kinetics of coal matrix upon adsorption of CH_4 are dominated by diffusion of unadsorbed molecules. The same is likely true for adsorption of CO_2 and N_2 as the adsorption site density, which determines site spacing, falls in the same range of 0.7-3mol/kg_{coal} for CH_4, CO_2 and N_2 (c.f. Battistutta et al., 2010; Gensterblum et al., 2013; Gensterblum et al., 2014). This suggests that our Model B can be widely applied to predict time-dependent swelling of coal matrix upon adsorption of all of these gases. All parameters in our Model B have clear physical meaning and can be easily obtained from swelling or sorption kinetics experiments. This means our Model B offers an important tool for modelling coal seam permeability evolution with time due to the swelling and shrinkage response of coal matrix during ECBM production.

2. Our Model B demonstrates that swelling kinetics of coal matrix upon adsorption CH_4 and probably also CO_2 and N_2, depend not only on the diffusion coefficient, but also on concentration of the sorbing species, increasing with increasing adsorbed concentration. This suggests that the shrinkage rates of coal matrix upon CBM recovery will decrease with decreasing adsorbed CH_4 concentration, while the swelling rates of coal matrix upon injection of CO_2 will increase with increasing adsorbed concentration of CO_2. This together with the finding that the diffusion coefficient for CO_2 is generally one or two orders higher than that for CH_4 (Busch and Gensterblum, 2011), suggests that swelling rates upon CO_2 injection would be much higher than shrinkage rates upon CBM recovery. This in turn implies that using CO_2 as a technique for the secondary

enhanced CBM recovery is unlikely to be a very successful strategy, in agreement with attempts at CO_2-ECBM (e.g. Fokker and van der Meer, 2004; Fujioka et al., 2010; van Bergen et al., 2006).

3. Our results suggest that for higher rank coal, the effect of swelling and internal stress evolution upon adsorption and diffusion of CH_4, CO_2 and N_2 on driving force for diffusion can be neglected, while for lower rank coals, this effect might need to be considered. This is because the partial molar volume of adsorbed molecules (i.e. V_0) in low rank coal is generally higher (by 1-3 times) than that in high rank coals (c.f. Day et al., 2012; Day et al., 2010; Fry et al., 2009; Hol et al., 2012a; Suuberg et al., 1993), and because the magnitude of the effect of swelling and internal stress development is proportional to V_0^2. In both models the swelling rates for low rank coal might be significantly faster than those for high rank coal due to the swelling effects on driving force.

4.6. Conclusions

We investigated the coupling between swelling kinetics, internal stress evolution and diffusion in coal matrix material during exposure to a single gas, by developing theoretical models and performing experimental tests.

Two models were developed, covering two basic possible mechanisms for transport of gas molecules occurring inside the coal matrix. These correspond to transport of adsorbed molecules being controlled by either jumps between adsorption sites, or by diffusion of unadsorbed molecules through longer diffusion paths inside the coal matrix (Models A and B, respectively).

Experimental tests were performed on a single cylindrical sample of Chinese Pingdingshan medium volatile bituminous coal. We measured temporal development of axial swelling of the coal matrix (4 mm in diameter and ~ 4 mm in length) during exposure to CH_4 at a number of CH_4 pressures up to 40 MPa, and at a constant

temperature of 40˚C, by using 1D high pressure dilatometry. Then, we compared our model predictions with the experimental data. The results show that the observed time-dependent swelling is well explained by Model B. This suggests that time-dependent swelling in this case is controlled not by the jumps of adsorbed gas molecules between adsorption sites, but by the diffusion of unadsorbed molecules. In addition, our model for diffusion of this type shows that the effect of swelling and associated internal stress evolution on diffusion of CH_4 (and probably CO_2 and N_2) in the coal such as those used in this study can be neglected, as the partial molar volume of the adsorbed molecules V_0 is small.

Nonetheless, our models demonstrate that a) the distribution of adsorption sites plays a role in determining the mechanism of diffusion; b) the effect of swelling and the internal stress evolution contributes to the driving force for diffusion processes independently of the gradient in adsorbed concentration, and that the importance of this effect strongly depends on the magnitude of V_0; c) swelling rates of coal matrix material depend not solely on diffusion coefficient, but also on adsorbed concentration.

Since all parameters used in our models have well-defined physical meaning and are easily obtained from sorption and swelling experiments, the models can be applied to any coal rank, and to any gas. Our models therefore offer an important tool for modelling coal matrix stress-strain evolution and hence coal seam/cleat permeability evolution with time, as influenced by adsorption /desorption and diffusion occurring during (E)CBM operations.

Acknowledgements

The China Scholarship Council (CSC) and Total S.A. are gratefully acknowledged for their financial support of first author Jinfeng Liu and of the research project.

References

Battistutta, E., Van Hemert, P., Lutynski, M., Bruining, H., Wolf, K.-H., 2010. Swelling and sorption experiments on methane, nitrogen and carbon dioxide on dry Selar Cornish coal. International Journal of Coal Geology 84, 39-48.

Busch, A., Gensterblum, Y., 2011. CBM and CO_2-ECBM related sorption processes in coal: A review. International Journal of Coal Geology 87, 49-71.

Busch, A., Gensterblum, Y., Krooss, B.M., Littke, R., 2004. Methane and carbon dioxide adsorption-diffusion experiments on coal: upscaling and modeling. International Journal of Coal Geology 60, 151-168.

Clarkson, C., Bustin, R., 1999. The effect of pore structure and gas pressure upon the transport properties of coal: a laboratory and modeling study. 2. Adsorption rate modeling. Fuel 78, 1345-1362.

Cui, X., Bustin, R.M., Chikatamarla, L., 2007. Adsorption-induced coal swelling and stress: Implications for methane production and acid gas sequestration into coal seams. Journal of Geophysical Research: Solid Earth 112.

Cui, X., Bustin, R.M., Dipple, G., 2004. Selective transport of CO_2, CH_4, and N_2 in coals: insights from modeling of experimental gas adsorption data. Fuel 83, 293-303.

Day, S., Fry, R., Sakurovs, R., Weir, S., 2010. Swelling of coals by supercritical gases and its relationship to sorption. Energ Fuel 24, 2777-2783.

Dutta, P., Bhowmik, S., Das, S., 2011. Methane and carbon dioxide sorption on a set of coals from India. International Journal of Coal Geology 85, 289-299.

Espinoza, D., Vandamme, M., Pereira, J.-M., Dangla, P., Vidal-Gilbert, S., 2014. Measurement and modeling of adsorptive–poromechanical properties of bituminous coal cores exposed to CO_2: Adsorption, swelling strains, swelling stresses and impact on fracture permeability. International Journal of Coal Geology 134, 80-95.

Fry, R., Day, S., Sakurovs, R., 2009. Moisture-induced swelling of coal. International Journal of Coal Preparation and Utilization 29, 298-316.

Gensterblum, Y., Busch, A., Krooss, B.M., 2014. Molecular concept and experimental evidence of competitive adsorption of H_2O, CO_2 and CH_4 on organic material. Fuel 115, 581-588.

Gensterblum, Y., Merkel, A., Busch, A., Krooss, B.M., 2013. High-pressure CH_4 and CO_2 sorption isotherms as a function of coal maturity and the influence of moisture. International Journal of Coal Geology 118, 45-57.

Goodman, A., Favors, R., Larsen, J.W., 2006. Argonne coal structure rearrangement caused by sorption of CO_2. Energ Fuel 20, 2537-2543.

Govindjee, S., Simo, J.C., 1993. Coupled stress-diffusion: Case II. J Mech Phys Solids 41, 863-887.

Gruszkiewicz, M., Naney, M., Blencoe, J., Cole, D.R., Pashin, J.C., Carroll, R.E., 2009. Adsorption kinetics of CO_2, CH_4, and their equimolar mixture on coal from the Black Warrior Basin, West-Central Alabama. International Journal of Coal Geology 77, 23-33.

Haward, R.N., 2012. The physics of glassy polymers. Springer Science & Business Media.

Hetnarski, R.B., Eslami, M.R., Gladwell, G., 2009. Thermal stresses: advanced theory and applications. Springer.

Hol, S., Peach, C.J., Spiers, C.J., 2011. Applied stress reduces the CO_2 sorption capacity of coal. International Journal of Coal Geology 85, 128-142.

Hol, S., Peach, C.J., Spiers, C.J., 2012a. Effect of 3-D stress state on adsorption of CO_2 by coal. International Journal of Coal Geology 93, 1-15.

Hol, S., Spiers, C.J., 2012. Competition between adsorption-induced swelling and elastic compression of coal at CO_2 pressures up to 100MPa. J Mech Phys Solids 60, 1862-1882.

Hol, S., Spiers, C.J., Peach, C.J., 2012b. Microfracturing of coal due to interaction with CO_2 under unconfined conditions. Fuel 97, 569-584.

Hui, C.Y., Wu, K.C., Lasky, R.C., Kramer, E.J., 1987a. Case-II diffusion in polymers. I. Transient swelling. J Appl Phys 61, 5129-5136.

Hui, C.Y., Wu, K.C., Lasky, R.C., Kramer, E.J., 1987b. Case-II diffusion in polymers. II. Steady‐state front motion. J Appl Phys 61, 5137-5149.

Karacan, C.Ö., 2003. Heterogeneous sorption and swelling in a confined and stressed coal during CO2 injection. Energ Fuel 17, 1595-1608.

Karacan, C.Ö., 2007. Swelling-induced volumetric strains internal to a stressed coal associated with CO_2 sorption. International Journal of Coal Geology 72, 209-220.

Larsen, J.W., 2004. The effects of dissolved CO_2 on coal structure and properties. International Journal of Coal Geology 57, 63-70.

Larsen, J.W., Green, T.K., Kovac, J., 1985. The nature of the macromolecular network structure of bituminous coals. The Journal of Organic Chemistry 50, 4729-4735.

Laxminarayana, C., Crosdale, P.J., 1999. Role of coal type and rank on methane sorption characteristics of Bowen Basin, Australia coals. International Journal of Coal Geology 40, 309-325.

Levine, J.R., 1996. Model study of the influence of matrix shrinkage on absolute

permeability of coal bed reservoirs. Geological Society, London, Special Publications 109, 197-212.

Liu, J., Chen, Z., Elsworth, D., Qu, H., Chen, D., 2011. Interactions of multiple processes during CBM extraction: A critical review. International Journal of Coal Geology 87, 175-189.

Mazumder, S., Vermolen, F., Bruining, J., 2011. Analysis of a Model for Anomalous-Diffusion Behavior of CO_2 in the Macromolecular-Network Structure of Coal. Spe J 16, 856-863.

Merkel, A., Gensterblum, Y., Krooss, B.M., Amann, A., 2015. Competitive sorption of CH_4, CO_2 and H_2O on natural coals of different rank. International Journal of Coal Geology 150, 181-192.

Myers, A., 2002. Thermodynamics of adsorption in porous materials. Aiche J 48, 145-160.

Pan, Z., Connell, L.D., 2007. A theoretical model for gas adsorption-induced coal swelling. International Journal of Coal Geology 69, 243-252.

Peng, Y., Liu, J., Wei, M., Pan, Z., Connell, L.D., 2014. Why coal permeability changes under free swellings: New insights. International Journal of Coal Geology 133, 35-46.

Pini, R., Ottiger, S., Burlini, L., Storti, G., Mazzotti, M., 2010. Sorption of carbon dioxide, methane and nitrogen in dry coals at high pressure and moderate temperature. Int J Greenh Gas Con 4, 90-101.

Pone, J.D.N., Halleck, P.M., Mathews, J.P., 2009. Sorption capacity and sorption kinetic measurements of CO_2 and CH_4 in confined and unconfined bituminous coal. Energ Fuel 23, 4688-4695.

Setzmann, U., Wagner, W., 1991. A new equation of state and tables of thermodynamic properties for methane covering the range from the melting line to 625 K at pressures up to 100 MPa. Journal of Physical and Chemical Reference Data 20, 1061-1155.

Shewmon, P., 1989. Diffusion in solids. The Minerals, Metals & Materials Society, Diffusion in Solids. Second Edition.(Retroactive Coverage)(United States), 1989, 246.

Shi, J.-Q., Durucan, S., 2003. A bidisperse pore diffusion model for methane displacement desorption in coal by CO_2 injection. Fuel 82, 1219-1229.

Staib, G., Sakurovs, R., Gray, E.M.A., 2013. A pressure and concentration dependence of CO_2 diffusion in two Australian bituminous coals. International Journal of Coal Geology 116, 106-116.

Staib, G., Sakurovs, R., Gray, E.M.A., 2014. Kinetics of coal swelling in gases: Influence of gas pressure, gas type and coal type. International Journal of Coal Geology 132, 117-122.

Thomas, N.L., Windle, A., 1982. A theory of case II diffusion. Polymer 23, 529-542.

van Bergen, F., Spiers, C., Floor, G., Bots, P., 2009. Strain development in unconfined coals exposed to CO_2, CH_4 and Ar: Effect of moisture. International Journal of Coal Geology 77, 43-53.

Zhao, Y., Liu, S., Jiang, Y., Wang, K., Huang, Y., 2016. Dynamic Tensile Strength of Coal under Dry and Saturated Conditions. Rock Mechanics and Rock Engineering 49, 1709-1720.

Chapter 5

Anisotropic swelling behaviour of coal matrix cubes exposed to water vapour: Effects of relative humidity and sample size

Jinfeng Liu, Colin J. Peach, Christopher J. Spiers

Also submitted to International Journal of Coal Geology

Abstract

Understanding the swelling behaviour of coal matrix material exposed to water vapour is of direct relevance to optimising (E)CBM recovery. However, accurate measurement of coal swelling due to water sorption presents a substantial challenge, because while measurement accuracy increases with sample size, so does equilibration time hence experiment duration. This paper reports dilatometry experiments conducted on 1 and 4 mm cubic samples of Brzeszcze high volatile bituminous coal. These were performed using a purpose-build, 3-dimensional (3D) dilatometer, consisting of sensitive eddy-current gap sensors. The aim was to accurately and continuously measure the volumetric response of coal matrix material during exposure to water vapour at relative humidities varied in the range of 0.1 to 95%, at a temperature of 40˚C. Our results show that the swelling strains attained at apparent equilibrium tend to be a factor of up to 1.45 higher perpendicular to bedding than in the bedding plane. In addition, the sample size strongly influences the swelling kinetics, but does not influence the equilibrium swelling strains. Moreover, the volumetric swelling strains attained at equilibrium show a near-linear dependence on relative humidity, reaching 1.37-1.43% at around 95% relative humidity. In an attempt to explain the observed behaviour, three models for swelling of unconfined coal matrix material due to water sorption were developed. These correspond to mono-layer adsorption, multiple-layer sorption, and combined mono plus multiple-layer sorption. The experimental data are equally well fitted by all three models, so that the mechanism responsible for swelling could not be uniquely identified. However, our findings do demonstrate that decreasing in-situ water activity causes significant anisotropic shrinkage of coal matrix material, pointing to injection and recirculation of dry nitrogen as a promising strategy for stimulating coal seams for CBM production and as a pre-treatment for later CO_2 injection and storage.

5.1. Introduction

Water present in coal seams is of profound importance in relation to coalbed methane (CBM) production, enhanced coalbed methane (ECBM) production and CO_2 storage in coal seams (e.g. Busch and Gensterblum, 2011). Water naturally present in coal must be pumped out to initiate CBM production (e.g. Moore, 2012; White et al., 2005). However, it is also frequently injected too, to stimulate reservoir permeability by means of hydrofracture (Pan and Wood, 2015; van Bergen et al., 2006). Its effects are manifold. First, the presence of water in coal reduces gas diffusivity (Pan et al., 2010). It also reduces the sorption capacity of coal to gases, such as CH_4 and CO_2, as coal has a greater affinity for adsorbing water (Busch and Gensterblum, 2011; Day et al., 2008c; Gensterblum et al., 2014; Gensterblum et al., 2013; Merkel et al., 2015). More importantly, sorption of water vapour by coal matrix material leads to several percent of swelling (Fry et al., 2009; Suuberg et al., 1993; van Bergen et al., 2009), with dry coals expanding more when exposed to a gas/water-vapour mixture than to pure CO_2 or CH_4 (Day et al., 2011). On the other hand, moist coals swell less upon exposure to CO_2 or CH_4 than dry coals (Day et al., 2011). These sorption-induced swelling effects directly influence cleat/fracture apertures and can therefore impact both coal seam permeability and gas productivity (e.g. Liu et al., 2011; van Bergen et al., 2006; van Bergen et al., 2009; White et al., 2005).

The above all point to the presence of water in coal seams having a largely negative impact on (E)CBM production and on CO_2 storage in coal seams. Conversely, removing water from a coal seam can potentially shrink the coal and increase the matrix permeability offering a stimulation technique (Fry et al., 2009; Pan, 2012). Investigation of the swelling/shrinkage behaviour of coal during exposure to water is therefore of key importance in designing and optimising ECBM production strategies.

Numerous studies have demonstrated that water molecules are primarily trapped by

oxygen-bearing functional groups (mostly by carboxyl groups) present in the coal matrix, via hydrogen bonds (c.f. Allardice and Evans, 1971; Busch and Gensterblum, 2011; Kaji et al., 1986; Mu and Malhotra, 1991; Suárez et al., 1993; Yu et al., 2013). This mechanism usually traps a first layer of adsorbed water molecules with relatively high binding energy (c.f. Dubinin, 1980; Dubinin and Serpinsky, 1981). The thus-adsorbed water molecules then form secondary sites for attachment of additional water molecules with lower binding energy, thereby forming water clusters (c.f. Charrière and Behra, 2010; Lynch and Webster, 1982; McCutcheon et al., 2003; Nishino, 2001; Švábová et al., 2011). The total water adsorption capacity of coal is directly related to water activity or relative humidity, and is well described by the multilayer Dent model and the combined multi/single layer D'Arcy and Watt model (Charrière and Behra, 2010; McCutcheon et al., 2003; Švábová et al., 2011). Water sorption by coal is accordingly quite well understood.

However, only a few studies have focused on the swelling/shrinkage behaviour of coal in response to sorption/desorption of water. Suuberg et al. (1993) reported a 30% (maximum) volumetric shrinkage of coal upon drying, for various coal ranks ranging from bituminous to lignite. They prepared 50-100 mg coal powder samples (grain size less than 600 μm) from freshly collected coal, assuming them to have identical in-situ moisture contents. The samples were deposited in 3mm inner diameter by 5mm long tubes and settled by means of centrifuging. The sample assembly was then dried in a vacuum oven and the accompanying volumetric shrinkage was determined by measuring the length change of the sample within its tube. The precision of this method was ~ 2% (absolute) at best. The mass loss upon drying was simultaneously determined by weighing the samples, and showed a linear relation between shrinkage and water loss. A similar linear relation between sample volume change and water content of coals, ranging from sub-bituminous to bituminous, was also reported by Fry et al. (2009). These authors measured the swelling behaviour of coal blocks ($3\times1\times1$ cm^3) during

exposure to water vapour at up to 97% RH (relative humidity), at room temperature, using both screw micrometer and optical methods. Large uncertainties in strain measurement were reported, as the smallest displacements developed were beyond the resolution of the screw micrometer. The results of more accurate (2-20%) optical methods were reported by (Day et al., 2008a). These showed maximum volumetric expansions of 0.5% for high rank coals exposed to 97% RH, increasing to 5% for lower rank coals. Pan (2012) simultaneously measured the uptake of water vapour and the associated dimensional changes of a single cylindrical sample (2.54cm in diameter and 8.26cm in length) of bituminous coal exposed to RH values up to 100% at room temperature, using gravimetric and screw micrometer methods. Due to the large sample size, equilibration in his experiments took around 53 days. The results showed that the sample expanded linearly with increasing sorbed water content (weight) in the first 42 days, at which point the water content of coal sample was less than 5% and the RH was ~ 97%. However, between days 42 and 53, when the sample was exposed to around 100% RH, the dimensions of the sample changed little, though the weight of the sample continued to increase as liquid water droplets formed.

Although the above authors successfully measured the rough volumetric response of coal samples to water adsorption, accurate measurement of the true equilibrium swelling/shrinkage behaviour of coal matrix material as a function of water vapour activity remains a major challenge. This is because a) the poor accuracy of the screw micrometer gauge and optical methods used requires large samples, b) large samples need long times to approach equilibrium and may fail to do so, and c) cleats present in large samples might result in reduced bulk swelling strains due to "lost swelling" at free fracture walls (Hol et al., 2014). Aside from the challenge of accurate measurements, more data are needed, than presently available, to assess the effects of swelling and shrinkage of coal due to water sorption and desorption under in-situ (E)CBM conditions, and to assess the potential for coal shrinkage and reservoir stimulation by drying.

In the present paper, we attempt to help fill these gaps in data on the volumetric response of coal to changing water activity. We report the results of continuous, 3D dilatometry experiments performed on unconfined coal matrix cubes of high volatile bituminous coal (Brzeszcze, Poland), having edge dimensions of 1 and 4 mm. In each experiment, the sample was equilibrated with water vapour at a constant temperature of 40˚C, using controlled RH values ranging from 0.1% to 95%. Our results show an anisotropic swelling response of the samples tied to the coal bedding. They also demonstrate a strong influence of sample size on swelling kinetics, but no influence on equilibrium strains. Our data further reveal a near-linear relation between swelling strain and relative humidity, hence water activity, which can be accurately fitted by both monolayer and multiple layer sorption-swelling models. After describing and discussing these effects, we consider the implications of our findings for ECBM production.

5.2. Experimental methods

5.2.1. Approach

In this study, we measured changes in the dimensions of 1 and 4mm cubic samples of high volatile bituminous coal matrix material during exposure to water vapour at different relative humidities (RH). The experiments were conducted at RH values of 0.1 to 95% at a fixed temperature of 40˚C, using a specially developed, three-dimensional (3D) dilatometer. This 3D dilatometer allowed us to measure the swelling/shrinkage response of the samples in three orthogonal directions, continuously and simultaneously, while RH was systematically varied. By correcting for effects of RH on the sensor system, equilibrium swelling/shrinkage displacements of around ±40 nm could be resolved.

5.2.2. Starting material and sample preparation

The experiments were performed on coal matrix samples taken from high volatile

bituminous coal obtained from the Upper Silesian Basin of Poland, Brzeszcze mine (seam 364). The Brezeszcze coal has a vitrinite reflectance of 0.77±0.05%, and contains 74.14% carbon, 5.27% hydrogen, 1.44% nitrogen, 0.70% sulfur and 18.45% oxygen (Hol et al., 2011). To speed up water vapour equilibration with the samples, and to investigate any effects of sample size on swelling kinetics and equilibrium swelling strain, we used two 1mm coal cubes (Samples P1 and P2) and one 4mm coal cube (Sample P3) for the present study.

The samples were prepared from a ~ 10 cm block of the Brzeszcze coal. Wafers with thickness of 1 mm and 4 mm were cut from this block, in orientations parallel to bedding. The sample cubes were then made by slicing the sheets parallel and normal to the butt cleat. This was all done by the Glass Workshop at Utrecht University, using a high-precision, digitally controlled, diamond wafering saw cooled by water. The many cubes thus prepared were subsequently dried in a vacuum oven at a temperature of 40˚C for several days to remove residual water and gas. After inspecting tens of cubes using an optical microscope, we chose two 1 mm cubes and one 4 mm cube, which were cleat-free and damage-free, for the present experiments. For each of the chosen samples, we defined the direction perpendicular to bedding plane as the z reference axis, with the x and y directions lying in the bedding plane in orientations perpendicular and parallel to the butt cleat (Fig. 1). It is assumed that x, y, and z correspond to the principal axes of sample anisotropy and therefore of swelling strain, though this cannot be guaranteed.

Immediately prior to mounting in the 3-D dilatometer, the dimensions of the 1 mm cubes were measured using a Leica DMRX optical microscope with image analysis (QWIN Pro) system, while the dimensions of the 4 mm cube were measured using a digital calliper (resolution 0.01 mm). The mass of each sample was measured using a METTLER TOLEDO MS205DU Semi-Micro Analytical Balance (resolution 0.01 mg). We took the average values of several measurements to determine the dimensions and mass of each sample (see Table 1).

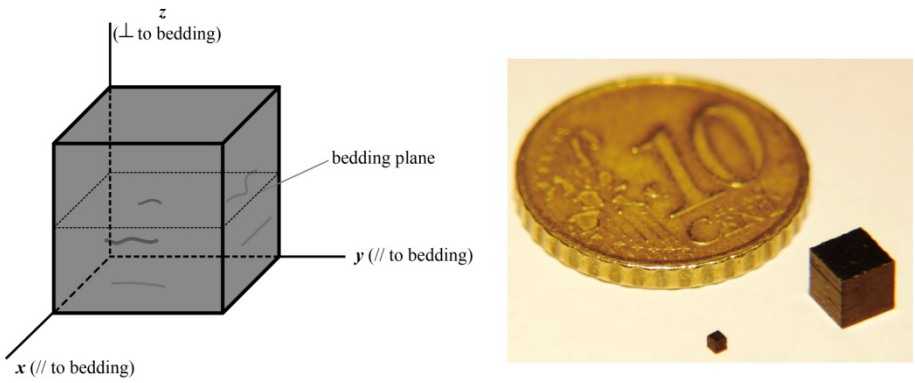

Fig.1. a) Schematic diagram illustrating the coal matrix sample geometry used in this study. Note the xyz reference frame corresponding to the 3-D dilatometer measurement axes. The x and y axes lie in the bedding plane (perpendicular and parallel to the butt cleat), while z was defined as the direction perpendicular to bedding. b) Photograph of the 1mm and 4mm samples.

Table 1. Starting dimensions and mass of the Brzeszcze 364 coal matrix cubes used as samples in this study. The lengths L_i (where i=x, y, z) represent the starting dimensions in the x, y and z directions, as used in all strain calculations.

Sample	initial sample mass (g)	initial sample length L_x (µm)	initial sample length L_y (µm)	initial sample length L_z (µm)
P1	0.00125	941.06	1058.54	973.64
P2	0.00132	1022.51	951.61	998.5
P3	0.0848	4070	4020	4080

5.2.3. Apparatus

The experimental setup is shown in Fig. 2. It consists of the 3-D dilatometer (see Fig. 3) mounted in a sealed glass chamber, which is itself connected to an air circulation system controlled at fixed RH using a saturated salt solution buffer. The entire system is enclosed in a temperature controlled box.

The 3D dilatometer (Fig.3) is composed of three independent Lion Precision type

ECL202 U3B eddy current sensors (A, B, and C) mounted orthogonally in a stainless steel, multiblock frame, housing a sample stage at its centre. The sample stage contains a corner-shaped recess that supports the cubic sample on three faces in a fixed position, with the x, y and z sample axes aligned opposite to and coaxially with the three sensor tips (see Fig.3). Expansion or contraction of the sample in the *x*, *y* and *z* directions is transmitted to three Aluminum eddy current targets via three, orthogonally mounted, spring cross-cantilevers that retain the sample in position. Displacement of each target, as the sample expands or contracts in the *x*, *y* or *z* direction, alters the eddy current field in the target and allows sample expansion and contraction to be measured. The full scale range of each eddy current sensor is 250μm and the measurement resolution at fixed RH is better than ±12.5 nm.

The relative humidity employed during the experiments ranged from 0.1% to 95%. As indicated above, RH was controlled using a set of carefully selected salt solution buffers. The RH buffer system consisted of a sealed flask containing excess salt plus saturated solution, supported on a glass-fiber wool bed to ensure solid-liquid-vapour equilibration. The flask was connected to the sample chamber via a closed loop tube system incorporating a low pressure KNF gas (air) pump, used to circulate air through the flask and the glass chamber. This allowed the system to reach constant “set point” relative humidity values within 2-3 hours of activation. Relative humidity within the system was measured using two SENSIRION SHT75 digital humidity sensors (accuracy ±1.8%), mounted in the inlet and outlet ports of the glass chamber containing the dilatometer. These gave consistent relative humidity values within 2% at worst. Salts used to control RH included $CuSO_4$ powders (RH=12%), $KC_2H_3O_2$ (RH=23%), $MgCl_2$•$6H_2O$ (RH=32%), $Mg(NO_3)_2$•$6H_2O$ (RH=49%), NaCl (RH=75%), KCl (85%), K_2SO_4 (RH=95%). To achieve the lowest RH value of 0.1%, phosphorus pentoxide (P_2O_5) powder was used to dry the whole buffer setup. The quality of RH control during a typical experimental run is illustrated in Fig. A1 of the Appendix.

To maintain constant temperature of the whole setup, a ~ 0.42 m^3 foam-polystyrene box was constructed around it. The temperature of the air and all components inside the box, including the sample, was controlled at 39.8˚C (±0.1˚C) by means of a digital CAL 9900 PID-controller, coupled to a 500W halogen construction lamp. Two electric fans were used to homogenize the temperature inside the box. The temperature of the sample was measured using a PT 100 element mounted on the sample stage of the dilatometer, inside the glass chamber. The controlled temperature of the whole system was measured using a PT 100 sensor located in the foam box. The quality of sample temperature control during a typical experimental run is illustrated in Fig.A2 of the Appendix.

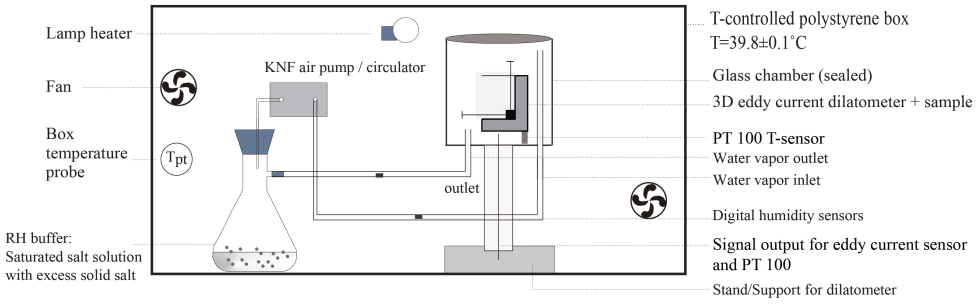

Fig.2. Schematic diagram of the full experimental setup. The 3-D dilatometer plus sample are housed in a glass chamber. This is connected to an air flushing system incorporating a flask containing a saturated salt solution buffer for RH control. A KNF pump is used to circulate the air through the RH control system. The whole system is contained in a heated foam-polystyrene box, maintained at a controlled temperature of nominally 40˚C (specifically 39.8±0.1˚C). The sample temperature and RH were measured using PT100 and digital humidity sensors, respectively.

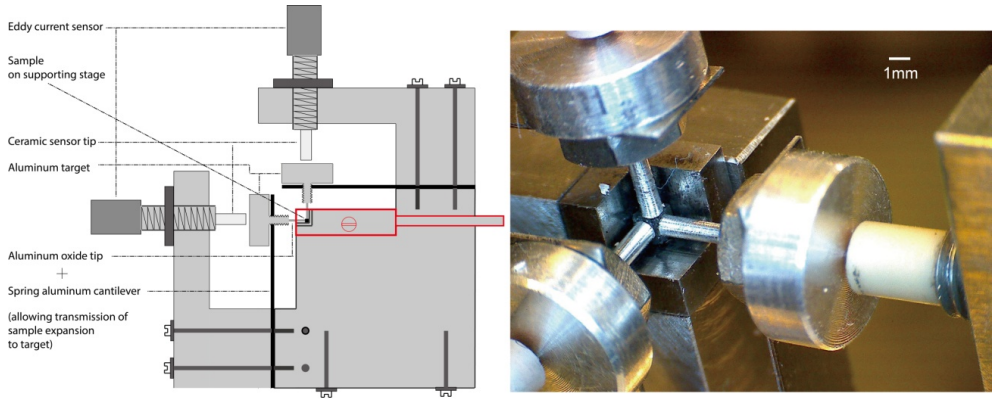

Fig. 3. The 3D dilatometer developed for this study. a) Semi-schematic diagram showing a 2D section through the sample and sample stage. Expansion or contraction of the cube-shaped sample is transmitted to three orthogonally positioned Aluminum targets via three spring cross-cantilevers that retain the sample in position. Displacement of the targets is measured using three corresponding eddy current sensors. Measurement resolution at constant RH is better than ±13nm. b) Photograph of the 3D dilatometer with close-up of sample-stage plus 1 mm sample. Note the ceramic sensor tips.

5.2.4. Dilatometer calibration and corrections

The change in each eddy current sensor signal (i.e. output voltage) with displacement of the sample target was calibrated using a specially constructed calibration jig driven by a digital micrometer screw gauge (resolution 0.1µm). This allowed controlled translation of each target relative to the corresponding sensor tip. Calibrations were carried out at room temperature (25˚C) and room humidity (RH≈50%), noting that the influence of temperature on sensitivity is known, from manufacturer's data, to be minor in the range 20-40˚C under these conditions. In each calibration run, the target was moved stepwise towards the sensor tip by rotation of the screw gauge, and the sensor output was recorded after signal stabilization. All three sensors were characterized by a closely linear relationship between voltage change and displacement over a displacement range of 250µm, corresponding to a sensitivity of 38.8 mV/µm (R^2=0.999) for sensor A, 37.4 mV/µm (R^2=0.999) for sensor B, and 39.3 mV/µm (R^2=0.999) for sensor C. This full

scale range is equivalent to a linear strain of ~25% for a 1mm sample and ~5.1% for a 4mm sample, with 2-3% being the maximum strains expected from previous data (Fry et al., 2009; van Bergen et al., 2009). Our calibration results demonstrated the resolution of the sensors in measuring sensor-target distance changes to be better than ±13nm at room conditions.

Dummy experiments performed using 1 and 4 mm stainless steel and 1mm quarts glass calibration cubes, instead of coal samples, showed that the eddy current sensor signals were systematically and reproducibly affected by changes in RH, presumably due to effects of water sorption on the sensor or changes in air permittivity. To calibrate this effect for all three sensors, control experiments were performed using the three dummy samples, closely replicating the experimental procedure employed in each experiment performed on coal (see details in Appendix). This allowed correction for both transient and equilibrium effects of changes in RH on sensor signals. Equilibrium effects were corrected for using accurately fitted hyperbolic functions describing equilibrium sensor signal expressed in terms of apparent displacement (μm) versus RH. These corrections were accurate to within ±0.04 μm. Transient effects were more crudely corrected for using a linear rescaling factor (based on the ratio of corrected to raw equilibrium signals) to remove the measured effect of RH on the sensors from the apparent displacement versus time data obtained for the coal samples. Comparison of the corrections applied with the apparent displacements measured using the dummy samples, showed that the corrections for transient effects of RH changes on sensor output were accurate within ±0.15 μm.

The dummy experiments confirmed that the eddy current sensor signals were only slightly affected by changes in temperature between 20 and 40 ˚C. Moreover, these changes were reversible. As temperature in the present experiments was controlled within ±0.1˚C, the influence of temperature on the sensor signals could therefore be safely neglected.

5.2.5. Testing procedure

Four experiments were performed in total (see Table 2):

Experiment 1 (Exp1) was performed on Sample P1 and consisted of two successive RH cycling runs. Experiment 2 (Exp2) was also performed on Sample P1 but after its removed and return to the apparatus. Exp2 consisted of three successive RH cycling runs. Experiment 3 (Exp3) was performed on Sample P2 and involved two RH cycling runs. Experiment 4 (Exp4) was performed on Sample P3 and employed a single RH cycling run.

Note here that each RH cycling run performed consisted of a complete relative humidity cycle made up of 5-7 incremental steps followed by 1-4 decremental steps. All RH runs were initiated and concluded by imposing dry reference conditions upon the sample, using P_2O_5 to maintain an RH of 0.1% in the RH control system. Changes in relative humidity were achieved by manually switching the salt buffer flask. This was done within 2-3 minutes, during which time a disturbance in temperature of typically ~ 0.4˚C occurred. After each change in RH, the three eddy current sensor signals showed a transient evolution response towards an apparent equilibrium state. This was assumed to be reached when no change in signals occurred within 3-4 hours. Once apparent equilibrium was reached after each RH step, we proceeded to implement the next RH step. Re-equilibration of the measured sensor signals typically took ~ 80 hours, whereas re-equilibration of the system temperature to 39.8±0.1˚C took only ~ 1 hour.

Table 2. Summary of experiments performed. The term "run" refers to a complete relative humidity cycle containing 5-7 incremental steps in RH followed by 1-4 decremental steps in RH.

Experiment	Sample	Nominal Sample Size	Number of Runs
Exp1	P1	1mm	2
Exp2	P1	1mm	3
Exp3	P2	1mm	2

Exp4	P3	4mm	1

5.2.6. Data acquisition and processing

5.2.6.1. General aspects

The sample temperature and three eddy current sensors signals were logged using a National Instruments, 16-channel DAOPad-6015 A/D convertor and VI-logger data acquisition system, at a sampling rate of 0.2 HZ. Relative humidity signals were digitally logged using an independent (EKH4views) system at a sampling rate of 0.1 HZ, taking the average value of the relative humidity measured by the two sensors as the relative humidity during each RH step performed. Swelling displacement and strain values obtained from the eddy current sensor signals were measured as positive. We use the term "uncorrected swelling" for apparent sample strains calculated directly from the eddy current sensor signals without accounting for the effects of RH on the sensor signals. "Corrected swelling" is used to refer to the true swelling of the coal samples as calculated by applying the RH correction.

5.2.6.2. Processing to obtain uncorrected swelling strain versus time

The uncorrected swelling strain of our coal samples was calculated as a function of time using the expression $e_i^{uc}(t) = \frac{[V_i(t) - V_{i0}]}{S_i L_{i0}} \times 10^5$. Here $e_i^{uc}(t)$ represents uncorrected sample strain in direction *i* (*i*=*x*, *y*, *z*) at time *t*. The quantity $V_i(t)$ (in V) represents the sensor output signal for direction *i* at time *t*, while V_{i0} (in V) represents the signal at *t*=0, i.e. at the initial reference condition when the sample was equilibrated at 0.1% relative humidity. In addition S_i (mV/μm) represents the sensor sensitivity in direction *i*, and L_{i0} (μm) is the initial dimension of the sample in this direction (before

assembly).

5.2.6.3. Obtaining the corrected or true swelling strain at equilibrium

The time-averaged value of each sensor signal, $V_i(t)$ as obtained over the final two hours of the *jth* RH step of each run, was taken as the mean output voltage $(\overline{V}_i)_j$ corresponding to equilibrium at RH level *j*. The corrected swelling strain $(e_i^{eq})_j$ expressed in % for direction *i* at equilibrium was computed using the expression $(e_i^{eq})_j = \dfrac{[(\overline{V}_i)_j - V_{i0}] \times 1000 / S_i - (C_i)_j}{L_{i0}} \times 100$. Here $(C_i)_j$ represents the correction for the effect of RH on sensor for direction *i* at equilibrium in RH step *j*. As the true swelling strains $(e_i^{eq})_j$ are expected to be small, the true or corrected volumetric strain of the sample at equilibrium at RH level *j* is given $(e_v^{eq})_j = \sum_{i=1}^{3} (e_i^{eq})_j$. Taking the accuracy of the corrected displacement signals in the *x*, *y* and *z* directions at equilibrium (±0.04 μm) as a measure of uncertainty, the uncertainty of corrected volumetric strain for the 1mm samples was within ±0.08% (absolute), while for the 4mm sample it was within ±0.02% (absolute).

5.2.6.4. Obtaining corrected swelling strain versus time

The uncorrected e_i^{uc} vs. *t* data obtained for our coal samples could not always be accurately corrected for RH-related effects on the sensor signals, because the duration of RH steps employed in our calibration tests did not always match those used in the coal runs (see details in Appendix A3). However, the sensor signal versus time curves obtained in the calibration tests were similar in form to the uncorrected swelling/shrinkage of coal samples versus time (see Appendix A3). As indicated in

Section 5.2.4, this enabled us to crudely correct the uncorrected orthogonal swelling strains $e_i^{uc}(t)$ for RH-related sensor effects, using the expression $e_i^c(t) = e_i^{uc}(t)\frac{(e_i^{eq})_j}{(e_i^{eq})_j^{uc}}$, where $e_i^c(t)$ represents the corrected swelling strain in direction *i*, and $(e_i^{eq})_j^{uc}$ represents the corresponding uncorrected swelling strain attained at equilibrium. Once again, comparison of the corrections applied with the apparent displacements measured using the dummy samples, showed that the relative errors in true displacement obtained using this method were less than 10% (up to ±0.15 μm absolute). The largest relative errors occurred at the start of a given RH step, and decreased with time approaching to zero at equilibrium. The thus-corrected swelling data are therefore adequate for comparing swelling development with time from sample to sample, and for comparing swelling kinetics qualitatively.

5.3. Results

Representative data showing corrected swelling strain development in the *x*, *y* and *z* directions, i.e. showing $e_i^c(t)$ versus time, for individual RH cycling runs are presented in Fig.4. The full set of (near or apparent) equilibrium swelling strains e_i^{eq} and corresponding volumetric strain e_v^{eq}, obtained for each experiment/run and each RH step (*j*) within each run, are presented in Table 3. Note that all swelling versus time curves presented here are plotted taking the strain and time at the onset of each experimental run as the origin.

5.3.1. Swelling strain development with time

With reference to Figure 4, all experiments and all runs showed broadly similar

swelling behaviour of the coal samples during exposure to water vapour. The samples expanded or shrank slowly with time, in the *x*, *y* and *z* directions, after each RH increment or decrement, gradually approaching an asymptotic swelling strain value in each direction. The magnitude of the (apparent) equilibrium strain systematically increased with increasing RH, and decreased with decreasing RH, in respectively the upward and downward stages of each RH cycling run. The equilibrium swelling strains e_i^{eq} attained at specific RH values were also similar in all experiments and runs, though the strains in the *z* direction were usually the highest, demonstrating significant swelling anisotropy especially at RH values above 12-48%. Changes in equilibrium strain per RH step were almost always largest in the *z* direction, with those in the *x* and *y* directions being up to 25% lower, though the 4 mm sample (Fig. 4d) was more isotropic in its behavior than the 1 mm samples (Fig. 4a-c). The maximum total axial swelling strain occurred at relative humidities of 92.2-95.6% in all runs, reaching values of 0.51-0.55% normal to bedding plane (*z* direction) and 0.4-0.48% parallel to bedding plane (*x* and *y* directions).

Overall, the swelling strains developed during RH cycling were closely recoverable (Fig.4). However, different levels of hysteresis were observed between experiments. Apparent equilibration was also faster for adsorption than for desorption, following similar changes in RH. In addition, equilibration times clearly depended on sample size. For example, the total time elapsed per run in Exp1-SampleP1-Run2 and Exp2_SampleP1_Run1 (1mm, 7 RH steps) was 490-520 hours, compared with a run duration for Exp4_SampleP3_Run1 (4mm, 7 RH steps) of approximately 2700 hours (Fig. 4b-d). Focusing on individual RH steps, in the experiments on the 1mm samples, the time taken to approach apparent equilibrium after each RH increment lay in the range 30-150 hours, depending on the magnitude of the RH change, and was about the same per RH step in all runs. By contrast, the times taken to reach apparent equilibrium per RH step in the run performed on Sample P3 (4mm, in Exp4_SampleP3) fell in the

range 100-1250 hours. In particular, when the relative humidity decreased from about 49% to 0.1%, apparent equilibration for Sample P1 (1mm) took 95-120 hours, while that for Sample P3 took about 1250 hours. Equilibration times were thus much longer for the 4mm than the 1mm samples.

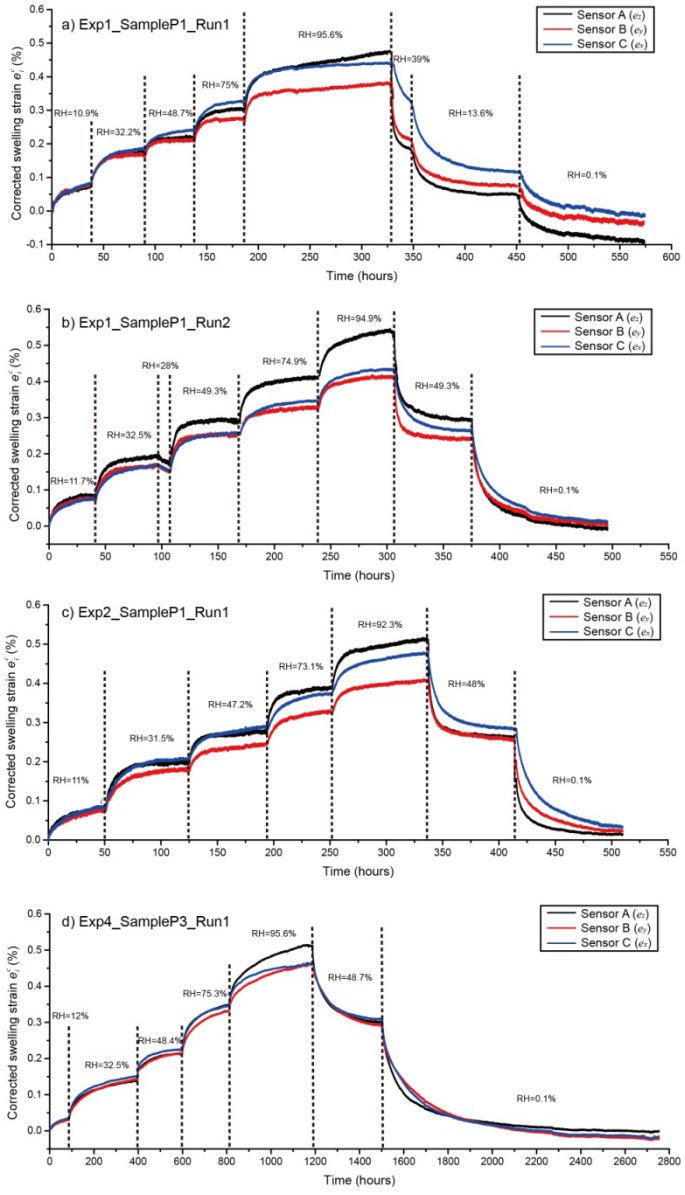

Fig.4. a) to d). Representative curves showing corrected swelling strain e_i^c (%) versus time data as obtained in the present experiments.

5.3.2. Equilibrium swelling strain versus relative humidity

As described above and visible from Table 3, the corrected swelling strains e_i^{eq} (*i=x, y, z*) attained at (apparent) equilibrium in all experiments were similar, for similar values of imposed relative humidity. Moreover, the equilibrium strains e_i^{eq} showed a systematic direct dependence on RH, increasing with increasing RH and decreasing with decreasing RH (Fig. 4, Table 3). This dependence is illustrated for Exp1_SampleP1, Exp2_SampleP1 and Exp4_SampleP3 in Fig.5. The data show a near-linear relation for each run, with similar sensitivities of strain to RH being obtained in all cases (around 5.4×10^{-3} % strain per % RH in z direction versus around 4×10^{-3} % strain per % RH in directions of *x* and *y*). In detail, Exp1_Run1 (Fig. 5a) showed a slightly lower sensitivity of equilibrium swelling strains e_z^{eq} (4.6×10^{-3} % strain per % RH) to RH compared with the other experiments.

Minor hysteresis was observed in the equilibrium strain vs. RH data obtained in upward vs. downward RH steps for Exp1_SampleP1_Run1 (Fig.5a). However, this disappeared in Run2 on the same sample (Fig. 5b). Exp2_SampeP1_Run1 (Fig.5c) also showed closely reversible behaviour in upward vs. downward RH steps. By contrast, Exp4_SampleP3_Run1 (see Fig. 5d) showed clear hysteresis. In this case, the equilibrium swelling strains obtained in all three directions at 49% RH were 30% higher in the downward RH steps than in the upward steps, though the sample finally shrank back to or even slightly beyond its initial dimensions when the relative humidity was returned to 0.1%.

Interestingly, in Exp4 (Sample P3, 4 mm), the equilibrium swelling strains attained at 12% relative humidity were e_z =0.031%, e_y=0.031% and e_x=0.035%, which are all about

one third of the values attained in Exp1 and Exp2 for the 1 mm sample P1 at 12% relative humidity. At the same time, we note that the time allowed for equilibration at 12% relative humidity in Exp4 was much shorter than allowed for the other RH values used in Exp4 (see Fig. 4d), suggesting that equilibrium was not yet attained at 12% relative humidity in Exp4.

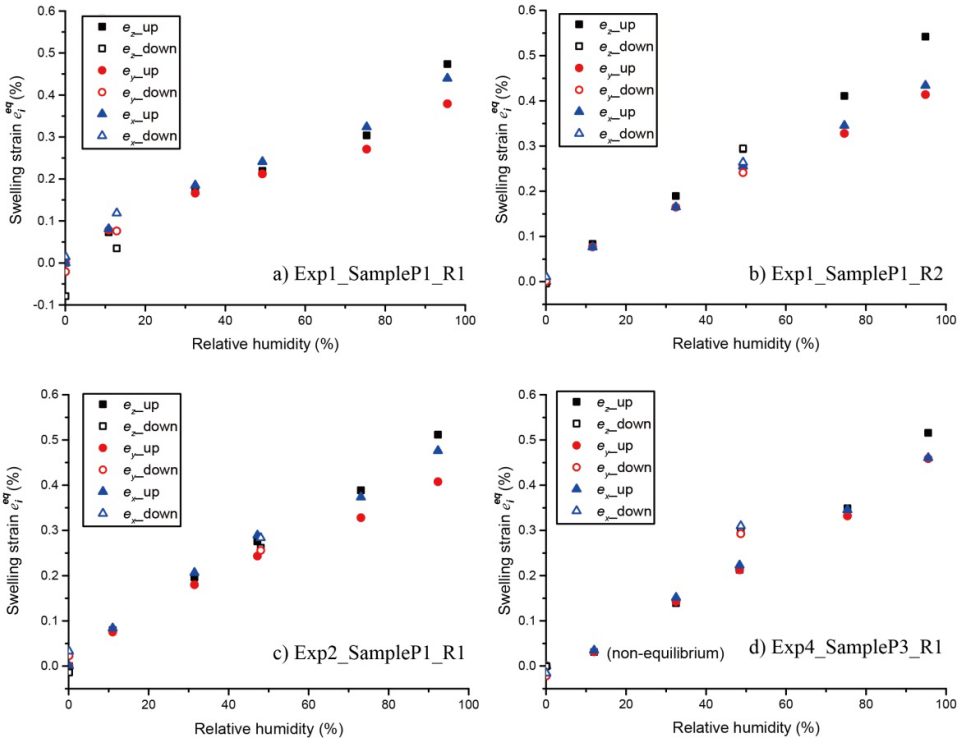

Fig.5. Representative data showing the swelling strains e_i^{eq} (%) attained at (apparent) equilibrium, in the x, y and z directions of our coal samples, as a function of relative humidity (%). "Up" refers to upward RH stepping (RH increments), while "down" refers to downward RH stepping (RH decrements).

5.3.3. Equilibrium volumetric swelling strain versus relative humidity

The true volumetric swelling strains (e_v^{eq}) obtained at apparent equilibrium, for all samples and all experimental runs are plotted in Fig.6 as a function of relative humidity.

All runs showed similar volumetric swelling strains (e_v^{eq}) at a given RH, except for Exp1_SampleP1_R1 which showed slightly lower swelling strain and about 0.1% of excess shrinkage at the end of the run. The volumetric swelling strain exhibited by all samples in all runs is seen to be nearly linearly proportional to relative humidity, reaching values of 1.37-1.43% at around 95% relative humidity (see Fig.6e). The sensitivity/slop of e_v^{eq} vs. RH data yielded 0.0141-0.0149 (R^2=0.99). Additionally, all experiments illustrate that the swelling/shrinkage deformation of our samples upon adsorption/desorption of water vapour is recoverable, though with different amounts of (minor) hysteresis. Exp4_SampleP3_R1 showed the most hysteresis, while Exp1 and Exp2 performed on sample P1 showed nearly fully reversible volumetric swelling.

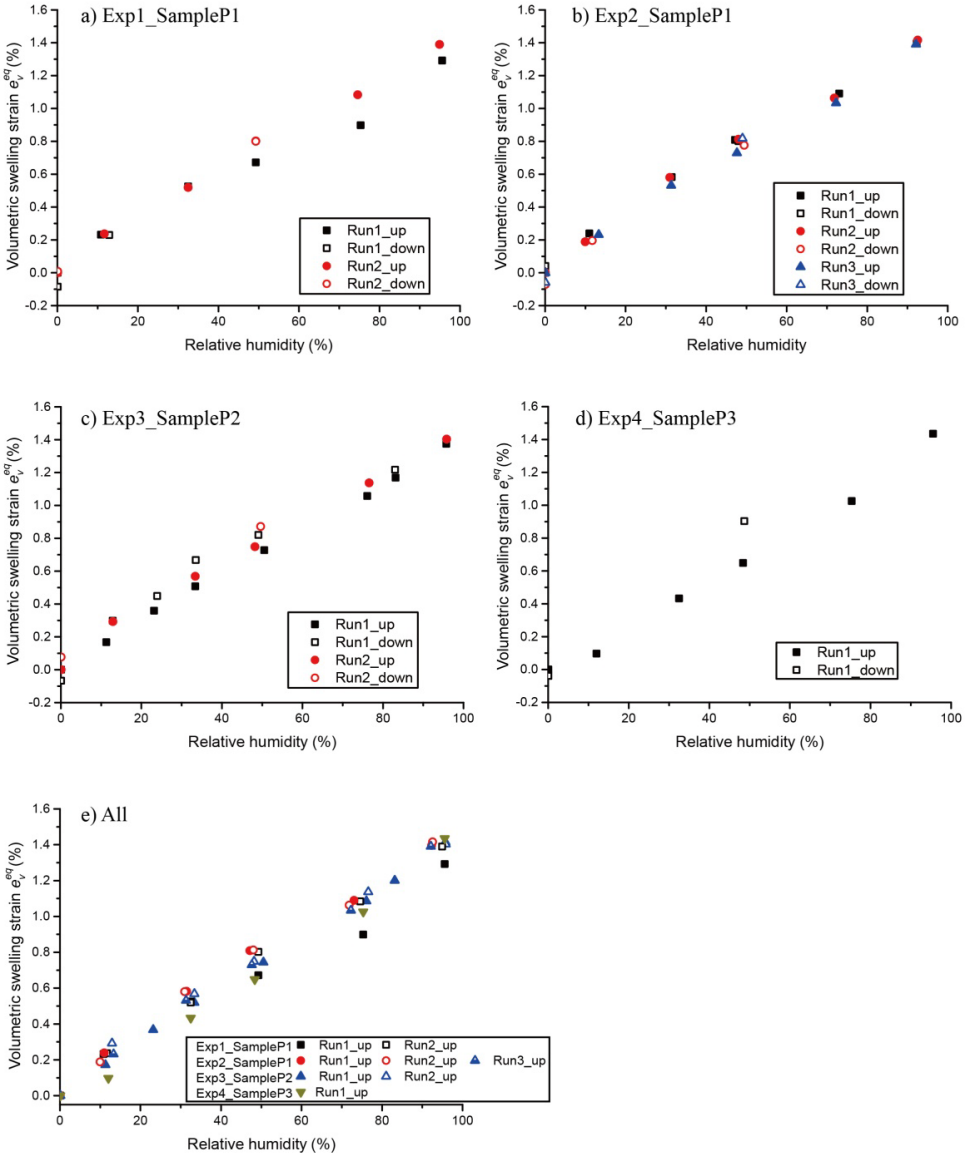

Fig.6. True volumetric swelling strain e_v^{eq} *(%) attained at (apparent) equilibrium for all samples, plotted as a function of relative humidity (%). a)-d) indicate Exp1-4 respectively, while e) shows all data combined for upward stepping RH. The RH down-stepping data are relative few and for this reason are not plotted separately here.*

Table 3. The full set of (near/apparent) equilibrium swelling strain (e_i^{eq}) data and corresponding volumetric strain (e_v^{eq}) data obtained for each experiment/run and each RH step within each run.

Sample/Exp.	Run1					Run2 (where performed)					Run3 (where performed)				
	RH (%)	e_x (%)	e_y (%)	e_z (%)	e_v (%)	RH (%)	e_x (%)	e_y (%)	e_z (%)	e_v (%)	RH (%)	e_x (%)	e_y (%)	e_z (%)	e_v (%)
SampleP1 /Exp1	0.1	0.000	0.000	0.000	0.000	0.1	0.000	0.000	0.000	0.000					
	10.8	0.073	0.078	0.081	0.232	11.7	0.083	0.077	0.077	0.237					
	32.5	0.174	0.166	0.185	0.525	32.5	0.189	0.165	0.165	0.519					
	49.3	0.219	0.212	0.241	0.672	49.3	0.293	0.254	0.255	0.802					
	75.3	0.304	0.271	0.324	0.898	74.6	0.411	0.328	0.345	1.084					
	95.6	0.473	0.379	0.440	1.292	94.9	0.542	0.414	0.434	1.390					
	12.9	0.035	0.076	0.119	0.229	49.3	0.295	0.241	0.264	0.800					
	0.1	-0.079	-0.021	0.015	-0.085	0.1	-0.004	0.001	0.011	0.008					
SampleP1 /Exp2	0.1	0.000	0.000	0.000	0.000	0.1	0.000	0.000	0.000	0.000	0.1	0.000	0.000	0.000	0.000
	11.0	0.080	0.075	0.084	0.239	10.0	0.066	0.059	0.063	0.188	13.3	0.081	0.075	0.075	0.232
	31.5	0.196	0.180	0.206	0.582	31.0	0.202	0.176	0.203	0.580	31.3	0.188	0.165	0.178	0.531
	47.2	0.276	0.243	0.289	0.808	48.1	0.285	0.242	0.286	0.813	47.6	0.269	0.222	0.238	0.729
	73.1	0.389	0.328	0.373	1.090	71.9	0.390	0.312	0.360	1.063	72.3	0.385	0.315	0.333	1.034
	92.3	0.512	0.408	0.476	1.395	92.6	0.548	0.403	0.465	1.415	92.2	0.523	0.412	0.456	1.391
	48.0	0.262	0.256	0.284	0.801	49.5	0.279	0.244	0.253	0.776	49.0	0.278	0.261	0.279	0.818
	0.1	-0.014	0.023	0.033	0.042	11.7	0.055	0.071	0.071	0.196	0.1	-0.036	-0.003	-0.020	-0.059
						0.1	-0.043	-0.013	-0.016	-0.072					
SampleP2 /Exp3	0.1	0.000	0.000	0.000	0.000	0.1	0.000	0.000	0.000	0.000					
	11.3	0.062	0.054	0.056	0.172	12.9	0.113	0.074	0.106	0.292					
	23.2	0.136	0.105	0.127	0.368	33.4	0.203	0.149	0.217	0.568					
	33.4	0.191	0.149	0.178	0.519	48.2	0.282	0.185	0.282	0.749					
	50.5	0.282	0.207	0.256	0.745	76.6	0.446	0.274	0.416	1.136					
	76.1	0.434	0.276	0.376	1.085	95.8	0.579	0.322	0.501	1.403					
	83.2	0.489	0.307	0.405	1.200	49.6	0.324	0.215	0.332	0.872					
	95.7	0.591	0.352	0.471	1.415	0.1	0.015	0.018	0.043	0.077					
	83.0	0.518	0.324	0.409	1.252										

	49.1	0.343	0.233	0.269	0.844		
	33.5	0.267	0.202	0.217	0.686		
	23.9	0.187	0.141	0.135	0.463		
	12.9	0.126	0.097	0.085	0.308		
	0.1	-0.011	-0.001	-0.052	-0.065		
SampleP4 Exp4	0.1	0.000	0.000	0.000	0.000		
	12.0	0.031	0.031	0.035	0.097		
	32.5	0.139	0.143	0.151	0.433		
	48.4	0.213	0.213	0.223	0.648		
	75.3	0.349	0.332	0.345	1.026		
	95.6	0.516	0.459	0.460	1.435		
	48.7	0.301	0.293	0.310	0.903		
	0.1	-0.001	-0.022	-0.016	-0.039		

5.3.4. Optical observations on samples before and after testing

Before and after each experiment, the samples tested (P1, P2, P3) were examined in reflected light using a Leica DMRX optical microscope. At the objective magnification (10x) and scale of optical resolution used (~5 μm), no changes in sample appearance and no evidence of damage were observed after the experiments. Representative micrographs of Sample P1 taken before and after Exp2 are presented in Fig.7.

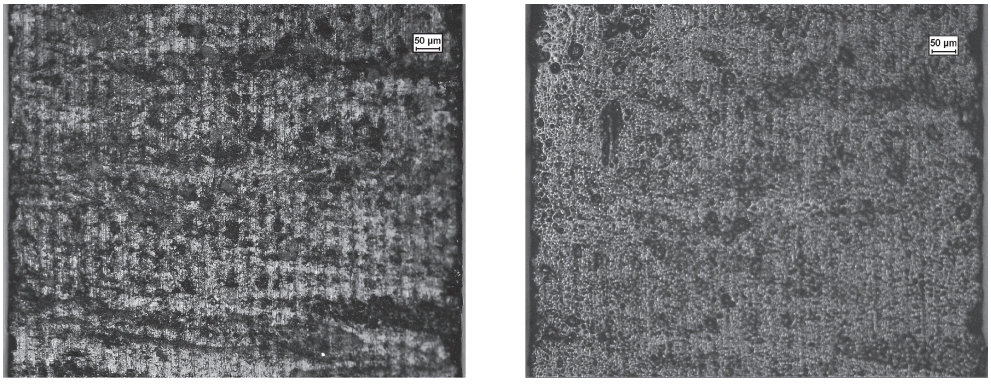

a) Exp2_SampleP1_before experiments b) Exp2_SampleP1_after experiments

Fig.7. Optical micrographs of Sample P1 taken before and after Exp2. Note that other than the difference in illumination conditions, the surface structure of the sample is unchanged after Exp2

compared with beforehand. No evidence of microcracking or other damage was found at the scale of observation used

5.4. Discussion

We have measured the 3-D strain response of 1 and 4mm, cleat-free, coal matrix cubes to changes in RH, hence water vapour activity, under unconfined conditions at 40˚C and at one atmosphere total pressure. Our experimental results show a) anisotropic swelling/shrinkage behaviour with the largest strains occurring mainly normal to bedding, b) recoverability of swelling strain but with hysteresis and minor permanent strain in some cases (e.g. Exp3_SampleP2_R2), c) a strong effect of sample size on equilibration time, but no effect on swelling strain attained at apparent equilibration, and d) a near-linear relation between (apparent) equilibrium swelling strains and relative humidity.

In the following, we discuss the mechanisms responsible for the observed anisotropy and hysteresis, and we attempt to explain the effects of sample size and relative humidity on swelling kinetics and equilibrium swelling strain. We also compare the swelling response of coal exposed to water vapour with the swelling caused by adsorption of other gases, such as CH_4, CO_2. In an attempt to gain insight into the single versus multilayer mechanism of water adsorption and the associated swelling response, we go on to compare our results on equilibrium swelling strain versus RH with presently available sorption/swelling models. Finally, we consider the possible implications of our findings for (E)CBM production.

5.4.1. Anisotropic swelling and hysteresis

5.4.1.1. Cause of anisotropic swelling behaviour

The results shown in Figs. 4 and 5 demonstrate that the swelling strains measured perpendicular to the bedding plane of our coal samples (i.e. in the *z* direction) tended to be larger than that parallel to bedding (in the *x* and *y* directions - refer Fig.1), especially

in the 1 mm samples and at RH values above 12-32%. The magnitude of this anisotropy, defined (following Day et al., 2010; Fry et al., 2009; Hol and Spiers, 2012; Pan and Connell, 2011) as the ratio of (apparent) equilibrium swelling strain in the *z* direction (e_z^{eq}) to the average value in the bedding plane, i.e. the average of e_x^{eq} and e_y^{eq}, is plotted versus relative humidity for all experimental runs in Fig.8. During upward stepping of RH, the swelling anisotropy ratio for all experimental runs generally increased with increasing RH from 0.90 to 1.25 (mean 1.08), at 12% RH, to 1.10 to 1.45 (mean 1.24) at ~95% relative humidity. Taking into account swelling anisotropy ratios for all RH steps during upward stepping RH, we obtained an overall average anisotropy ratio of 1.13. A similar average trend was also observed during downward stepping RH but with clear differences due to effects of swelling hysteresis and departures from recoverability. Within these trends, our results (Fig.8) show considerable variability not only amongst the samples, but also for individual samples depending on exposure history, i.e. from run to run on the same sample. In particular, the anisotropy ratios for the 4mm sample (Exp4_SampleP3), and for the first run on 1 mm Sample P1, are consistently lower than for the other runs performed on 1mm samples.

Similar, anisotropic swelling behaviour of coal due to adsorption of water vapour was reported by Fry et al. (2009). These authors found similar maximum volumetric swelling strain magnitudes (1.32-1.74% at 97% RH) to ours for high volatile bituminous coal, and similar anisotropy ratios (on average around 1.2) to ours for coals ranking from sub-bituminous to bituminous and for all relative humidity steps employed in their experiments. However, the anisotropy ratios were found to vary remarkably amongst the samples. Fry et al. argued that, besides measurement errors, the observed variability might be related to the inhomogeneity of the samples, with different macerals responding differently to moisture sorption. However, they did not propose any explanation for the cause of the swelling anisotropy. Here, we propose that the swelling anisotropy of coal matrix material is caused either by a) anisotropic elastic properties

due to the layered structure of coal matrix material, or b) anisotropic/layered sorption. These hypotheses are tested in the following, by comparison of our data with literature findings for adsorption of gases, such as CO_2 and CH_4.

Swelling anisotropy effects in coal, due to adsorption of gases, such as CO_2, CH_4 and N_2, have been widely reported by other workers (e.g. Day et al., 2010; Hol and Spiers, 2012; Pan and Connell, 2011). Pan and Connell (2011) proposed that swelling anisotropy is caused by anisotropy in the coal's elastic properties which is in turn determined by its layered/bedded matrix structure. Their argument was supported by good agreement between a model that assumes an anisotropic, linear elastic swelling response to isotropic internal stressing, caused by isotropic sorption, with swelling data for an unconfined Australian bituminous coal. Pan and Connell's explanation is also supported by a similar model developed by Espinoza et al. (2013), which successfully explained the experimental data reported by Hol and Spiers (2012) on anisotropic swelling of unconfined high volatile bituminous coal matrix samples exposed to CO_2 (Brzeszcze coal cylinders 4mm in diameter, by 4mm in length).

However, the anisotropic elastic swelling models proposed by Pan and Connell (2011) and by Espinoza et al. (2013) cannot explain all of our findings, notably that swelling anisotropy is related to relative humidity and exposure history (Fig. 8). This is because elastically controlled swelling anisotropy (linear elastic constants) should be independent of relative humidity value and of exposure history. Our experiments showed considerable effects, and considerable variability in effects, of RH and exposure history on swelling anisotropy. Therefore while part of the anisotropic swelling/shrinkage behaviour seen in our samples is likely due to linear elastic anisotropy of the samples, other factors must play a role too. Possibilities include a) an anisotropic distribution of micro-fractures present in the coal matrix, imparting anisotropic, non-linear elastic swelling behaviour or anisotropic water vapour access (Hol et al., 2014), b) a preferred orientation distribution (layering) of adsorption sites (i.e. oxygen functional groups)

(Pan and Connell, 2011) or c) multiple layer adsorption of water molecules or molecular clusters in layers parallel to bedding. To distinguish between the above possible explanations, further studies are needed.

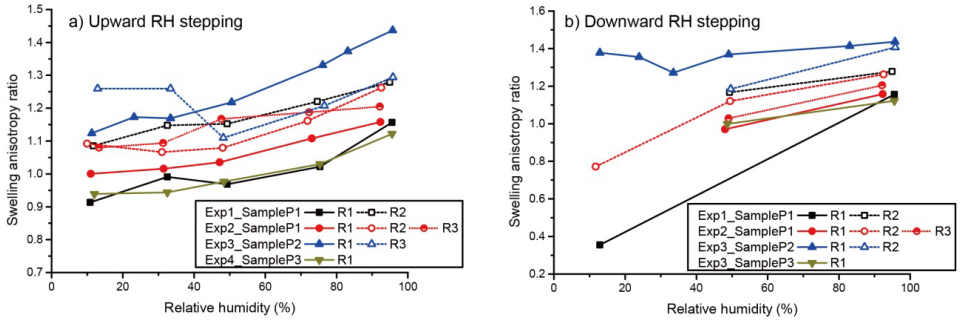

Fig. 8. Swelling anisotropy ratio $e_z^{eq} / (\frac{e_x^{eq} + e_y^{eq}}{2})$ *versus RH data plotted for the present coal samples. Note that* e_z^{eq} *is the swelling strain measured perpendicular to bedding, whereas the swelling strain of the coal matrix samples parallel to bedding is taken as the average of* e_x^{eq} *and* e_y^{eq}*. a) Data obtained during upward stepping of RH. b) Data obtained during downward stepping of RH.*

5.4.1.2. Recoverability of swelling strain

The swelling/shrinkage versus RH data presented in Fig.5 and Fig. 6 show closely recoverable behaviour (i.e. recovery of starting sample dimensions) after almost all experimental runs. An exception is Exp_SampleP1_R1, which showed excess shrinkage after RH cycling. In most cases, though, no permanent expansion or contraction occurred during adsorption-desorption. Similar recoverable swelling of coal upon water vapour sorption was also reported by Fry et al. (2009). This behavior is consistent with swelling being caused by reversible adsorption of water (see also Pan, 2012). On this basis, we infer that permanent coal softening or plasticisation effects (c.f. Immergut and

Mark, 1965) play little or no role in determining the swelling behaviour of coal during exposure to water vapour (as inferred for CO_2 sorption by Hol et al., 2012b). In Exp1_SampleP1_R1 (Fig. 5a), the 0.08% excess shrinkage observed in the z direction after RH cycling might result from residual moisture trapped in the sample prior to performing the experiments (Hol et al., 2012b), despite the fact that the sample was dried for one week under vacuum and was then exposed to 0.1% relative humidity at the start of Exp1. This explanation is supported by the evidence that the maximum swelling strains measured at RH=95% in Exp1_SampleP1_R1, if added to the final excess shrinkage, take values of $e_z^{eq} = 0.55\%$, $e_y^{eq} = 0.4\%$, $e_x^{eq} = 0.44\%$, which are closely similar to the maximum e_i^{eq} values measured in Exp1_R2 and Exp2 performed on Sample P1. The implication for Sample P1 is that trapped moisture present before Run1 may have been removed through new transport paths created in the coal matrix during Run1, via the development of micro-fractures caused by heterogeneous swelling, e.g. on the maceral scale (see also Espinoza et al., 2015; Hol et al., 2014; Hol et al., 2012b).

5.4.1.3. Swelling hysteresis

Swelling/shrinkage hysteresis was observed in almost all of our experiments (see Fig.5 and Fig.6). The origin of this hysteresis cannot be directly determined from the current experimental results. However, the following possible causes of swelling hysteresis have been proposed in the literature on coal. These are now discussed in comparison with our experimental observations.

1) Sorption hysteresis. This refers to hysteresis observed in isothermal, water adsorption-desorption experiments performed on coal, i.e. to hysteresis in adsorbed water concentration versus RH data (Charrière and Behra, 2010; McCutcheon et al., 2001; McCutcheon et al., 2003). As swelling of coal is caused by sorption of water vapour (Fry et al., 2009; Pan, 2012), true sorption hysteresis must result in swelling hysteresis. However, the mechanisms responsible for water sorption hysteresis remain

unresolved in previous studies. McCutcheon et al. (2003) attributed sorption hysteresis, observed in low rank coal (Carbon content less than 84.3%) at relative humidities > 45%, to a capillary condensation-evaporation effect. This effect leads to differences in the relative pressure of filling versus emptying small pores, and was also argued by Lin (2010) to be the cause of hysteresis in the sorption behaviour of mesoporous solids in general (i.e. solids containing pores within 2-50 nm). This explanation for sorption hysteresis is consistent with the hysteresis effects seen in our experiments, and with our finding that equilibration times for swelling upon adsorption were different from those for shrinkage upon desorption. Capillary condensation may therefore have played a role in our experiments. However, the capillary condensation-evaporation effect cannot explain sorption hysteresis observed in high rank coal or in low rank coal at relative humidities < 45% (McCutcheon et al., 2003). Under these conditions, sorption hysteresis is generally attributed to effects of swelling hysteresis, i.e. to the effect of swelling on changes in pore structure of coal (e.g. Charrière and Behra, 2010; Mahajan and Walker, 1971; McCutcheon et al., 2003). On the basis of our data, and in the context of our experiments, we see no way to distinguish between cause and effect.

2) Heterogeneous swelling of coal upon water sorption. Hol et al. (2012b) reported hysteresis in the swelling behaviour of high volatile bituminous coal samples (4mm cylinder) exposed to CO_2 at pressures up to 100MPa and at 40˚C. However, the hysteresis disappeared after one or two CO_2 pressure cycles. Based on SEM observations, Hol et al. argued that the hysteresis was caused by development of micro-fractures in the first CO_2 pressure cycle, due to heterogeneous swelling at the maceral scale. This explanation is consistent with the observation by Hol et al. that the equilibration was much faster in CO_2 cycles beyond the first. However, heterogeneous swelling and associated microcracking do not explain the swelling hysteresis observed in the present experiments, because a) no change in apparent equilibration time was observed between our first and second relative humidity runs, and b) the observed

swelling hysteresis did not disappear after the first cycle of exposure to water vapour.

3) Other possibilities. We note that the different extents of hysteresis visible in Fig. 6 might also reflect a) sampling effects related to the relatively few data obtained on shrinkage upon desorption of water vapour, b) incomplete equilibration following individual RH steps, or c) errors caused by correcting for RH effects on the dilatometer sensor signals.

Clearly, to understand the cause of swelling hysteresis in the coal matrix material investigated here, more swelling/shrinkage and corresponding sorption/desorption data are needed.

5.4.2. Effects of sample size on equilibration rate and equilibrium swelling strain

It is clear from the swelling strain versus time curves presented in Fig.4 that the rate at which (apparent) equilibrium was approached was much faster in our experiments on 1mm samples (Exp1-3, Samples P1, P2) than on the 4mm sample (Exp4, Sample P3). To illustrate this further, we use the standard graphical method applied in the literature to analyze sorption/swelling kinetics (c.f. Busch and Gensterblum, 2011; Li et al., 2010; Staib et al., 2014; Staib et al., 2013). For a given sample, this method involves plotting the change in normalized volumetric swelling strain ($\Delta e_v(t)/\Delta e_v^{eq}$) versus time ($t$) elapsed after imposing a specific step in gas/vapour pressure or activity (in our case RH). In this ratio, $\Delta e_v(t)$ is the evolving change in volumetric strain per step, and Δe_v^{eq} is the change in equilibrium strain value resulting from each step. Representative plots of this ratio ($\Delta e_v(t)/\Delta e_v^{eq}$) versus time are presented in Fig. 9 for samples P1, P2, and P3, for the relative humidity step from ~ 75% to 95%. This figure confirms that the swelling rates for 1mm samples (P1 and P2) are similar, and that the swelling rate of sample P3 (4mm) is much slower following a given change in relative humidity. On this basis, we infer that the swelling kinetics of our samples during exposure to water vapour are

indeed strongly influenced by sample size. It follows from this length scale dependence that the rate of time-dependent swelling of coal matrix during exposure to water vapour must be controlled by diffusion of water molecules through the nanoporous coal matrix, and not by the kinetics of the sorption reaction between water vapour molecules and their specific adsorption sites in the coal.

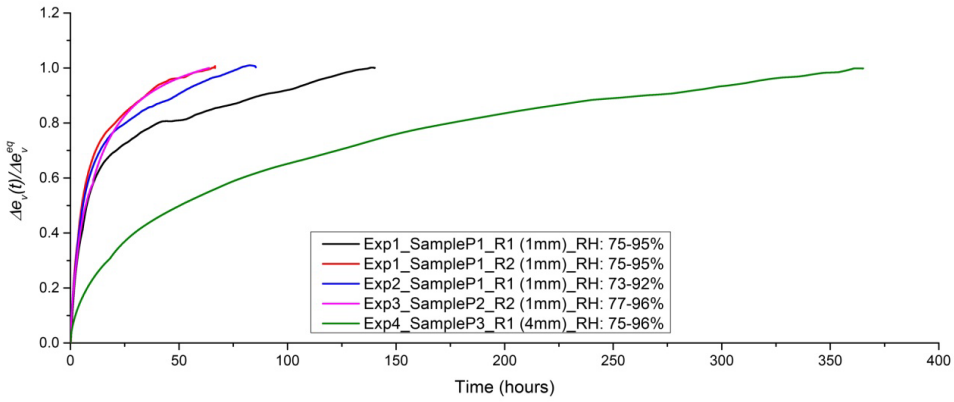

Fig. 9. Normalized volumetric swelling strain of samples P1, P2 and P3, (expressed as the ratio $\Delta e_v(t) / \Delta e_v^{eq}$ *) versus elapsed time following a step increase in relative humidity from ~ 75 to 95%. The quantity* $\Delta e_v(t)$ *represents the time-dependent change in volumetric swelling strain following the imposed step in RH (corrected for transient effects of RH on dilatometer sensor signals). The quantity* Δe_v^{eq} *represents the change in near equilibrium volumetric swelling strain produced by the RH step.*

At the same time, our results in Fig.6e clearly demonstrate that the volumetric swelling strain attained at equilibrium, at any given relative humidity, is similar for samples P1 and P2 (1 mm) and for P3 (4 mm). This implies that the equilibrium swelling strain of coal exposed to water vapour is insensitive to sample size, at least for the cleat-free coal matrix material. Moreover, our results show that the equilibrium volumetric strains of 1.37-1.43% attained in our Breszcze high volatile bituminous coal

samples, when equilibrated with water vapour at 95% relative humidity at 40˚C, are similar to those reported in the literature for different coals and different sample sizes (Fry et al., 2009; Pan, 2012; van Bergen et al., 2009). Specifically, Fry et al. (2009) measured (apparent) equilibrium volumetric strains in the range of 1.32-1.74% for seven different high volatile bituminous coals, using 30×9×9 mm^3 cylindrical samples tested at room temperature at 97% relative humidity. We infer that the effects of sample size and the presents of cleats on equilibrium swelling strain are probably small provided sufficient time is allowed for true equilibrium. On the other hand, our swelling kinetics analysis (Fig.9) demonstrates that it might be impossible to reach true equilibration in experiments on coal samples beyond several cm in size, at least on practical lab time scales. Failure to reach equilibrium swelling in some experiments might even be due to sorption-induced swelling at fracture walls, causing fracture closure and reducing sample permeability even under unconfined conditions allowing free-expansion. A similar notion was recently put forward by Peng et al. (2014), who developed a conceptual model for permeability changes in coal due to diffusion and adsorption of gases.

5.4.3. Relationship between equilibrium swelling strain and RH: comparison with theory

5.4.3.1. Models for volumetric swelling strains versus activity of water vapour

The present results demonstrate a direct dependence of swelling strain at (apparent/near) equilibrium upon RH (see Figs 4-6). Now we consider the relationship between adsorption-induced volumetric swelling strain (e_v^{eq}), adsorbed water concentration (C), and relative humidity (RH) or water vapour activity (a_g) from a theoretical perspective. We first consider the relationship between swelling strain e_v^{eq} and adsorbed water concentration C. It has been shown experimentally that, for coal ranking from lignite to bituminous, the swelling strain produced by water vapour

sorption is linearly proportional to the adsorbed concentration C (mol/kg$_{coal}$) (Fry et al., 2009; Suuberg et al., 1993). On this basis, and noting the similar relation obtained by Hol and Spiers (2012) for swelling of unconfined coal matrix due to adsorption of CO_2, the equilibrium volumetric swelling strain caused by adsorption of water vapour can be expressed as

$$e_v^{eq} = C\rho V_0 \tag{1}$$

Here ρ represents the density (m^3/kg) of the coal matrix material, and V_0 (m^3/mol) represents the bulk volume change of the coal matrix due to adsorption of one mole of water molecules. V_0 can thus be viewed as the partial molar volume of adsorbed water molecules. The magnitude of V_0 for water molecules will in general depend on sorption bond strength and the response of the coal matrix to accommodating adsorbed molecules. V_0 accordingly depends on coal rank. Generally speaking, the higher the coal rank, the lower the measured magnitude of V_0. Fry et al. (2009) systematically measured the expansion and sorption response of 14 different bituminous coals and 1 sub-bituminous coal, to exposure to water vapour at relative humidities up to 97% at room temperature (22˚C). The results showed a linear relationship resembling equation 1 between the volumetric swelling strain and adsorbed concentration of water, yielding V_0=4.3×10^{-6} m^3/mol. From drying/shrinkage experiments on coals ranging from lignite to bituminous, Suuberg et al. (1993) obtained V_0=12.9×10^{-6} m^3/mol. In the present study on high volatile bituminous coal, we assume a value of V_0 based on the data of Fry et al. (2009), i.e. we assume V_0=4.3×10^{-6} m^3/mol.

Now we focus on the relation between adsorbed water concentration and water vapour activity. Direct measurement by FTIR (Mu and Malhotra, 1991) and ionic thermal current methods (Suárez et al., 1993) confirmed that adsorption of water vapour is strongly related to oxygen-bearing functional groups. Water molecules are therefore generally considered to be trapped primarily by oxygen-bearing functional groups present in the coal matrix, via hydrogen bonds (Allardice and Evans, 1971; Kaji et al.,

1986; Mahajan and Walker, 1971; McCutcheon et al., 2003). Water thus adsorbed forms the first layer of adsorbed molecules, having high biding energy (c.f. Dubinin, 1980; Dubinin and Serpinsky, 1981). These adsorbed water molecules then form the secondary sites for attachment of additional water molecules with lower binding energy (c.f. Charrière and Behra, 2010; Lynch and Webster, 1982; McCutcheon et al., 2003; Nishino, 2001; Švábová et al., 2011). This multiple layer sorption mechanism is supported by experimental data on the concentration of adsorbed water molecules versus relative pressure obtained from isothermal sorption experiments performed on different rank coals (c.f. Charrière and Behra, 2010; McCutcheon et al., 2003; Švábová et al., 2011). The Brunauer-Emmett-Teller (BET) model, developed for multilayer sorption on the basis of Langmuir model (Brunauer et al., 1938), is the best-known and most commonly used model to describe water sorption (Charrière and Behra, 2010). It reduces to the Langmuir model if only single layer adsorption occurs. However, the BET model only fits water sorption data obtained at low relative humidity (Charrière and Behra, 2010; Skaar, 2012). Dent (1977) accordingly modified the BET model, assuming that the thermodynamic properties of water molecules adsorbed primarily by coal are different from those adsorbed secondarily. Writing the relative pressure of water vapour in terms of the activity of water vapour, the Dent model can be expressed as

$$C_1 = \frac{C_s K_1 a_g}{1 - K_2 a_g + K_1 a_g} \tag{2a}$$

$$C_2 = \frac{C_s K_1 K_2 a_g^{\,2}}{(1 - K_2 a_g)(1 - K_2 a_g + K_1 a_g)} \tag{2b}$$

where C_1 (mol/kg$_{coal}$) and C_2 (mol/kg$_{coal}$) represent the concentration of water molecules associated with primary adsorption and secondary adsorption, respectively. The quantity C_s (mol/kg$_{coal}$) represents the total number of localized adsorption sites (in mol) present in one kilogram of coal matrix for water molecules, while K_1 and K_2 represent the equilibrium constants for primary adsorption and secondary adsorption. Like the BET

model, the Dent model assumes that the adsorption sites present in coal are available for both monolayer adsorption and multiple-layer adsorption. If no secondary adsorption occurs, the Dent model reduces to the single layer Langmuir model expressed in terms of gas activity as

$$C_1 = \frac{C_s K_1 a_g}{1 + K_1 a_g} \tag{3}$$

which is identical also to the single layer, localized sorption site model developed by Hol et al. (2012a) and by Liu et al. (Chapter 3).

By contrast to the BET, Dent and Langmuir models, D'Arcy and Watt (1970) assumed that different functional groups present in the coal matrix are characterized by different adsorption mechanisms. They assumed that some adsorption sites allow monolayer adsorption with strong binding energy, some adsorption sites allow monolayer adsorption with weak binding energy, and some allow multiple layer adsorption. Neglecting the monolayer adsorption with weak binding energy, the D'Arcy and Watt (DW) model (Barton et al., 1994; Furmaniak et al., 2008; McCutcheon et al., 2003; Švábová et al., 2011) was formulated as a combination of the Langmuir isotherm for monolayer adsorption with strong binding energy (Langmuir, 1918), and the Dubinin and Serpinsky (DS1) isotherm (Dubinin and Serpinsky, 1981) for multiple-layer adsorption. Upon replacing the relative pressure of water vapour by the activity of water vapour, the result can be expressed as

$$C = \frac{C_{s1} K_1 a_g}{1 + K_1 a_g} + \frac{C_{s2} K_2 a_g}{1 - K_2 a_g} \tag{4}$$

Here C (mol/kg$_{coal}$) represents the total concentration of water molecules adsorbed, while C_{s1} and C_{s2} (mol/kg$_{coal}$) represent the number of localized adsorption sites (in mol) present in one kilogram of coal matrix for monolayer adsorption and for multiple-layer adsorption, respectively. The quantities K_1 and K_2 represent the

equilibrium constants for monolayer adsorption and multiple-layer adsorption. In the DW model, monolayer adsorption is again identified as primary adsorption, while further multiple-layer adsorption is identified as secondary adsorption (McCutcheon et al., 2003; Švábová et al., 2011). If only single layer adsorption occurs, the model again reduces to the Langmuir type equation (c.f. equation 3).

Having established relations between e_v^{eq} and C, and between C and a_g, we now consider the relation between e_v^{eq} and a_g, by combining equations 1-4. We start from an end-member case that the swelling of coal upon water adsorption is caused solely by adsorption of a first layer of water molecules, as expressed via the Dent model (equation 3), or solely by monolayer adsorption with strong biding energy as described via the DW model (equation 4). Using equation 1, this end-member case can thus be formulated as

$$e_v^{eq} = \frac{C_s K a_g}{1 + K a_g} \rho V_0 \tag{5}$$

which is identical to the model developed by Hol and Spiers (2012) for swelling of unconfined coal matrix caused by adsorption of CO_2. For simplicity, we refer to this end-member case (i.e. equation 5) as the HS swelling model. For the more general case, where the swelling is caused by both primary and secondary adsorption, we assume that V_0 is the same for all adsorbed water molecules, regardless of adsorption site type. Using the Dent and DW models, we accordingly obtain the following expressions for the total swelling of coal matrix material due to adsorption of water vapour, namely

$$\begin{aligned} e_v^{eq} &= \rho V_0 (C_1 + C_2) \\ &= \rho V_0 C_s \left(\frac{K_1 a_g}{1 - K_2 a_g + K_1 a_g} + \frac{K_1 K_2 {a_g}^2}{(1 - K_2 a_g)(1 - K_2 a_g + K_1 a_g)} \right) \end{aligned} \tag{6}$$

for the Dent-based case, and

$$e_v^{eq} = \rho V_0 \left(\frac{C_{s1} K_1 a_g}{1 + K_1 a_g} + \frac{C_{s2} K_2 a_g}{1 - K_2 a_g}\right) \quad (7)$$

for the DW-based case. Henceforth, we refer to equations 6 and 7 as the Dent-based swelling model and the DW-based swelling model.

5.4.3.2. Swelling models versus experimental data

To compare our experimental data with the above models, we first convert our equilibrium volumetric swelling strain (e_v^{eq}) versus RH data (Fig.6e) into e_v^{eq} versus water activity data. To do this, the activity (a_g) of water vapour at the experimentally imposed RH values was calculated using the EoS for water developed by Wagner and Pruß (2002). The results obtained for the upward RH steps of all experimental runs are plotted in Fig. 10 (omitting the data obtained for Exp1_SampleP1_R1, and that obtained for Exp4_SampleP3_R1 at an RH value of 12%, which have been shown above to be influenced by excess shrinkage and non-equilibrium swelling effects). Best fits of the HS, the Dent-based and the DW-based swelling models to the data plotted in Fig. 10 were obtained by means of non-linear regression, using V_0=4.3×10^{-6} m^3/mol (see Fig. 10). It is clearly seen that all three models fit the experimental data equally well. The HS model showed a near-linear fit, while the Dent-based and the DW-based models showed almost identical sigmoidal fits. The corresponding fitting parameter values are presented in Table 4, and all are reasonable when compared with those obtained from fits to previous sorption versus relative pressure data (c.f. Charrière and Behra, 2010; McCutcheon et al., 2003; Pan, 2012; Švábová et al., 2011). This means that the present study cannot distinguish between the three swelling models. For further progress, then, a better understanding of the mechanism for swelling of coal matrix material due to adsorption of water vapour is needed.

Table 4. Fitting parameter values of the models.

Model	C_s(mol/kg$_{coal}$)	K	C_{s1}(mol/kg$_{coal}$)	C_{s2}(mol/kg$_{coal}$)	K_1	K_2
HS	18.288	0.161				
Dent-based	1.671				2.346	0.480
DW-based			2.966	0.587	1.11	0.65

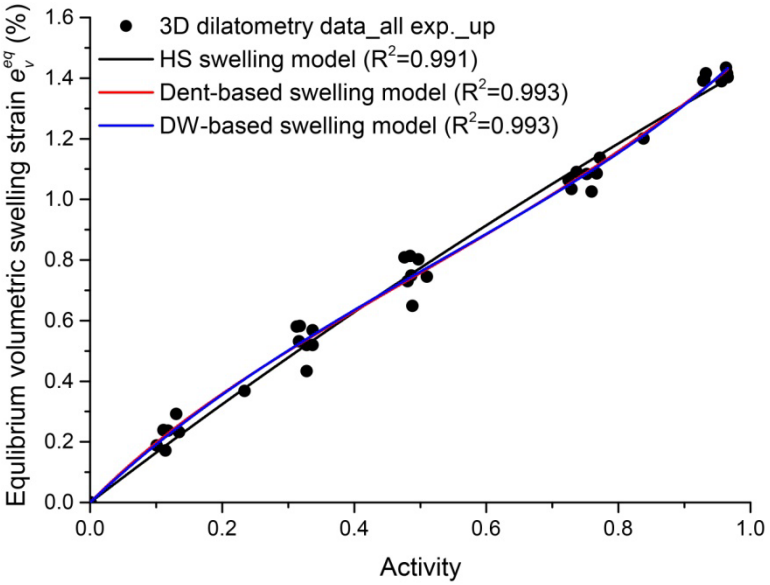

Fig. 10. Volumetric swelling strain at equilibrium versus water vapour activity. The black dots represent the experimental data obtained from the RH up-stepping portions of all experimental reported in Fig.6e, except for Exp1_SampleP1_R1 and the data point attained at a RH value of 12% of Exp4_SampleP3_R1 (see text). The solid lines represent the best fits of the HS, the Dent-based and the DW-based models (equations 5, 6, 7 respectively).

5.4.4. Implications for ECBM

Our findings have a number of implications for (E)CBM production. These are considered pointwise below.

1. Our results demonstrate that the swelling of coal upon adsorption of water vapour

increases with increasing relative humidity. This suggests that the use of water-free fluids for hydraulic fracturing of coal seams will produce better stimulation results than using aqueous fluids.

2. The present experiments have shown that the exposure of Brzeszcze high volatile bituminous coal to water vapour at 95% relative humidity at 40˚C, leads to adsorption-induced volumetric swelling strains of 1.37-1.43% at equilibrium. However, the same coal exhibits an equilibrium volumetric swelling strain of only 1.29-1.39% upon adsorption of CH_4 at a pressure of 10MPa at 40˚C (Liu et al., Chapter 3). Upon adsorption of CO_2 at the same *PT* conditions, equilibrium volumetric swelling strains of 2.37-2.47% are obtained (Hol and Spiers, 2012). This suggests that for high volatile bituminous coal, such as the Brzeszcze coal, reducing the in-situ water activity or relative humidity might shrink the coal, thus releasing methane, causing further shrinkage and hence creating self-enhancing transport paths (e.g. Fry et al., 2009; Levine, 1996; Liu et al., 2011; Moore, 2012).

3. On the basis of points 1 and 2, and taking into account that coal swelling strains caused by adsorption of N_2 are generally about half of that caused by CH_4 sorption at the same *PT* conditions (c.f. Battistutta et al., 2010; Day et al., 2012; Day et al., 2010), it might be a good strategy to use (liquid) N_2 as a hydraulic-fracturing fluid to stimulate CBM production from coal seams, which is also technically feasible (c.f. McDaniel et al., 1997). This could be followed by circulating dry gaseous N_2 to promote matrix shrinkage by removing water and methane. After such a phase of N_2-ECBM production, i.e. after removing water and methane, CO_2 could be injected into the coal seam for geological storage. This strategy has two advantages. The first is that shrinkage upon removing water and CH_4 from coal seam will create more transport paths for CO_2 injection and storage. The second is that the larger swelling effect caused by adsorption of CO_2, compared with the shrinkage effect of removing water and CH_4 may result in self-sealing of coal seams.

4. Our experimental results demonstrate that the swelling/shrinkage response of coal matrix material to exposure to water vapour is rate controlled by diffusion. This means that diffusion of water between coal matrix material and cleat/fracture systems must be considered in predicting in-situ coal seam permeability evolution during (E)CBM production.

5.5. Conclusions

In this study, we have reported the results of detailed 3D dilatometry experiments performed on two 1mm and one 4mm cubes of high volatile bituminous coal matrix material (Brzeszcze, Poland), exposed to water vapour. The experiments were conducted at relative humidities varied in the range 0.1 to 95%, under unconfined conditions and at a constant temperature of 40˚C. We considered the effects of sample size and relative humidity on swelling kinetics and on equilibrium swelling strain. The main findings and conclusions are summarized as follows:

1. The swelling response of our samples to water adsorption was anisotropic with the swelling strain developed perpendicular to bedding being on average about 1.13 times that occurring parallel to bedding on average, though this ratio varied with relative humidity. The swelling response was largely reversible and/or recoverable, with some hysteresis effects. The observed dependence of the swelling strain anisotropy ratio on RH suggests that the anisotropic swelling effect is not solely determined by elastic anisotropy of the coal studied.
2. Sample size was found to strongly influence the swelling kinetics of coal matrix material at a given relative humidity, but does not influence the magnitude of swelling strain attained at equilibrium. This confirms that time-dependent swelling/shrinkage of unconfined coal matrix during exposure to water vapour is controlled by diffusion of water molecules as opposed to sorption reaction kinetics.

3. The volumetric swelling strains attained by our coal samples at equilibrium showed a near-linear relation with relative humidity, reaching a value of 1.37-1.43% at around 95% relative humidity. This volumetric swelling strain, caused by exposure of Brzeszcze high volatile bituminous coal to water vapour at 95% relative humidity, is similar to that produced by exposure to and sorption of CH_4 at 10MPa. By contrast, the observed volumetric swelling strain is about 0.6 times that caused by sorption of CO_2 at 10MPa pressure.
4. Three models for swelling of unconfined coal matrix material due to water sorption have been developed. The three models respectively address the equilibrium swelling strain caused by mono-layer adsorption, by multiple-layer sorption, and by combined mono- plus multiple-layer adsorption. The equilibrium swelling strain versus RH or water activity data obtained in the present experiments can be well fitted by all three models, so that the mechanism dominating water vapour adsorption and associated swelling could not be pinpointed.
5. Our findings suggest that it might be a good strategy to use (liquid) N_2 as a hydraulic-fracturing fluid to stimulate the coal seams for CBM production, then circulating dry N_2 to promote the shrinkage due to removal of water and methane. CO_2 might later be injected into the coal seam for geological storage, resulting in self-sealing of fractures in the coal bed system due to the relatively large swelling strain caused by CO_2 sorption.

Appendix

A1. The quality of RH control achieved using saturated salt solution buffers in the experiments reported in this paper is illustrated in Fig.A1 for a coal sample run. Note the rapid equilibration of RH throughout the system.

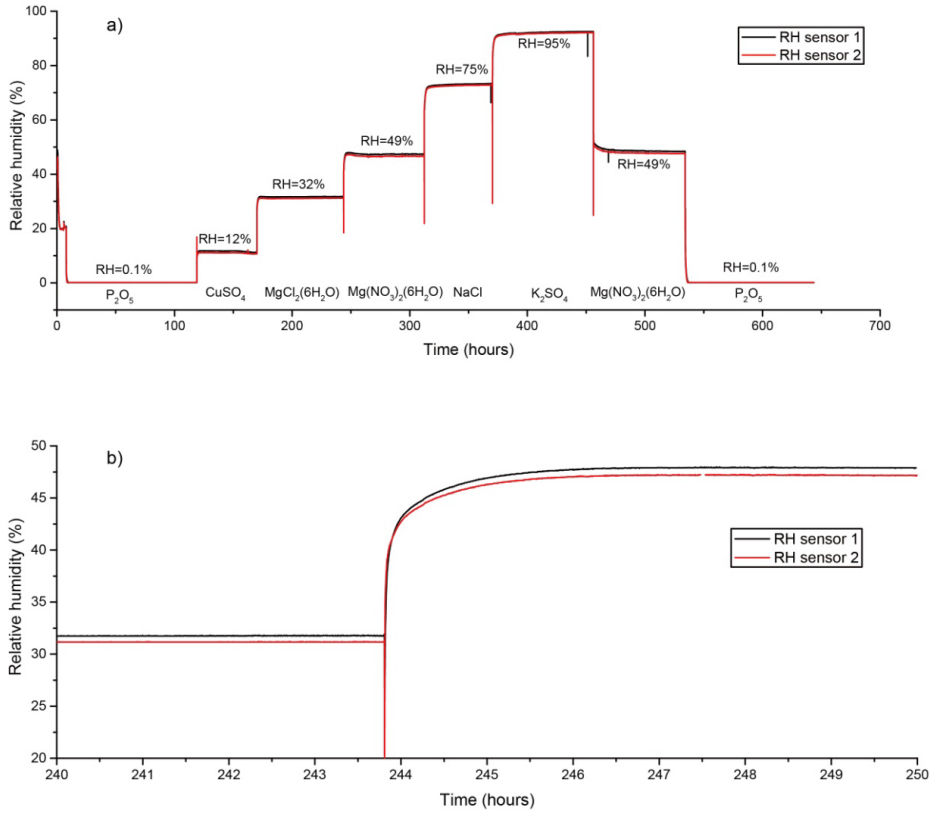

Fig.A1. Representative data showing relative humidity (%) measured by the digital relative humidity sensors as a function of time during our experiments. a) RH control achieved during a typical experiment using the salt buffer solutions indicated. b) Blow up of transient in RH upon change in RH from 32 ($MgCl_2$•6H2O) to 49% ($Mg(NO_3)_2$•6H2O).

A2. The quality of temperature control achieved in the experiments in illustrated in Fig. A2.

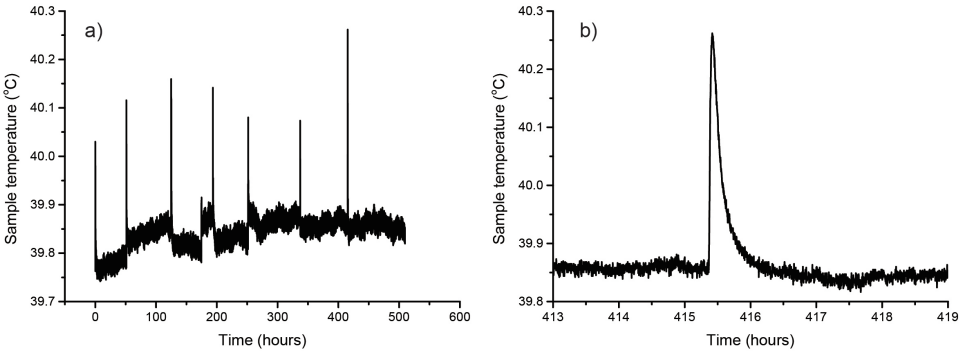

Fig.A2. Representative data showing the sample temperature measured using a PT-100 element versus time during a typical experiment. a) Aside from the spikes that occurred upon changing RH buffer, the sample temperature remained constant within ~0.1˚C. b) After an RH step (buffer change), stabilization of temperature took ~1 hour.

A3. Calibration of RH effect on sensor signals

Since the 3D eddy current sensor is fully exposed to water vapour, sorption of water vapour on the sensor and by the electrical insulation covering the sensor cables (e.g. Pons et al., 2014) leads to time-dependent effects on the 3 orthogonal sensor signals. To determine the magnitude of these RH-related effects on sensor signals, control experiments were performed on three different dummy samples, namely one 4mm stainless steel cube, one 1mm stainless steel cube, and one 1mm quartz glass cube, following identical experimental procedures as applied when using coal samples. After each relative humidity step, sensor signal changes slowly with time, typically reaching equilibrium in 1-2 days. The results confirm that the RH effects on sensor signals are insensitive to sample material and sample size. A typical curve for RH effects on sensor signals, expressed in terms of equivalent apparent swelling displacement, versus time, obtained from the control experiments, is plotted in Fig. 11. It is seen that the apparent swelling displacement versus time curve was similar in form to the uncorrected swelling/shrinkage of coal samples versus time.

In addition, the results shown in Fig. 11 demonstrate that the RH effects on sensor

signals cannot be neglected. This means that to determine the true response of coal sample during exposure to water vapour, we must correct for this effect. Equilibrium effects of RH changes on sensor signals were corrected for using fitted functions describing near equilibrium sensor signals, expressed in terms of apparent displacement (μm), versus RH. For RH upward stepping, we applied the non-linear regression method to fit the hyperbolic function $y = \frac{ax}{1-bx}$ to the apparent displacement versus RH data for each sensor at or near equilibrium (see Fig.12a). For RH downward steps, the apparent displacement data were fitted using linear regression (see Fig.12b), because insufficient data points were obtained from the two relative humidity steps implemented to allow non-linear regression. The best fits (dashed lines) shown in Fig. 12 were used to describe the effect of RH on sensor signal and apparent equivalent swelling at equilibrium.

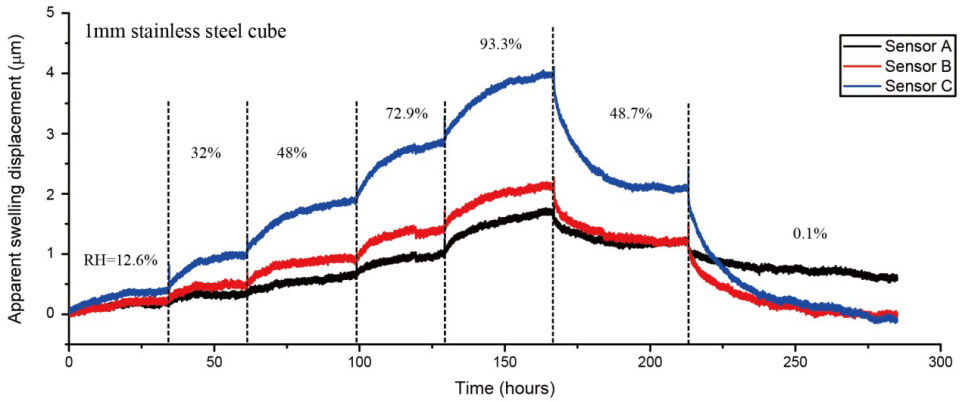

Fig.11. Representative data showing RH effects on sensor signals, expressed in terms of equivalent apparent swelling displacement (μm) versus time.

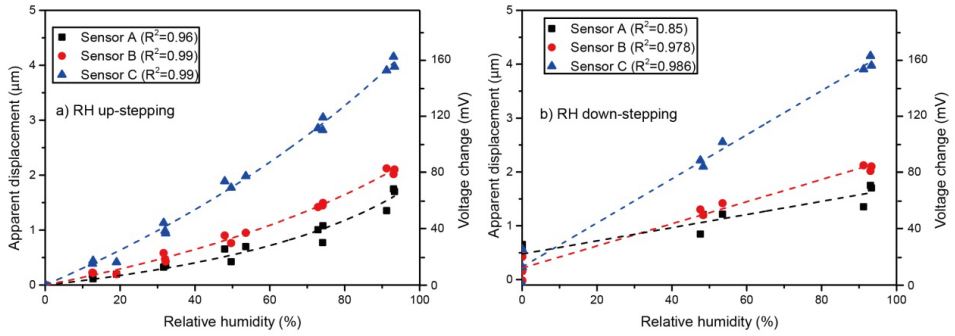

Fig. 12. Apparent displacement measured by each sensor in the 3D dilatometer at or near equilibrium for all dummy samples, plotted as a function of relative humidity. a) RH up-stepping sequence. The solid symbols represent the apparent target displacement by each sensor purely due to the effect of RH change on the sensor system. The dashed lines represent non-linear regression fits. b) RH down-stepping sequence. The solid symbols again represent apparent target displacement measured by each sensor, and the dashed lines represent the linear regression fits to the very limited data.

Acknowledgements

The China Scholarship Council (CSC) and Total S.A. are gratefully acknowledged for their financial support of first author Jinfeng Liu and of the research project.

References

Allardice, D., Evans, D., 1971. The-brown coal/water system: Part 2. Water sorption isotherms on bed-moist Yallourn brown coal. Fuel 50, 236-253.

Barton, S., Evans, M., MacDonald, J., 1994. Adsorption of water vapor on nonporous carbon. Langmuir 10, 4250-4252.

Battistutta, E., Van Hemert, P., Lutynski, M., Bruining, H., Wolf, K.-H., 2010. Swelling and sorption experiments on methane, nitrogen and carbon dioxide on dry Selar Cornish coal. International Journal of Coal Geology 84, 39-48.

Brunauer, S., Emmett, P.H., Teller, E., 1938. Adsorption of gases in multimolecular layers. J

Am Chem Soc 60, 309-319.

Busch, A., Gensterblum, Y., 2011. CBM and CO_2-ECBM related sorption processes in coal: A review. International Journal of Coal Geology 87, 49-71.

Charrière, D., Behra, P., 2010. Water sorption on coals. J Colloid Interf Sci 344, 460-467.

D'Arcy, R., Watt, I., 1970. Analysis of sorption isotherms of non-homogeneous sorbents. Transactions of the Faraday Society 66, 1236-1245.

Day, S., Fry, R., Sakurovs, R., 2008a. Swelling of Australian coals in supercritical CO_2. International Journal of Coal Geology 74, 41-52.

Day, S., Fry, R., Sakurovs, R., 2011. Swelling of moist coal in carbon dioxide and methane. International Journal of Coal Geology 86, 197-203.

Day, S., Fry, R., Sakurovs, R., 2012. Swelling of coal in carbon dioxide, methane and their mixtures. International Journal of Coal Geology 93, 40-48.

Day, S., Fry, R., Sakurovs, R., Weir, S., 2010. Swelling of coals by supercritical gases and its relationship to sorption. Energ Fuel 24, 2777-2783.

Day, S., Sakurovs, R., Weir, S., 2008b. Supercritical gas sorption on moist coals. International Journal of Coal Geology 74, 203-214.

Dent, R., 1977. A multilayer theory for gas sorption part I: sorption of a single gas. Textile Research Journal 47, 145-152.

Dubinin, M., 1980. Water vapor adsorption and the microporous structures of carbonaceous adsorbents. Carbon 18, 355-364.

Dubinin, M., Serpinsky, V., 1981. Isotherm equation for water vapor adsorption by microporous carbonaceous adsorbents. Carbon 19, 402-403.

Espinoza, D., Pereira, J.-M., Vandamme, M., Dangla, P., Vidal-Gilbert, S., 2015. Desorption-induced shear failure of coal bed seams during gas depletion. International Journal of Coal Geology 137, 142-151.

Espinoza, D., Vandamme, M., Dangla, P., Pereira, J.M., Vidal-Gilbert, S., 2013. A transverse isotropic model for microporous solids: Application to coal matrix adsorption and swelling. Journal of Geophysical Research: Solid Earth 118, 6113-6123.

Fry, R., Day, S., Sakurovs, R., 2009. Moisture-induced swelling of coal. International Journal of Coal Preparation and Utilization 29, 298-316.

Furmaniak, S., Gauden, P.A., Terzyk, A.P., Rychlicki, G., 2008. Water adsorption on carbons—Critical review of the most popular analytical approaches. Advances in colloid and interface science 137, 82-143.

Gensterblum, Y., Busch, A., Krooss, B.M., 2014. Molecular concept and experimental

evidence of competitive adsorption of H_2O, CO_2 and CH_4 on organic material. Fuel 115, 581-588.

Gensterblum, Y., Merkel, A., Busch, A., Krooss, B.M., 2013. High-pressure CH_4 and CO_2 sorption isotherms as a function of coal maturity and the influence of moisture. International Journal of Coal Geology 118, 45-57.

Hol, S., Gensterblum, Y., Massarotto, P., 2014. Sorption and changes in bulk modulus of coal—experimental evidence and governing mechanisms for CBM and ECBM applications. International Journal of Coal Geology 128, 119-133.

Hol, S., Peach, C.J., Spiers, C.J., 2011. Applied stress reduces the CO_2 sorption capacity of coal. International Journal of Coal Geology 85, 128-142.

Hol, S., Peach, C.J., Spiers, C.J., 2012a. Effect of 3-D stress state on adsorption of CO_2 by coal. International Journal of Coal Geology 93, 1-15.

Hol, S., Spiers, C.J., 2012. Competition between adsorption-induced swelling and elastic compression of coal at CO_2 pressures up to 100MPa. J Mech Phys Solids 60, 1862-1882.

Hol, S., Spiers, C.J., Peach, C.J., 2012b. Microfracturing of coal due to interaction with CO_2 under unconfined conditions. Fuel 97, 569-584.

Immergut, E.H., Mark, H.F., 1965. Principles of plasticization.

Kaji, R., Muranaka, Y., Otsuka, K., Hishinuma, Y., 1986. Water absorption by coals: effects of pore structure and surface oxygen. Fuel 65, 288-291.

Langmuir, I., 1918. The adsorption of gases on plane surfaces of glass, mica and platinum. J Am Chem Soc 40, 1361-1403.

Levine, J.R., 1996. Model study of the influence of matrix shrinkage on absolute permeability of coal bed reservoirs. Geological Society, London, Special Publications 109, 197-212.

Li, D., Liu, Q., Weniger, P., Gensterblum, Y., Busch, A., Krooss, B.M., 2010. High-pressure sorption isotherms and sorption kinetics of CH_4 and CO_2 on coals. Fuel 89, 569-580.

Lin, W., 2010. Gas sorption and the consequent volumetric and permeability change of coal.

Liu, J., Chen, Z., Elsworth, D., Qu, H., Chen, D., 2011. Interactions of multiple processes during CBM extraction: A critical review. International Journal of Coal Geology 87, 175-189.

Lynch, L.J., Webster, D.S., 1982. Effect of thermal treatment on the interaction of brown coal and water: a nuclear magnetic resonance study. Fuel 61, 271-275.

Mahajan, O., Walker, P., 1971. Water adsorption on coals. Fuel 50, 308-317.

McCutcheon, A., Barton, W., Wilson, M., 2001. Kinetics of water adsorption/desorption on

bituminous coals. Energ Fuel 15, 1387-1395.

McCutcheon, A.L., Barton, W.A., Wilson, M.A., 2003. Characterization of water adsorbed on bituminous coals. Energ Fuel 17, 107-112.

McDaniel, B., Grundmann, S.R., Kendrick, W.D., Wilson, D.R., Jordan, S.W., 1997. Field applications of cryogenic nitrogen as a hydraulic fracturing fluid, SPE Annual Technical Conference and Exhibition. Society of Petroleum Engineers.

Merkel, A., Gensterblum, Y., Krooss, B.M., Amann, A., 2015. Competitive sorption of CH_4, CO_2 and H_2O on natural coals of different rank. International Journal of Coal Geology 150, 181-192.

Moore, T.A., 2012. Coalbed methane: A review. International Journal of Coal Geology 101, 36-81.

Mu, R., Malhotra, V., 1991. A new approach to elucidate coal-water interactions by an in situ transmission FT-ir technique. Fuel 70, 1233-1235.

Nishino, J., 2001. Adsorption of water vapor and carbon dioxide at carboxylic functional groups on the surface of coal. Fuel 80, 757-764.

Pan, Z., 2012. Modeling of coal swelling induced by water vapor adsorption. Frontiers of Chemical Science and Engineering 6, 94-103.

Pan, Z., Connell, L.D., 2011. Modelling of anisotropic coal swelling and its impact on permeability behaviour for primary and enhanced coalbed methane recovery. International Journal of Coal Geology 85, 257-267.

Pan, Z., Connell, L.D., Camilleri, M., Connelly, L., 2010. Effects of matrix moisture on gas diffusion and flow in coal. Fuel 89, 3207-3217.

Pan, Z., Wood, D.A., 2015. Coalbed methane (CBM) exploration, reservoir characterisation, production, and modelling: A collection of published research (2009–2015). Journal of Natural Gas Science and Engineering 26, 1472-1484.

Peng, Y., Liu, J., Wei, M., Pan, Z., Connell, L.D., 2014. Why coal permeability changes under free swellings: New insights. International Journal of Coal Geology 133, 35-46.

Pons, E., Yrieix, B., Heymans, L., Dubelley, F., Planes, E., 2014. Permeation of water vapor through high performance laminates for VIPs and physical characterization of sorption and diffusion phenomena. Energy and Buildings 85, 604-616.

Skaar, C., 2012. Wood-water relations. Springer Science & Business Media.

Staib, G., Sakurovs, R., Gray, E.M., 2014. Kinetics of coal swelling in gases: Influence of gas pressure, gas type and coal type. International Journal of Coal Geology 132, 117-122.

Staib, G., Sakurovs, R., Gray, E.M.A., 2013. A pressure and concentration dependence of

CO_2 diffusion in two Australian bituminous coals. International Journal of Coal Geology 116, 106-116.

Suárez, N., Laredo, E., Nava, R., 1993. Characterization of four hydrophilic sites in bituminous coal by ionic thermal current measurements. Fuel 72, 13-18.

Suuberg, E.M., Otake, Y., Yun, Y., Deevi, S.C., 1993. Role of moisture in coal structure and the effects of drying upon the accessibility of coal structure. Energ Fuel 7, 384-392.

Švábová, M., Weishauptová, Z., Přibyl, O., 2011. Water vapour adsorption on coal. Fuel 90, 1892-1899.

van Bergen, F., Pagnier, H., Krzystolik, P., 2006. Field experiment of enhanced coalbed methane-CO_2 in the upper Silesian basin of Poland. Environmental Geosciences 13, 201-224.

van Bergen, F., Spiers, C., Floor, G., Bots, P., 2009. Strain development in unconfined coals exposed to CO_2, CH_4 and Ar: Effect of moisture. International Journal of Coal Geology 77, 43-53.

Wagner, W., Pruß, A., 2002. The IAPWS formulation 1995 for the thermodynamic properties of ordinary water substance for general and scientific use. Journal of Physical and Chemical Reference Data 31, 387-535.

White, C.M., Smith, D.H., Jones, K.L., Goodman, A.L., Jikich, S.A., LaCount, R.B., DuBose, S.B., Ozdemir, E., Morsi, B.I., Schroeder, K.T., 2005. Sequestration of carbon dioxide in coal with enhanced coalbed methane recovery a review. Energ Fuel 19, 659-724.

Yu, J., Tahmasebi, A., Han, Y., Yin, F., Li, X., 2013. A review on water in low rank coals: the existence, interaction with coal structure and effects on coal utilization. Fuel Process Technol 106, 9-20.

Chapter 6

Effect of applied stress on swelling of coal due to adsorption of water

Jinfeng Liu, Peter A. Fokker, Colin J. Peach, Christopher J. Spiers

Abstract

This paper investigates whether or not applied stress reduces swelling of coal upon adsorption of water, and, if so, what mechanisms are responsible. With this aim, thermodynamic models were developed addressing the effect of a general applied stress on water adsorption capacity and associated swelling behaviour of coal matrix material, assuming monolayer, multilayer and mixed mono/multilayer adsorption mechanisms. These all predict that applied stress reduces water adsorption capacity and hence swelling. In addition, experiments were performed on both a solid disc and on pre-compacted powders of Brzeszcze high volatile bituminous coal at a constant temperature of 40˚C, using a uniaxial compaction/compression apparatus. The mechanical response of the samples to stepwise axial loading was determined under both evacuated (i.e. 0% relative humidity) and water-exposed (i.e. 100% relative humidity) conditions. The evacuated samples showed reversible, elastic behaviour. Water-exposed samples exhibited elastic deformation, time-dependent reversible deformation, plus permanent creep. Axial swelling strains due to introduction of distilled water (i.e. 100% relative humidity) at a constant fluid pressure of 0.1 MPa were also measured for samples subjected to fixed axial stresses in the range of 25-100 MPa. The results demonstrated that swelling due to water adsorption is reduced by the applied stress. Comparison with predictions made using the three models investigated shows that stress-driven reduction in sorption-induced swelling is caused by the combined effects of a) permanent time-dependent (compressive) deformation (creep), b) the thermodynamic effect of a stress-driven reduction in water sorption capacity and c) stress-driven closure of transport paths within the coal matrix. For the solid disc investigated, mechanism (c) contributed mostly, while for powdered samples, mechanism (a) dominated. Nonetheless, our results show that the above effects of stress on the swelling response of (Brzeszcze) high volatile bituminous to water are minor at typical in-situ stresses of 10-30 MPa. This means that the large shrinkage effect due to drying seen in unconfined experiments is not changed by in-situ stresses. The implication is that, removing water from coal seams under in-situ (E)CBM conditions, by processes such as nitrogen flushing, may be capable of initiating self-enhancing shrinkage and (micro)cracking of the coal, thus enhancing methane production.

6.1. Introduction

Subsurface coal seams generally consist of low permeability coal matrix material cross cut by a multiscale network of joints or cleats (Hol et al., 2012a; Laubach et al., 1998; Levine, 1996). These systems often contain large amounts of methane (CH_4) and water, in part trapped in fluid form in the cleat system but mostly trapped in adsorbed form in the nanoporous coal matrix (White et al., 2005). Primary production of coalbed methane (CBM) is typically accomplished by drawing down the pressure of pore water trapped in the cleat system. Methane then desorbs from the coal matrix as the pressure transmitted to free methane present in the cleats falls below the equilibrium pressure measured with respect to the adsorbed methane content (c.f. Moore, 2012; White et al., 2005). However, the rate of transport from the low permeability coal matrix into the cleat system generally limits primary CBM production by pressure depletion methods to 20-60% of the estimated reserves, leaving 40-80% of the methane initially present in place (White et al., 2005). Besides this residual methane, pressure depletion also leaves large amounts of water trapped in the coal matrix via sorption (White et al., 2005).

Sorption of both methane and water by coal matrix material leads to several percent swelling, while desorption produces similar shrinkage (Day et al., 2011; Fry et al., 2009; Liu et al., Chapter 3, Chapter 5; Pan, 2012; Suuberg et al., 1993). Against this background, removing water and CH_4 from coal seams by injection of dry N_2 has recently been suggested as a possible method of secondarily enhancing CBM recovery (ECBM) (c.f. Liu et al., Chapter 5; Moore, 2012; White et al., 2005). This concept is based on the fact that a) the swelling of coal upon adsorption of N_2 is around half of that occurring upon adsorption of CH_4 at similar *PT* conditions (e.g. Day et al., 2012; Day et al., 2010), and b) the swelling/shrinkage response of coal to adsorption and desorption of water (at 100% relative humidity) is similar to that caused by adsorption and desorption of CH_4 at a pressure of 10MPa (c.f. Liu et al., Chapter 3, Chapter 5). The

implication is that injection of dry N_2 into a depleted coalbed methane reservoir, followed by on-going flushing, may be capable of initiating self-enhancing shrinkage and (micro)cracking of the coal, hence enhanced methane production, as methane and water are progressively removed and replaced by sorbing N_2. Understanding swelling/shrinkage effects in coal due to adsorption and desorption of water, under in-situ conditions of temperature, water activity (i.e. partial pressure or relative humidity, RH) and rock stress is therefore of direct importance for designing and optimising enhanced (E)CBM production strategies.

Recent experiments on swelling of coal due to water vapor adsorption have demonstrated that the equilibrium swelling strain is linearly proportional to the concentration of adsorbed water molecules (Fry et al., 2009; Suuberg et al., 1993), and to the imposed relative humidity or activity of water vapor (Liu et al., Chapter 5; Fry et al., 2009). It has also been shown that transient, time-dependent swelling, following a change in RH, is controlled by diffusion of water molecules (Liu et al., Chapter 5). However, little attention has been paid in the literature to the effect of in-situ rock stress on water sorption and the associated swelling. Such effects may nonetheless be important under subsurface conditions, bearing in mind that the applied stress is known to reduce the sorption capacity of coal with respect to CO_2 and CH_4. This has been demonstrated experimentally (Hol et al., 2011; Hol et al., 2012a; Liu et al., Chapter 3; Pone et al., 2009) and predicted theoretically via thermodynamic models addressing the stress-strain-sorption behaviour of coal, as developed by Hol et al. (2011; 2012a; see also Vandamme et al., 2010) and Liu et al. (Chapter 3). These models show that the additional stress-strain work done, due to sorption-induced swelling of coal matrix material against an applied (rock) stress, increases the chemical potential of the adsorbed molecules and hence reduces sorption capacity. As the theory applies in its broad lines to any solid sorbent plus sorbate system, it follows that the in-situ stress pertaining in coal seams will likely reduce the sorption capacity of coal with respect to water, hence

reducing the sorption-induced swelling response. Strictly, however, the theory assumes monolayer (discrete site) adsorption behavior of the sorbate molecules, whereas adsorption of water by coal, unlike adsorption of CH_4 and CO_2, is widely accepted to involve multiple layer adsorption (c.f. Busch and Gensterblum, 2011; Charrière and Behra, 2010; McCutcheon et al., 2003; Švábová et al., 2011; Yu et al., 2013). To understand the effects of stress on water sorption and associated swelling, under conditions corresponding to thermodynamic equilibrium, the existing monolayer theory needs to be extended to cover multilayer adsorption. On the other hand, equilibrium thermodynamic models for stress-strain-sorption behavior may not apply on the coal seam scale, as changes in coal stress state might close or open pre-existing micropore or (micro)fracture networks inside the coal, changing the accessibility of water to the coal matrix and preventing homogeneous equilibration (c.f. Cui et al., 2004; Day et al., 2008; Hol et al., 2012a; Pone et al., 2009). Permanent deformation and creep effects might also occur when wet coal experiences changing long-term stress states. To gain insight into the influence of applied stress on the swelling behavior of coal upon adsorption of water, progress is needed in understanding all of these effects.

In this study, we attempt to determine whether or not applied stress influences the swelling response of coal caused by exposure to and adsorption of water, and, if so, to determine the mechanisms responsible. To achieve this, we first extend our previous thermodynamic model (Liu et al., Chapter 3) for the stress-strain-sorption behaviour of coal matrix material to address not only monolayer but also multiple layer adsorption of water. We then report the results of experiments designed to determine the effects of applied stress on swelling strain development in coal samples exposed to distilled water at atmospheric pressure (0.1 MPa). The experiments were performed on both coal disc and pre-compacted powder samples at a constant temperature of 40˚C and at applied stresses in the range 25-100 MPa, using a uniaxial compaction apparatus.

6.2. Thermodynamic models for swelling of coal matrix material due to adsorption of water under a general stress state σ_{ij}

6.2.1. Starting assumptions and cases considered

Throughout our analysis, compressive stresses and fluid pressure are measured positive, as is swelling strain. Following Liu et al. (Chapter 3), we begin by considering a small coal matrix cube of mass m and side l ($\leq$1mm) (density ρ, kg/m^3), surrounded by water vapour or liquid water present at constant pressure P, absolute temperature T, and chemical potential μ_g. The coal matrix cube, also at uniform temperature T, is independently subjected to a general stress state σ_{ij} via a permeable loading frame that allows free access of water vapor or water to the coal. The cube is considered homogeneous in structure and composition at the particle length scale l, but may be anisotropic in properties. It is further assumed to contain nano-pores only, so that there is no Darcian flow and negligible storage of free (unadsorbed) gas. In other words, the coal particle is so small that it is cleat free and can take up water only by molecular diffusion and adsorption. The coal particle is accordingly elastic but not poro-elastic.

Previous studies employing experimental approaches (such as sorption tests coupled with infrared spectroscopy and ionic thermal current measurements) and thermodynamic/kinetic modeling methods (Dubinin, 1980; Dubinin and Serpinsky, 1981; Kaji et al., 1986; McCutcheon et al., 2003; Mu and Malhotra, 1991; Nishino, 2001; Suárez et al., 1993; Švábová et al., 2011) show that water molecules are primarily trapped by oxygen-bearing functional groups (mostly by carboxyl groups) present in the coal matrix via hydrogen bonds. Water thus adsorbed forms a first layer of adsorbed molecules, having high binding energy due to a strong interaction between the active functional groups and the adsorbed molecules (Charrière and Behra, 2010; Dubinin, 1980; Dubinin and Serpinsky, 1981; McCutcheon et al., 2003; Švábová et al., 2011).

These adsorbed water molecules then form secondary sites for attachment of additional water molecules via hydrogen bonds with lower binding energy (Lynch and Webster, 1982; McCutcheon et al., 2003; Nishino, 2001). Based on experimental findings that the volumetric swelling strains of coals (ranking from lignite to bituminous) caused by water adsorption is linearly proportional to concentration of water adsorbed (Fry et al., 2009; Suuberg et al., 1993), we assume that the volumetric swelling strain (e_v^{eq}) developed in coal when water adsorbs is proportional to the adsorbed concentration of water vapor C (mol/kg$_{coal}$) and to the volumetric swelling V_0 produced by sorption of 1 mole of water molecules, with V_0 being indistinguishable for primary and secondary adsorption in cases where both occur. For single layer adsorption (primary adsorption), this assumption can be expressed as $e_v^{eq} = C\rho V_0$ (Hol et al., 2012a; Hol and Spiers, 2012). For multiple layer adsorption (primary plus secondary adsorption), it becomes $e_v^{eq} = \rho(C_1 V_{01} + C_2 V_{02})$, where the subscript 1 denotes primary adsorption and 2 denotes secondary adsorption, and where $V_{01} = V_{02}$

In the following, we consider three possible mechanisms responsible for swelling of coal matrix material due to water adsorption, which we will refer to as Mechanisms 1-3. These form the basis for the development of three corresponding models for coupled stress-strain-sorption behaviour, identified as Models 1-3.

Mechanism I: In this case, we assume that only primary adsorption (i.e. monolayer adsorption) occurs inside coal matrix material. This means that the swelling of coal matrix material by Mechanism I is controlled by monolayer adsorption of water molecules in the primary sites. Here, $e_v^{eq} = C\rho V_0$, where C represents the concentration of the first layer of water molecules.

Mechanism II: Here, swelling of coal matrix material is contributed to by all adsorbed water molecules, and adsorption of water is assumed to involve multiple layer

adsorption. In this case, we assume that the total concentration of adsorbed water molecules is described by the widely accepted multiple layer model proposed by Dent (1977). Dent (1977) treated the first adsorbed layer of water molecules as primary adsorption, and all subsequent layers as secondary adsorption. Dent further assumed that thermodynamic properties of water adsorbed in the various secondary layers (second, third, fourth and so on) are identical, but different from the properties of the water adsorbed in the primary layer. In line with our assumption above that V_0 is the same for all adsorbed water molecules, to obtain swelling strain from the Dent model for water adsorption, we can write $e_v^{eq} = \rho V_0 (C_1 + C_2)$, where C_1 and C_2 represent the concentration of water molecules associated with primary adsorption and secondary adsorption.

Mechanism III: In this case, we again assume that swelling is caused by all the adsorbed water molecules, but that these are distributed between separate mono- and multi-layer adsorption sites. Sorption by this mechanism is described by the widely used D'Arcy and Watt model (D'Arcy and Watt, 1970) for water sorption by coal. In the D'Arcy and Watt (DW) model, the monolayer adsorption sites are considered to be the primary adsorption sites while multilayer adsorption sites are the secondary adsorption sites (Barton et al., 1994; McCutcheon et al., 2003; Švábová et al., 2011). In applying this model, we again assume that V_0 is the same for all adsorbed water molecules, regardless of adsorption site type, so that $e_v^{eq} = \rho V_0 (C_1 + C_2)$, where C_1 and C_2 represent the concentration of water molecules associated with the primary (monolayer) adsorption sites and the secondary (multilayer) adsorption sites.

Note here that the effects of stress on adsorption by Mechanism I has already been explored by Hol et al. (2012a) and by Liu et al. (Chapter 3), assuming that general states of stress are supported by the coal matrix material. These authors arrived at general stress-strain-sorption relations for monolayer adsorption of any

sorbate species. To date, however, the Dent and the DW models have only been developed and applied for describing water adsorption by unstressed coal, i.e. for describing sorbed water concentration versus RH or relative pressure in the case of unstressed coal. Here, we will review the monolayer models derived by Hol, Liu and co-workers, identifying how stress supported by a solid sorbent influences sorption site occupancy in general. We then apply this result to extend the Dent and DW sorption models to obtain stress-strain-sorption relations for the multilayer sorption mechanisms that they represent (Mechanisms 2 and 3, respectively).

6.2.2. Model 1: Monolayer sorption/swelling model (modified Hol and Spiers model)

For monolayer sorption of a pure sorbate species such as CH_4, CO_2, N_2 or H_2O, Liu et al. (Chapter 3) gave the potential of the adsorbed molecules in stressed sorbent (coal) matrix material, expressed in J/mol, as

$$\mu_s = \mu_s^{P_0} + RT\ln(\frac{\theta}{1-\theta}) + (\overline{\sigma} - P_0 + \frac{1}{3}\sigma_{ij}^{'}A_{ij})V_0 \quad (1)$$

Here, the quantity $\mu_S^{P_0}$ (J/mol) represents the potential of the adsorbed molecules at a reference pressure P_0=0.1MPa. This depends solely on temperature for a given sorption reaction. The quantity θ represents the concentration of adsorbed gas measured in terms of primary/monolayer adsorption site occupancy, T (K) is the thermodynamic (absolute) temperature, R (J•K^{-1}•mol^{-1}) is the gas constant, and the term $R\ln(\frac{\theta}{1-\theta})$ is the molar configurational entropy of the adsorbed molecules. In addition, V_0 (m^3/mol) represents the partial molar volume of the adsorbed gas molecules, A_{ij} is a second rank tensor representing the swelling strain anisotropy (see details in Chapter 3), and the term $\left(\bar{\sigma} + \frac{1}{3}\sigma'_{ij}A_{ij} - P_0\right)V_0$ represents the stress-strain work done on the surroundings as coal swells against the effective stress $(\sigma_{ij} - P_0\delta_{ij})$ when one mole of sorbate molecules are adsorbed. It is clearly seen from equation 1 that the chemical potential

depends not only on the adsorbed occupancy, but also on the stress-strain work done. It is also clear that the magnitude of the stress effect on the chemical potential depends on the partial molar volume of the adsorbed molecules V_0.

At equilibrium, the chemical potential of the adsorbed molecules (μ_s) must be equal to that of the gas molecules ($\mu_g = \mu_{g0} + RT \ln a_g$). Setting equation 1 equal to μ_g then yields the following relationship for the sorption capacity C (mol/kg$_{coal}$) of the stressed coal matrix (Liu et al., Chapter 3):

$$C = C_s\theta = \frac{C_s a_g \exp(\frac{\mu_{g0} - \mu_s^{P_0}}{RT}) \exp(\frac{-(\overline{\sigma} - P_0)V_0}{RT}) \exp(\frac{-\sigma_{ij}^{'} A_{ij} V_0}{3RT})}{1 + a_g \exp(\frac{\mu_{g0} - \mu_s^{P_0}}{RT}) \exp(\frac{-(\overline{\sigma} - P_0)V_0}{RT}) \exp(\frac{-\sigma_{ij}^{'} A_{ij} V_0}{3RT})} \tag{2a}$$

Here C_s (mol/kg$_{coal}$) represents the total number of localized adsorption sites (in mol) present in one kilogram of coal matrix, a_g represents the activity of gas at given PT conditions, μ_{g0} represents the chemical potential of gas molecules at a reference pressure P_0=0.1MPa, and the term $\exp(\frac{\mu_{g0} - \mu_s^{P_0}}{RT})$ is the equilibrium constant K^0 for the sorption reaction, which depends solely on temperature. From equations 1 and 2, it is clear, while that the term $(\overline{\sigma} - P_0 + \frac{1}{3}\sigma_{ij}^{'} A_{ij})V_0$ expresses the stress-strain work done on the surroundings as coal swells against the effective stress $(\sigma_{ij} - P_0\delta_{ij})$, the term $E(\sigma_{ij}, P_0) = \exp(\frac{-(\overline{\sigma} - P_0)V_0}{RT}) \exp(\frac{-\sigma_{ij}^{'} A_{ij} V_0}{3RT})$ expresses the reduction in adsorption site occupancy caused by the applied stress in excess of the reference pressure P_0.

Note that when sorption-induced swelling is negligible (i.e. $V_0 \to 0$) or when no

stress is applied to the solid framework in excess of P_0, equation 2a reduces to

$$C = \frac{C_s a_g K^0}{1 + a_g K^0} \tag{2b}$$

This is the well-known Langmuir equation (Langmuir, 1918), which is classically derived assuming that there is no sorption-induced swelling (V_0=0), expressed in terms of gas activity. When the coal matrix is subjected to a hydrostatic stress σ ($\sigma > P_0$) or a gas pressure of the same magnitude, equation 2a becomes (see Liu et al., Chapter 3)

$$C = C_s \theta = \frac{C_s a_g K^0 \exp(\frac{-(\sigma - P_0)V_0}{RT})}{1 + a_g K^0 \exp(\frac{-(\sigma - P_0)V_0}{RT})} \tag{2c}$$

Assuming now that V_0 is insensitive to both adsorbed concentration and the applied stress states, and that the swelling of coal matrix upon adsorption is caused by V_0, the volumetric swelling strain (e_v^{eq}) of the stressed coal upon adsorption is given from the above as

$$e_v^{eq} = C \rho V_0 \tag{3a}$$

$$\text{or} \quad e_v^{eq} = \rho V_0 C_s \frac{a_g K^0 \exp(\frac{-(\overline{\sigma} - P_0)V_0}{RT}) \exp(\frac{-\sigma_{ij}^{'} A_{ij} V_0}{3RT})}{1 + a_g K^0 \exp(\frac{-(\overline{\sigma} - P_0)V_0}{RT}) \exp(\frac{-\sigma_{ij}^{'} A_{ij} V_0}{3RT})} \tag{3b}$$

$$\text{or} \quad e_v^{eq} = \rho V_0 C_s \frac{a_g K^0 E(\sigma_{ij}, P_0)}{1 + a_g K^0 E(\sigma_{ij}, P_0)} \tag{3c}$$

Similarly, the full strain tensor representing the general, anisotropic adsorption–induced, swelling response of coal subjected to a general stress state σ_{ij} is given

$$\varepsilon_{ij}^{eq} = \frac{A_{ij} + \delta_{ij}}{3} e_v^{ads} = \frac{A_{ij} + \delta_{ij}}{3} C\rho V_0 \tag{4a}$$

or $$\varepsilon_{ij}^{eq} = \frac{A_{ij} + \delta_{ij}}{3} \rho V_0 C_s \frac{a_g K^0 E(\sigma_{ij}, P_0)}{1 + a_g K^0 E(\sigma_{ij}, P_0)} \tag{4b}$$

The effect of applied stress on adsorbed concentration and the associated swelling embedded in the occupancy reduction term $E(\sigma_{ij}, P_0) = \exp(\frac{-(\overline{\sigma} - P_0)V_0}{RT}) \exp(\frac{-\sigma_{ij}^{'} A_{ij} V_0}{3RT})$ forms the physical basis for the models developed in this paper for swelling of stressed coal matrix material upon adsorption of water.

6.2.3. Model 2: Dent-based swelling model

Dent (1977) assumed that the thermodynamic properties of water molecules adsorbed primarily by coal are different to those adsorbed secondarily, and applied the well-known the Brunauer-Emmett-Teller (BET) model for multiple layer adsorption (Brunauer et al., 1938) to describe the corresponding sorption behaviour. Writing the partial pressure of water in terms of water activity (a_g), the resulting Dent variant of the BET model can be expressed as

$$\begin{aligned} C &= C_1 + C_2 \\ &= \frac{C_s K_1 a_g}{1 - K_2 a_g + K_1 a_g} + \frac{C_s K_1 K_2 a_g^{\,2}}{(1 - K_2 a_g)(1 - K_2 a_g + K_1 a_g)} \end{aligned} \tag{5}$$

where C_1 (mol/kg$_{coal}$) and C_2 (mol/kg$_{coal}$) represent the concentration of water molecules adsorbed in primary and secondary adsorption sites at equilibrium, and where K_1 and K_2 represent the equilibrium constants for primary adsorption and secondary adsorption. If no secondary adsorption occurs, the Dent model reduces to the single layer Langmuir

model expressed in terms of gas activity, i.e. equation 5 reduces to 2b.

Applying the analysis above for the effect of stress on site occupancy for single layer sorption, and extending this to the thermodynamically analogous case of secondary adsorption, the Dent model for water adsorption by stressed coal matrix material becomes

$$\begin{aligned} C &= C_1 + C_2 \\ &= \frac{C_s K_1 E(\sigma_{ij}, P_0) a_g}{1 - K_2 E(\sigma_{ij}, P_0) a_g + K_1 E(\sigma_{ij}, P_0) a_g} \\ &\quad + \frac{C_s K_1 K_2 E^2(\sigma_{ij}, P_0) {a_g}^2}{(1 - K_2 E(\sigma_{ij}, P_0) a_g)(1 - K_2 E(\sigma_{ij}, P_0) a_g + K_1 E(\sigma_{ij}, P_0) a_g)} \end{aligned} \tag{6}$$

Inserting equation 6 into 3a and 4a, the following results are hence obtained for the swelling of coal matrix material due to multiple layer adsorption of water under stressed conditions:

$$e_v^{eq} = \rho V_0 C_s \left\{ \begin{array}{c} \dfrac{K_1 E(\sigma_{ij}, P_0) a_g}{1 - K_2 E(\sigma_{ij}, P_0) a_g + K_1 E(\sigma_{ij}, P_0) a_g} \\ + \dfrac{K_1 K_2 E^2(\sigma_{ij}, P_0) {a_g}^2}{[1 - K_2 E(\sigma_{ij}, P_0) a_g][1 - K_2 E(\sigma_{ij}, P_0) a_g + K_1 E(\sigma_{ij}, P_0) a_g]} \end{array} \right\} \tag{7a}$$

$$\varepsilon_{ij}^{eq} = \frac{A_{ij} + \delta_{ij}}{3} \rho V_0 C_s \left\{ \begin{array}{c} \dfrac{K_1 E(\sigma_{ij}, P_0) a_g}{1 - K_2 E(\sigma_{ij}, P_0) a_g + K_1 E(\sigma_{ij}, P_0) a_g} \\ + \dfrac{K_1 K_2 E^2(\sigma_{ij}, P_0) {a_g}^2}{[1 - K_2 E(\sigma_{ij}, P_0) a_g][1 - K_2 E(\sigma_{ij}, P_0) a_g + K_1 E(\sigma_{ij}, P_0) a_g]} \end{array} \right\} \tag{7b}$$

6.2.4. Model 3: DW-based swelling model

The D'Arcy and Watt (DW) model (Barton et al., 1994; Furmaniak et al., 2008; McCutcheon et al., 2003; Švábová et al., 2011) was formulated as a combination of the

Langmuir isotherm for monolayer adsorption with strong binding energy (Langmuir, 1918), and the Dubinin and Serpinsky (DS1) isotherm for multiple-layer adsorption (Dubinin and Serpinsky, 1981). Upon replacing the partial pressure of water vapour by the activity of water vapour, the result obtained by D'Arcy and Watt can be expressed as

$$C = \frac{C_{s1} K_1 a_g}{1 + K_1 a_g} + \frac{C_{s2} K_2 a_g}{1 - K_2 a_g} \tag{8}$$

Here C_{s1} and C_{s2} (mol/kg$_{coal}$) represent the number of localized adsorption sites (in *mol*) present in one kilogram of coal matrix for monolayer adsorption and for multiple-layer adsorption, respectively, while the quantities K_1 and K_2 represent the corresponding equilibrium constants. If only single layer adsorption occurs, the model reduces to the Langmuir type equation, of course (c.f. equation 2b).

Again applying the term $E(\sigma_{ij}, P_0)$ to account for the effects of stress on both primary and secondary site occupancy, we modified the DW model for water adsorption by the stressed coal to obtain

$$C = \frac{C_{s1} K_1 E(\sigma_{ij}, P_0) a_g}{1 + K_1 E(\sigma_{ij}, P_0) a_g} + \frac{C_{s2} K_2 E(\sigma_{ij}, P_0) a_g}{1 - K_2 E(\sigma_{ij}, P_0) a_g} \tag{9}$$

Inserting equation 9 into 3a and 4a, we obtain our Model 3 for swelling of coal matrix material due to adsorption of water, i.e.

$$e_v^{eq} = \rho V_0 \left\{ \frac{C_{s1} K_1 E(\sigma_{ij}, P_0) a_g}{1 + K_1 E(\sigma_{ij}, P_0) a_g} + \frac{C_{s2} K_2 E(\sigma_{ij}, P_0) a_g}{1 - K_2 E(\sigma_{ij}, P_0) a_g} \right\} \tag{10a}$$

and $$\varepsilon_{ij}^{eq} = \frac{A_{ij} + \delta_{ij}}{3} \rho V_0 \left\{ \frac{C_{s1} K_1 E(\sigma_{ij}, P_0) a_g}{1 + K_1 E(\sigma_{ij}, P_0) a_g} + \frac{C_{s2} K_2 E(\sigma_{ij}, P_0) a_g}{1 - K_2 E(\sigma_{ij}, P_0) a_g} \right\} \tag{10b}$$

6.2.5. Swelling under stressed versus unstressed conditions: A comparison of model predictions

All three models expressed in equations 3-10 demonstrate that swelling of coal matrix material upon adsorption of water at a reference fluid pressure of P_0=0.1MPa under an applied stress state $\sigma_{ij} > P_0\delta_{ij}$ or under a hydrostatic stress state $\sigma > P_0$, is clearly lower than that under conditions, where $\sigma_{ij} = P_0\delta_{ij}$. The same applies for any fluid pressure P ($\sigma = P$), of course. The effect is due to the influence of the term $E(\sigma_{ij}, P_0)$, i.e. to the stress-strain work done in association with sorption-induced swelling against the positive effective stress $(\overline{\sigma} - P_0)$ and against the deviatoric stress $\sigma_{ij}^{'}$ under stressed conditions, which reduce the adsorbed concentration of water by coal matrix. Our Models 1-3 therefore all predict that the higher the applied stress in excess of P_0, the lower the sorbed water content at equilibrium and the lower the resulting swelling strain. It is also clear from all models that at a given applied stress state, the magnitude of the effect of the applied stress in reducing sorbed concentration and swelling depends on V_0. This crucial term, V_0 , i.e. the volumetric swelling that occurs per mole of adsorbed water, can be derived from sorption-induced swelling experiments on either stressed or unstressed coal, via equation 3a, and typically lies in the range 4 to 13×10^{-6}m^3/mol (Suuberg et al., 1993; Fry et al., 2010).

6.3. Experiments

As shown above, our models (i.e. equations 3-10) predict that an (effective) stress applied in excess of the reference pressure P_0 reduces swelling of coal matrix upon adsorption of water. In the following, we test the validity of our models by experimentally investigating the swelling response of coal samples upon adsorption of

water at different applied stress states, using a uniaxial compaction apparatus. Experiments were performed on a solid disc and pre-compacted powdered coal samples at a constant temperature of 40˚C. The mechanical response of the samples, under both vacuum dry (i.e. 0% relative humidity) and wet (i.e. 100% relative humidity) conditions was first determined by loading axially in a stepwise manner. Note that the terms "evacuated state" and "water-exposed state" are used to refer to vacuum dry and wet conditions. We also measured the axial swelling strain response of (vacuum) dry samples to the introduction of distilled water at a fluid pressure of 0.1 MPa, at constant applied stress states.

6.3.1. Staring materials and sample preparation

The samples used in all experiments were prepared from high volatile bituminous coal which was obtained from the Brzeszcze mine (seam 364) in the Upper Silesian Basin of Poland. The Brezeszcze coal has a vitrinite reflectance of 0.77±0.05%, and contains 74.14% carbon, 5.27% hydrogen, 1.44% nitrogen, 0.70% sulfur and 18.45% oxygen (Hol et al., 2011). Experiments were conducted on both a single 1mm thick solid disc and 10 pre-compacted powdered samples (grain size of 180-212 μm). The samples were tested in the titanium sample vessel shown in Figure 1a (inner diameter 12.18 mm, outer diameter19.1 mm, Liteanu and Spiers, 2009). The titanium vessel, plus sample, porous plate (< 100 μm) and titanium pistons will be referred to henceforth as the sample assembly. This was assembled and transferred to the main experimental apparatus in order to execute the experiments.

6.3.1.1. Coal disc sample

After identifying the bedding plane of a ~ 10 cm slab, several cores with a diameter of 11.8 mm and length of ~ 5 mm were drilled along the direction perpendicular to the bedding plane using a water-cooled pillar drill. Subsequently, the 5mm long cylinders were accurately sectioned into 1mm thick discs. Both ends of the discs were ground flat.

This was done by Glass Workshop of Utrecht University. One optically cleat-free disc was chosen for the present experiments. The sample was pre-dried in an oven at 40˚C under vacuum for ~ 3 days. The mass and dimensions of the sample were then measured, immediately prior to experimentation, and average values were recorded (Table 1). Porosity of the sample P_disc_5 was estimated, taking the average density obtained from two 1 mm sized cube (same coal material with less micropores), as used by Liu et al. (Chapter 5) as the reference density of matrix material (1320±34 kg/m^3).

Note here that the diameter of disc sample is 11.80 mm, which is less than the inner diameter 12.18 mm of the titanium sample vessel. The space between the disc and the vessel wall was accordingly 0.38mm, which is equivalent to a 3.2% strain of the disc sample in the radial direction. This means there is enough space for the disc to freely expand radially, without touching the vessel wall, in response to either elastic deformation (< 1.5%) or sorption induced swelling (< 0.5%). The axial swelling strain of the disc sample measured in the experiments can be therefore assumed to represent the laterally unconstrained deformation subject to a uniaxial stress applied perpendicular to the disc and internal bedding plane orientation. At the same time, the free space around the sample rim means that water will diffuse into the sample from both the top and rim of the sample, though with different characteristic times due to differing length scale and likely anisotropic diffusion coefficients in the radial versus axial directions.

Table 1. Dimensions, mass and porosity of the Brzeszcze 364 coal samples (i.e. both the disc and powdered coal samples) used in this study. The listed dimensions were used for all strain and porosity (change) calculations. Note that the listed dimensions obtained for Sample P_disc_5 were measured before the experiments. Any change after experiments was below measurement resolution (digital calliper). The dimensions listed for the powdered samples were measured after the experiments. The types of experiment (Exp) performed on each sample are also indicated. Porosity values quoted are total porosity including matrix porosity and, in the case of the powdered samples, intergranular porosity.

Sample	initial sample mass (g)	sample thickness *l* (mm)	sample diameter *d* (mm)	porosity (%)	Exp.
P_disc_5	0.13852	1.000	11.80	3.99	Compression/Swelling
Powder_1	0.20203	1.740	12.18	24.47	Compression/Swelling (25.6MPa)
Powder_2	0.19927	1.735	12.18	25.29	Swelling (43.2MPa)
Powder_3	0.21033	1.800	12.18	23.99	Swelling (60.5MPa)
Powder_4	0.19679	1.700	12.18	24.70	Swelling (77.8MPa)
Powder_5	0.15722	1.420	12.18	27.98	Swelling (25.6MPa)
Powder_6	0.153747	1.340	12.18	25.36	Swelling (43.2MPa)
Powder_7	0.14404	1.240	12.18	24.43	Swelling (60.5MPa)
Powder_8	0.204078	1.720	12.18	22.82	Swelling (77.8MPa)
Powder_9	0.22370	1.940	12.18	24.99	Swelling (60.5MPa)
Powder_10	0.22318	1.910	12.18	23.99	Swelling (60.5MPa)

6.3.1.2. Powdered coal samples

The grain size of the powdered coal samples used in the present experiments was 180-212μm. This grain size fraction was prepared by crushing and sieving the remaining part of the slab used for preparing the solid coal disc sample. Samples weighting 0.15-0.2 grams were used for each experiment on coal powder, pre-drying in an oven at 40˚C under a vacuum condition for 1 day. In setting up each experiment, the sample powder was distributed evenly in the titanium vessel and a flat, disc-shaped sample was pre-formed by manually compressing it by hand-loading the upper and lower titanium pistons. The thickness of the disc-shape powdered sample measured after the experiments was taken as the dimensions used in all strain and initial dimension calculations and ranged from 1.2-1.9 mm (Table 1). The estimated porosity of the pre-compacted samples lay in the range of 23-28%.

Note here that the pre-compacted powders were only able to expand in the axial direction, because expansion in radial direction was constrained by the titanium sample vessel. This means the axial swelling strain measured in the experiments on powdered

samples represents both the axial and the volumetric swelling strain of the samples.

6.3.2. Apparatus

The experimental setup shown in Fig.1b consists of a uniaxial, oedometer-type (i.e. one dimensional) compaction vessel, constructed of Remanit 4122 stainless steel, mounted in an Instron 8562 servo-controlled loading frame to apply axial load (*c.f.* Hol et al., 2011; Zhang et al., submitted). In this study, the Instron loading frame was operated in load control mode. The sample assembly (Figure 1a) was axially loaded, within the Remaint vessel via two Remanit pistons (diameter 19 mm) sealed against the Remanit compaction vessel using Viton o-rings. Applied axial load was measured external to the compaction vessel using a 100 kN capacity Instron loadcell, which allows load control to within ±0.0023 kN. Axial displacement of the upper piston relative to the Remanit vessel top (i.e. axial sample deformation) was measured using a high precision LVDT (measuring stroke ±1mm, accuracy better than ±0.1 μm). This allowed changes in sample thickness to be measured accurately at any instant, by correcting for piston distortion. The liquid distilled water was introduced into the sample through the inlet in the upper Remanit piston. The pressure of the fluid was measured using a Honeywell pressure transducer.

The temperature of the compaction vessel and sample were controlled at 40˚C (±0.1˚C) in the present experiments by means of an external furnace mounted around in the Remaint compaction vessel. This was regulated by means of a Eurotherm temperature controller, connected to a type K thermocouple located in the external furnace windings. Sample temperature was measured using a second type K thermocouple placed in a small recess in the outer compaction pressure vessel at a distance of ~0.5 mm from the titanium sample vessel. To minimize distortion of the Instron loading frame caused by temperature fluctuations, a 1.5 m^3 foam-polystyrene box was constructed around the setup to control the air temperature in the box at 30±0.2˚C, using an internal lamp, fan and CAL 9900 PID-controller (see Figure 1b, c.f.

Hol and Spiers, 2012).

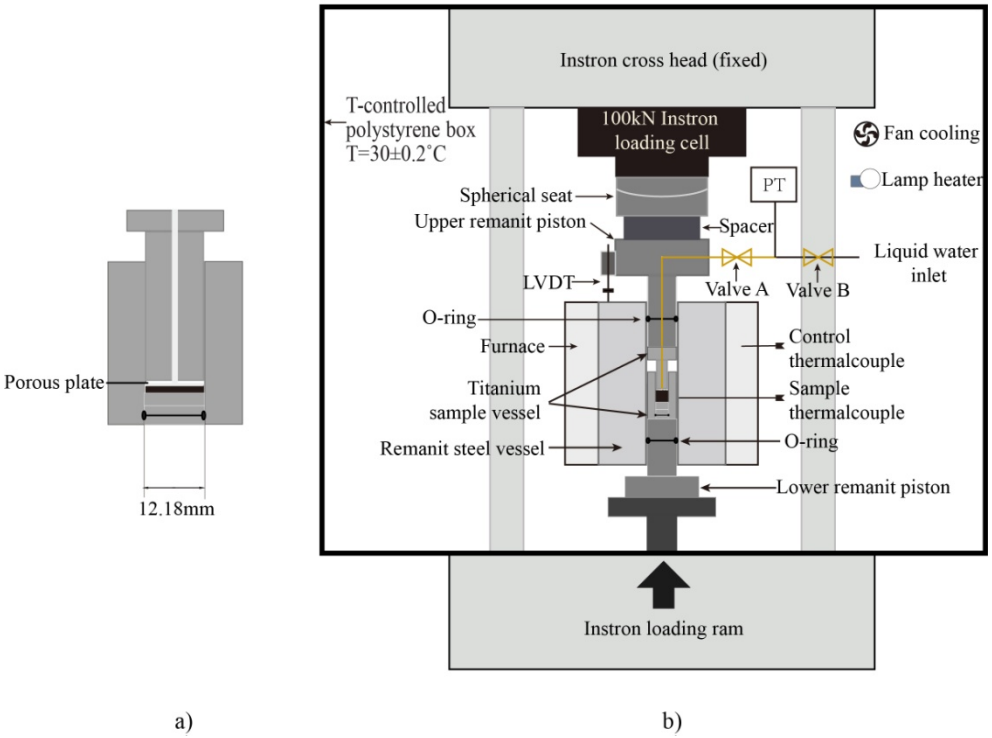

Fig.1. Schematic diagram of the present 1-D loading system (modified after Zhang et al. submitted). a) Sample assembly consisting of titanium sample vessel, piston, porous plate, and sample. b) Compaction cell constructed of Remanit steel located in an Instron loading frame operated in a load control mode. The sample assembly was located inside the bottom of the Remanit steel vessel, in series with the loading piston. In wet experiments, liquid distilled water was introduced into the sample through the inlet in the upper piston. An external LVDT mounted on the upper Remanit piston was used to measure the deformation of the sample in the axial direction, correcting for apparatus distortion. The temperature of the vessel and sample were controlled at a temperature of 40˚C (±0.1˚C). A heated polystyrene box enclosed the full setup, maintaining a constant air temperature in the box of 30˚C (±0.2˚C) and thus avoiding effects of thermal expansion of the Instron, and other components, caused by temperature fluctuations.

6.3.3. Testing procedures

Compression tests were performed in stepwise loading mode on both the solid disc

sample P_disc_5 and one powdered sample (Powder_1) to determine the mechanical response of the samples in both the evacuated and water-exposed states. Swelling tests were then performed on both P_disc_5 and ten powdered samples (Powder_1-10) to measure the time-dependent swelling behaviour of the samples during exposure to distilled liquid water (at 0.1 MPa) at fixed applied stress. Note that in all experiments, we assumed an apparent equilibrium state when no change in displacement, i.e. in LVDT (< 0.2 μm) signal could be identified within a period of 2 hours.

6.3.3.1. Compression tests under evacuated vs. water-exposed conditions

These experiments, performed on samples P_disc_5 and Powder_1, involved four sequential stages:

1) Pre-compaction and cyclic loading under vacuum. To minimize permanent deformation and remove the residual water content of the coal samples, both the fresh P_disc_5 and Powder_1 were pre-compacted at 13 kN under vacuum (applied via Valves A and B in Fig.1b). This load condition is equivalent to 118.9 MPa for P_disc_5 and 111.6 MPa for Powder_1. Pre-compaction was carried out for ~20 hours for P_disc_5 and ~40 hours Powder_1. The samples were then unloaded to the target starting load of the experiments, i.e. to 9.15 MPa for P_disc_5 and to 25.95 MPa for Powder_1. A slow expansion of the sample was subsequently observed, apparently caused by the release of elastic energy stored in the coal samples during pre-compaction via time dependent (creep) processes. After re-equilibration at the target load conditions, load cycling was conducted several times, in the range of ~9 MPa to ~100 MPa at a rate of 0.1 MPa/s, to further minimize permanent deformation effects during subsequent testing .

2) Stepwise compression tests in the evacuated state. To determine the mechanical response of the samples due to changes in applied stress states, we performed axial compression experiments under vacuum (i.e. 0% relative humidity), by applying the following upward loading steps. The stresses applied to P_disc_5 were 9.15 MPa, 27.45 MPa, 45.74 MPa, 64.04 MPa, 82.34 MPa, and 100.64 MPa, while for Powder_1 the

applied stresses were 25.93 MPa, 43.22 MPa, 60.50 MPa, 77.79 MPa, and 95.08 MPa. Re-equilibration time with respect to deformation occurring after each stress step was around 5 minutes for P_disc_5, and around 15 minutes for Powder_1. Note that to minimize the thermodynamic stress-strain-sorption effects potentially occurred for wet samples (c.f. Hol et al., 2011; Hol et al., 2012a; Liu et al., Chapter 3) during loading, the loading rate employed for compression tests was rapid and constant at 0.2 kN/s, which is equivalent to ~1.83 MPa/s for P_disc_5, and ~1.73 MPa/s for Powder_1. This loading rate allowed each loading step in the compression experiments to be completed within 10 seconds. Compression testing was terminated by unloading the samples from the maximum compressive stress applied, back to the starting load and reaching equilibrium at that stress (9.15 MPa for P_disc_5 and 25.93 MPa for Powder_1).

3) Equilibration with distilled liquid water (water-exposed state). After equilibration at the starting stress (of 9.15 MPa applied to P_disc_5 and of 25.93 MPa to Powder_1) under vacuum (evacuation of the samples via Valves A and B, Fig.1b), Valve A was closed and degassed distilled (liquid) water was introduced into the pipe between Valves A and B in Fig.1b. This led to a slight change in LVDT signal due to the temperature fluctuation caused by opening the temperature-controlled box and the cold water injection. After the output signal of the LVDT re-stabilized, i.e. the temperature of both the box and water were re-stable at 30˚C, the Valve A was re-opened to allow liquid water to enter into the sample. Initial equilibration took around 24 hours for P_disc_5 at an initial stress state of 9.15 MPa and for Powder_1 at an initial stress state of 25.93 MPa.

4) Stepwise compression tests in the water-exposed state. Once the samples had approached equilibrium with liquid water at the above initial applied stress state, the applied stress was increased in steps, allowing apparent equilibrium to be reached or at least approached after each increment. Two loading-unloading runs or cycles were performed on P_disc_5, while a single cycle was performed on the pre-compacted

Powder_1, following the loading steps described in Stage 2.

6.3.3.2. Swelling measurements at fixed stress states

In these experiments, we measured the time-dependent swelling strains of P_disc_5 and our ten pre-compacted powdered samples (Powder_1-10) upon introduction of distilled liquid water (at 0.1MPa) at fixed stress states (Table 1). The stress was kept constant throughout each experiment but varied from test to test. In all swelling experiments, the sample was first pre-compacted and cyclically loaded, under vacuum, following the above procedure (point 1). Water was then introduced, again following the above procedure (point 3). We performed 5 independent swelling experiments on P_disc_5 at fixed stress states of 27.45 MPa, 45.74 MPa, 64.04 MPa, 82.34 MPa, and 100.64 MPa. The ten experiments on pre-compacted powdered samples (Table 1) were performed at stress states of 25.93 MPa, 43.22 MPa, and 77.79 MPa (two experiments per stress), and at stress states of 60.50 MPa (four experiments).

6.3.4. Calibrations

6.3.4.1. Compression test calibrations

The loading frame and compaction cell pistons inevitably experience elastic deformation when load is applied to any sample (apparatus compressibility effect). To obtain the true deformation of the sample versus loading stress (in the compression experiments), the displacement measurements obtained from the external LVDT was corrected using apparatus distortion calibrations. Apparatus distortion or compliance was calibrated by cyclic loading under conditions identical to those used in the compression experiments, with no sample being present. Based on a linear fit (R^2>0.99) to the external LVDT data versus axial load data, apparatus compliance was obtained. We also note that friction between the loading pistons and O-rings was negligible as the O-rings supported a max pressure difference of only 0.1 MPa (1 atm) in the evacuated condition.

6.3.4.2. Swelling test calibrations

In our swelling tests at a constant load, the introduction of liquid water into the evacuated sample, at a fluid pressure of 0.1MPa, causes a change in applied stress states that leads to minor deformation of the apparatus. This deformation was calibrated by measuring the change in external LVDT signal due to introduction of 0.1 MPa liquid water at loading force 1 kN, 3 kN and 5 kN, without sample being present. The results yielded a small, rapid, time-independent deformation, which was insensitive to load. The magnitude corresponded to a swelling displacement of around 0.75 μm, which means a 0.075% (absolute) swelling strain of the 1mm thick coal disc, and 0.04-0.06% (absolute) strain of the coal powder samples. This was used to correct our experimental data where significant. As in the compression tests, O-ring friction effects were of course negligible in the swelling tests. Friction at the interface between sample and titanium compaction vessel were inferred to be negligible too, as graphite-lubricated test runs yielded the same results as runs without graphite.

6.3.5. Data acquisition and processing

The temperature (˚C) of the samples, the polystyrene box, and the Instron, the output signals of the external LVDT (mm), and the Instron load (kN) and position (mm), were recorded using a National Instrument, 16-channel DAOPad-6015 A/D convertor and VI-logger data acquisition system, employing a sampling rate of 0.2Hz.

6.3.5.1. Compression data processing

The axial (compressive) strains of the samples occurring under both evacuated and water-exposed states upon changes in applied stress states were obtained by correcting for the distortion of the apparatus as described above. Note here that zero axial strain of the samples refers to the initial stress state of 9.2 MPa for P_disc_5 and 25.9 MPa for Powder_1, and compressive stress and strain are taken as positive.

For the water-exposed state, deformation of the samples upon changes in applied

stress states includes rapid deformation (i.e. essentially time-independent deformation) and slow time-dependent deformation. The time-dependent axial compressive strain (e^i) of the sample at stress level of *i* was calculated by subtracting the rapid deformation. From the compression tests performed in the evacuated state, equilibration of the rapid deformation associated with elastic deformation took 5 minutes for P_disc_5 and 15 minutes for the pre-compacted sample Powder_1, probably reflecting thermal effects. We therefore calculated the time-dependent compressive strain attained at apparent equilibrium for the wet samples, at stress level *i*, by subtracting the rapid deformation that occurred within the first 10-20 minutes at the *i*th stress state, assuming that this is purely caused by thermo-elastic effects.

6.3.5.2. Swelling data processing

The total axial swelling strain e^{total} (swelling measured as positive) measured in the swelling tests includes rapid deformation (e^{dis}, see 3.4.2) of the apparatus due to introduction of 0.1MPa liquid water, rapid elastic deformation (e^{el}) of the sample due to the change in stress state caused by introduction of 0.1MPa liquid water, and slow time-dependent swelling strain ($e(t)$) of the sample. The elastic deformation of the sample was estimated using the sample compliance obtained from the compression tests in the evacuated state. This elastic deformation amounted to a ~ 0.06 μm displacement for P_disc_5 and a ~0.1 μm displacement for the powdered samples, which were small enough to be neglected.

In the case of P_disc_5, time-dependent swelling strain ($e(t)$) of the sample was obtained from the total swelling strain (e^{total}) by subtracting the distortion of the

apparatus (e^{dis}), i.e. $e(t) = e^{total} - e^{dis}$. Since e^{dis} occurred immediately after the introduction of water into the sample, the time-dependent axial swelling strain (positive) of the sample (%) can be calculated using the expression $e(t) = \frac{L(t) - L_0}{l}$. Here, L_0 (mm) represents the output signal of the LVDT at the instant immediately after the rapid change in LVDT signal, while $L(t)$ (mm) represents the LVDT signal after *t* seconds of subsequent time-dependent swelling. The quantity *l* (mm) represents the initial thickness of the sample. The average value of $e(t)$ over the final 2 hours was taken as the equilibrium axial swelling strain (e^{eq}) of the sample during exposure to water.

In the case of the powdered samples, the time-dependent swelling strain measured upon introducing water is assumed to equal the total swelling strain measured, as the elastic distortion of the apparatus and sample are small enough to be neglected.

6.4. Results

6.4.1. Compression test data: P_disc_5 vs. pre-compacted Powder_1

Compression data for P_disc_5 and the pre-compacted powdered sample Powder_1, as obtained under both evacuated and initial water-exposed states, are shown in Fig.2 and Fig.3, respectively. Compressive axial strain (%) and the applied axial stress (MPa) are measured as positive. Axial strain was arbitrarily set to zero at the starting stress state of each loading run, i.e. at the initial applied stress of 9.15 MPa for P_disc_5 and of 25.93 MPa for Powder_1.

In the case of the sample P_disc_5 loaded under vacuum (i.e. in the evacuated state), raw LVDT (mm) and applied load (kN) data are plotted as a function of time (mins) in Fig. 2a. The corresponding stress-strain data (full set) are plotted in Fig. 2b. Fig. 2a

shows that strain "equilibration" following each applied load increment typically took about 5 minutes, reflecting instantaneous elastic deformation during active loading followed by minor (reversible) time-dependent deformation presumably due to thermal effects. Total test duration was about 55 minutes. The strain-stress data shown in Fig. 2b illustrate non-linear (load-stiffening) mechanical behaviour of the sample that is closely recoverable but with marked hysteresis. For the water-exposed sample P_disc_5, the raw LVDT (mm) and applied load data are plotted as a function of time (hours) in Fig. 2c. The corresponding stress-strain data (full set) are plotted in Fig. 2d. Fig. 2c shows that apparent equilibration at each applied load took 13-34 hours, during which time significant time-dependent strains were accumulated after active loading. The total test duration was ~240 hours. Similar non-linear (load-stiffening) stress-strain behavior was observed, as during loading under vacuum (compare Figs. 2d and 2b). However, as seen in Fig. 2d, a total permanent strain of 0.55% remained after the first loading cycle, while closely recoverable deformation occurred in the second loading cycle. Marked hysteresis was observed in both loading cycles. The cumulative, time-dependent strains occurring after 10 minutes of ceasing active loading (to avoid thermal effects observed in the evacuated state, Fig. 2a) are plotted for the water-exposed samples in Fig. 2e as a function of the applied axial stress. The total time-dependent deformation accumulated at maximum stress during each up-loading run was ~ 0.32% while a small residual time-dependent permanent (hence creep) deformation of ~ 0.14% was observed after unloading to, and equilibration at, the initial stress of 9.15 MPa in both loading cycles on the wet disc (Fig. 2e). This demonstrates that the time-dependent deformation shown in Fig. 2e consists of a reversible component of time-dependent compressive deformation (~ 0.18% strain) plus a time-dependent permanent or creep component (~ 0.14% strain). A non-linear relation between cumulative, time-dependent strains and applied axial stress is also visible from Fig. 2e. When the stress increased from 9.2 MPa to 45.7 MPa, the time-dependent deformation generated at each stress step was ~ 0.04%, while it was

~0.08% when the stress was increased from 45.7 MPa to 100.6 MPa.

Similar behaviour to that reported above for sample P_disc_5 was observed for the pre-compacted coal sample Powder_1, in the both evacuated and water-exposed states (see Fig. 3). However, there are also some important differences in behaviour. In the evacuated condition, sample Powder_1 showed larger time-dependent deformations in the approach to equilibrium strain after each loading increment, with equilibration to a plateau strain taking around 15 minutes per step (see Fig. 3a). The duration of the single run performed under vacuum was around 160 minutes. The full set of strain-stress data shown in Fig. 3b illustrate near-linear (thermo-elastic) behaviour of the sample under vacuum, this behaviour being closely recoverable but with clear hysteresis.

For the water-exposed state, the data obtained for sample Powder_1 show that apparent equilibration took 8-22 hours after each change in applied load (Fig. 3c). The single load cycle performed took ~80 hours in total. Active loading during upward stress stepping yielded relatively linear stress-strain behavior as shown in the full set of strain-stress curve presented in Fig. 3d. However, large amounts of time-dependent deformation occurred in the water-exposed state at each stress state applied, typically around 0.2 to 0.8% strain per stress level (see vertical data segments in Fig. 3d). Upon unloading from the maximum stress applied (95.05 MPa) to the initial applied stress of 25.93 MPa, irreversible behaviour with a total permanent strain of ~ 0.9% was observed after equilibration (Fig. 3d). Cumulative, time-dependent strains versus applied axial stress data are shown in Fig. 3e. This shows that the higher the stress state, the more and the faster time-deformation occurred. A total time-dependent compressive strain of ~ 1.09% was observed after equilibration at maximum applied stress, of which ~ 0.84% strain was permanent (the strain after equilibration upon unloading to the initial stress of 25.93 MPa) and ~ 0.25% was reversible (Fig. 3e).

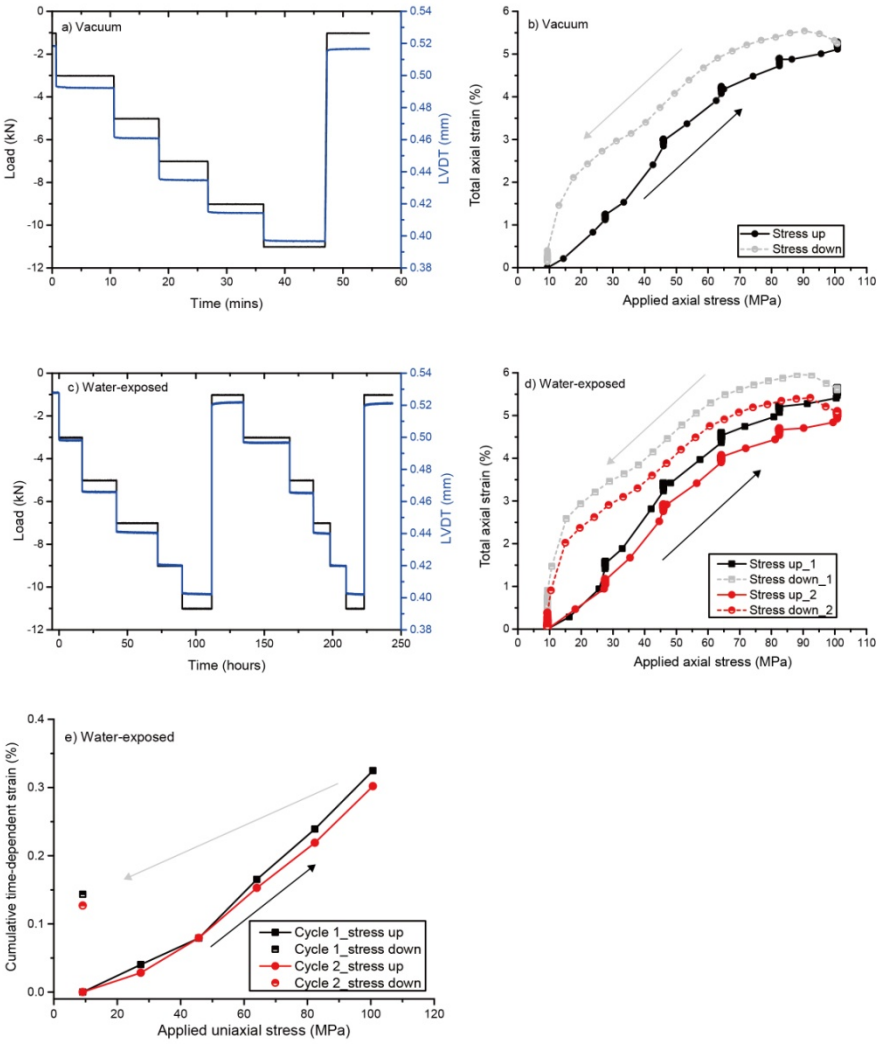

Fig. 2. Compression test data for sample P_disc_5. a) Raw LVDT (mm) and applied load (kN) data are plotted as a function of time in the evacuated state. b) The corresponding total axial strain (%) versus applied axial stress (MPa) data in the evacuated state. c) Raw LVDT (mm) and applied load (kN) data are plotted as a function of time in the water-exposed state. d) The corresponding total axial strain (%) versus applied axial stress (MPa) data in the water-exposed state. e) The cumulative time-dependent (compressive) strains for the water-exposed sample against the applied axial stress. Time dependent compressive strain during each period of constant stress was obtained from apparent equilibrium strain

subtracting rapid deformation occurred within first 10 minutes after a change in applied axial stress. Note that "stress up" refers to upward loading, while "stress down" refers to downward part of cycle.

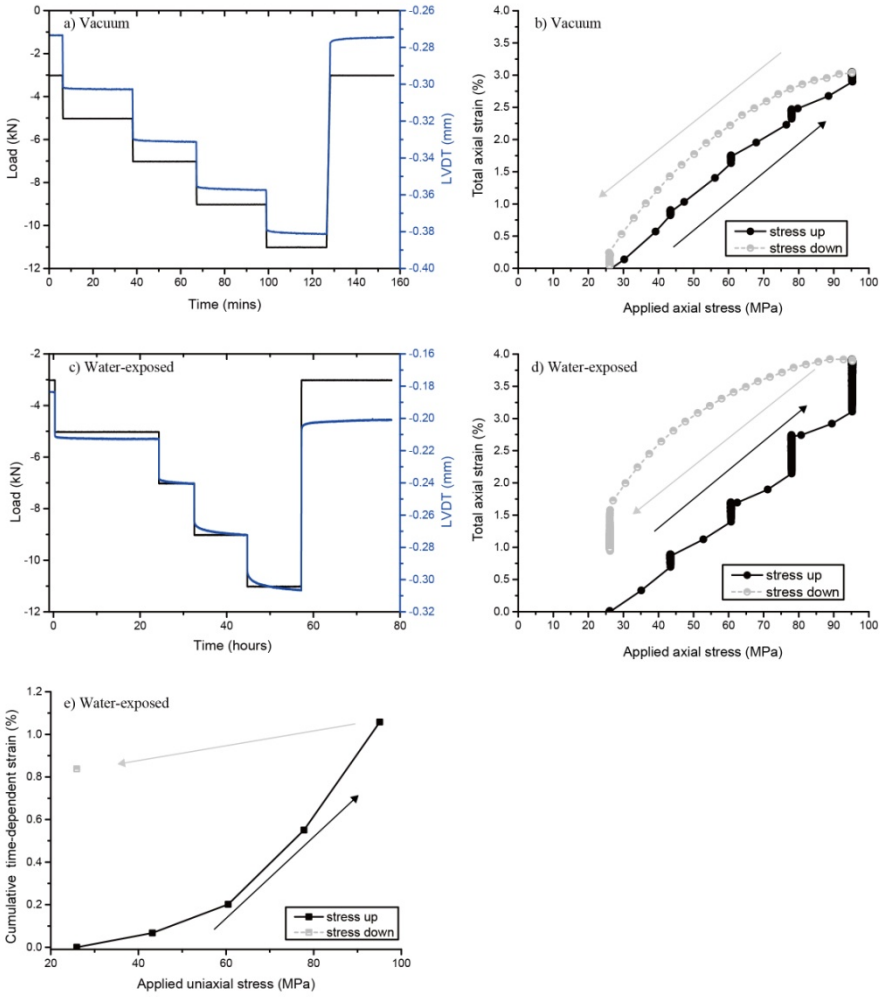

Fig. 3. Compression test data for the pre-compacted powdered sample Powder_1. a) Raw LVDT (mm) and applied load (kN) data are plotted as a function of time in the evacuated state. b) The corresponding total axial strain (%) versus applied axial stress (MPa) data in the evacuated state. c) Raw LVDT (mm) and applied load (kN) data are plotted as a function of time in the water-exposed state. d) The corresponding total axial strain (%) versus applied axial stress (MPa) data in the water-exposed state. e) The cumulative time-dependent compressive strains for the water-exposed sample against the

applied axial stress. Time-dependent compressive strain during each period of constant stress was obtained from apparent equilibrium strain subtracting rapid deformation occurred within first 20 minutes after a change in applied axial stress. Note that "stress up" refers to upward loading, while "stress down" refers to downward part of cycle.

6.4.2. Swelling data: P_disc_5 vs. pre-compacted powdered samples

The axial swelling strain data obtained for sample P_disc_5 and the full suite of pre-compacted powdered samples, upon introduction of water into the evacuated samples at fixed stress states, are shown in Fig.4 and Fig.5, respectively. Note here that axial swelling strains are measured positive, as are the applied compressive stresses. Broadly speaking, all samples (P_disc_5 and samples Powder_1-10, Figs. 4 and 5), expanded in a time-dependent manner, after introduction of liquid water, until an asymptotic or apparent equilibrium strain value was reached (Fig.4a and Fig. 5a). Importantly, the swelling strains attained at apparent equilibrium decreased with increasing applied stress states. In the case of P_disc_5, axial swelling strain gradually developed with time after introducing water via Valve A (Fig. 1), approaching a nearly constant or apparent equilibrium strain after 22-40 hours in most cases (Fig. 4a). Swelling strains attained at ~22 hours for all experiments performed on P_disc_5 are presented against applied axial stress in Fig. 4b (black dots). These data show that the axial swelling strains obtained normal to bedding, as equilibrium was approached, decreased non-linearly from 0.569% to 0.168% as the applied axial stress increased from 27.4 MPa to 100.6 MPa. Swelling strains attained (at > 40 hours) in the three experiments that ran for 40 hours or more are also plotted in Fig. 4b (red dots). These decreased with increasing applied axial stress following a similar trend, though the absolute strains are slightly higher than that attained at ~ 22 hours at the same applied axial stress, because equilibrium was more closely approached at 40 hours.

In the case of the pre-compacted powdered samples, axial swelling strain development with time is shown in Fig.5a. The origin of the time axis in Fig. 5a refers to the moment that we opened the Valve B, shown in Fig.1, to let liquid water enter the

pipe section A-B, keeping Valve A closed in an attempt to maintain the sample in the vacuum dry state. The zero point on the strain axis in Fig. 5a refers to the LVDT output or strain state just prior opening Valve A. From this figure, it is clear that in the seven tests performed on samples Powder_3 and Powder_5-10, large time-dependent expansions were observed after opening Valve B but before opening Valve A (i.e. before the liquid water entered the sample). These time-dependent expansions approached asymptotic (or apparent equilibrium) swelling strains of 0.22-0.93% within a period of 2.5 to 6 hours after opening Valve B. This swelling, was presumably caused by adsorption of water vapor that diffused into the samples through Valve A after opening Valve B. However, after water was admitted to the sample by opening Valve A, rapid expansion developed within the first hour in all tests, with the swelling strains attained in this stage reaching more than 95% of the final apparent equilibrium strain measured with respect to the zero point on the strain axis. After this fast expansion, slow expansions were observed at the applied stress states of 25.9 and 43.2MPa, while slow, time-dependent compaction occurred at 60.5 MPa and 77.8 MPa. The total, near-equilibrium (plateau) swelling strains, averaged over the last two hours of each experiment, are plotted versus the applied uniaxial stress states in Fig.5b. Note that these swelling strain data include the apparent equilibrium swelling strain caused by water vapor entering via Valve A before liquid water was admitted to the samples, plus the apparent equilibrium swelling strain caused by adding the liquid water. The results show that the total equilibrium swelling strain attained at apparent equilibrium decreased more or less linearly, from 1.889% strain to to 0.615% strain, when the applied uniaxial stress state increased from 25.9 MPa to 77.8 MPa (Fig. 5b).

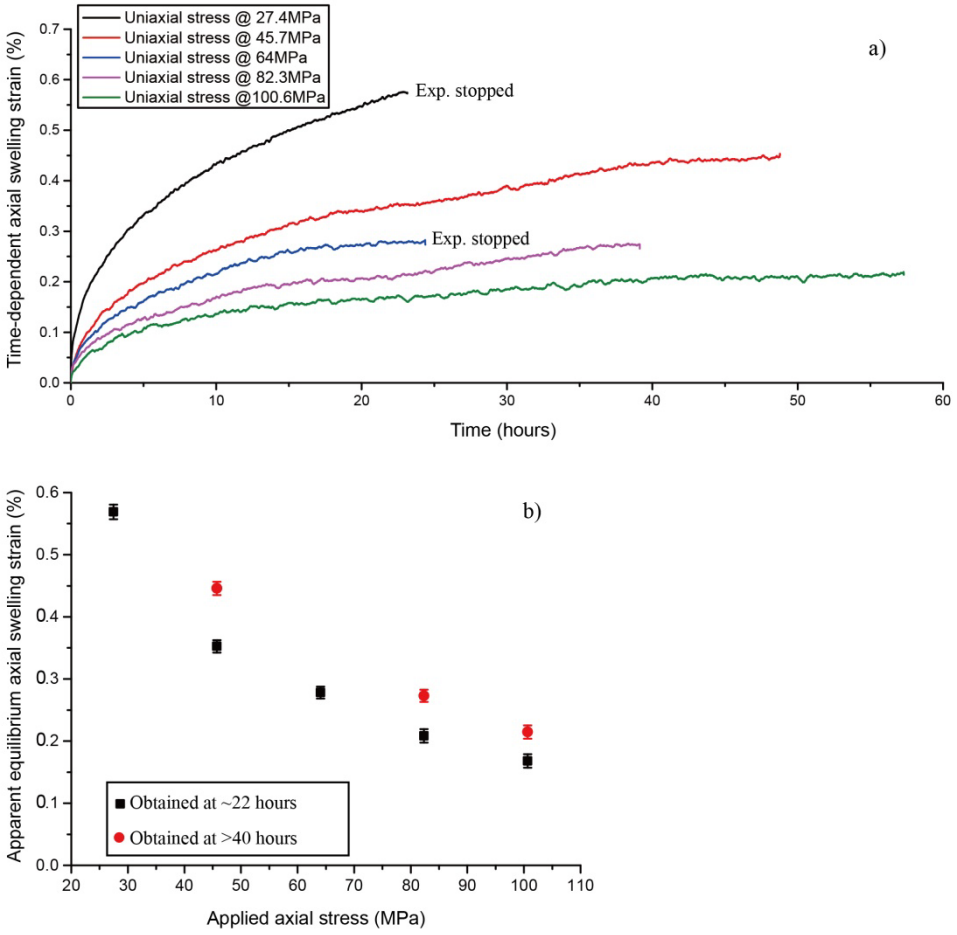

Fig.4. Axial swelling strain (%) attained for P_disc_5 in the direction perpendicular to bedding during exposure to distilled liquid water at an absolute fluid pressure of 0.1 MPa (1 atm). a) Axial swelling strain versus time, corrected for apparatus distortion and elastic deformation of the sample due to injection of 0.1 MPa liquid water into the evacuated sample. b) Axial swelling strain, measured in the approach to equilibrium at 22 and 40 hours elapsed time, versus applied axial stress.

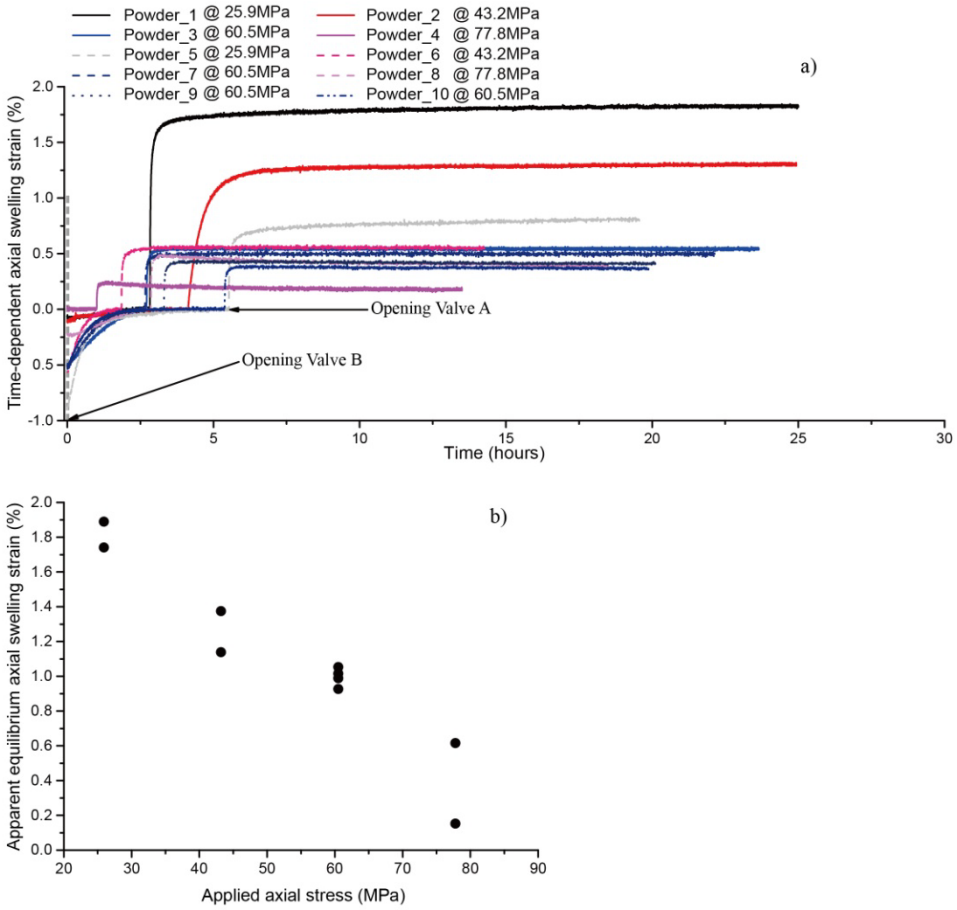

Fig.5. Axial swelling strain (%) attained for all pre-compacted powdered samples during exposure to distilled liquid water at an absolute fluid pressure of 0.1MPa. a) Axial swelling strain versus time. The origin of the time axis refers to the moment that we opened the Valve B (Fig. 1b) to let liquid water enter pipe segment A-B in Fig. 1, keeping Valve A closed in an attempt to maintain the sample in the vacuum dry state. The zero strain point on the strain axis refers to the LVDT output or equivalent strain at the moment just prior to admitting liquid water into the sample by opening Valve A. b) Total axial swelling strains attained at apparent equilibrium versus applied uniaxial stress. The total swelling strain data shown in (b) were obtained by averaging the swelling strain data obtained in the final two hours shown in a, all measured relative to the strain at the fist onset of swelling. The swelling strain data in b thus include the apparent equilibrium swelling strain caused by water vapor entering via Valve A before liquid water was admitted to the samples, plus the apparent equilibrium swelling strain

caused by adding the liquid water.

6.4.3. Swelling kinetics data

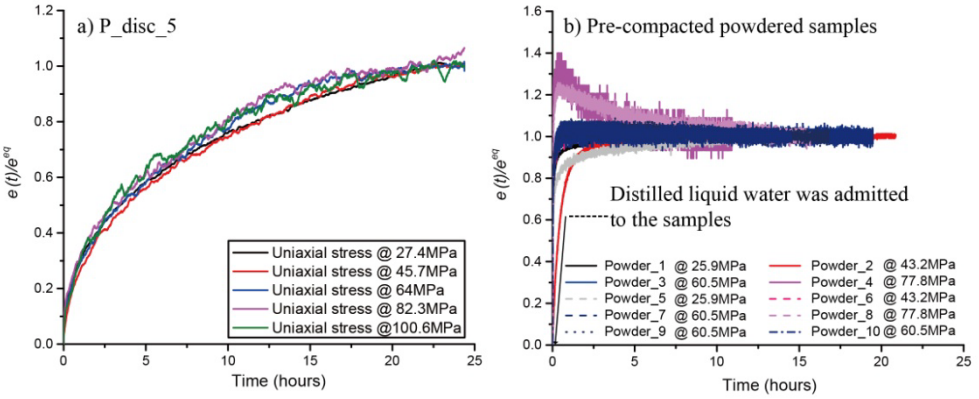

Fig.6. Normalized swelling strains of samples (expressed as the ratio $e(t)/e^{eq}$) upon adsorption of distilled water at given fixed applied stress states versus time. a) P_disc_5. b) Pre-compacted powdered samples after liquid water was admitted to the samples.

Following the standard treatment employed in presenting sorption and swelling data as a function of time to investigate process kinetics (c.f. Busch and Gensterblum, 2011; Li et al., 2010; Staib et al., 2014; Staib et al., 2013), normalized swelling strains ($e(t)/e^{eq}$) due to adsorption of distilled water at given fixed applied stress states are plotted in Fig.6 as a function of time, for all of our samples. Note here that the swelling data for the pre-compacted powdered samples plotted in Fig.6b represent swelling strain data (measured with respect to the zero point on the strain axis in Fig. 5a) plotted against elapsed time from the moment at which the distilled (liquid) water was admitted to the samples via Valve A (thus avoiding displaying the rate of swelling that occurred in cases where water vapour diffused into the samples via Valve A at an earlier stage). It is clear from Fig. 6a that swelling rates for P_disc_5 are insensitive to applied stress state. However, from Fig 6b, it is evident that the swelling rate of the pre-compacted powdered samples (grain size within 180-212 μm) is much faster than that for P_disc_5 (1mm disc) at similar applied stresses. Moreover, the effect of applied stress on swelling kinetics of

the pre-compacted powdered samples (Fig.6b) is much more complicated than in the case of sample P_disc_5 (Fig. 6a), as considerable variability in swelling behaviour occurred in the swelling experiments due to the complications of water vapour entering some samples before liquid water was admitted, and of some powdered samples showing minor, late stage compaction (see Fig. 5a). The effects visible in Fig.5a, namely a) the time-dependent swelling behaviour seen before admitting liquid water into the samples, and b) the time-dependent compaction behaviour seen at higher stress states after contact with liquid water, strongly influence the swelling rates shown in Fig.6b. Note, however, behavior of Sample Powder_2 at a stress state of 43.2 MPa. In this experiment, there was no time-dependent swelling before the sample was exposed to liquid water, nor did time-dependent compaction occur after liquid water was admitted into the sample (see Fig. 5a). This sample shows the slowest swelling rate in Fig.6b.

6.5. Discussion

The swelling data presented above for our coal disc and powdered coal samples have demonstrated that the higher the axial stress applied to the samples, the lower the swelling of coal samples due to adsorption of water after introduction and equilibration at a fixed absolute fluid pressure of 0.1 MPa. This finding is consistent with the model predictions of all of our models for the thermodynamic effect of stress on sorption capacity. However, the stepwise loading tests performed on the water-exposed samples (P_disc_5 and Powder_1) showed the strains achieved at (apparent) equilibrium to consist of a reversible elastic component, a reversible component of time-dependent deformation, plus a permanent component of time-independent deformation (1st run) as well as time-dependent deformation (creep). This means that the reduction in swelling strain observed with increasing applied stress in the swelling tests might be due not only to a stress-related reduction in adsorbed water concentration at equilibrium, but to additional mechanisms allowing both a) permanent creep, and b) reversible

time-dependent deformation that is independent of reversible sorption and associated time-dependent deformation.

In the following, we will further discuss the mechanisms responsible for the stress-driven reduction in swelling. We start this by comparing our experimental data with predictions made regarding reversible thermodynamic stress-strain-sorption effects using the three models presented in Section 6.2, with the aim of explaining departures from this in terms of other possible processes. We go on to discuss the differences in behaviour observed between the disc and powered samples, and the difference in mechanical response of the samples seen between dry and wet states. Finally, we consider the likely implications of our findings for (E)CBM recovery.

6.5.1. Mechanisms responsible for the stress-driven reduction in swelling

6.5.1.1. Thermodynamic effect of applied stress on water adsorption: comparison with model predictions

To determine whether the stress-driven reduction in swelling that we measured in the swelling experiments is explained by stress-driven reduction in water adsorption capacity, versus other processes such as creep, we compare our swelling data for both disc and powdered samples with the predictions made by the three models derived in Section 6.2. To predict the magnitude of swelling strain caused by adsorption of water using our models (equations 3, 4, 7 and 10), we need to know the stress states, the swelling strain anisotropy tensor A_{ij}, the volumetric swelling per mole of adsorbed water molecules V_0, the equilibrium constants (K^0, K_1, K_2) and adsorption site concentrations (C_s, C_s^1, C_s^2) for both the disc and powdered samples.

We consider two end-member stress states as potentially applying to sample P_disc_5 (see 5.2.1.), i.e. uniaxial stress $\sigma_{ij} = \begin{pmatrix} \sigma & 0 & 0 \\ 0 & 0 & 0 \\ 0 & 0 & 0 \end{pmatrix}$ (laterally unconfined case, taking the compression direction and bedding plane normal to be the x_1 direction) and

hydrostatic stress $\sigma_{ij} = \sigma\delta_{ij}$ (laterally confined and assuming constant sample volume). These correspond respectively to the minimum and maximum possible effects that the applied axial stress can exert on the sorption capacity of Sample P_disc_5, according to the models we have developed. For the pre-compacted powdered samples, which were constrained laterally from the outset, we assume that the stress state was approximately hydrostatic, so that $\sigma_{ij} = \sigma\delta_{ij}$. Also assuming that the pre-compacted samples were mechanically more or less isotropic, this assumed hydrostatic stress state corresponds to the maximum impact that the applied stress can have on reducing water adsorption capacity due to the thermodynamic stress-strain-sorption effects captured in our models.

Regarding A_{ij}, the swelling strain anisotropy tensor, for P_disc_5, this was assumed to be given by $A_{ij} = \begin{pmatrix} 0.14 & 0 & 0 \\ 0 & -0.07 & 0 \\ 0 & 0 & -0.07 \end{pmatrix}$. The principal components of this tensor were estimated from the experimental data reported by Liu et al. (Chapter 5), who measured the swelling strains developed in cubic samples of the present coal matrix material during adsorption of water vapour in the range of 0.1-95% relative humidity (RH) at 40˚C. Since we assume that the stress state for the pre-compacted powdered samples was hydrostatic, and since that the axial swelling strain measured in our swelling experiments yields the volumetric swelling strain, the term $\exp(\frac{-\sigma'_{ij}A_{ij}V_0}{3RT})$ appearing in equations 3, 4, 7 and 10 and in the function $E(\sigma_{ij}, P_0)$ simplify to unity for the powdered samples.

To estimate the parameter V_0 for water molecules adsorbed in our coal samples, we used the swelling strain measured for P_disc_5 at a low applied axial stress (i.e. at 27.4MPa where stress driven creep effects are likely to be small) using the expression

$V_0 = (\frac{e_v^{eq}}{C\rho})_\sigma$. Here, e_v^{eq} for P_disc_5 at 27.4MPa applied stress was estimated based on the axial swelling strain e_z^{eq} measured for P_disc_5 at 27.4 MPa, using equation 4a, yielding 1.498%, which is similar to the values of 1.37-1.43% obtained for cubic sample of the same coal matrix material at 95% relative humidity under unconfined conditions (Liu et al., Chapter 5). The corresponding adsorbed amount of water (C) at a stress state of 27.4 MPa was estimated as 2.27 mol/kg$_{coal}$ based on the mass difference measured for the sample before and immediately after the experiment. Using the density of our sample P_disc_5 of 1267.2 kg/m^3, we obtain V_0=5.21×10^{-6} m^3/mol for P_disc_5, which is reasonably in line with the average value of 4.3×10^{-6} m^3/mol in literature for coals of bituminous rank (Fry et al., 2009). We assume this value also holds for the pre-compacted powdered samples.

We now focus on constraining the equilibrium constants for the three models. Since the equilibrium constants K^0, K_1 and K_2, for water adsorption by coal, depend only on temperature and coal rank (in other words, since they are independent of water activity), they can be obtained from best fits of the three models to the experimental data on e_v^{eq} vs. RH, and hence vs. a_g , reported for solid cubic samples by Liu et al. (Chapter 5). Those data were for the same coal material under unstressed conditions at the same temperature. Fitting the HS model (Model 1) to those data gave K^0=0.161, whereas the Dent-based swelling model (Model 2) gave K_1=2.236 and K_2=0.480, and the DW-based swelling model (Model 3) gave K_1=1.11 and K_2=0.65. We assume that these equilibrium constant values for the three models apply for P_disc_5 and for our pre-compacted powdered samples.

Finally, we consider the parameter C_s for the three models. Values of C_s were calculated by fitting equations 4b, 7b and 10b to the swelling data obtained at a specific

axial reference stress of σ_{ref}, forcing the requirement that $(\varepsilon_{11}^{eq})_{\sigma_{ref}} = (\varepsilon_{11}^{measured})_{\sigma_{ref}}$, where $(\varepsilon_{11}^{eq})_{\sigma_{ref}}$ is the axial swelling strain predicted by the three models at stress σ_{ref}, and where $(\varepsilon_{11}^{measured})_{\sigma_{ref}}$ is the (average) axial swelling strain measured upon introduction of water into our samples at stress σ_{ref}. Here σ_{ref} = 27.4 MPa for P_disc_5 and 25.9 MPa for pre-compacted powdered sample Powder_1, in line with the choice of the applied stress state for estimation of V_0. The full set of parameter values obtained for the three models for P_disc_5 and the pre-compacted powered samples are summarized in Table 2.

Using the parameters obtained as above, and setting the water activity a_g=1, we applied our three models (equations 3, 4, 7 and 10) to predict the swelling strains expected for P_disc_5 and the pre-compacted powdered samples versus applied stress states (see Fig. 7). Of course, all three models predict trends that pass through the (average) swelling strains measured experimentally at the reference stresses of 27.4 MPa (sample P_disc_5) and 25.9 MPa (powdered samples), as the models were fitted to these measured data points. It is clear from Fig. 7, that the swelling strains predicted by the three models decrease near-linearly with increasing applied stress, with each model yielding a similar sensitivity of swelling strain to applied stress. The largest reduction in swelling with increasing stress, caused by the thermodynamic stress-strain-sorption effect, is predicted by Model 3 (DW-based swelling model), assuming that the stress state of our samples was hydrostatic. This model predicts a) that swelling strain decreases from 0.569% to 0.481% for P_disc_5 when the applied stress increases from 27.4 MPa to 100.6 MPa, and b) that swelling strain decreases from 1.826% to 1.571% for pre-compacted powdered samples when the applied stress increases from 25.9 MPa to 77.8 MPa. However, even using Model 3, the predicted swelling strains are much higher than the measured swelling strains at the same stress. Indeed, Model 3 predicts that the largest sensitivity of swelling strain to hydrostatic stress is -1.2×10^{-3} % strain per

MPa for P_disc_5 and -4.9×10^{-3} % strain per MPa for pre-compacted powdered samples. However, the average sensitivity of measured swelling strain to applied stress is around -4.8×10^{-3} to -5.5×10^{-3} % strain per MPa, for P_disc_5, and around -21.1×10^{-3} to 23.2×10^{-3} % strain per MPa for pre-compacted powdered samples (Fig. 7). Taking into account the permanent time-dependent compressive creep strain i) of ~0.14% observed for P_disc_5 when the applied stress decreased from 100.6 MPa to 9.2 MPa (Fig. 2e), and ii) of ~0.84% observed for Powder_1 when the applied stress decreased from 95MPa to 25.9MPa (Fig. 3e), observed in the stress-stepping compression experiments, the sensitivity of swelling strain to applied stress caused by permanent creep is estimated to be ~ -1.6×10^{-3} % strain per MPa for P_dis_5 and ~ -12×10^{-3} % strain per MPa for the pre-compacted powdered samples. This means that the stress-driven reduction in swelling observed for our samples in the swelling experiments, even after accounting for the permanent time-dependent deformation (creep) component from our data, is not only due to the thermodynamic effect of stress on water adsorption capacity, but also due to other mechanisms. Specifically, for P_disc_5, around half the reduction in measured swelling can be accounted for by approximately equal contributions from the thermodynamic stress-strain-sorption effect (Models 1-3) plus the permanent strain effect and the other half by a third mechanism. However, for the pre-compacted powdered samples, around ½ the reduction in measured swelling is caused by permanent compaction creep strain effect, while ¼ of the reduction can be accounted for by the stress-strain-sorption effect embodied in Models 1-3, meaning that yet another ¼ of the reduction is due to a third effect.

Table 2. Parameter values obtained for the three models used in this study.

Model	$C_s(mol/kg_{coal})$	K^0	C_s^1 (mol/kg_{coal})	C_s^2 (mol/kg_{coal})	K_1	K_2	$V_0(m^3/mol)$
P_disc_5 assuming a uniaxial stress state							
1	16.661	0.161					5.21×10^{-6}
2	1.48				2.346	0.480	5.21×10^{-6}
3			1.646	0.326	1.110	0.650	5.21×10^{-6}
P_disc_5 assuming a hydrostatic stress state							
1	17.159	0.161					5.21×10^{-6}
2	1.542				2.346	0.480	5.21×10^{-6}
3			2.737	0.542	1.110	0.650	5.21×10^{-6}
Powdered samples assuming hydrostatic stress states							
1	26.392	0.161					5.21×10^{-6}
2	2.37				2.346	0.480	5.21×10^{-6}
3			4.27	0.833	1.110	0.650	5.21×10^{-6}

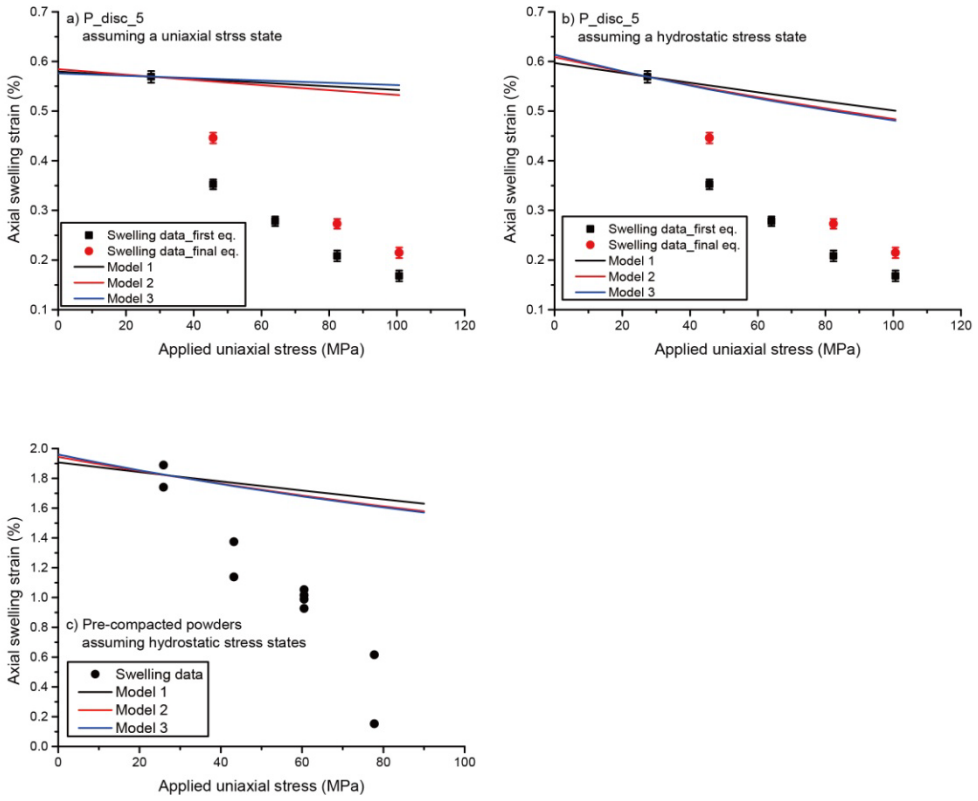

Fig.7. Comparison of axial swelling strains (%) obtained for our samples versus applied stress, with the predictions of Models 1, 2 and 3 applied for a) P_disc_5 assuming a uniaxial stress state, b) P_disc_5 assuming a hydrostatic stress state, and c)the pre-compacted powdered samples assuming hydrostatic stress states. The dots represent the experimental data shown in Fig.4 and Fig.5, while the solid lines represent predictions made by the three models as indicated.

Aside from the above, our models can also predict the response expected in the stepwise compression experiments, performed on samples P_disc_5 and Powder_1, due to the thermodynamic effect of stress on water adsorption capacity. These predictions can then be compared with the cumulative time-dependent compression data shown in Fig. 2e and Fig. 3e. Such a comparison is shown in Fig. 8, taking the swelling strains predicted by the three models at the lowest applied stress (27.4MPa for P_disc_5 and 25.9MPa for pre-compacted powdered samples) employed in the swelling experiments

as reference data points, which the models are constrained to pass through, and taking compression as positive. The predicted deformation caused by the thermodynamic stress-strain-sorption effect embodied in Models 1-3 increases near-linearly with increasing applied stress, with the sensitivity to applied stress obtained for P_disc_5 being around 0.3×10^{-3} to 1.1×10^{-3} % strain per MPa, and for Powder_1 being around 2.9×10^{-3} to 3.8×10^{-3} % strain per MPa. The average sensitivity of reversible cumulative time-dependent (compressive) strains versus applied stress measured for P_disc_5 was around 2×10^{-3} % strain per MPa (see unloading data in Fig. 2e) and for Powder_1 around 3.1×10^{-3} % strain per MPa (see unloading data in Fig. 3e). Therefore, in the compression tests, around ½ of the reversible time-dependent deformation observed for P_disc_5 can be accounted for thermodynamic stress-strain-sorption effect (Models 1-3), and the other half for a third mechanism. For Powder_1, the reversible time-dependent deformation can be fully accounted for thermodynamic stress-strain-sorption effect (Models 1-3)

The above analyses confirm that, in general, the time-dependent deformation exhibited by our samples during exposure to water cannot be explained purely by the thermodynamic stress-strain-sorption effect plus permanent creep, but must also have involved at least one other mechanism.

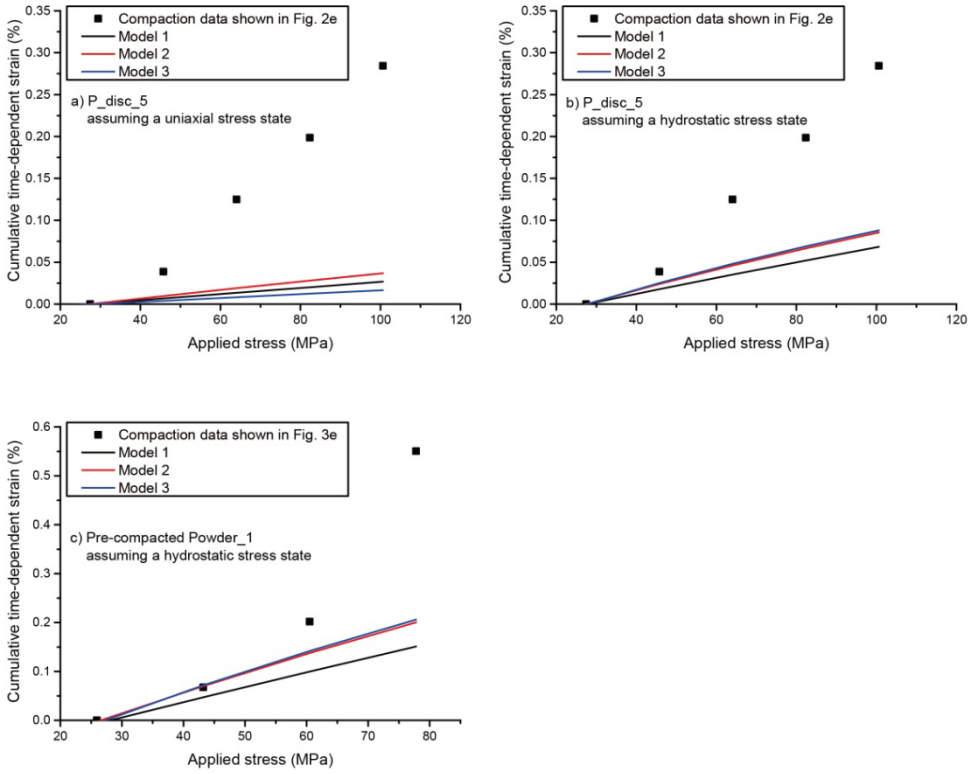

Fig. 8. Comparison of the time-dependent compressive strain (%) versus applied stress data, obtained in our stepwise compression tests, with the predictions of Models 1, 2 and 3 applied for a) P_disc_5 assuming a uniaxial stress state, b) P_disc_5 assuming a hydrostatic stress state, and c) pre-compacted powdered sample Powder_1 assuming a hydrostatic stress state. The dots represent the experimental data shown in Fig.2e and Fig.3e, while solid lines represent the predictions made by the three models.

6.5.1.2. Stress-driven closure of transport paths

Another possible mechanism contributing to the observed stress-driven reduction in swelling of our samples is the stress-driven closure of transport paths in the samples. Closure of the transport paths can potentially occur via the compaction of the coal disc matrix or the matrix within individual grains driven by the applied stress. Closure of the transport paths would reduce access of water into the coal matrix, and hence reduce the swelling measured upon adsorption of water due to equilibrium being established only in accessed portions of the coal matrix. This interpretation is supported by the following

evidence.

1. Swelling strains measured for the powered samples were larger than the disc sample. The estimated volumetric swelling of P_disc_5 at the stress state of 27.4 MPa using equation 4a was 1.5% (see Section 6.5.1.1.), which is less than the measured volumetric swelling strain of ~1.8% for pre-compacted powdered samples at similar stress states (see Fig. 5b). This is consistent with our model fits, which show that the calculated values of adsorption site density C_s for P_disc_5 were less than those for pre-compacted powdered samples (see Table 2). The difference in calculated adsorption site density C_s is in turn consistent with the water accessibility to powdered samples being higher than to the disc sample, as a result of the porosity of powdered samples (~25%) being higher than the disc sample (~4%).

2. The observed swelling kinetics were influenced by the applied stress states. The swelling kinetics data shown in Fig.6 indicate that swelling rates for pre-compacted powdered samples decreased when the applied stress increased from 25.9 MPa to 43.2 MPa. This is consistent with stress-driven closure of transport paths in individual grains in the pre-compacted powdered samples. On the other hand, the effect was not observed for P_disc_5. This argues against an effect of stress on transport but could also mean that the axial stress acting on sample P_disc_5 mainly closed transport paths in the bedding plane of P_disc_5, thus influencing radial diffusion along the bedding with diameter of 11.8mm, but with the swelling kinetics being mainly determined by diffusion perpendicular to bedding, as the thickness of P_disc_5 is only 1mm.

3. Stress-driven reduction of swelling strains measured in our swelling experiments (see Figs. 4b and 5b) was larger than the cumulative, time-dependent compressive strains measured for wet samples in our compression tests (Figs. 2e and 3e). In our compression experiments, distilled water was injected into the sample at the lowest applied stress (9.15 MPa for P_disc_5 and 25.93 MPa for Powder_1), while in the swelling experiments it was injected at higher stresses (~25 to ~100 MPa). If applied

stress can close transport paths in the coal matrix, and hence reduce water accessibility, then the reduction in swelling strain caused by this mechanism in the swelling experiments should indeed be larger than the cumulative time-dependent deformation, driven by the same mechanism, measured in the compression tests. At the same time, the reduction in swelling strain occurring in swelling tests, caused by the thermodynamic effect of stress and/or permanent creep effect, should be similar to the cumulative time-dependent compressive strain caused by the same mechanisms occurring for similar stress differences in the compression tests. In Fig. 9, we plot a comparison of the total, stress-driven reduction in swelling strains (Δe_S), obtained in the swelling tests versus the cumulative time-dependent strain data, Δe_D, obtained for water-exposed samples in the compression tests. In the swelling tests, Δe_S is the reduction of swelling strains at a given stress, compared to the reference stress (27.4 MPa for P_disc_5, and 25.9 MPa for the powdered samples). In the compression, Δe_D is the change in cumulative, time-dependent strains at a given stress, compared to the same reference stress. It is clear that $\Delta e_S > \Delta e_D$. Fig. 9 therefore supports the hypothesis that the stress-driven closure of transport paths is one of the mechanisms responsible for stress-driven reduction in swelling in (all) our experiments.

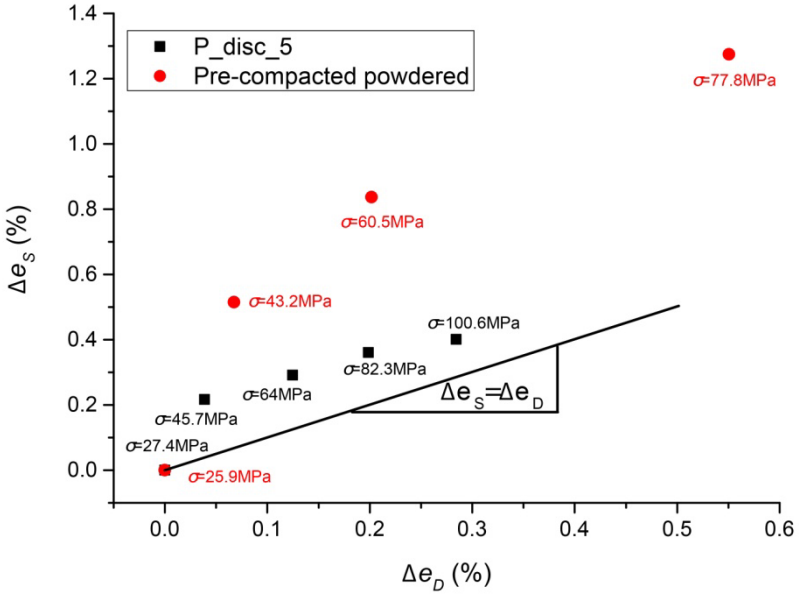

Fig. 9. A comparison of the total, stress-driven reduction in swelling strains (Δe_S), obtained in the swelling tests versus the cumulative time-dependent strain data, Δe_D, obtained for water-exposed samples in the compression tests.

In addition to the above arguments, stress-driven closure of transport paths has also been reported in the literature. Pone et al. (2009) measured the CH_4 sorption capacity of bituminous coal (a cylinder of 25 mm in diameter) under both stressed (confined) and unstressed (unconfined) conditions using volumetric methods. They present evidence that confining stresses of 6.9 and 13.8MPa caused a reduction in CH_4 sorption capacity of 85 and 91% respectively, at a CH_4 pressure of 3.8MPa at room temperature. Liu et al. (Chapter 3) showed that this large reduction reported by Pone et al. was due to both a) a direct effect of stress on equilibrium sorption capacity, and b) a reduction in the volume of coal sample that was accessible to CH_4 as sample permeability decreased with increasing confining stress.

To sum up, the analysis in Sections 6.5.1.1. and 6.5.1.2. suggest that the mechanisms responsible for stress-driven reduction in swelling caused by water adsorption are the combined effects of a) permanent time-dependent deformation (creep), b) the

thermodynamic influence of stress on water adsorption capacity, and c) stress-driven closure of transport paths within the coal matrix material. For the disc sample, mechanism (c) contributed mostly (see Section 6.5.1.1.), while for powdered samples, mechanism (a) contributed mostly (see Section 6.5.1.1.).

6.5.2. Comparison of the samples used in the present study: disc versus powders

We have performed experiments on disc sample P_disc_5 and pre-compacted powdered samples. The experimental results consistently showed that applied stress reduces swelling response. However, the results also showed that the disc sample behaved differently in terms of mechanical response under both evacuated and wet conditions, and in terms of swelling behaviour upon introduction of water at constant applied stress, compared with the powdered samples. These differences are compared and analyzed as follows.

1. In the evacuated state, Sample P_disc_5 yielded non-linear recoverable/elastic behaviour (see Fig. 2b), while the pre-compacted powdered sample Powder_1 yielded near-linear recoverable/elastic behaviour (see Fig. 3b). This difference can potentially be explained by the different stress states supported by the disc versus powdered samples under the same or similar uniaxial stress. In the experiments, the true stress state supported by P_disc_5 was likely uniaxial, due to the loose fit in the titanium sample vessel, or perhaps approaching hydrostatic, due to friction generated when the sample deforms laterally against the porous plate. The changes in stress applied to P_disc_5 during loading may well have influenced the uniaxial versus hydrostatic nature of the stress state within the sample, causing the non-linear behaviour observed in the experiments. By contrast, the pre-compacted powdered sample Powder_1 was laterally constrained, so that changes in internal sample stress state during the experiments are likely to have been less marked. In addition to the above, the presence of micro-fractures in Sample P_disc_5 (11.8×1 mm^2) might also lead to the non-linear elastic behaviour observed in our compression experiments, with the apparent stiffness of the sample

increasing with increasing applied stress. Compared to P_disc_5 (11.8×1 mm^2), the pre-compacted grains (180-212 μm) likely contained fewer or no micro-fractures because the grain size is small.

2. In the water-exposed state, more permanent creep was attained in the pre-compacted powdered sample Powder_1 than in the experiment on P_disc_5 (see Figs 2e and 3e). This might be due to a) the presence of water reducing friction between the grains in the powder sample, promoting rearrangement of the grains, and/or b) the thus reduced intergranular friction increasing the stresses supported by the grains, hence increasing compaction of the granular samples. These effects might also explain the late stage, time-dependent compaction that occurred in the powdered samples at high stresses in the swelling tests (Fig. 5a). They would not be expected to occur in solid sample P_disc_5. This is consistent with the fact that the time-dependent compression was not observed in the swelling experiment on P_disc_5. In addition, the difference observed in permanent compaction between wet P_disc_5 and wet Powder_1 may have been influenced by the stress state in the samples due to the difference in lateral confinement, as postulated for explaining the non-linearity in recoverable/elastic behaviour of P_disc_5 versus Powder_1 under Point 1.

3. Our swelling experiments (Figs 4 and 5) showed that the volumetric swelling strains measured for the pre-compacted powdered samples were bigger than estimated for P_disc_5 at similar applied stresses. This can be explained by a) greater water accessibility to the coal matrix in the powdered samples than in P_disc_5 (also see 5.1.2. point 1), or b) faster equilibration or a higher level of equilibration in the powdered samples than in P_disc_5.

Based on the above analysis, it is inferred that the differences in mechanical response between the disc and powdered samples are mainly caused by differences in pore structure, for example the presence of microfractures in P_disc_5 versus the large intergranular porosity of the powdered samples with an absence of microfractures within

the grains. In other words, the pore structure of the samples played an important role in controlling their response to loading and presence of water.

6.5.3. Effect of water on mechanical response of the samples

Our stepwise compression test data visible in Figs 2 and 3 show that the presence of water changed the mechanical response of both the disc and powdered samples to loading. Compared to the samples loaded in the evacuated state, incremental loading of the wet samples involved a reversible component of time-dependent deformation plus permanent creep. These effects influenced the apparent elastic modulus of the samples in the presence of water, as seen from a comparison of the strain-stress curves shown in Figs 2b and 2d, for P_disc_5, and in Figs 3b and 3d, for Powder_1. These figures show there was a minor influence of water on the apparent modulus in the case of P_disc_5, but a large influence in the case of Powder_1.

Focusing now on the reversible component of time-dependent compaction, we have already inferred in Section 6.5.1.1. that this reversible component of deformation during stepwise loading is controlled by the thermodynamic stress-strain-sorption effect plus the closure of transport paths driven by elastic deformation. The permanent creep component observed in the present experiments might also be related to the presence of water, again as already discussed. For example, in the powdered samples, the presence of water might reduce friction between the grains, thus resulting in the permanent compaction creep due to either rearrangement of grains or an increase in stress supported by the grains (see also Section 6.5.2). On the other hand, in sample P_disc_5, microfractures could be generated due to sorption and swelling (as reported by Hol et al., 2012b; Liu et al., Chapter 4), and thus cumulative microcracking could potentially cause or promote permanent compaction creep.

6.5.4. Likely implications for (E)CBM

Our findings have a number of implications for (E)CBM production. These can be

summarized as follows.

First, our models predict that applied stress reduces water sorption capacity and associated swelling, and this effect depends on the magnitude of partial volume of adsorbed molecules (V_0). In the case of the Brzeszcze high volatile bituminous coal samples used in the present study, the estimated V_0 is small (5.21×10^{-6} m^3/mol), and the thermodynamic effect of stress on water adsorption capacity, and the resulting reduction in swelling (see Fig 7), are small and can be neglected at in-situ, lithostatic stress states (which typically lie in the range 10-30 MPa). However, as V_0 for adsorbed water molecules in principle depends on coal rank, for lower rank coal with a generally higher value of V_0 (e.g. V_0=13×10^{-6} m^3/mol for lignite, see Suuberg et al., 1993), the thermodynamic effect of in-situ stress on water adsorption capacity and on the associated swelling might have to be considered when designing and optimising enhanced (E)CBM production strategies.

Second, in the case of Brzeszcze high volatile bituminous coal, our experiments show volumetric swelling strains caused by water adsorption (at 100% relative humidity) of ~ 1.5 to ~ 1.8% at applied axial stresses of ~ 25 MPa (equivalent to an in-situ burial depth of ~1000m). These swelling strains are similar to the volumetric swelling strains (1.37-1.43%) measured for similar Brzeszcze coal matrix samples at 95% relative humidity under unconfined conditions (Liu et al., Chapter 5). This suggests that effects of permanent creep and closure of intra-matrix transport paths, driven by in-situ stress, on the swelling behaviour of coals like the Brzeszcze coal are also small enough to be negligible in practice. This is further supported by the fact that our experiments on the disc sample was not fully confined laterally and the powdered samples had high intergranular porosity, so that larger creep strains were likely possible than would occur in dense coal under in-situ conditions.

Finally, the present results have shown that the effect of lithostatic stress on the swelling/shrinkage response of coal to water is minor and for practical purposes

negligible for Breszcze high volatile bituminous coal. This means that the large shrinkage effects due to drying seen in the unconfined experiments (Liu et al., Chapter 5) are not changed by in-situ stresses. The implication is that the (E)CBM strategy, proposed by Liu et al. (Chapter 5) (i.e. of removing water from coal seams by nitrogen flushing thus initiating self-enhancing shrinkage and (micro)cracking of the coal and enhanced methane production) is not significantly influenced by effects of in-situ stress on swelling/sorption.

6.6. Conclusions

In an attempt to understand the effect of applied stress on water adsorption by coal and on the associated swelling, thermodynamic models for swelling of coal matrix material due to water adsorption under stressed conditions were developed, assuming three adsorption mechanisms (i.e. mono-layer adsorption, multiple-layer adsorption, and the combined mono- plus multiple-layer adsorption). Our models predict that applied stresses reduce water sorption capacity and the associated swelling. In addition, experiments were performed on both a solid disc and on pre-compacted powders of Brzeszcze high volatile bituminous coal at a constant temperature of 40˚C, using a uniaxial compaction apparatus. The mechanical response of the samples to stepwise axial loading was determined under both evacuated (i.e. 0% relative humidity) and water-exposed (i.e. 100% relative humidity) conditions. The evacuated samples showed reversible, elastic behaviour. Water-exposed samples exhibited elastic deformation, time-dependent reversible deformation, plus permanent compaction creep. Axial swelling strains due to introduction of distilled water (i.e. 100% relative humidity) at a constant fluid pressure of 0.1 MPa were also measured for samples subjected to fixed axial stress states applied in the range of 25-100 MPa. The experimental results demonstrate that swelling due to water adsorption is reduced by increasing applied stress. Comparison with predictions made using the three models investigated suggests that

stress-driven reduction in sorption-induced swelling is not caused solely by the thermodynamic effect of a stress-driven reduction in water adsorption capacity. Permanent creep also occurred. Another likely mechanism contributing to the stress-driven reduction in swelling is the stress-driven closure of the transport paths. In summary, this means that the stress-driven reduction in swelling upon adsorption of water is caused by the combined effects of a) permanent compaction creep, b) the thermodynamic effect of a stress-driven reduction in water sorption capacity and c) stress-driven closure of the transport paths. For the disc sample, mechanism (c) led to around half the reduction of swelling, while the other mechanisms contributed equally to the remaining reduction. For powdered samples, mechanism (a) led to about half the reduction of swelling, while mechanisms (a) and (b) contributed roughly equally to the remainder. Nonetheless, our results have shown only minor effects of stress on the swelling response of (Brzeszcze) high volatile bituminous to water at typical in-situ stresses of 10-30 MPa. This means that large shrinkage effects due to drying seen in unconfined experiments is not changed by in-situ stresses. The implication is that under in-situ (E)CBM conditions, removing water from coal seams, for example by flushing with dry N_2, can potentially initiate self-enhancing shrinkage and (micro)cracking of the coal, thus enhancing methane production.

Acknowledgements

The China Scholarship Council (CSC) and Total S.A. are gratefully acknowledged for their financial support of first author Jinfeng Liu and of the research project.

References

Barton, S., Evans, M., MacDonald, J., 1994. Adsorption of water vapor on nonporous carbon. Langmuir 10, 4250-4252.

Busch, A., Gensterblum, Y., 2011. CBM and CO_2-ECBM related sorption processes in coal: A review. International Journal of Coal Geology 87, 49-71.

Charrière, D., Behra, P., 2010. Water sorption on coals. J Colloid Interf Sci 344, 460-467.

Cui, X., Bustin, R.M., Dipple, G., 2004. Selective transport of CO_2, CH_4, and N_2 in coals: insights from modeling of experimental gas adsorption data. Fuel 83, 293-303.

D'Arcy, R., Watt, I., 1970. Analysis of sorption isotherms of non-homogeneous sorbents. Transactions of the Faraday Society 66, 1236-1245.

Day, S., Fry, R., Sakurovs, R., 2011. Swelling of moist coal in carbon dioxide and methane. International Journal of Coal Geology 86, 197-203.

Day, S., Fry, R., Sakurovs, R., 2012. Swelling of coal in carbon dioxide, methane and their mixtures. International Journal of Coal Geology 93, 40-48.

Day, S., Fry, R., Sakurovs, R., Weir, S., 2010. Swelling of coals by supercritical gases and its relationship to sorption. Energ Fuel 24, 2777-2783.

Day, S., Sakurovs, R., Weir, S., 2008. Supercritical gas sorption on moist coals. International Journal of Coal Geology 74, 203-214.

Dent, R., 1977. A multilayer theory for gas sorption part I: sorption of a single gas. Textile Research Journal 47, 145-152.

Dubinin, M., 1980. Water vapor adsorption and the microporous structures of carbonaceous adsorbents. Carbon 18, 355-364.

Dubinin, M., Serpinsky, V., 1981. Isotherm equation for water vapor adsorption by microporous carbonaceous adsorbents. Carbon 19, 402-403.

Fry, R., Day, S., Sakurovs, R., 2009. Moisture-induced swelling of coal. International Journal of Coal Preparation and Utilization 29, 298-316.

Furmaniak, S., Gauden, P.A., Terzyk, A.P., Rychlicki, G., 2008. Water adsorption on carbons—Critical review of the most popular analytical approaches. Advances in colloid and interface science 137, 82-143.

Hol, S., Peach, C.J., Spiers, C.J., 2011. Applied stress reduces the CO_2 sorption capacity of coal. International Journal of Coal Geology 85, 128-142.

Hol, S., Peach, C.J., Spiers, C.J., 2012a. Effect of 3-D stress state on adsorption of CO_2 by coal. International Journal of Coal Geology 93, 1-15.

Hol, S., Spiers, C.J., 2012. Competition between adsorption-induced swelling and elastic compression of coal at CO_2 pressures up to 100MPa. J Mech Phys Solids 60, 1862-1882.

Hol, S., Spiers, C.J., Peach, C.J., 2012b. Microfracturing of coal due to interaction with CO_2 under unconfined conditions. Fuel 97, 569-584.

Kaji, R., Muranaka, Y., Otsuka, K., Hishinuma, Y., 1986. Water absorption by coals: effects of pore structure and surface oxygen. Fuel 65, 288-291.

Langmuir, I., 1918. The adsorption of gases on plane surfaces of glass, mica and platinum. J Am Chem Soc 40, 1361-1403.

Laubach, S., Marrett, R., Olson, J., Scott, A., 1998. Characteristics and origins of coal cleat: A review. International Journal of Coal Geology 35, 175-207.

Levine, J.R., 1996. Model study of the influence of matrix shrinkage on absolute permeability of coal bed reservoirs. Geological Society, London, Special Publications 109, 197-212.

Li, D., Liu, Q., Weniger, P., Gensterblum, Y., Busch, A., Krooss, B.M., 2010. High-pressure sorption isotherms and sorption kinetics of CH_4 and CO_2 on coals. Fuel 89, 569-580.

Liteanu, E., Spiers, C.J., 2009. Influence of pore fluid salt content on compaction creep of calcite aggregates in the presence of supercritical CO_2. Chem Geol 265, 134-147.

Lynch, L.J., Webster, D.S., 1982. Effect of thermal treatment on the interaction of brown coal and water: a nuclear magnetic resonance study. Fuel 61, 271-275.

McCutcheon, A.L., Barton, W.A., Wilson, M.A., 2003. Characterization of water adsorbed on bituminous coals. Energ Fuel 17, 107-112.

Moore, T.A., 2012. Coalbed methane: A review. International Journal of Coal Geology 101, 36-81.

Mu, R., Malhotra, V., 1991. A new approach to elucidate coal-water interactions by an in situ transmission FT-ir technique. Fuel 70, 1233-1235.

Nishino, J., 2001. Adsorption of water vapor and carbon dioxide at carboxylic functional groups on the surface of coal. Fuel 80, 757-764.

Pan, Z., 2012. Modeling of coal swelling induced by water vapor adsorption. Frontiers of Chemical Science and Engineering 6, 94-103.

Pone, J.D.N., Halleck, P.M., Mathews, J.P., 2009. Sorption capacity and sorption kinetic measurements of CO_2 and CH_4 in confined and unconfined bituminous coal. Energ Fuel 23, 4688-4695.

Staib, G., Sakurovs, R., Gray, E.M., 2014. Kinetics of coal swelling in gases: Influence of gas pressure, gas type and coal type. International Journal of Coal Geology 132, 117-122.

Staib, G., Sakurovs, R., Gray, E.M.A., 2013. A pressure and concentration dependence of CO_2 diffusion in two Australian bituminous coals. International Journal of Coal Geology 116, 106-116.

Suárez, N., Laredo, E., Nava, R., 1993. Characterization of four hydrophilic sites in bituminous coal by ionic thermal current measurements. Fuel 72, 13-18.

Suuberg, E.M., Otake, Y., Yun, Y., Deevi, S.C., 1993. Role of moisture in coal structure and the effects of drying upon the accessibility of coal structure. Energ Fuel 7, 384-392.

Švábová, M., Weishauptová, Z., Přibyl, O., 2011. Water vapour adsorption on coal. Fuel 90, 1892-1899.

Vandamme, M., Brochard, L., Lecampion, B., Coussy, O., 2010. Adsorption and strain: the CO_2-induced swelling of coal. J Mech Phys Solids 58, 1489-1505.

White, C.M., Smith, D.H., Jones, K.L., Goodman, A.L., Jikich, S.A., LaCount, R.B., DuBose, S.B., Ozdemir, E., Morsi, B.I., Schroeder, K.T., 2005. Sequestration of carbon dioxide in coal with enhanced coalbed methane recovery a review. Energ Fuel 19, 659-724.

Yu, J., Tahmasebi, A., Han, Y., Yin, F., Li, X., 2013. A review on water in low rank coals: the existence, interaction with coal structure and effects on coal utilization. Fuel Process Technol 106, 9-20.

Chapter 7

Conclusions and suggestions for future research

This has presented the results of a theoretical and experimental study of the response of (vacuum) dry coal matrix material to pure CH_4, pure H_2O and CH_4-CO_2 mixtures under conditions relevant to the recovery of methane from coal seams. The study focused primarily on quantifying and understanding the physical phenomena and processes associated with adsorption, diffusion and swelling under both unconfined and confined mechanical conditions. In particular, the study addressed the coupling between stress, swelling, sorption and diffusion in coal-gas systems under isothermal conditions. The work was motivated by a need for an improved understanding of the mechanical effects on sorption processes in coal in the context of (enhanced) coalbed methane (CBM) operations, in order to help advance the basis for constructing (E)CBM reservoir models.

The specific aims of this thesis were:

1. To develop the thermodynamic models for the swelling of unconfined coal matrix upon adsorption of mixed gases, addressing the equilibrium state and focusing on binary gas mixtures.
2. To evaluate the magnitude of the effect of in-situ lithostatic stresses on sorption capacity of coal matrix material more rigorously, in relation to predicting in-situ CBM content.
3. To determine the coupled effect of swelling, internal stress evolution and diffusion on swelling kinetics of coal matrix material during exposure to methane or to any gas species.
4. To quantify the volumetric response of coal matrix to water vapour under unconfined conditions, and to determine the effect of sample size on both swelling kinetics and equilibrium swelling.
5. To determine whether the applied stresses reduce the swelling of coal upon adsorption of water, and to investigate the likely mechanisms responsible for any observed effects.

These aims were addressed by means of thermodynamic analysis of sorption and diffusion under stress, and by means of one-dimensional compression experiments, hydrostatic loading tests, and unconfined dilatometry experiments (including 1D and 3D strain measurements). All experiments were performed on crushed or intact coal matrix samples of bituminous coal. The main conclusions drawn are summarised below, along with a brief evaluation of their implications for ECBM production and with recommendations for future research.

7.1. Main conclusions

7.1.1. Swelling of unconfined coal matrix upon adsorption of mixed gases: Thermodynamics models

Four models were derived that can potentially describe the swelling of unconfined coal due to the adsorption of mixed gases or fluid species, specifically binary mixtures. Three of the models can be viewed as end-members of the fourth, generalized model. Model 1 assumes independent adsorption sites for different adsorbing species. Adsorption of gas/fluid species α and β accordingly leads to independent swelling responses that accumulate to a total volumetric strain. Model 2 assumes that the adsorption sites for the components of the mixture are fully shared. This model is thermodynamically equivalent to the extended Langmuir model for ideal gases. When applied to ideal gases (which is justified for gases at low pressure), the predicted adsorbed concentrations reduce to the Langmuir isotherm for mixed gases. Model 3 assumes partially shared adsorption sites for an end-member case, i.e. only a sub-set of the population of adsorption sites is shared by gases α and β, while the rest adsorptions can only be occupied by gas β. Model 4 finally includes Models 1-3 as special cases. Model predictions were compared with literature data on the swelling behaviour of Bowen Basin coal exposed to CH_4/CO_2 mixtures at total pressures up to 15MPa and at 55˚C. The results show that swelling of the Bowen Basin coal exposed to CO_2/CH_4

mixtures is best explained by Model 3, which in turn implies that adsorption and swelling is in this case determined by both partial pressure and selective adsorption (affinity) effects. It is inferred that, CH_4 is displaced by CO_2 due to both the reduction of CH_4 partial pressure (dilution of CH_4) in the mixed gas phase and selective adsorption of CO_2. This result is different from previous suggestions that both CH_4 and CO_2 have access to all adsorption sites and that swelling solely depends on partial pressure, or that swelling depends on site accessibility solely. Model 3 is easy to parameterize and can therefore straightforwardly be applied in practice to predict the swelling behaviour of coal exposed to CH_4-CO_2 mixture during ECBM production, at least to sub-bituminous coals similar to those of the Bowen Basin. The results further imply that Model 3 should be the most suitable for evaluating whether CO_2-N_2 mixtures will be effective in limiting coal swelling and permeability reduction in ECBM operations in sub-bituminous coals, such as those of the Bowen Basin.

7.1.2. Effect of lithostatic stress on methane sorption by coal: Theory vs. experiment

A corrected model was derived for adsorption of any pure gas species by coal under stressed conditions. In this model, the equilibrium constant K^0 for sorption employs the standard free energy change $(\mu_s^{P_0}(T) - \mu_{g0}(T))$, which depends only on temperature for a given coal and gas/fluid species. The model demonstrates that an applied stress reduces the gas sorption capacity of coal and that the magnitude of the reduction depends on the partial molecular volume (Ω_0) of the adsorbed molecule. The thermodynamic model, and specifically its predictions on the effect of stress on the CH_4 sorption capacity of coal, was tested by experiments performed on a single composite coal sample (Brzeszcze 364 high volatile bituminous coal) containing artificially introduced transport paths, which minimized the influence of the positive Terzaghi effective stress on sample permeability and hence accessibility of the sample to CH_4. The amount of CH_4 expelled from the sample was measured by increasing the

hydrostatic stress or confining pressure in the range 11-43 MPa, after initial equilibration of the sample with CH_4 at a fixed methane pressure of 10 MPa and at a fixed temperature of 40˚C. The correct amount of CH_4 desorbed from the sample was obtained by subtracting the poro-elastic gas expulsion from the total measured amount, as determined by means of helium (a non-sorbing gas) control experiments. The results show that about 0.05 mol/kg_{coal} of CH_4 is desorbed from the solid sample when the applied confining pressure increased from 11 MPa to 43 MPa, which corresponds to ~6.2% of the initial uptake of 0.808 mol/kg_{coal}. This result was well predicted by the present model, which successfully captures the physical process of gas adsorption by coal that supports a stress state applied in excess of the pressure of the sorbing gas species.

7.1.3. Coupling of swelling, internal stress evolution and diffusion in coal matrix material during exposure to methane

Two models were developed, covering two basic possible mechanisms for transport of gas molecules occurring inside the coal matrix. These correspond to transport of adsorbed molecules being controlled by either jumps between adsorption sites (Model A), or by diffusion of unadsorbed molecules through longer diffusion paths inside the coal matrix (Model B). Validation through dilatomery experiments performed on a single 4mm sized cylindrical sample of medium volatile bituminous coal showed that the observed time-dependent swelling is well explained by Model B, applied assuming a single-valued diffusion coefficient that is independent of gas pressure and adsorbed concentration. Time-dependent swelling behaviour of the sample is therefore controlled not by the jumps of adsorbed gas molecules between adsorption sites, but by the diffusion of unadsorbed molecules. In addition, both models for diffusion show that the effect of swelling and associated internal stress evolution on diffusion of CH_4 (and probably CO_2 and N_2) in the coal such as those used in this study can be neglected, as the partial molar volume of the adsorbed molecules V_0 is small. The models demonstrate

that a) the distribution of adsorption sites plays a role in determining the mechanism of diffusion; b) the effect of swelling and the internal stress evolution contributes to the driving force for diffusion processes independently of the gradient in adsorbed concentration, and that the importance of this effect strongly depends on the magnitude of V_0; c) swelling rates of coal matrix material depend not solely on diffusion coefficient, but also on adsorbed concentration. Since all parameters used in both models have well-defined physical meaning and are easily obtained from sorption and swelling experiments, the models can be applied to coal of any rank, and to any gas. They therefore offer an important tool for modelling coal matrix stress-strain evolution and hence coal seam/cleat permeability evolution with time, as influenced by adsorption /desorption and diffusion occurring during (E)CBM operations.

7.1.4. Anisotropic swelling behaviour of coal matrix cubes exposed to water vapour: Effects of relative humidity and sample size

Dilatometry experiments, performed using a purpose-built, high sensitivity 3-dimensional dilatometry system, were conducted on 1mm and 4mm sized cubic samples at relative humidities varied in the range 0.1 to 95%, under mechanically unconfined conditions and at a constant temperature of 40˚C. The swelling response of the samples to water adsorption was anisotropic with the swelling strain developed perpendicular to bedding being on average about 1.13 times that occurring parallel to bedding, though this ratio varied with relative humidity. The swelling response was mostly reversible and/or recoverable, with some hysteresis effects. The observed dependence of the swelling strain anisotropy ratio on RH suggests that the anisotropic swelling effect is not solely determined by elastic anisotropy of the coal studied. Sample size was found to strongly influence the swelling kinetics of coal matrix material at a given relative humidity, but does not influence the magnitude of swelling strain attained at equilibrium. This confirms that time-dependent swelling/shrinkage of unconfined coal matrix during exposure to water vapour is controlled by diffusion of water molecules as

opposed to sorption reaction kinetics. The volumetric swelling strains attained by our coal samples at equilibrium showed a near-linear relation with relative humidity, reaching a value of 1.37-1.43% at around 95% relative humidity. Three models for swelling of unconfined coal matrix material due to water sorption have been developed. The three models respectively address the equilibrium swelling strain caused by mono-layer adsorption, by multiple-layer sorption, and by combined mono- plus multiple-layer adsorption. The equilibrium swelling strain versus RH or water activity data obtained in the present experiments can be well fitted by all three models, so that the mechanism dominating water vapour adsorption and associated swelling could not be pinpointed.

7.1.5. Effect of applied stress on swelling of coal upon adsorption of water

Thermodynamic models for swelling of coal matrix material due to water adsorption under stressed conditions were developed, assuming three adsorption mechanisms (i.e. mono-layer adsorption, multiple-layer adsorption, and the combined mono- plus multiple-layer adsorption). Our models predict that applied stresses reduce water sorption capacity and associated swelling. In addition, experiments were performed on both a solid disc and on pre-compacted powder samples of Brzeszcze high volatile bituminous coal at a constant temperature of 40˚C, using a uniaxial compression/compaction apparatus. The mechanical response of the samples to stepwise axial loading was determined under both evacuated (i.e. 0% relative humidity) and water-exposed (i.e. 100% relative humidity) conditions. The evacuated samples showed reversible, elastic behaviour. Water-exposed samples exhibited elastic deformation, time-dependent reversible deformation, plus permanent time-dependent deformation (creep). Axial swelling strains due to introduction of distilled water (i.e. 100% relative humidity) at a constant fluid pressure of 0.1 MPa were also measured for samples subjected to fixed axial stress states applied in the range of 25-100 MPa. The experimental results demonstrate that swelling due to water adsorption is reduced by

increasing applied stress. Comparison with predictions made using the three models investigated suggests that stress-driven reduction in sorption-induced swelling is not caused solely by the thermodynamic effect of a stress-driven reduction in water adsorption capacity. Permanent creep also occurred. Another likely mechanism contributing to the stress-driven reduction in swelling is the stress-driven closure of the transport paths. In summary, this means that the stress-driven reduction in swelling upon adsorption of water is caused by the combined effects of a) permanent compaction creep, b) the thermodynamic effect of a stress-driven reduction in water sorption capacity and c) stress-driven closure of the transport paths. For the disc sample, mechanism (c) led to around half the reduction of swelling, while the other mechanisms contributed equally to the remaining reduction. For powdered samples, mechanism (a) led to about half the reduction of swelling, while mechanisms (a) and (b) contributed roughly equally to the remainder. Nonetheless, our results have shown that the effects of stress on the swelling response of (Brzeszcze) high volatile bituminous to water, at typical in-situ stresses of 10-30 MPa, are relatively minor. This means that large shrinkage effects due to drying seen in unconfined experiments will not be changed changed by in-situ stresses. The implication is that under in-situ (E)CBM conditions, removing water from coal seams can potentially initiate self-enhancing shrinkage and (micro)cracking of the coal, enhancing methane production significantly.

7.2. Implications for ECBM production

The present study can be used to formulate a number of implications for methane production from coal seams. I will briefly summarize here what I see as the main issues.

1. The theoretical model developed in Chapter 3 predicts the in-situ CBM concentration distribution with depth for dry, high volatile bituminous coal, for an assumed geothermal gradient of 32˚C/km. The results indicate a maximum CH_4 concentration of ~0.76mol/kg_{coal} at a burial depth of ~900m, which is ~3%

lower than conventional predictions made without considering sorption-induced swelling and the associated effect of stress. The reduction is minor but the model helps to explain why gas saturation is generally lower than expected from conventional sorption measurements on unconfined coal powders. More importantly, the results confirmed that there is an intimate coupling between in-situ stress, strain and sorption in coal that needs to be considered in gas-enhanced CBM strategies. When combined with poro-elastic deformation, the model offers a theoretical basis for developing new techniques making use of the effect of in-situ stress, temperature and gas pressure on gas sorption, which can potentially be applied in (E)CBM production. For example, if there is a CH_4-rich coal seam that has been partially mined, the gradient in stress state between the mined and unmined regions will provide an additional driving force, in excess of the gradient in gas pressure and concentration, driving CH_4 flow from the unmined coal to the mined region. In such cases, a coal seam that has been partially mined, or where the stress state has been otherwise perturbed, might become more productive. In addition to CH_4, the model offers an improved tool for estimating the amount of CO_2 that can be adsorbed by coal seams or can be sequestrated in coal seams at given injection pressure, stress state and temperature.

2. The findings reported in Chapter 4 suggest that for most coal ranks, the swelling kinetics of coal matrix upon adsorption of CH_4, CO2, or N_2 are dominated by diffusion of unadsorbed molecules, and can be described using the diffusion model B (path-controlled as opposed to jump-controlled). As all parameters in the model have physical meanings and can be easily obtained from swelling or sorption kinetics experiments, this model offers an important tool for modeling coal seam (fracture) permeability evolution with time upon swelling and shrinkage of coal matrix during ECBM production. The effect of the swelling

strain and the associated internal stress evolution on diffusion in higher rank coal, for which the partial molar volume of adsorbed molecules (V_0) is generally low, can be neglected. For lower rank coal, where V_0 is higher, this effect might need to be considered, as the magnitude of this effect is proportional to V_0^2. Swelling rates for low rank coal might therefore be faster than those for high rank coal due to the swelling effects on driving force. In addition to this effect, the favoured diffusion model (path-controlled diffusion) implies that the swelling kinetics of coal matrix upon adsorption of CH_4, CO_2, or N_2 depends not only on the diffusion coefficient, but also on the adsorbed concentration, increasing with increasing adsorbed concentration. This suggests that the shrinkage rates of coal matrix upon CBM recovery will decrease with decreasing adsorbed CH_4 concentration, while the swelling rates of coal matrix upon injection of CO_2 will increase with increasing adsorbed concentration of CO_2. This together with the finding that the diffusion coefficient for CO_2 is generally one or two orders higher than that for CH_4, suggests that swelling rates upon CO_2 injection would be much higher than shrinkage rates upon CBM recovery. This in turn implies that using CO_2 as a technique for the secondary enhanced CBM recovery is unlikely to be a very successful strategy, in agreement with attempts at CO_2-ECBM.

3. The results obtained in Chapter 5 suggest a strategy to use (liquid) N_2 as a hydraulic-fracturing fluid to stimulate CBM production from coal seams. This could be followed by circulating dry gaseous N_2 to promote matrix shrinkage by removing water and methane. After such a phase of N_2-ECBM production, CO_2 could be injected for geological storage. This strategy has two advantages. The first is that shrinkage upon removing water and CH_4 from coal seam will create more transport paths for CO_2 injection and storage. The second is that the larger swelling effect caused by adsorption of CO_2, compared with the shrinkage effect

of removing water and CH_4 may result in self-sealing of coal seams. Importantly, the above strategy would not be influenced by in-situ stresses (which typically lie in the range 10 to 30 MPa), at least in the case of Brzeszcze high bituminous coal, as the large shrinkage effects due to drying seen in the unconfined experiments on Brzeszcze coal are not changed by in-situ lithostatic stresses (see Chapter 6).

4. The generalized model developed in Chapter 2 for swelling of unconfined coal matrix upon adsorption of mixed gases can be widely applied to any coal rank, to any binary gas mixture and to any *PT* conditions, provided that proper parameter values are available. The model offers an important tool for modeling swelling and coal seam (fracture) permeability evolution during ECBM operations. It may be suitable to explain why sorption and swelling of some coals seem to be dominated by partial pressure effects and others by selective sorption effects.

7.3. Suggestions for future research

The results of the work described in this thesis have contributed to the understanding of mechanical effects on sorption processes in coal matrix exposure to a single gas and a gas mixture, and they help provide a basis for improved (E)CBM reservoir modelling and hence for the assessment of the feasibility of (E)CBM operations. Nonetheless, the models employed embody several assumptions, and there are shortcomings in the experimental methods and the equipment. Moreover, new problems were identified, and several questions remain unsolved or still need to be addressed. I will now briefly discuss these issues and make suggestions for future research.

1. In all models employed in this study, the coal matrix was considered to contain nanopores only. Unadsorbed molecules are transported into the coal matrix solely by diffusion and trapped by the potential well associated with

the adsorption sites in the sorption process. The swelling, is caused by the absorbed molecules. The storage of unadsorbed molecules in nanopores is minor, and therefore they likely cannot behave as gas phase. I successfully described experimental data for mm-scale bituminous coal samples with this model, but for bigger coal samples (cm-scale) or for other coals, a bidisperse pore structure model might better represent the heterogeneous properties of coal. In such cases, more complicated mechanisms for the sorption and diffusion processes in coal need to be considered. For the experimental part of the swelling kinetics, I wish to stress that the real state of unadsorbed molecules in nanopores, and how that is influenced by the pore dimensions, remains unknown. To resolve this, advanced spectroscopy techniques or molecular dynamic methods are needed.

2. The present models for swelling upon adsorption of mixed gases focused on unconfined coal matrix, addressing equilibrium states and binary gas mixtures, without considering the coupled effects of swelling, stress and diffusion. A model that fully couples stress-strain-sorption-diffusion behaviour of coal exposed to mixed gases should be considered in future work. Moreover, a complete reservoir model linking coal seam (fracture) permeability to the stress-strain-sorption-diffusion behaviour of stressed coal exposed to mixed gases is needed.
3. Only two different bituminous coals were used in this study, as I mainly focused on a fundamental study and on testing generic theoretical models against experiments. The applicability of the present results to coals of other rank and different geological settings is therefore only qualitatively implied, but not quantitatively demonstrated in a general sense.. Future experimental studies of coupling between swelling, stress, sorption and diffusion should address a wider variety of coal types.

4. In Chapter 5, the specially developed 3-dimensional dilatometry system, using sensitive eddy-current gap sensors, allowed us to accurately measure the 3D volumetric response of 1mm coal matrix to adsorption of water vapour. However, the transient effects of changes in relative humidity (RH) on the eddy current sensor signals could not be corrected for with high accuracy, because the duration of RH steps employed in the calibration tests did not always match those used in the coal runs (see details in Chapter 5). Clearly, the eddy current sensors were somehow influenced by effects of water sorption on the sensor, perhaps modifying the measured eddy currents, or by changes in air permittivity (water has a very high dielectric constant compared with dry gasses). This means that to quantitatively determine swelling kinetics with better accuracy, better isolation of the eddy current sensor and capacitive electrical lead/connections system from the moist environment used for RH testing would be helpful. More tests are still needed to clarify this issue and to fix this problem.
5. To accurately determine the uptake or expulsion of CH_4 and He in the experimental tests presented in Chapter 3, a linear leak rate correction had to be applied to the raw ISCO pump volume data, with the result that the waiting time required to ensure equilibrium had been approached was much increased. In future, leakage can possibly be reduced by including either a bellows-type fluid separator between the ISCO or other high pressure syringe pumps typically used in such experiments, filling the pump and bellows with a stiff, more viscous liquid that is less likely to leak past the travelling and static seals. Another problem encountered with our ISCO pumps was the accuracy of control in pressure control mode, which introduced noise into the pump volume signal. This might be solved by using a better-designed control system and more closely matched range of the pressure transducer.

6. This study addressed the mechanical effects of sorption processes in coal matrix material, specifically stress-strain-sorption and associated diffusion processes in coal exposed to methane and water. Describing the effects on the macroscopic permeability of the coal cleat system of with the swelling and shrinkage behaviour of the coal matrix was an original additional aim of the study but turned out to be beyond the scope coverable in the time available. This aspect is, however, an essential ingredient of reservoir models aiming at production-scale operations. Future studies should therefore extend the present results to the matrix-fracture scale, i.e. they should investigate this coupled effect of stress, swelling, sorption and diffusion on fracture permeability of coal under in-situ boundary conditions (Espinoza et al., 2014; Liu et al., 2011a; Liu et al., 2011b; Peng et al., 2014; Wang et al., 2011). This can be approached by seeking to develop models linking our thermodynamic models (developed in Chapters 2, 3 and 4) and (fracture) permeability models (Pan and Connell, 2012; Shi and Durucan, 2005, 2014; Shi et al., 2014; Wang et al., 2012; Yi et al., 2009). These then need to be tested against experiments that investigate how (fracture) permeability depends on (pore) gas pressure and (effective) confining pressure (Cai et al., 2014; Kumar et al., 2015; Wang et al., 2015; Zhong et al., 2016).

References

Cai, Y., Liu, D., Mathews, J.P., Pan, Z., Elsworth, D., Yao, Y., Li, J., Guo, X., 2014. Permeability evolution in fractured coal—Combining triaxial confinement with X-ray computed tomography, acoustic emission and ultrasonic techniques. International Journal of Coal Geology 122, 91-104.

Espinoza, D., Vandamme, M., Pereira, J.-M., Dangla, P., Vidal-Gilbert, S., 2014. Measurement and modeling of adsorptive–poromechanical properties of bituminous coal cores exposed to CO_2: Adsorption, swelling strains, swelling stresses and impact on fracture permeability. International Journal of Coal Geology 134, 80-95.

Kumar, H., Elsworth, D., Liu, J., Pone, D., Mathews, J.P., 2015. Permeability evolution of propped artificial fractures in coal on injection of CO_2. Journal of Petroleum Science and Engineering 133, 695-704.

Liu, J., Chen, Z., Elsworth, D., Qu, H., Chen, D., 2011a. Interactions of multiple processes during CBM extraction: A critical review. International Journal of Coal Geology 87, 175-189.

Liu, J.S., Chen, Z.W., Elsworth, D., Miao, X.X., Mao, X.B., 2011b. Evolution of coal permeability from stress-controlled to displacement-controlled swelling conditions. Fuel 90, 2987-2997.

Pan, Z., Connell, L.D., 2012. Modelling permeability for coal reservoirs: A review of analytical models and testing data. International Journal of Coal Geology 92, 1-44.

Peng, Y., Liu, J., Wei, M., Pan, Z., Connell, L.D., 2014. Why coal permeability changes under free swellings: New insights. International Journal of Coal Geology 133, 35-46.

Shi, J.-Q., Durucan, S., 2005. A model for changes in coalbed permeability during primary and enhanced methane recovery. Spe Reserv Eval Eng 8, 291-299.

Shi, J.-Q., Durucan, S., 2014. Modelling laboratory horizontal stress and coal permeability data using S&D permeability model. International Journal of Coal Geology 131, 172-176.

Shi, J.-Q., Durucan, S., Shimada, S., 2014. How gas adsorption and swelling affects permeability of coal: a new modelling approach for analysing laboratory test data. International Journal of Coal Geology 128, 134-142.

Wang, S., Elsworth, D., Liu, J., 2011. Permeability evolution in fractured coal: The roles of fracture geometry and water-content. International Journal of Coal Geology 87, 13-25.

Wang, S., Elsworth, D., Liu, J., 2012. A mechanistic model for permeability evolution in fractured sorbing media. Journal of Geophysical Research: Solid Earth 117.

Wang, Y., Liu, S., Elsworth, D., 2015. Laboratory investigations of gas flow behaviors in tight anthracite and evaluation of different pulse-decay methods on permeability estimation. International Journal of Coal Geology 149, 118-128.

Yi, J., Akkutlu, I.Y., Karacan, C.O., Clarkson, C., 2009. Gas sorption and transport in coals: A poroelastic medium approach. International Journal of Coal Geology 77, 137-144.

Zhong, Z., Elsworth, D., Hu, Y., 2016. Evolution of Strength and Permeability in Stressed Fractures with Fluid–Rock Interactions. Pure and Applied Geophysics 173, 525-536.

Samenvatting

Ondergrondse steenkoollagen bestaan over het algemeen uit laag-permeabel koolmatrix materiaal, doorsneden met een netwerk van scheurtjes en breuken op vele schalen. Deze systemen bevatten vaak grote hoeveelheden methaan (CH_4) en water, gedeeltelijk in de vorm van vloeistof in het breuksysteem maar vooral in geadsorbeerde vorm in de nanoporiën van de matrix. Andere gassen zoals kooldioxide (CO_2) en stikstof (N_2) kunnen ook door de koolmatrix worden geadsorbeerd. De adsorptie van deze gassen kan tot procenten zwelling veroorzaken, en desorptie vergelijkbare krimp. De zwelling en krimp van in-situ steenkool beïnvloedt de permeabiliteit van het netwerk van breuken in sterke mate en speelt daarom een sleutelrol bij de beoordeling van de mogelijkheid van methaanproductie uit steenkool door "Enhanced coalbed methane" (ECBM) productie. ECBM houdt in dat CO_2 wordt geïnjecteerd, wat vervolgens preferentieel wordt geadsorbeerd aan de kool om de methaan desorptie en productie te verbeteren, in combinatie met lange-termijn geologische opslag van CO_2. Eerder werk in vrijwel alle nu bekende veld experimenten heeft echter laten zien dat een koppeling van spanning, vervorming en adsorptie in steenkool-CO_2 systemen resulteert in een grote reductie van de CO_2 injectiviteit en CH_4 productiviteit. De desorptie van water en CH_4 uit steenkoollagen kan krimp veroorzaken en daarmee de opening en verdere propagatie van microscheuren, hetgeen de methaan productie ten goede komt – echter, de directe koppeling van spanning, vervorming, sorptie en diffusie in steenkool-CH_4 en steenkool-H_2O systemen is nog slecht begrepen. In dit proefschrift presenteer ik de resultaten van een theoretische en experimentele studie naar de respons van droog koolmatrix materiaal op puur CH_4, puur H_2O en CH_4-CO_2 mengsels onder in-situ (E)CBM condities.

In **Hoofdstuk 1** worden het onderzoeksgebied en de context van dit proefschrift geïntroduceerd, wordt eerder werk bediscussieerd en worden de belangrijkste kennisleemten geïdentificeerd. Dit resulteert in de beschrijving van de doelen van dit proefschrift.

De eerste kwestie die in dit proefschrift aan de orde komt (**Hoofdstuk 2**) is de zwelling van koolmatrix bij afwezigheid van een mechanische spanning door de adsorptie van gemengde gassen. Daarvoor ontwikkel ik nieuwe thermodynamische modellen voor de evenwichtstoestand, specifiek gericht op binaire gas mengsels. Vier modellen worden afgeleid: drie met specifiek gekozen interacties en één met een algemeen gedefinieerde toestand. De specifieke modellen corresponderen met adsorptie van de gassen α en β op verschillende locaties (Model 1); op volledig gedeelde locaties (Model 2) en op gedeeltelijk gedeelde locaties (Model 3). Model 4 is een algemeen model dat de modellen 1 – 3 als speciale gevallen omvat. Model voorspellingen worden vergeleken met literatuur data over het zwelgedrag van Bowen Basin steenkool blootgesteld aan CH_4/CO_2 mengsels onder drukken tot 15 MPa op een temperatuur van 55˚C. De experimenteel waargenomen zwelling van de Bowen Basin steenkool kan het best worden verklaard met Model 3. Blijkbaar wordt adsorptie en zwelling voor dit kooltype bepaald door de partiële drukken van de gassen en door de selectieve adsorptie (affiniteit) van de gassoorten aan de adsorptie locaties. Model 3 is het beste model om te bepalen of CO_2-N_2 mengsels effectief zijn om zwelling en permeabiliteitsreductie te beperken bij ECBM operaties in sub-bitumineuze steenkool zoals die uit het Bowen Basin. Voordelen van Model 3 zijn dat het eenvoudig te parameteriseren is en dat de toepasbaarheid op specifieke steenkool en gas mengsels eenvoudig te bepalen is. Het generieke Model 4 is minder eenvoudig te parameteriseren maar kan wel worden toegepast op elke koolrank en elk binair gas mengsel. Zijn bredere toepasbaarheid maakt het daarom een belangrijk stuk gereedschap voor de modellering van zwelling en de daarmee geassocieerde permeabiliteitsontwikkeling gedurende ECBM operaties.

In **Hoofdstuk 3** wordt het effect van een lithostatische spanning op CH_4 sorptie onderzocht. Ik herzie het bestaande thermodynamische model van Hol en Spiers (2012a) voor de effecten van spanning op sorptie van CO_2 en pas het toe op CH_4. Het herziene model voorspelt dat de hoeveelheid geadsorbeerd gas inderdaad niet alleen bepaald

wordt door de gewoonlijk in aanmerking genomen geologische kenmerken als koolrank, compositie, vochtgehalte, temperatuur, en gasdruk, maar ook door de mechanische spanningen, die gewoonlijk verwaarloosd worden. De voorspelling is getest door middel van experimenten op een composiet cilindrisch monster van Brzeszcze 364, bitumineuze steenkool met een hoog gehalte aan vluchtige componenten, onder een methaan gasdruk van 10 MPa en een temperatuur van 40˚C, waarbij een hydrostatische spanning werd opgelegd die varieerde van 11 tot 43 MPa. Met deze experimenten heb ik bepaald wat de hoeveelheid van de van het steenkoolmonster gedesorbeerde CH_4 was ten gevolge van een vergrote hydrostatische spanning op het monster door de poro-elastische expulsie van CH_4 af te trekken van de totale expulsie – onder de aanname dat de eerste gelijk is aan de expulsie van gas in een controle experiment met Helium. De experimentele resultaten laten zien dat de uiteindelijke sorptie capaciteit voor CH_4 bij 10 MPa gas druk en 11 MPa mechanische spanning (1 MPa Terzaghi effectieve spanning) 0.808 $mmol/g_{coal}$ was. Deze waarde verminderde met tenminste ~6% als de spanning werd verhoogd tot 43 MPa (33 MPa effectieve spanning). De metingen komen overeen met modelvoorspellingen en bevestigen de geldigheid van het model. Ik pas derhalve het model toe om de in-situ CBM concentratie te voorspellen als functie van de diepte van de steenkoollaag voor droge bitumineuze steenkool met een hoog gehalte aan vluchtige componenten, en een geothermische gradiënt van 32˚C/km. De resultaten geven een maximum CH_4 concentratie van ~0.76 mol/kg_{coal} aan op een diepte van ~900m, ongeveer 3% minder dan conventionele voorspellingen. Hoewel dit verschil vrij klein is verklaart het toch waarom gevonden gas saturaties in ondergrondse steenkoollagen over het algemeen kleiner zijn dan verwacht op grond van conventionele sorptie metingen op steenkool poeders die geen mechanische spanning ervaren. Belangrijker echter is dat de resultaten bevestigen dat er een sterke koppeling is tussen de in-situ spanning, de vervormingen en het sorptiegedrag. Deze koppeling dient in aanmerking te worden genomen bij het ontwikkelen van ECBM strategieën.

De koppeling tussen zwelgedrag, spanningsontwikkeling, sorptie en diffusie in koolmatrix materiaal blootgesteld aan methaan wordt verder onderzocht in **Hoofdstuk 4**. Ik construeer theoretische modellen voor de tijdsafhankelijke zwelling van koolmatrix als gevolg van adsorptie van een gas, waarin de gekoppelde effecten van spanning, vervorming, chemische potentiaal en diffusie zijn verdisconteerd. Twee modellen worden ontwikkeld. Zij corresponderen met diffusie – en dientengevolge zwelling – die wordt gecontroleerd door de frequentie van het "springen" van geadsorbeerde moleculen tussen nabije adsorptie locaties (Model A) en met transport dat gecontroleerd wordt door diffusie van niet-geadsorbeerde moleculen over diffusiepaden die van elkaar verwijderde adsorptielocaties aan elkaar verbinden (Model B). Om de geldigheid van de modellen te testen heb ik axiale zwelexperimenten uitgevoerd op een enkel 4-mm-groot cilindrisch monster van bitumineuze steenkool met een gemiddeld gehalte aan vluchtige componenten, blootgesteld aan CH_4 gasdrukken tot 40 MPa op een constante temperatuur van 40°C, gebruikmakend van 1D hoge druk dilatometrie. De experimentele data worden vergeleken met de modelvoorspellingen, en zij worden goed verklaard door Model B met één enkele diffusieconstante die onafhankelijk is van gasdruk of hoeveelheid geadsorbeerd gas. Dit houdt in dat de tijdsafhankelijke zwelling wordt gecontroleerd door diffusie van niet-geadsorbeerde moleculen; niet door de "springfrequentie" van geadsorbeerde moleculen of door effecten van de poriegrootteverdeling zoals in de literatuur gerapporteerd. Verder laten de modellen zien dat de ontwikkeling van interne spanningen, aangedreven door de zwelling, een significant effect kunnen hebben op de adsorptie en de diffusie in de koolmatrix als het partiële molaire volume van de geadsorbeerde moleculen (V_0) groot genoeg is. In de huidige experimenten echter lijkt dit effect te verwaarlozen te zijn in vergelijking met dat van het diffusiemechanisme, omdat V_0 klein is voor sorptie van CH_4 door steenkool. De gepresenteerde modellen beschrijven echter wel een volledige koppeling tussen spanning, vervorming, sorptie en diffusie in termen van parameters die een heldere

fysische betekenis hebben en die eenvoudig te bepalen zijn met behulp van zwelexperimenten op steenkool van uiteenlopende rank met elk gas. Zij bieden daarom een belangrijk middel om de permeabiliteitsontwikkeling gedurende (E)CBM operaties te modelleren.

Een andere belangrijke kwestie voor ECBM productie is de noodzaak om zwelling en krimp van de koolmatrix ten gevolge van adsorptie en desorptie van waterdamp nauwkeurig te bepalen. In **Hoofdstuk 5** rapporteer ik dilatometrie experimenten uitgevoerd op 1-mm en 4-mm grote kubische monsters van Brzeszcze bitumineuze steenkool met een hoog gehalte aan vluchtige componenten. De experimenten werden verricht met een speciaal gebouwde, zeer gevoelige 3D dilatometer. Doel was een precieze en continue meting van de volumetrische respons van steenkool gedurende blootstelling van aan waterdamp onder relatieve vochtigheid van 0.1 tot 95%, bij een temperatuur van 40°C. De resultaten laten zien dat de zwelling in de evenwichtssituatie tot een factor 1.45 groter is in de richting loodrecht op het laagvlak dan in de richting parallel met het laagvlak. De monstergrootte beïnvloedt in sterke mate de kinetiek van het zwelgedrag, maar zij beïnvloedt niet de uiteindelijk bereikte relatieve zwelling. De uiteindelijke volumeverandering is vrijwel lineair afhankelijk van de relatieve vochtigheid en bereikt een waarde van 1.37-1.43% bij 95%. In een poging om het geobserveerde gedrag te verklaren werden drie modellen ontwikkeld voor het zwellen van koolmatrix materiaal bij afwezigheid van een mechanische spanning als gevolg van de adsorptie van water: monolaag adsorptie; multilaag adsorptie; en gecombineerde mono- en multilaag adsorptie. De experimentele resultaten kunnen door alle modellen even goed worden beschreven, dus het verantwoordelijke mechanisme kon niet worden bepaald. De bevindingen laten echter wel duidelijk zien dat een verlaging van de in-situ water activiteit een significante anisotrope krimp van de koolmatrix veroorzaakt. Dit wijst op injectie en recirculatie van droge stikstof als een veelbelovende strategie voor de stimulatie van steenkoollagen CBM, en als een voorbehandeling voor latere CO_2

injectie en opslag.

Hoofdstuk 6 tracht te bepalen of een opgelegde spanning de zwelrespons van steenkool als gevolg van blootstelling aan en adsorptie van water beïnvloedt; en tracht, indien dat het geval is, te bepalen wat het verantwoordelijke mechanisme is. Hiertoe breid ik eerst het in Hoofdstuk 3 ontwikkelde thermodynamische model voor het spanning-vervorming-sorptie gedrag uit, zodat het niet alleen monolaag adsorptie maar ook multilaag adsorptie beschrijft. Daarna rapporteer ik de resultaten van experimenten die waren ontworpen om de effecten van opgelegde spanning op de ontwikkeling van de zwelvervorming van steenkoolmonsters blootgesteld aan gedestilleerd water op atmosferische druk vast te stellen. De experimenten werden uitgevoerd op zowel steenkoolschijfjes als op voorgecompacteerde steenkoolpoedermonsters van Brzeszcze bitumineuze steenkool met een hoog gehalte aan vluchtige componenten, op een constante temperatuur van 40˚C, met een uniaxiaal compactie apparaat. Eerst werd de mechanische respons van de monsters bepaald voor zowel vacuüm (i.e. 0% relatieve vochtigheid) als natte (i.e. 100% relatieve vochtigheid) condities. De vacuüm monsters toonden reversibel, elastisch gedrag. De natte monsters vertoonden elastische deformatie, tijdsafhankelijk reversibele deformatie en permanente tijdsafhankelijke deformatie (kruip). De axiale zwelvervorming werd gemeten als gevolg van de adsorptie van gedestilleerd water (i.e. 100% relatieve vochtigheid) bij een constante vloeistofdruk van 0.1 MPa onder een constante opgelegde axiale spanning (25 – 100 MPa). De experimentele resultaten laten zien dat de uiteindelijke zwelvervorming gereduceerd wordt door een opgelegde spanning. Een vergelijking met voorspellingen vanuit de drie modellen laat zien dat de spannings-gedreven reductie in sorptie-geïnduceerde zwelling wordt veroorzaakt door het gecombineerde effect van a) permanente tijdsafhankelijke (comprimerende) vervorming (kruip); b) het thermodynamische effect van een spannings-gedreven reductie in water adsorptie capaciteit en c) spannings-gedreven sluiten van transportpaden in de koolmatrix. Voor het schijfmonster was mechanisme (c)

dominant; voor de poedermonsters mechanisme (a). Mijn resultaten laten echter zien dat de genoemde effecten van spanning op de zwelrespons van dit type (Brzeszcze) steenkool op water verwaarloosbaar zijn voor typische in-situ spanningen van 10 – 30 MPa. Dit betekent dat de grote krimp effecten ten gevolge van drogen zoals geobserveerd in experimenten zonder een mechanische spanning, onveranderd blijven in aanwezigheid van in-situ spanningen. Daarom kan het verwijderen van water onder in-situ (E)CBM condities zelf-versterkende krimp en scheurvorming veroorzaken, en op die wijze de methaan productie vergroten.

Hoofdstuk 7 vat de belangrijkste bevindingen samen, verwoordt de implicaties van dit werk voor ECBM, rapporteert overblijvende vragen en doet suggesties voor toekomstig onderzoek. De belangrijkste conclusies zijn als volgt: In de eerste plaats zullen in-situ lithostatische spanningen de sorptie capaciteit van koolmatrix reduceren. Dit effect zal leiden tot lagere CBM volume voorspellingen dan eerder gemaakt met conventionele methodes. In de tweede plaats blijken de zwelsnelheden ten gevolge van CO_2 injectie veel hoger te zijn dan de krimpsnelheden ten gevolge van koolbed-methaan productie. Dit houdt in dat het gebruik van CO_2 stimulatie als techniek voor secondaire "enhanced CBM" niet de beste strategie lijkt te zijn. In de derde plaats lijkt het gebruik van (vloeibare) stikstof (N_2) als een hydraulic-fracturing vloeistof voor de stimulatie van steenkoollagen, gevolgd door circulatie van droge N_2 om krimp te bevorderen doordat geadsorbeerd water en methaan wordt verwijderd, wel een geschikte strategie voor (E)CBM productie. Na de productie van methaan kan CO_2 in de steenkoollaag worden geïnjecteerd voor geologische opslag – dit zal resulteren in het sluiten van het netwerk van scheuren en breuken door de relatief grote zwelvervorming resulterend van CO_2 adsorptie.

Acknowledgements

Here, I wish to express my sincere gratitude to my supervisors, colleagues, research fellows, friends and family for their help and support over the past five years.

I could not have got the present result, this thesis, without the supervision and help of my supervisors **Chris Spiers**, **Colin Peach** and **Peter Fokker**. **Chris**, my promotor, you are one of the best teachers that I have ever met and you have shown me how to conduct proper science. It is my honor to have had the opportunity to work with you and I really enjoyed that. I learned a tremendous amount from you in an efficient, enjoyable way. I am very grateful for all of your guidance, support and encouragement. **Colin**, I learned a lot from your accurate understanding of physics and experimental techniques. Thank you very much for your guidance and support, specifically in experiments. **Peter**, I am really happy to have worked with you. It would have been more difficult without your efforts; I greatly appreciate this.

Dating back to the origin of this PhD journey, the China Scholarship Council (CSC) and Total S.A. are acknowledged for their financial support of me and of the research project. Specifically, many thanks go to **Hongwei Zhou**, my master's supervisor, for your support in my application for the CSC scholarship, and for recommending me to **Chris**. **Chris**, thank you for receiving me and for guiding me to prepare a proposal for this PhD project. I am also grateful to **Lijun** for her suggestions on enrolling the Dutch community, her invitation to a Chinese New Year dinner in the Netherlands, for her understanding and support of **Chris** in supervising me. **Cong Zhang** is also thanked for his advice on the application for the CSC grant. With respect to Total S.A., I want to express my appreciation to **Xu Zhonghua** and **Sandrine Vidal-Gilbert** for giving me the opportunity to enter the present research field. **Sandrine** is especially acknowledged for her support and suggestions regarding my PhD research.

During this long journey, it was my pleasure to work with colleagues at the High Pressure and Temperature (HPT) lab. For me, the HPT lab is a family in the Netherlands! HPTers played different roles in my different stages in the Netherlands. **Magda**, the

mother of the HPT lab, you are the pillar and foundation of the HPT family. Thank you for taking care of me in arrangements and organization. I would like to thank **Hans de Bresser** for discussions on non-linear regression and for your double-checking of my calculations. Regarding technical support, **Thony van der Gon Netscher, Eimert de Graaff**, **Gert Kastelein, Peter van Krieken** and **Floris van Oort** are much appreciated for their perfect support. I want to thank **Eimert** for your efforts on electronic matters, particularly on the design of the 3D dilatometer. I am also really grateful for the efforts made by **Gert** and **Floris** on high pressure systems, including vessels, pipes and jackets. **Peter** is thanked for his instructions on sample preparation and on the Leica optical microscope. I would also like to thank **Thony** for his quick responses when I needed his help.

I would now like to thank the HPT brothers and sisters for all their support. First, I thank the earlier generations of the HPT lab: **Amir, Andre, Anne, Bart, Elisenda, Jianye, Jon, Ken, Loes**, **Nawaz, Tim, Sabine, Sander, Sander** and **Suzanne**. Without their help and encouragement, it would be more difficult to enrol myself in my PhD project and the Dutch community at the beginning of my PhD research. **Sander Hol** is specifically thanked for your guidance and discussions in understanding your model and experimental apparatus. Thanks **Tim** for the discussions on transport problems and for instructions on the Instron. **Suzanne** is appreciated for her suggestions on the general chapters of my PhD thesis, and for her proofreading a print sample of the thesis. Many thanks should also go to my Dutch colleagues, who all helped me a lot with Dutch issues. A special thanks goes to my officemate **Eli** for her nice arrangements in the office and for taking care of me. I also enjoyed the time with **Andre** for beer and football; thanks for this. **Bart** and **Jianye**, my paranymphs, are thanked for their company and support. Second, I would like to express my appreciation of the younger generation of the HPT lab who always brought new blood: **Amin**, **Ayumi**, **Evangelos**, **George**, **Joost**, **Luca**, **Luuk**, **Maartje**, **Mariska**, **Martijn**, **Miao**, **Michiyo**, **Piercarlo**, **Ronald**, **Wen**, **Yang**,

Yu and **Zahra**. I want to thank **Maartje** and **Miao** for their instructions on apparatus and for discussions on sorption and transport problems. **Miao** is also appreciated for you taking care of my long term experiments when I was travelling for a conference and a visit. **Luuk** is specially thanked for his proofreading of the Dutch summary of this thesis.

Besides the HPT group, I would like to thank many research fellows. I am grateful to my reading committee for their suggestions and comments on my manuscript: **Hans van Duijn**, **Sevket Durucan**, **Derek Elsworth**, **Bernhard Krooss** and **Hongwei Zhou**. I also would like to thank many of the journal reviewers who contributed to improving my paper and hence the chapters in this thesis. **Bernhard Krooss** and **Yves Gensterblum** are thanked for allowing me to visit their laboratory at the Institute of Geology and Geochemistry of Petroleum and Coal, Aachen University. I did learn a lot about sorption and the sorption measurements using manometric methods, and I enjoyed the discussions with **Yves** and **Alexej**. Moreover, I want to thank **Barbara Dutka, Jerzy Krawczyk** and **Mirosław Wierzbicki** for giving me an opportunity to work with them at the Strata Mechanics Research Institute of the Polish Academy of Science. **Mateusz Kudasik** and **Norbert Skoczylas** are also appreciated for their kindly help. I really enjoyed the time in Krakow. Last but not least, I am grateful to **Bartłomiej Jura** and **Jacek Skiba** for collecting more coal samples from the Brzeszcze mine for my on-going research. **Dominika Kasjaniuk** is also thanked for the negotiation and transportation of the coal samples.

Finally, I would like to convey my thanks to the Chinese community in the Netherlands, to my friends in China, and to my parents and family members. 感谢在荷兰的兄弟姐妹，是你们的存在让这里不太寂寞。感谢帅哥，你的陪伴和招待总是很给力。感谢我国内的朋友们，感谢陈老师，张老师，感谢矿大篮球队的兄弟们，你们的热情招待让我感动，谢谢你们，一辈子的兄弟。感谢王大牌帮助设计封面图片。感谢张璟玮，你的鼓励与支持让我变的更好：金玉良缘，坚金砺所利，玉琢器乃成。

感谢父母、家人的支持，陪伴，以及默默的付出。我知道你们永远在家里牵挂着我，等待着我，不论我长到多大，走到多远。我永远深深的爱着你们！最后，将这本论文送给那一去不复返的青春。怒吼吧，青春：“我要纵身跳入时代的奔走，我要纵身跳入时代的年轮：苦痛，欢乐，失败，成功，我都不问，男儿的事业原本要昼夜不停”（歌德《浮士德》）。

Curriculum Vitae

Jinfeng Liu

Date of birth:	30 August 1985
2001-2004:	Shengli No.1 high school, Shandong, China
2004-2008:	B.Sc. in Engineering Mechanics, China University of Mining and Technology, Beijing, China
2008-2011:	M.Sc. in Engineering Mechanics, specialised in geo-mechanics, China University of Mining and Technology, Beijing, China
2011-2016:	Ph.D. Experimental Rock Deformation, Utrecht University, Utrecht, The Netherlands